BINARY (e,2e) SPECTROSCOPY and MOMENTUM SPACE CHEMISTRY

by

JOHN P.D. COOK

B.Sc.(Hons), McGill University, 1976

A THESIS SUBMITTED IN PARTIAL FULFILMENT OF

THE REQUIREMENTS FOR THE DEGREE OF

DOCTOR OF PHILOSOPHY

in

THE FACULTY OF GRADUATE STUDIES

(Department of Chemistry)

We accept this thesis as conforming

to the required standard:

THE UNIVERSITY OF BRITISH COLUMBIA

November 1981

In presenting this thesis in partial fulfilment of the requirements for an advanced degree at the University of British Columbia, I agree that the Library shall make it freely available for reference and study. I further agree that permission for extensive copying of this thesis for scholarly purposes may be granted by the head of my department or by his or her representatives. It is understood that copying or publication of this thesis for financial gain shall not be allowed without my written permission.

Department of CHEMISTRY

The University of British Columbia
2075 Wesbrook Place
Vancouver, Canada
V6T 1W5

Date 27 NOVEMBER 1981

ABSTRACT

Binary (e,2e) spectroscopy is an intermediate energy electron scattering coincidence technique measuring the binding energy and spherically-averaged momentum distributions of individual valence electrons in small gaseous molecules. Momentum space chemistry is a term used to refer to the study of the attributes of molecular orbitals in the momentum space representation, rather than the usual position space representation. The relation between the two spaces is the Fourier Transform.

This thesis discusses experimental measurements and theoretical calculation of the binding energy spectra and/or momentum distributions of H_2S, COS, CO_2, NO and O_2 in detail. It also attempts to bring into the ken of ordinary chemistry concepts and principles for dealing with momentum-space molecular orbital density functions, which are essential to the understanding of the nature of momentum distributions. In order to illustrate this, specific examples of theoretical momentum and charge density maps for several molecules are discussed. Significant new understanding of the electronic structure of these molecules is attained.

The design, construction, and preliminary testing of a new binary (e,2e) spectrometer incorporating a multi-channel plate detector for improved data collection efficiency is presented.

Finally, some propositions for future directions of study are put forward.

C.E. Brion

Thesis supervisor

CONTENTS

FIGURES

Chapter 1

Chapter 2

Chapter 3

Chapter 7

Chapter 8

Appendix C

TABLES

FOREWORD

> I desired to do this for my own satisfaction,
> and I had little hope that other people
> would be interested in this work...

Due to the limitations of the computer hardware used to print the text, no subscript or superscript or bold face letters are available, and only a limited set of Greek characters can be used. Therefore, all subscript and some superscript letters are represented within curly brackets: for instance Y{lm}(θ,ϕ) denotes the complex spherical harmonic function of the polar angles θ and ϕ, with angular and magnetic quantum numbers l and m, and 2σ{u} is used to denote the σ^*(2s) antibonding orbital of N_2 with its ungerade symmetry; scalar quantities are indicated by a symbol 'x', vectors by an underscored symbol '$\underline{r}$', and matrices by a doubly-underscored symbol '$\underline{\underline{\Sigma}}$'. A full glossary of mathematical terms and nomenclature used in this work is included among the appendices to eliminate any possible confusion.

Many different molecules are discussed in this work, and as their electronic molecular orbital term symbols are difficult to remember, a table of valence electronic structure has been included in Appendix C as a reference.

Throughout this thesis an attempt is made to standardize on atomic units wherever appropriate. This means that all dimensions which describe molecular properties assume this system of units, with the notable exception of orbital energies, where electron volts are usually used.

References to articles in the scientific literature are enclosed in curly brackets. The complete citation and thesis page cross-references may be found in Appendix D.

Finally it should be noted that the substance of Chapters 4 and 5 have already appeared in the literature {Brion (1978b), Cook (1980), Cook (1981)}. Chapter 6 will shortly be submitted for publication in form similar to that appearing here. Much of the content of Chapter 7 is discussed in a paper accepted for publication in the near future, also. Each of these chapters may be read more or less independently once Chapters 1 and 2 are digested. Chapters 3 and 8 may be understood after reading Chapter 1.

ACKNOWLEDGEMENTS

'I don't know half of you
half as well as I should like;
and I like less than half of you
half as well as you deserve.'

Scientific research can seldom these days be done by one person alone, and, even though we graduate students call our theses 'original research', the ground out of which our ideas germinate has been trod by many other people. As the reader considers this dissertation he should bear in mind that it could not have been achieved without the help of these people.

For many hours of fruitful discussions about chemistry, plus many more hours spent in their company outside the lab, I must express my appreciation and high regard for Adam and Ilona Hitchcock.

For their patience, ideas, cooperation and good cheer may I thank the staff of the Department of Chemistry Technical Shops, especially Joe Sallos, Harold Chow, Mike Hatton, Brian Greene, Joe Shim, Brin Powell, and Bill Henderson. Extraordinary mention should be made of the contribution of Dr. Edward P. Gomm to the design, construction, and maintenance of the spectrometers used in

this thesis work. (The degree is honorary, and was awarded by our research group on behalf of all those with whom Dr. Gomm has worked in his 21 years, to date, at UBC.) The staff and services of the UBC Computing Centre are also gratefully acknowledged.

Many thanks to members of the Chemistry Faculty for helpful discussions, especially Dr. D. Chong and his group, Dr. Snider, and Dr. J.A.R. Coope, and from Physics, Dr. M. McMillan.

Much of this work was supported with post-graduate fellowships from UBC and NSERC, and with a pre-doctoral fellowship from the Killam Foundation. For the relief from laboratory teaching duties at the very least, and, more important, for the distinction of being selected for these awards, I express my appreciation to these institutions.

I should like to thank especially Dr. R. Mikula and Ben Clifford for their humour and assistance in my research and teaching duties at UBC. Perhaps an honourable mention in this category should go to S.F.B. Pickett who is a fascinating specimen of what appears to be a new species of graduate student.

It is a pleasure to acknowledge my good fortune in finding Dr. Chris Brion for a research supervisor. His contributions in carrying out these studies in binary (e,2e) spectroscopy were invaluable, as were his comments from a

critical reading of this thesis.

Quotations throughout this thesis are taken from that inestimable work 'The Lord of the Rings' by Professor J.R.R. Tolkien (Allen and Unwin), with the exception of that of Chapter 8 which is taken from 'The Hobbit', by the same author.

Particular contributions to specific aspects of this thesis are given below.

Chapter 4 Hydrogen Sulphide

The contributions of Dr. M.F. Guest in making available his optimised basis for H_2S and Dr. W.R. Richards for help with using the ATMOL2 package on the Oxford University computer are gratefully acknowledged. Dr. W. Domcke and his co-workers were helpful in their correspondence concerning many-body effects. I should also like to thank Dr. G. Zeiss for providing me with the results of his diffuse Gaussian basis calculations. I am indebted to Dr. I. Suzuki for the idea for the correlation diagrams. Dr. Andrew Hamnett of Oxford University provided expert assistance in the calculations and in the discussion of d-function contributions in H_2S, and pleasant hospitality during my visit to Oxford, which is much appreciated.

Chapter 5 Carbonyl Sulphide

This work was carried out in collaboration with Drs. W. von Niessen, W. Domcke, and L.S. Cederbaum, who did the theoretical work in computing the many-body Green's function ionization potentials. The experimental determination of the COS dipole (e,2e) spectrum was done by Dr. M.G. White and Mr. K.T. Leung.

Chapter 6 Carbon Dioxide

I am grateful for the assistance of Dr. D.P. Chong and co-workers in doing the Gaussian 76 calculations and for providing me with the results of the HAM/3-CI calculation. The correspondence of Dr. A. Giardini-Guidoni in the matter of the momentum density maps was very helpful.

Chapter 7 Nitric Oxide and Oxygen

The experimental results in this section were recorded at Flinders University by Dr. C.E. Brion, Prof. E. Weigold, and coworkers. Calculations of NO and O_2 wavefunctions were generously provided by Dr. A.B. Kunz and Mr. K. Bedford.

Chapter 8 The New Spectrometer

I wish to acknowledge helpful discussions with Dr. Prof. M.J. van der Wiel and Dr. S. Daviel.

To My Parents

Sam went red to the ears and muttered
something inaudible, as he clutched
the box and bowed as well as he could.

CHAPTER 1 INTRODUCTION AND THEORY

'Ah!' said Gandalf.
'That is a very long story...
I will risk a brief tale...'

This dissertation is an exploration of the electronic structure and momentum space chemistry of some small gaseous molecules, as revealed by their binding energy spectra and momentum distributions obtained from theoretical models and binary (e,2e) spectroscopic measurements.

The term 'electronic structure' refers to the energies and wavefunctions of the electrons in the molecule, and is generally understood by all chemists.

'Momentum space chemistry' is on the other hand a very rarely encountered term and needs amplification. While a particle may be completely described (independent of time) by its wavefunction in terms of the three orthogonal spatial coordinates, it is also true that this wavefunction may be recast in the three orthogonal momentum coordinates: both representations are equally valid, and neither could be said to take precedence over the other, but for practical

purposes we have come to use the former almost exclusively. The use of the term 'momentum space chemistry' therefore denotes the electronic structure and bonding behaviour of atoms and molecules as viewed in the momentum-space representation. The investigation of this field is not only a novel and interesting exercise in itself, but is also vital to the understanding of momentum distributions, and constitutes a large part (Chapter 2) of this thesis.

Whenever one can establish the energies of all the free electrons in an ionizing collision with some target, one has the ability to measure the 'binding energy' of the ionized particle, namely: that minimum energy necessary to remove the particle from the target. This is not quite the same thing as the energy that the ionized particle had when it was bound in the molecule, but is closely related to it, and is an important piece of information. Binding energy spectra, both for their intrinsic value and in comparison with theory, also form a large part of this thesis (Chapters 4-6). The theoretical calculation of binding energy spectra has made great progress in the last decade, especially in the many-body Green's function method. Much of the experimental work presented here complements these theoretical predictions, sometimes revealing their inadequacy and sometimes showing impressive agreement.

The term 'momentum distribution', like 'momentum space chemistry', is seen uncommonly in the mainstream of

chemistry, usually enjoying use only in Compton scattering and solid state chemistry circles. It means almost exactly what it says: the distribution of momentum irrespective of direction, or in other words, a probability distribution of the magnitude of a particle's momentum. The ability to measure orbital-selective momentum distributions is the feature which distinguishes and elevates binary (e,2e) spectroscopy in relation to other techniques, which allow only such indirect probes of the electronic structure as binding energies, Compton profiles, branching ratios, Franck-Condon envelopes, shape resonances, and so on: the momentum distribution is the closest that chemistry has yet come to measuring the wavefunctions of the electrons in their molecular orbitals. (One should of course always bear in mind that the molecular orbital is not a physical phenomenon, but is only a convenient concept arising out of the one-electron self-consistent field approximation of the N-electron wavefunction, yet is adequate for much of the discussion in this work. Also, it is in fact the probability density, or the squared modulus of the wavefunction which is a measurable quantity, not the wavefunction itself.) The experimental measurement, theoretical calculation, and discussion of momentum distributions form the most important part of this thesis (Chapters 2,4-7).

Though I have been speaking of both theoretical and experimental investigations into binary (e,2e) spectroscopy,

this thesis must finally be considered to be an experimental work. I shall spend considerable time discussing the instrument used to record the data (Chapter 3) and the design, construction, and preliminary testing of a new spectrometer incorporating significant technological advances (Chapter 8).

1.1 The (e,2e) Reaction

In the following discussions it should be noted that no attempt has been made to be rigorous and complete in the derivations and equations. This is the realm of the scattering theorist, and as an experimental chemist I accept their findings and shall attempt to demonstrate the principles and approximations of the theory without delving into the complex mathematical framework. The theory has been extensively discussed in the literature {Neudachin (1969), Hood (1973), McCarthy (1976a), McCarthy (1976b), Weigold (1978)}.

(e,2e) electron impact spectroscopy is a scattering experiment in which an incident electron, with energy E_0 and momentum vector $\underline{k}_0$, collides with a target system M which initially has N-electrons and total energy E(M) and is assumed to be at rest in the laboratory frame. The incident

electron is made sufficiently energetic to ionize a bound electron from M giving rise to two outgoing electrons of energies E_1 and E_2 and momenta $\underline{k}_1$ and $\underline{k}_2$ respectively, leaving behind an (N-1)-electron system M^{*+} with total energy $E(M^{*+})$. The target is usually initially in its electronic ground state, but after the collision the (N-1)-electron system need not necessarily be in its ion ground state, hence the asterisk in the notation M^{*+}. The reaction can be written:

$$(1.1)\quad e_0(E_0,\underline{k}_0) + M(N,E(M)) \longrightarrow$$

$$M^{*+}(N-1,E(M^{*+})) + e_1(E_1,\underline{k}_1) + e_2(E_2,\underline{k}_2)$$

The (e,2e) spectrometer is arranged so that the kinematics of all the free electrons entering and leaving the scattering region (i.e. the energies and trajectories E_0, E_1, E_2, $\underline{k}_0$, $\underline{k}_1$ and $\underline{k}_2$) are completely determined (to within some experimental uncertainty). At this point it can be seen that the (e,2e) technique can measure the binding energies of the electrons of the target. Conservation of energy requires that:

$$(1.2)\quad E_0 + E(M) = E(M^{*+}) + E_1 + E_2$$

so one can define ϵ as:

$$(1.3)\quad \epsilon = E(M^{*+}) - E(M) = E_0 - E_1 - E_2$$

where ϵ is understood as the binding energy of the electron

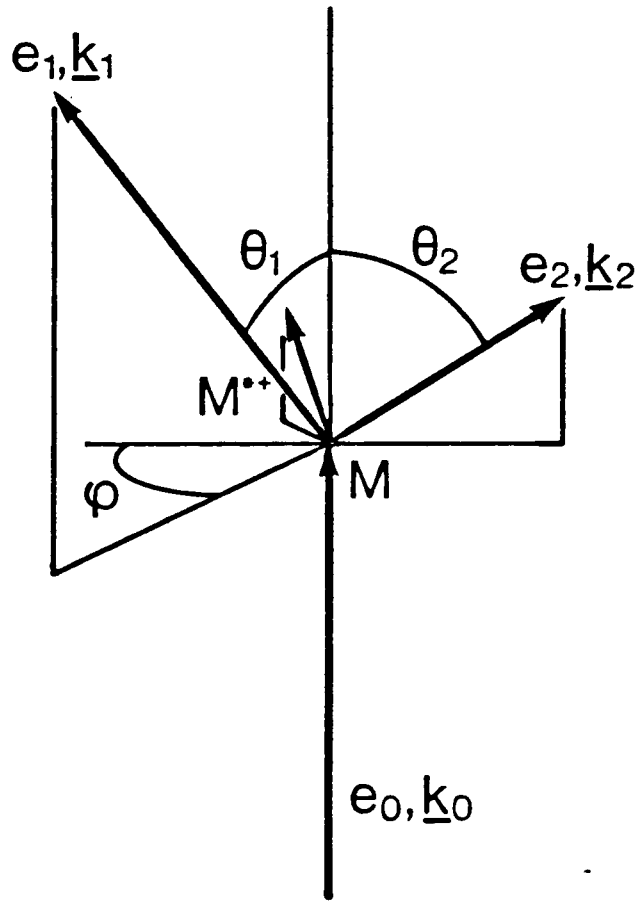

Figure 1.1 Kinematics of the (e,2e) reaction

that is ionized from the target, or more precisely, the difference in the energies of the N-electron target before collision and the (N-1)-electron target after the collision. Therefore the measurement of the (e,2e) signal as a function of E_0 shows the spectrum of final (N-1)-electron state energies of the target relative to the N-electron ground state. This historically has been called a binding energy spectrum since in earlier days it was found that, in simple systems and over a limited energy range, ionization of an electron from an orbital produced one final ion state, and so, one peak in the energy spectrum. However, since we now know that in many instances more than one final ion state can result from the ionization of one electron, perhaps the term 'binding energy spectrum' should be retired, and be replaced with the more accurate term 'final state energy spectrum'. The term 'separation energy' has also been used in this context {McCarthy (1976a)}.

One of the assets of the (e,2e) technique is that binding energy spectra are not limited in their range, unlike He-I PES spectra, and are able to explore the region beyond 21.2eV, opening up much new structure.

1.2 The Binary (e,2e) Process

One now goes on to place some restrictions on the kinematics of the general (e,2e) process. The experiment is required to detect only those collisions where:

(1) The interaction between the incident electron and the electron to be ionized is the strongest interaction in the collision event;

(2) The incoming and outgoing electrons do not interact significantly with the other particles in the target system.

This is known as the 'binary encounter condition', and gives rise to the name 'binary (e,2e)' for this experiment.

The first condition is met in the 'symmetric' scattering geometry where:

(1.4) $E_1=E_2=\frac{1}{2}(E_0-\epsilon)$; $\theta_1=\theta_2=45^\circ$

This geometry means that the incident electron and the bound electron will pass (thinking in classical mechanics for the moment) close to each other, and therefore that the interaction between them is strong. The second criterion can be obtained by ensuring that the incident and exit electrons are of sufficiently high energy as to be undisturbed to any significant extent by the other particles in the system from their energies and trajectories specified in the first criterion.

1.2.1 The binary (e,2e) form factor

Putting this into a mathematical formulation requires some definitions: take the initial state wavefunction of the entire scattering system Ψ to be the product of the N-electron target ground state $\Psi_0\{N\}$ and the free incident electron state wavefunction $X_0(\underline{k}_0,\underline{r}_0)$:

(1.5) $\Psi = \Psi_0\{N\}\ X_0(\underline{k}_0,\underline{r}_0)$

Similarly the total final state wavefunction Φ is taken as the product:

(1.6) $\Phi = \Phi\{N-1\}\ X_1(\underline{k}_1,\underline{r}_1)\ X_2(\underline{k}_2,\underline{r}_2)$

where $\Phi\{N-1\}$ is the (N-1)-electron final ion state, and X_1 and X_2 are the outgoing free electron wavefunctions. The amplitude M for a system to go from its initial state Ψ to its final state Φ in the influence of some interaction potential V is (using Dirac bra-ket notation):

(1.7) $M = \langle\Phi|V|\Psi\rangle$

Since the only interaction allowed is that between the incident and bound electrons, the interaction potential reduces to the Coulomb potential between these two electrons. This is written as $T(\underline{r}_1,\underline{r}_2;\underline{r},\underline{r}_0)$: the amplitude for two electrons starting at $\underline{r}$ and $\underline{r}_0$, to scatter via the r^{-1} potential to points $\underline{r}_1$ and $\underline{r}_2$. Now the amplitude for the binary (e,2e) process is given by:

$$(1.8)\quad M = \langle X_1(\underline{k}_1,\underline{r}_1)\ X_2(\underline{k}_2,\underline{r}_2)\ \Phi\{i,N-1\} \times |T(\underline{r}_1,\underline{r}_2;\underline{r},\underline{r}_0)|\Psi_0\{N\}\ X_0(\underline{k}_0,\underline{r}_0)\rangle$$

Next, the following approximations will be made on the above equation:

(1) The N-electron target wavefunction will be expressed as an antisymmetrized product of N one-electron molecular orbital wavefunctions, and the (N-1)-electron ion state wavefunction by a similar product, leaving out the ith MO from which an electron was ionized:

$$(1.9)\quad \Psi_0(N) = A \prod_j \psi\{j\}(\underline{r})$$

$$\Phi\{i,N-1) = A \prod_{j\neq i} \psi\{j\}(\underline{r})$$

where A is the antisymmetrization operator and $\psi\{j\}(\underline{r})$ is a one-electron molecular-orbital wavefunction. If necessary, configuration interaction may be incorporated in both the initial and final states.

(2) The impulse approximation is made in the treatment of the collision between the incident electron and the bound electron. In other words, it is assumed that the collision event takes very nearly zero time and therefore is separable from the motion of other particles in the target.

(3) The free electron wavefunctions in and out of the

scattering region are treated as plane waves. This assumes that the free electrons do not interact significantly with the electrons of the target other than with the electron being ionized, and that they are negligibly distorted by the potential of the nuclei. The wavefunction of a free electron with momentum $\underline{k}$ is written as:

$$X(\underline{k},\underline{r}) = e^{i\underline{k}.\underline{r}}$$

Approximations 2 and 3 above comprise what is known as the plane wave impulse approximation (PWIA).

Under these approximations the amplitude is separable:

$$(1.10)\quad |M|^2 = |T|^2\ |C|^2\ |F|^2$$

where $|C|^2 = |\langle\Phi\{i,N-1)|\Psi\{i,N-1)\rangle|^2$

The information of interest to chemists is contained in the last factor, which is written in full as:

$$(1.11)\quad |F|^2 = \left|\int d\underline{r}\ e^{-i\underline{q}.\underline{r}}\ \psi\{i\}(\underline{r})\right|^2$$

where $\underline{q} = \underline{k}_1 + \underline{k}_2 - \underline{k}_o$

The significance of $\underline{q}$ is understood by the following argument: if the N-electron target system is assumed to be at rest and the ith electron has a momentum $\underline{p}$ at the instant

of collision, then the total momentum of the 'core' (the remaining particles of the target) must be $-\underline{p}$. If the core is assumed to be so massive that its motion is unaffected by the (e,2e) collision, then conservation of momentum requires that:

(1.12) $\underline{k}_o = \underline{k}_1 + \underline{k}_2 - \underline{p}$

or $\underline{p} = \underline{k}_1 + \underline{k}_2 - \underline{k}_o = \underline{q}$

In other words $\underline{q}$ in equation 1.11 is identical to the momentum of the bound electron at the instant of ionization. This means that equation 1.11 is the Fourier Transform of the ith position-space molecular orbital into its momentum space representation.

$$(1.13)\quad \psi\{i\}(\underline{p}) = (2\pi)^{-3/2} \int d\underline{r}\; e^{-i\underline{p}.\underline{r}}\; \psi\{i\}(\underline{r})$$

and

$$(1.14)\quad |M|^2 = |T|^2\, |C|^2\, |\psi\{i\}(\underline{p})|^2$$

Generally $\underline{p}$ and $\underline{q}$ will be used interchangeably, although $\underline{q}$ carries the connotation of being experimentally determined, and $\underline{p}$ of being the independent variable of a theoretical wavefunction. The general name for T is the 'half-off-shell Mott scattering factor' and is sometimes written $\sigma\{Mott\}$. Mott scattering is named after its originator N.F. Mott, and denotes the scattering behaviour of any two identical free particles in the Coulomb potential including exchange

effects. 'Half-off-shell', or more fully, 'half-off the energy shell', refers to the fact that one electron is not actually free, but has a binding energy ϵ, although it is treated as if it were a free particle. T is an exactly known function and is given by this equation:

$$(1.15)\quad T = \frac{1}{4\pi^4}\,\frac{2\pi\eta}{e^{2\pi\eta}-1}\left[\,|\underline{\kappa}'-\underline{\kappa}|^{-4} + |\underline{\kappa}'+\underline{\kappa}|^{-4} - |\underline{\kappa}'-\underline{\kappa}|^{-2}|\underline{\kappa}'+\underline{\kappa}|^{-2}\cos(\eta\ln\{|\underline{\kappa}'+\underline{\kappa}|^2\,|\underline{\kappa}'-\underline{\kappa}|^{-2}\})\right]$$

where $\eta = (2\kappa')^{-1}$; $\underline{\kappa} = \frac{1}{2}(\underline{k}_0+\underline{q})$; $\underline{\kappa}' = \frac{1}{2}(\underline{k}_1-\underline{k}_2)$.

Plots of $|T|^2$ as a function of θ and ϕ at 400eV and 1200eV are given in figures 3.10 and 3.11.

$|C|^2$ is the relaxation factor describing the overlap of the remaining non-interacting electron wavefunctions in the target, and in the frozen orbital approximation is assumed to be unity.

Since the target is usually a gaseous species and at thermal energies its orientation is completely random one must replace $|\psi\{i\}(\underline{p})|^2$ by its spherical average:

$$(1.16)\quad |\psi\{i\}(p)|^2 = (4\pi)^{-1}\int d\Omega\ |\psi\{i\}(\underline{p})|^2 = F\{i\}(q)$$

where $p = |\underline{p}|$, and $d\Omega = \sin\theta d\theta d\phi$.

By simple trigonometry it is possible to define q as a function of scattering angles and energies, which are the

quantities determined by the electron source and detectors in the spectrometer. For the symmetric scattering geometry:

$$(1.17)\quad q = \{(2k\cos\theta - k_0)^2 + (2k\sin\theta \sin\tfrac{1}{2}\phi)^2\}^{\frac{1}{2}}$$

where $k=k_1=k_2$; $\theta=\theta_1=\theta_2$.

The full equation for the binary (e,2e) differential cross-section for scattering of two electrons of energy $E_1=\frac{1}{2}(E_0-\epsilon)$ into solid angles $d\Omega_1 d\Omega_2$ is:

$$(1.18)\quad \frac{\Delta^5\sigma}{dE_1 d\Omega_1 d\Omega_2} = (2\pi)^4\, N\{occ\}\, S\{i\}\, \frac{k_1 k_2}{k_0}\, |T|^2\, F\{i\}(q)$$

The factor k_1k_2/k_0 is a kinematic normalization factor; N{occ} gives the occupancy of the orbital being ionized; S{i} includes all effects which alter the relative intensity of the measured structure, but do not change its shape: these include relaxation effects, pole strengths (discussed in section 1.4.1), absorption effects, and so on, but not experimental factors like gas density, resolution, etc.

1.2.2 The momentum distribution

If the spectrometer is arranged so that both analysers are fixed at $\theta=45°$ and one analyser is allowed to revolve in the ϕ dimension (see figure 1.2), then the functional form of σ\{Mott\} is much simplified and is nearly constant as a function of ϕ angle, and a large range of p may be accessed:

$$(1.19)\quad |T|^2 = \frac{1}{2\pi^4}\,|\underline{k}_o-\underline{k}|^{-4}\,\frac{2\pi n}{e^{2\pi n}-1}$$

$$2\pi n = \pi\{\sqrt{2}k\sin\theta\,\sqrt{\cos\phi+1}\}^{-1}$$

$$|\underline{k}_o-\underline{k}|^{-4} = \{k^2+k_o^2-2kk_o\cos\theta\}^{-2}$$

In this arrangement the binary (e,2e) cross-section, in the PWIA, is proportional to the spherical average of the squared momentum-space wavefunction of the molecular orbital selected by the energy conservation rules. This is called the symmetric non-coplanar scattering geometry, and is the technique used to obtain the experimental results presented in this dissertation. Another usual scattering geometry is the symmetric coplanar arrangement where the azimuthal angle is fixed at $\phi=0°$, and θ, the polar angle of the two analysers, is the scanned parameter (figure 1.2). However here the cross-section is a strong function of both $|T|^2$ and the form factor F{i}(q). This geometry has more application in investigating the physics of the collision process, but is less useful for probing the momentum distribution (and thus exploring momentum space chemistry) as, in order to get the form factor out, the behaviour of the incident and scattered waves must be accurately approximated. The measurement of the binary (e,2e) cross-section in the symmetric non-coplanar geometry (or the calculation of this function) plotted against q defines the term 'momentum distribution' (MD), used in this dissertation. This function

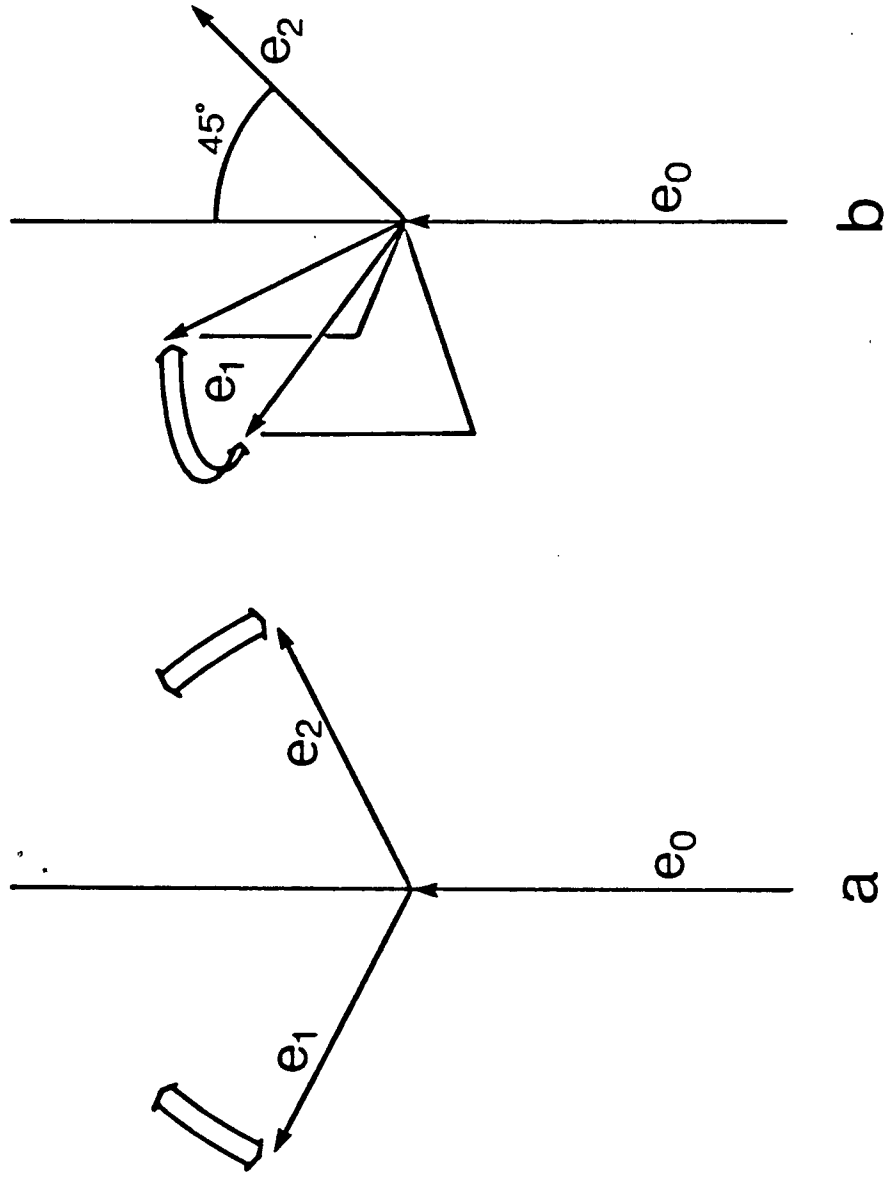

Figure 1.2 Binary (e,2e) scattering geometries:
(a) Symmetric coplanar
(b) Symmetric non-coplanar

is so closely related to the position-space molecular orbital wavefunction that it is very useful in studying the electronic structure of atoms and molecules, and also in judging the quality of theoretical electronic wavefunctions. The momentum distribution, since in principle it is unique to the ionizing molecular orbital, is also a definitive tool in the assignment of peaks in binding energy spectra {Hood (1976b)}.

Where ionization from a given ground state molecular orbital produces more than one final ion state, the binary (e,2e) technique is in principle capable of identifying the origin of each final state peak (as each peak will show a momentum distribution characteristic of a particular ground state orbital) {Hamnett (1977), Cook (1980), McCarthy (1976a)}. Since the momentum distribution is a unique fingerprint of the orbital, the binary (e,2e) method provides more detailed information on the identity of peaks than does photoelectron spectroscopy. In this regard the momentum distribution information is in most cases more specific than that provided by the arguments used in PES based on variations in the relative intensity of σ and π orbitals with photon energy {Siegbahn (1969), Rabalais (1977)}. It must first be made clear, however, under what conditions the PWIA approximations are valid and where they break down.

1.2.3 The validity of the PWIA

It has been established by several studies {McCarthy (1976a), McCarthy (1976b), Camilloni (1977), Camilloni (1978)} that generally for valence electrons an incident energy of 400eV (plus the binding energy ϵ) is necessary to ensure that the measured form factor is equivalent to the shape of the momentum distribution, though not necessarily of the correct intensity relative to the momentum distributions of other molecular orbitals in the target. This means that the free electron velocities are high enough that their motions are very nearly undisturbed by the potential of the nuclei and the other electrons of the system, and therefore, that plane waves are a sufficiently accurate mathematical representation of the free electron wavefunction. In order to get reasonably correct relative intensities it has been found necessary to go to incident energies of 1000eV or more. This has advantages and disadvantages over 400eV operation which are discussed in Chapter 3.

In determining the shape of a momentum distribution, breakdown of the PWIA is most likely to occur for the inner valence and core orbitals, as these are spatially deeper inside the molecule where the incident and outgoing particle waves are more likely to be distorted by the field of the nuclei. If such a breakdown occurs, it usually takes the form of a distortion of the momentum distribution in the

region $q>1.5a_0^{-1}$ as this region is somewhat more sensitive to the form of the R-space wavefunction near the nuclei. (This is a consequence of the Reciprocity property of the Fourier Transform relationship of R-space and P-space, further described in Chapter 2.)

1.3 Binary (e,2e) in Comparison with Other Methods

As the binary (e,2e) results will be compared with other types of spectroscopic data, a short description of some of them is included here.

1.3.1 Binding energy spectra

There are many other techniques capable of measuring the binding energies of electrons: photoelectron and photoabsorption spectroscopy in their many forms, dipole (e,2e) spectroscopy and electron energy-loss spectroscopy, and others. The one most closely related to binary (e,2e) is, not surprisingly, dipole (e,2e) spectroscopy {Inokuti (1971), Brion (1975), Brion (1977), Brion (1978a), Brion (1981)}. As the experimental work in this thesis is often discussed in relation to dipole (e,2e) results I shall briefly describe this technique.

The dipole and binary (e,2e) reactions are similar in

that there is one electron incident on a target, the target is ionized by the passage of this electron, and two electrons exit: they differ in that the one requires fast forward scattering kinematics, and the other symmetric scattering. 'Fast forward scattering' means that the incident electron has very high energy (E_0>3keV), and, in collision with the target, suffers only a relatively small loss of energy (E) to the target and its direction remains (in the ideal case) unaltered. Whereas symmetric scattering implies a binary encounter collision - the closest possible between the interacting electrons - fast forward scattering implies a large impact parameter, wherein the interaction between incident and target electrons takes place over a large distance. The electric field felt by the target in such a collision is, to a very good approximation, the same as that induced by the absorption of a photon of energy E. When the energy loss is sufficient, an electron may be ionized from the target with selection rules which are identical to their optical counterparts, and the cross-section is related to the photoionization cross-section by a simple kinematic relation. As with binary (e,2e), the kinematics of all free electrons are determined by the spectrometer, and binding energy spectra are obtained by scanning the ejected electron energy spectrum. However, the peak intensities in such a spectrum are determined partly by the dipole matrix element and are only indirectly related to binary (e,2e) peak intensities; such factors as

occupation number, final state CI coefficients, relaxation factors - anything not directly involved in the e-e interaction - will of course be the same for both methods. The full dipole (e,2e) cross-section is given by {Inokuti (1971), Brion (1981), Hamnett (1976)}:

$$(1.20)\quad \frac{d\sigma}{d\Omega} = \frac{2}{E}\,\frac{k\{n\}}{k_0}\,\frac{1}{K^2}\,\frac{df(K)}{dE}$$

where E and K are the energy loss and momentum transfer respectively of the incident electron to the target, k{n} and k_0 are the momenta of the ejected and incident electrons, and df(K)/dE is the generalized oscillator strength for the ionization event. In the limit of very small momentum transfer, $K^2 \to 0$, the generalized oscillator strength reduces to the optical oscillator strength df_0/dE.

1.3.2 Momentum distributions

There is no technique other than binary (e,2e) spectroscopy which is capable of determining momentum distributions of individual electrons in molecules. There are several techniques for measuring total molecular momentum distributions - Compton scattering and positron annihilation are examples - but these are crude tools, sensitive to individual molecular orbital momentum distributions only insofar as they affect the total N-electron distribution.

1.4 Theoretical Treatments

Many types of theoretical calculations are compared with the experimental results. The following two sections give brief descriptions of them.

1.4.1 Binding energies

Given an LCAO-MO-SCF wavefunction the simplest approximation for the electron binding energies in a molecule is Koopmans' theorem {Koopmans (1933)}: the ionization potentials are assumed to be equal to the orbital energies which are the eigenvalues of the one-electron Fock operator:

(1.21) $IP = -\epsilon\{i\}$

The theorem ignores relaxation and correlation effects, but in the outer valence orbitals of all but the most electronegative elements the two effects are found empirically to nearly cancel.

The accuracy of these orbital energies depends on the size of the Fock space, and the theorem gives energies to second order if the Fock space is large (i.e. if the quality of the wavefunction approaches the Hartree-Fock limit). There is still, nevertheless, only one ionization potential predicted per ground state molecular orbital, which is grossly inaccurate for some systems. The revelation of

complex many-electron structure in the ionization of certain electrons of certain molecules, and the breakdown of Koopmans' theorem which predicts only the centroid of such structure, is discussed in some detail in the following chapters.

The many-body Green's function method (MBGF) {Cederbaum (1975a), Cederbaum (1975b), Cederbaum (1977)} is one which goes beyond Koopmans' theorem and will be shown to be successful in accounting semi-quantitatively for much of the complex structure in the ionization of inner valence electrons. The one-electron picture assumes that ionization of a valence electron from a molecule will result in only one final ion state (ignoring effects like spin-orbit splitting), and consequently give rise to only one peak in the binding energy spectrum. For many molecules {Cederbaum (1977)} the one-electron picture is obviously breaking down to a very significant extent, and ionization of especially the more strongly bound inner valence electrons gives rise to a host of final ion states distributed in energy from 20 to 50eV. This is called 'Multiple Final State (MFS) structure'. No single one of these states has the relatively large transition amplitude attributable to a clearly identifiable, single particle 'parent' ion state. This is different from the situation in core ionization where there is a high intensity peak clearly identifiable as a parent, with a number of much less intense

satellites around it.

The MBGF method is based on diagrammatic propagator theory {Mattuck (1967), Thouless (1961)}: the one-electron propagator $G(\underline{r},t;\underline{r}',t')$ is the amplitude for a particle created in a system at point $\underline{r}$ at time t to propagate via all possible paths to point $\underline{r}'$ at time t'. One such path is that where the particle is free, with energy ϵ_0, and goes straight from $\underline{r}$ to $\underline{r}'$ without interaction with any potential: this is described by the free particle propagator $G_0(\underline{r},t;\underline{r}'t')$ and is represented diagrammatically in figure 1.3a. If the free electron is perturbed by some potential V, then another path is for the electron to propagate to point $\underline{r}_1$, in time t_1, interact with the potential (e.g. another electron in the system), and then propagate to $\underline{r}'$ at time t'. Diagrammatically this is represented in figure 1.3b. Yet another pathway would be scattering twice off the potential before propagating to $\underline{r}',t'$ (figure 1.3c), and so on:

$$(1.22)\quad G(\underline{r},t;\underline{r}',t') = G_0(\underline{r},t;\underline{r}',t') + \int dt_1\, G_0(\underline{r},t;\underline{r}_1,t_1)VG_0(\underline{r}_1,t_1;\underline{r}',t') + \iint dt_1 dt_2\, G_0(\underline{r},t;\underline{r}_1,t_1)VG_0(\underline{r}_1,t_1;\underline{r}_2,t_2)VG_0(\underline{r}_2,t_2,\underline{r}',t') + \ldots$$

The influence of this potential is said to convert the simple free particle of energy ϵ_0, into a quasi-particle of energy ϵ. When the Fourier transform from the time to the

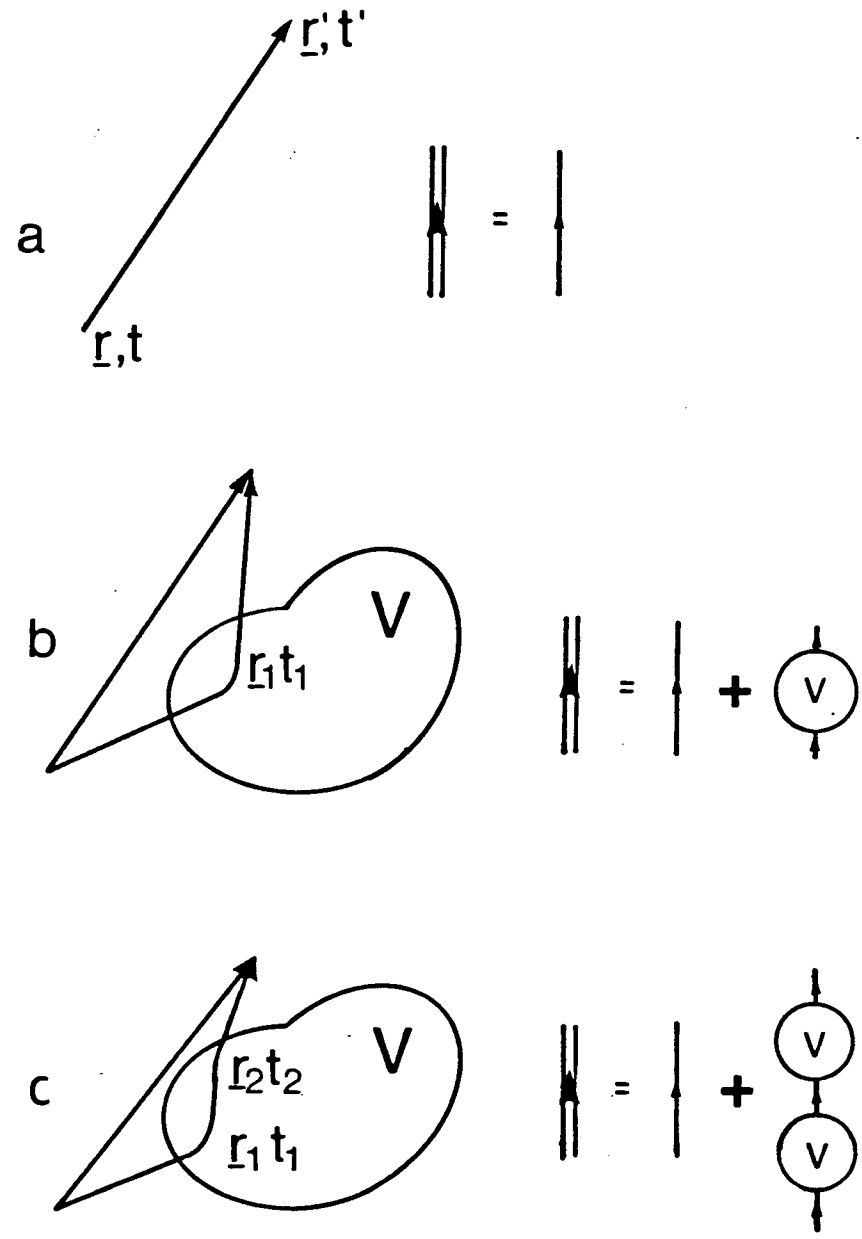

Figure 1.3 Green's function propagators:
(a) Free particle: $G=G_0$
(b) Single interaction: $G=G_0+G_0VG_0$
(c) Double interaction: $G=G_0+G_0VG_0VG_0$

energy representation is taken, the folded products become simple products:

$$(1.23)\quad G(\omega) = G_0(\omega) + G_0(\omega)VG_0(\omega) + G_0(\omega)VG_0(\omega)VG_0(\omega) + \ldots$$
$$= G_0(\omega) + G_0(\omega)VG(\omega)$$
$$= G_0(\omega)\ \{1+VG_0(\omega)+(VG_0(\omega))^2+(VG_0(\omega))^3+\ldots\}$$

and the form of $G(\omega)$ is $(\omega-\epsilon+i\delta)^{-1}$ where ϵ is the particle's energy. It is seen that the propagator $G(\omega)$ has a pole at the energy of the particle. The imaginary part of the energy $i\delta$ gives the quasi-particle a finite lifetime, if δ is not zero. Correspondingly the form of $G_0(\omega)$ is $(\omega-\epsilon_0)^{-1}$ where ϵ_0 is the energy of the particle when it is unperturbed by the potential. The second factor in equation 1.23 is a geometric series which is equal in the limit to $(1-VG_0)^{-1}$. Substituting this back gives:

$$G(\omega) = G_0(\omega)\{1-VG_0(\omega)\}^{-1}$$

or

$$(1.24)\quad G^{-1}(\omega) = G_0^{-1}(\omega) - V = \omega - \epsilon_0 - V$$

This is a simple version of the Dyson equation: if $G(\omega)$ has a pole at the energy of the quasi-particle ϵ then $G^{-1}(\omega)$ must have a node or zero point here, and so the energy of the quasi-particle is found by looking for the place where:

$$(1.25)\quad \omega-\epsilon_0 = V$$

This situation applies equally to the propagation of a quasi-hole state - i.e. how the hole created by the instantaneous removal of a particle from a system propagates. Instantaneous removal of an electron is a fairly good description of the (e,2e) ionizing event, and so the technique finds application here. There are differences of course: the totally free quasi-hole is replaced by the Hartree-Fock limit approximation (i.e. Koopmans' theorem) and the simple potential V is replaced by $\underline{\underline{\Sigma}}(\omega)$, the 'self-energy' matrix which describes the effect, beyond the HF limit, of all the other electrons on the propagation of the quasi-hole; but the basic method of searching for zeroes of $\underline{\underline{G}}^{-1}(\omega)$ by solving $\omega\underline{\underline{1}}-\underline{\underline{\epsilon}}=\underline{\underline{\Sigma}}(\omega)$ is still the same, except that $\underline{\underline{\epsilon}}$ is now a matrix of the eigenvalues of the one-electron Fock operator:

$$(1.26)\quad \underline{\underline{G}}^{-1}(\omega) = \omega\underline{\underline{1}} - \underline{\underline{\epsilon}} - \underline{\underline{\Sigma}}(\omega)$$

It is in the calculation of $\underline{\underline{\Sigma}}(\omega)$ where the greatest difficulties arise, and where most of the efforts of Cederbaum and coworkers have been expended. They include all diagrams of second and third order in their computation of $\Sigma(\omega)$, and some diagrams of fourth order. Where the final ion state energy structure is very complex the two-particle-one-hole Tamm-Dancoff approximation (2ph-TDA) {Schirmer (1978)} is made: only diagrams with two hole lines and one particle line are allowed in $\underline{\underline{\Sigma}}(\omega)$.

The Green's function may also be written in the form of propagation of particle states in time:

$$(1.27)\quad G(t,t') = e^{-i(E\{N-1\}-E\{N\})(t-t')} \times \sum_i \langle\Psi_0\{N\}|a^*\{k\}|\Psi\{i,N-1\}\rangle\langle\Psi\{i,N-1\}|a\{j\}|\Psi_0\{N\}\rangle$$

where $a^*\{k\}$ and $a\{j\}$ are the creation and annihilation operators for particles in states k and j respectively. This describes the propagation of a hole created in orbital j as it interacts with the remaining electrons, and in the energy representation is:

$$(1.28)\quad G(\omega) = \sum_i \frac{\langle\Psi_0\{N\}|a^*\{k\}|\Psi\{i,N-1\}\rangle\langle\Psi\{i,N-1\}|a\{j\}|\Psi_0\{N\}\rangle}{\omega + E\{N-1\} - E\{N\} - i\delta}$$

This again shows that $G(\omega)$ will have poles at the ionization potentials of the system, but also that the strength of such poles (determined numerically from solutions of equation 1.26) is given by:

$$(1.29)\quad p\{n\} = \sum_i |x\{i,n\}|^2$$

where $x\{i,n\} = \langle\Psi\{n,N-1\}|a\{i\}|\Psi_0(N)\rangle$

This pole strength is a factor in the binary (e,2e) intensity. $x\{i,n\}$ is called the 'hole state amplitude'. The diagonal approximation has been made in equation 1.29: interference terms of the type $x^*\{i,n\}x\{j,n\}$ are ignored,

although experimental verification of this interference effect has recently been found {Bradshaw (1980)} for acetylene. When the one-particle ionization picture is valid and relaxation effects are small, then all terms in the summation vanish except for i=n, and there is one main pole whose strength approaches unity. When relaxation and correlation effects become important then the single main pole splits into many poles over which the total intensity is distributed. It should be noted that the calculated energies and intensities of the numerous inner valence lines cannot be expected to be quantitatively accurate owing to the limitations inherent in the 2ph-TDA approach as well as to the usually significant basis set dependence of the results in this energy region {Cederbaum (1980)}.

This technique has recently had much success in modelling binding energy spectrum structure which arises when ionization fron one ground state orbital leads to many final ion states. For a comprehensive treatment of this technique the reader is directed to their excellent review article {Cederbaum (1977)} and to other articles {Domcke (1979), Schirmer (1977), Cederbaum (1978), Cederbaum (1980)}.

Other methods of computing IPs beyond Koopmans' theorem will also be cited, but as these are more familiar to us, I shall not describe them here.

1.4.2 Momentum distributions

Almost all the wavefunctions used to compute theoretical momentum distributions for comparison with experiment are the result of LCAO-MO-SCF Roothaan-Hartree-Fock calculations. The qualifying factor in such wavefunctions is the size and flexibility of the basis set used in the calculation. Owing the the energy optimization criterion (variational principle) used in the usual type of LCAO-MO-SCF calculation, the resulting molecular orbital wavefunctions sometimes poorly represent the true spatial distribution of electron density {Hood (1976a), Hood (1977), Goddard (1978)} except in the nuclear regions where the major contribution to molecular energies is made. It is, however, the more spatially extended regions of the charge distribution which are of prime importance in the understanding of chemical bonding, momentum distributions, and reactivity. It is part of the aim of this dissertation to offer to the researchers who carry out such calculations some direction in their choice of basis set which will produce not only good energies, but also good wavefunctions; the one does not always imply the other. Good wavefunctions in turn allow the accurate calculation of dipole moments, polarizabilities {Zeiss (1979)} and so on.

CHAPTER 2 MOMENTUM SPACE CHEMISTRY

...in secret chambers withered men
compounded strong elixirs or in
high towers asked questions of the stars.

Almost all of modern chemistry is conceptualized in position space (R-space): we think about the 'location' of a particle, or the spatial 'shape' or 'size' of an orbital, or the 'structure' of a molecule. However, in dealing with the results of binary (e,2e) spectroscopy one requires some facility in thinking in momentum space (P-space) - which does not come easily when one is firmly rooted, bodily and conceptually, in position space. This chapter is an exploration of the properties of momentum-space wavefunctions, and attempts to present some simple rules for estimating the shape of orbitals in P-space from a knowledge of their R-space counterparts and of the Fourier Transform relationship.

Most of the principles of momentum space chemistry have already been briefly outlined in the literature {Coulson (1944), Epstein (1973), Epstein (1977)} , but it is appropriate to restate and amplify them here, for they are

not generally known or understood, and also such discussions have usually been applied to Compton scattering or positron-annihilation results, not binary (e,2e).

The figures used to illustrate this chapter are contour maps of the electron and momentum density, ρ, evaluated in a plane:

$$\begin{aligned} \rho\{i\}(\underline{p}) &= \psi^*\{i\}(\underline{p})\psi\{i\}(\underline{p}) \\ \rho\{i\}(\underline{r}) &= \psi^*\{i\}(\underline{r})\psi\{i\}(\underline{r}) \end{aligned} \qquad (2.1)$$

For most diagrams 9 contour lines are shown, spaced at fractions 0.1, 0.2, 0.3 ... 0.9 of the maximum density, and in some cases three more contours are added at fractions 0.01, 0.02, and 0.05. A small numeral 9 or 12 in the figure indicates the number of contours. This is not the best way to depict density functions: it would be preferable to plot contours which enclose various fractions of the total density, but such computer algorithms were not available when these programs were written.

The sign of the wavefunction is indicated where necessary or appropriate. All R-space wavefunctions presented here are real functions. However, due to the nature of the Fourier Transform, the corresponding P-space function may be complex. Signs are only included in the P-space diagrams when both the real and imaginary parts of the function change sign.

Schematic diagrams showing the orientation of the contour map plane are given in Appendix C. All planes include the origin. Almost all the diagrams are on the same scale (spanning 5 atomic units in both directions), except the R-space maps for CO_2 (figure 6.3), and the P-space maps for the N_2 $1\sigma\{g\}$ and $1\sigma\{u\}$ orbitals (figure 2.12) and the O_3 $3a_1$ orbital (figure 2.13).

2.1 The Fourier Transform Definition

The relationship between the position-space representation of a wavefunction, $\psi(\underline{r})$, and its momentum-space counterpart, $\psi(\underline{p})$, is the well-known unitary Fourier Transform (FT) {Dirac (1958)}:

$$(2.2)\quad \psi(\underline{p}) = (2\pi)^{-3/2}\int d\underline{r}\; e^{-i\underline{p}.\underline{r}}\; \psi(\underline{r})$$

and its inverse:

$$(2.3)\quad \psi(\underline{r}) = (2\pi)^{-3/2}\int d\underline{p}\; e^{i\underline{p}.\underline{r}}\; \psi(\underline{p})$$

Position space (R-space) refers to the space of the three orthogonal dynamical variables $\underline{r}=(x,y,z)$: momentum space (P-space) refers to the corresponding space of $\underline{p}=(p\{x\},p\{y\},p\{z\})$, the three orthogonal momentum directions.

2.2 The FT Symmetry Property

The Fourier Transform preserves all aspects of the symmetry of the R-space wavefunction in P-space. In addition the FT introduces (if it is not already present) the symmetry element i, (symmetry on inversion through the P-space origin). Inversion symmetry is necessary if the particle described by the wavefunction is to have no net translational motion.

Preservation of symmetry means that all R-space nodal planes (see definition, Appendix A) will also appear in P-space. Note, however, that nodal surfaces (see also definition, Appendix A) will not necessarily be preserved unless they are also symmetry elements. An example of a nodal surface which is preserved in the FT is the spherical nodal surface of a hydrogen-like 2s orbital, since atoms obviously have spherical symmetry. An example of a nodal surface that is not preserved is that of a σ^* orbital of a heteronuclear diatomic molecule (figure 7.2).

A straightforward consequence of the rotational invariance of the FT is that atomic orbitals will have the same angular dependence in both representations and that only the radial dependence will differ:

(2.4) $\psi\{nlm\}(\underline{r}) = N\ R\{nl\}(r)\ Y\{lm\}(\theta,\phi)$

(2.5) $\psi\{nlm\}(\underline{p}) = N\ P\{nl\}(p)\ Y\{lm\}(\theta,\phi)$

where N is a normalization factor, R{nl}(r) and P{nl}(p) give the radial dependence of the wavefunction, Y{lm}(θ,ϕ) is the spherical harmonic function of angle, and n, l, and m are respectively the principal, azimuthal and magnetic quantum numbers. This means that s-orbitals are spherical, that p-orbitals have the characteristic 'dumbbell' shape and so on, in both spaces (see figure 2.1). (Note that 'radial' is used thoughout this thesis in the sense of 'the magnitude of the coordinate vector' ($\underline{r}$ or $\underline{p}$); it is not intended to refer to 'the radial component of the momentum of a particle' in the sense of the component of the particle's motion towards or away from a point in R-space.) The radial functions are related by the spherical Bessel transform:

$$(2.6)\quad P\{nl\}(p) = \sqrt{\frac{2}{\pi}}\,(-i)^{l}\int r^{2}dr\; j\{l\}(pr)\; R\{nl\}(r)$$

An observation that can be made immediately from this is that only an s-orbital (l=0) will have non-zero amplitude at p=0. This arises because only the l=0 Bessel function has non-zero intensity at pr=0. All other l$\neq$0 Bessel functions have zero amplitude at the origin. Hence the origin of the nomenclature 's-type' and 'p-type' in referring to the type of momentum distribution measured on atoms. This 's-type' and 'p-type' nomenclature is also applied loosely to molecules to refer to distributions which are mainly s-type or mainly p-type but with a small admixture of the other type. Such small contributions which arise out of the

lowered symmetry in molecules compared to atoms mean that mainly s-type distributions may have increased intensity at medium to high q, and that mainly p-type distributions may have some intensity at q=0, relative to atomic distributions.

The analytical form of Slater-type and Gaussian atomic orbital radial functions are presented in detail in Appendix B. These radial forms are quite similar in both spaces, as is seen in figure 2.1. An s-orbital has the familiar monotonically decreasing form in R-space and P-space, and a p-orbital has zero amplitude at the origin and a maximum at some point removed from the origin.

2.3 The Reciprocity principle

A basic property of the Fourier Transform is that a dilatation of a dimension in one space causes a contraction of the corresponding dimension in the other space and vice versa. This defines the Reciprocity principle.

A consequence of this principle is first seen in comparing sizes (assuming roughly similar radial forms) of orbitals in R-space and P-space:

(1) Core orbitals, which are tightly confined spatially around the atomic centres ($r<.1a_0$) will

extend in P-space to large values of momentum ($q>5a_0^{-1}$).

(2) Valence orbitals, which are relatively diffuse in R-space ($r>2a_0$) have fairly compact ($q<2a_0^{-1}$) distributions in P-space.

The Reciprocity principle manifests itself in several different mathematical forms. One is the above dilation/contraction property. Another is to consider that the Fourier Transform projects out the spectrum of constituent sinusoidal frequencies in a function. A sharply peaked R-space wavefunction (as in core orbitals) is said to contain large high-frequency components, and by the de Broglie relation:

$$(2.7)\quad p = h\nu/c$$

this means also large high-momentum components. The converse argument may be made for broad R-space wavefunctions (as in valence orbitals).

A third way of looking at the Reciprocity property is to consider the form of the quantum mechanical momentum operator $\underline{P}$:

$$(2.8)\quad \underline{P} = -i\underline{\nabla}$$

This implies that the momentum of a particle is related to the gradient of its wavefunction. Thus a spatially broad wavefunction with a generally shallow gradient emphasizes

low values of momentum, and vice versa. (Note that $\langle \underline{p} \rangle$ is zero due to the inversion symmetry of P-space wavefunctions, but $\langle p \rangle$ will reflect the radial extent of $\Psi(\underline{p})$.)

The above concepts are, of course, in accord with our basic chemical intuition about the nature of orbitals: we say that electrons in tightly bound, highly energetic orbitals are fast-moving particles, and that more loosely bound electrons are relatively slow-moving. To illustrate this, figure 2.1 shows contour maps of approximate atomic orbitals {Clementi (1974)} in position space and momentum space for hydrogen and some atoms of the first row of the periodic table.

An important, but sometimes misunderstood, aspect of the FT relationship is that there is no one-to-one mapping of points in R-space into P-space. One cannot say that changing the amplitude at a given point in R-space will necessarily produce a change at a related point in P-space. One can only refer in the most general way to regions of the two spaces as being related, and this is due to the nature of wavefunctions: the large r regions are generally shallow functions, and so tend to contribute to low momentum, and near the nuclei the R-space wavefunction is usually rapidly changing, thus contributing to high momentum regions. The only way to think of correspondences between points in R- and P-space is that amplitude at a point in P-space is a result of R-space amplitude in areas which are separated by

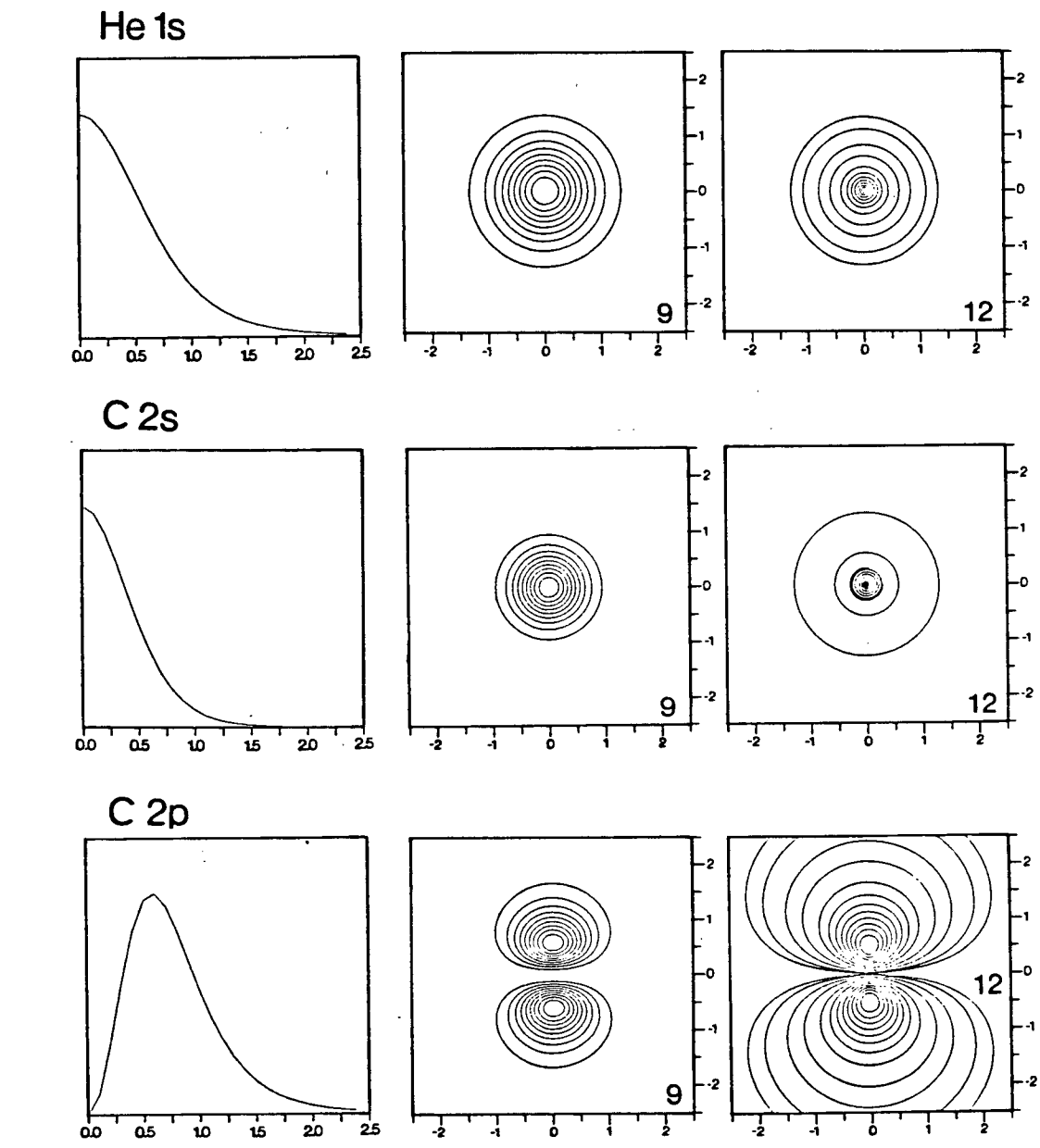

Figure 2.1 Momentum distributions and momentum and charge density maps for atomic orbitals

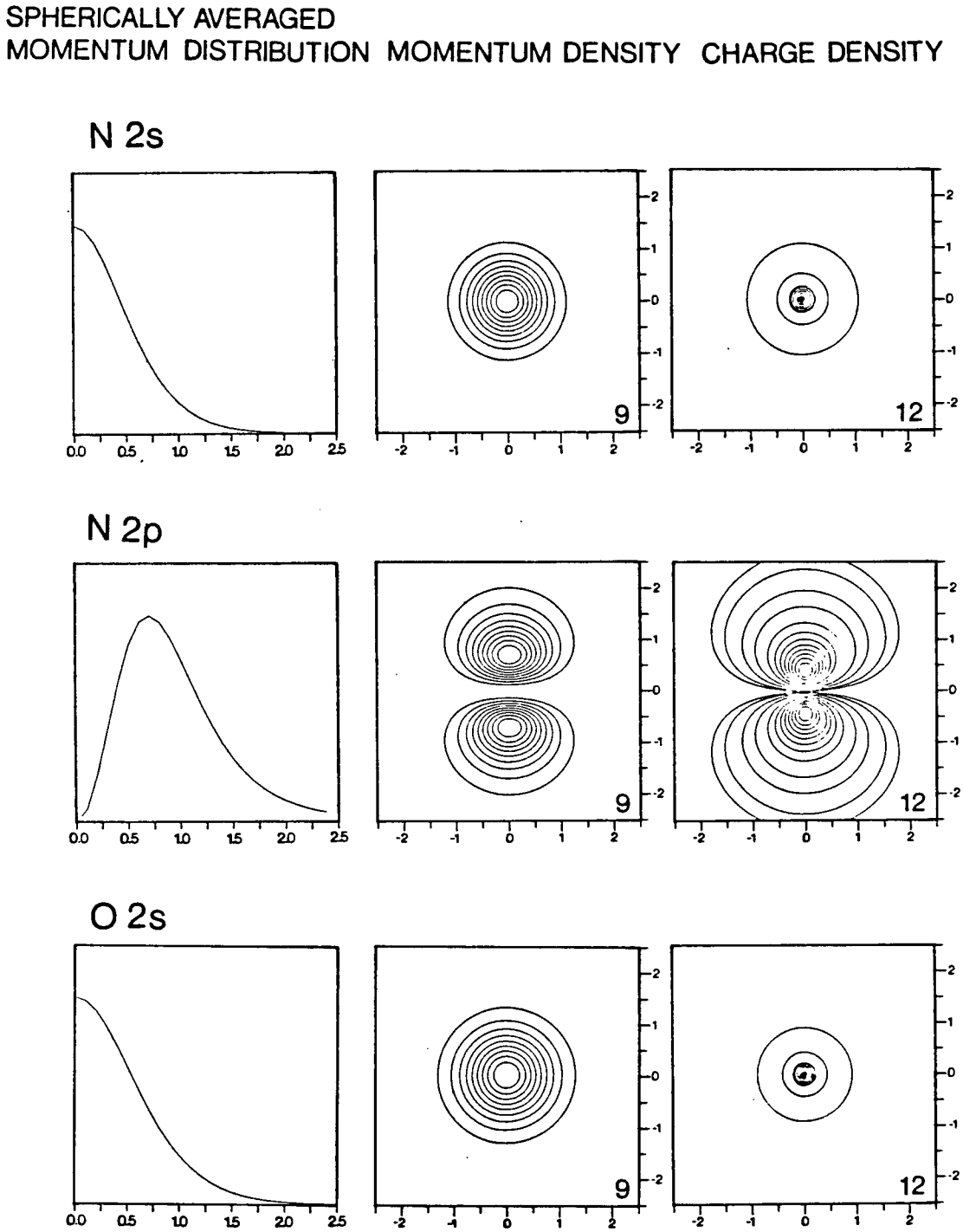

Figure 2.1 continued

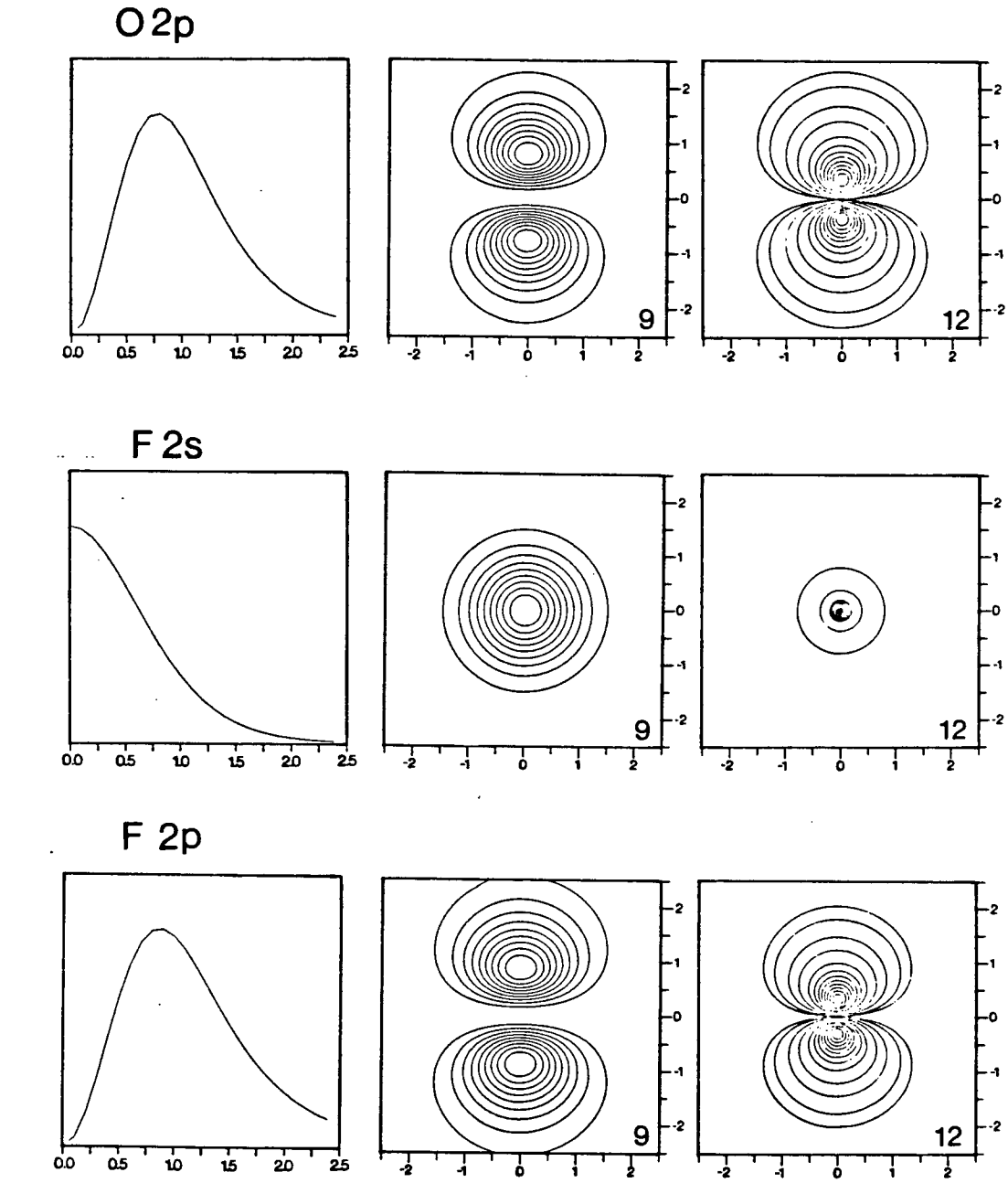

Figure 2.1 continued

SPHERICALLY AVERAGED
MOMENTUM DISTRIBUTION MOMENTUM DENSITY CHARGE DENSITY

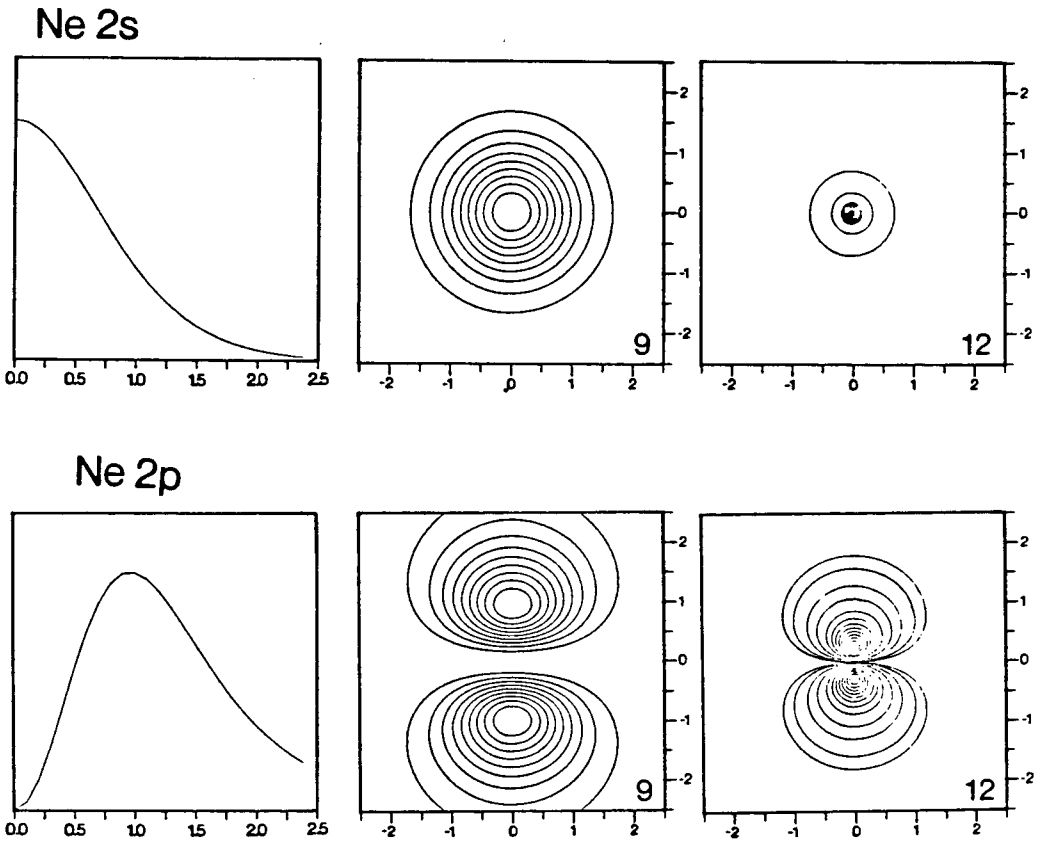

Figure 2.1 continued

$n\pi/\underline{r}$, where n=0,1,2,3... This is the basis for bond oscillation discussed further in section 2.6 and for bonding in polyatomics, in section 2.5.3.

2.4 The One-dimensional Wavefunction Projection Q

Because it is a time-consuming and expensive process to compute momentum density maps exactly from the molecular orbital coefficients, it is desirable to be able to form some idea of the shape of the momentum density from a knowledge of the R-space function and from some familiarity with the effects of the Fourier Transform. To this end I shall classify several types of wavefunctions according to their symmetry and nodal structure, and illustrate their appearance in the R- and P-space representations.

Define the function Q(r') as the projection of the total three-dimensional R-space wavefunction $\psi(\underline{r})$ onto a line parallel with the vector $\underline{r}'$:

$$(2.9)\quad Q(r') = \mathcal{P}(\psi(\underline{r});\underline{r}')$$

The Fourier Transform of the resulting one-dimensional function Q(r') gives the amplitude Q(p') of the momentum-space wavefunction along a line passing through the P-space origin with the same direction as vector $\underline{r}'$:

$$(2.10)\quad Q(p') = (2\pi)^{-1/2} \int dr'\, e^{-ip'r'} Q(r')$$

This function is useful, because there are only a small number of different classes of the function Q, which can easily be worked out. It is then usually possible to sketch, or visualise mentally the entire momentum density if one knows the form of $|Q(p')|^2$ along two or three lines. It is assumed that Q(r') is everywhere real; however, if this is so, Q(p') is not necessarily also everywhere real, but may have an imaginary part, and for this reason I shall look at the magnitude $|Q(p')|^2$. As the binary (e,2e) form factor and momentum density maps are also squared functions, this is not inappropriate. Figure 2.2 shows schematically the various classes of projections. Gaussian functions have been used to simulate the projections. The scale for Q(r') is arbitrary; the scale for $|Q(p')|^2$ is symmetric about the midpoint where p=0. Table 2.1 is a summary of examples of each class of projection.

When working out the form of Q(r') of a valence orbital it is permissible to ignore the very low r region when the wavefunction here is rapidly changing due to contributions from inner shell atomic orbitals. By the Reciprocity principle these will affect only the very large p regions which are usually not displayed in the momentum density maps in this work.

2.4.1 Class O: Centrosymmetric systems

All atomic orbitals and single-centre, completely non-bonding molecular orbitals have the same shape in R-space and P-space (Symmetry property). Their radial forms are slightly different.

2.4.2 Class I: One lobe

This is the simplest case: Q(r') is pure s-type (i.e. symmetric about its point of maximum amplitude), falls off monotonically on either side, and is everywhere the same sign. $|Q(p')|^2$ is a similarly shaped function. It is found in atomic 1s STOs and also in the σ-orbitals of asymmetric linear systems perpendicular to the bond axis. Class I is different from class O in that it can be used to represent orbitals which are mainly s-type, but also elongated or contracted in some dimension, as, for instance, the σ-bonding MO in a homonuclear diatomic.

2.4.3 Class II: Two lobes

The next simplest case, class II, comprises those projections Q(r') where there are two lobes of positive and negative amplitude, separated by a nodal point. This class breaks into two subclasses, IIi and IIa. Class IIi comprises the symmetric case (hence the notation II*i*) where the wavefunction has a nodal plane perpendicular to the

projection axis. Here $|Q(p')|^2$ is zero at p=0 and rises on either side to give two equal areas of momentum density. This subclass is exemplified in 2p STOs and in the σ^* MOs of homonuclear diatomic molecules.

Class IIa refers to the asymmetric case (notation IIa), where the positive and negative lobes are different. The distinguishing feature in $|Q(p')|^2$ is that there is now some density at p=0. This is how the momentum density maps of heteronuclear and homonuclear diatomic molecules may be told apart. Homonuclear MOs will all be class I or IIi. Heteronuclear MOs will be somewhere between class O and IIa. Examples of class IIa are found in the mostly-antibonding σ^* MOs of heteronuclear diatomics, and also in the outer a_1 MOs of bent AH_2 molecules.

2.4.4 Class III: Three lobes

Following the trend from classes I to II the next logical extension is to three lobes: i.e. Q(r') has two nodal points separating three areas of amplitude of oscillating sign.

In class III there are four subclasses. Class $IIIi_1$ refers to the case where the positive and negative parts of the projection exactly cancel in the overlap with the zero frequency (p=0) FT wave; this case will have no amplitude at p=0. This subclass occurs in the $1t_2$ orbital of CH_4, taken

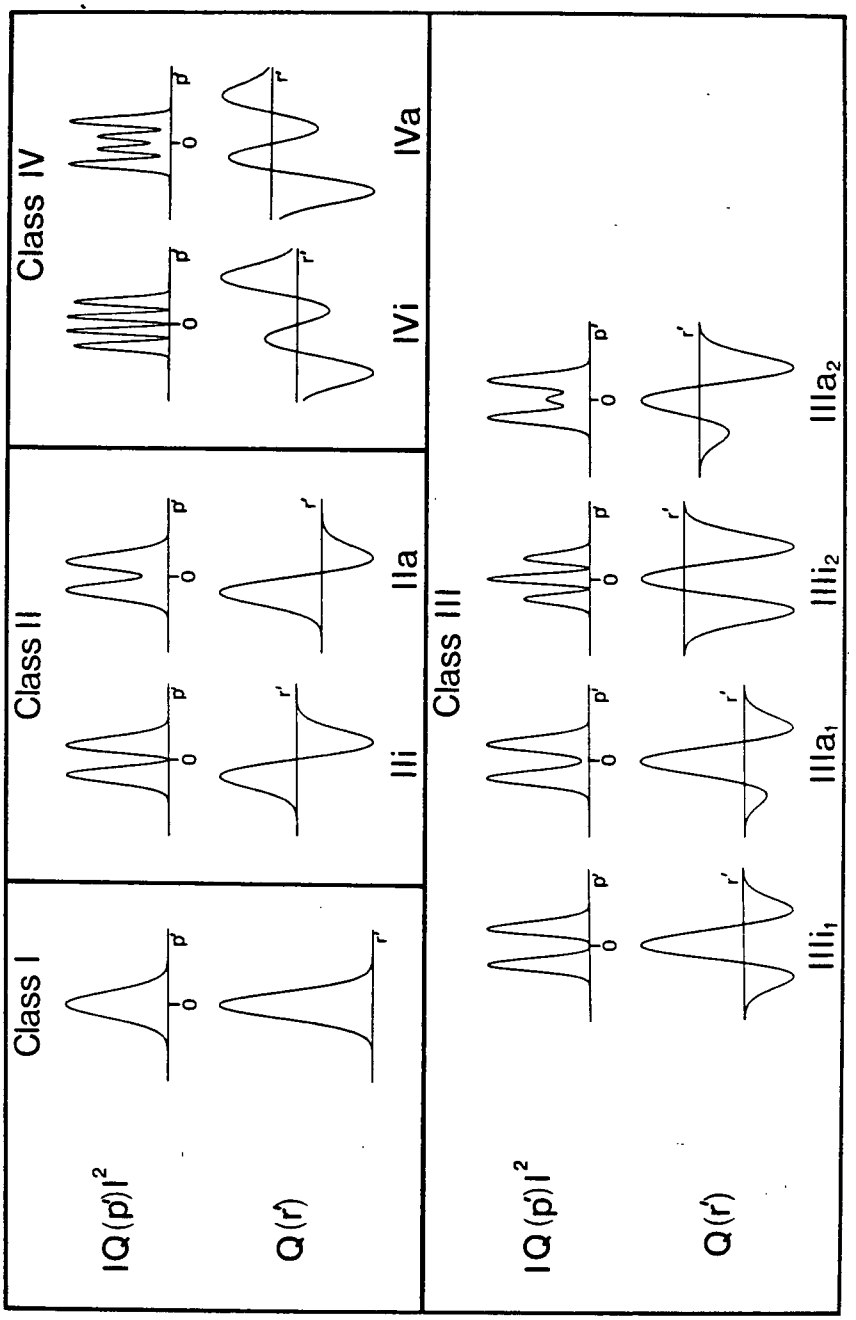

Figure 2.2 Schematic diagrams of one-dimensional Q-projections.

Table 2.1 Examples of Q projections

Class O	All atomic orbitals Non-bonding orbitals that are essentially atomic
Class I	All s atomic orbitals σ-bonding orbitals H_2 $1\sigma\{g\}$, N_2 $2\sigma\{g\}$, CO_2 $3\sigma\{g\}$
Class IIi	All p atomic orbitals Diatomic $\sigma\{u\}$ orbitals N_2 $2\sigma\{u\}$, CO_2 $2\sigma\{u\}$ Diatomic $\pi\{u\}$ orbitals N_2 $1\pi\{u\}$, NO 2π, O_2 $1\pi\{u\}$, CO_2 $1\pi\{u\}$,
Class IIa	Certain hydride outer valence orbitals: NH_3 1e, $3a_1$, H_2O $3a_1$, $1b_2$, $2a_1$ HF 3σ, 2σ Asymmetric diatomic π orbitals parallel to bond axis: NO 2π
Class $IIIi_1$	CH_4 $1t_2$ orbital on a line parallel to H-atoms of like sign, all orbitals of d-type symmetry
Class $IIIa_1$	Outer a_1 MOs in H_2O and H_2S in H-H direction π^* orbitals O_2 $1\pi\{g\}$, CO_2 $1\pi\{g\}$
Class $IIIi_2$	Symmetric triatomic (AX_2) $\sigma\{g\}$ orbitals: CO_2 $4\sigma\{g\}$
Class $IIIa_2$	Higher heteronuclear diatomic σ orbitals: NO 5σ
Class IVi	Higher AX_2 σ orbitals CO_2 $3\sigma\{u\}$
Class IVa	Higher σ orbitals of asymmetric triatomics (ABC)

in the direction joining H atoms of like sign, and in MOs of d-type symmetry (two perpendicular planes of symmetry) in any direction except those of the nodal planes. In all the other subclasses the amounts of the positive and negative lobes are not equal and so $|Q(p')|^2$ always has non-zero density at p=0.

Class $IIIa_1$ refers to the case where the total amplitude in the middle lobe of Q(r') outweighs the sum of the outer ones, and the projection may be symmetric or asymmetric about the midpoint. The resulting $|Q(p')|^2$ is similar to $IIIi_1$ except that there is density at p=0. Examples are the $3a_1$ and $5a_1$ MOs of H_2O and H_2S respectively, taken in the direction joining the H atoms.

Class $IIIi_2$ concerns the situations where amplitude in the two outer lobes of Q(r') is greater than in the middle, and the function is symmetric about its midpoint. One finds that $|Q(p')|^2$ has three peaks separated by nodal points. Examples of this class include the $4\sigma\{g\}$ orbital and the (unoccupied) $2\pi\{u\}$ orbital of CO_2.

Class $IIIa_2$ is the asymmetric case of $IIIi_2$. Here $|Q(p')|^2$ shows that the nodes of the class $IIIi_2$ P-space function are filled in. Class $IIIa_2$ is seen in the 5σ MO of nitric oxide (see Chapter 7).

2.4.5 Four lobes

The number of possible subclasses increases with the number of nodes in Q(r'); however, for the purposes of this thesis, only two are important.

Subclass IVi describes the symmetric case where four peaks are seen in $|Q(p')|^2$ and where the density at p=0 is zero. The amounts of intensity in the two inner $|Q(p')|^2$ peaks relative to the outer two is inversely proportional to the amount of intensity in the inner lobes of Q(r') relative to the outer ones. Class IVi is exemplified in the $3\sigma\{u\}$ orbital of CO_2.

When the symmetry in subclass IVi is reduced, the nodes in $|Q(p')|^2$ fill in, giving the subclass IVa. When Q(r') is made very asymmetric, eventually $|Q(p')|^2$ will start to look like one of the other a-type classes.

2.5 The Bonding Principle

We have seen that atomic orbitals, whether plotted in R-space or P-space, look almost the same except for the reciprocal size relationship. Next, I shall consider the effect of bonding between atoms as viewed in momentum space. As most of the calculations done in this work are of

LCAO-MO-SCF wavefunctions I shall use the concepts and nomenclature of MO theory in this chapter.

A disconcerting feature of momentum space is that, unlike position space, there is nowhere to plot the positions of the nuclei. This makes life conceptually difficult because, as chemists, we are used to hanging the electron density on the nuclear geometry skeleton. It would seem, at first then, to mean a serious loss of information in going to P-space, but it will be shown later that in fact the nuclear geometry information is still present in the P-space representation, but in a somewhat obscured form.

2.5.1 Hydrides (AHn)

The molecular orbitals of hydrides (AHn) {Basch (1972)} (figures 2.3, 2.5-7) are similar in character to the atomic orbitals of the constituent heavy atom, and so the momentum density maps will also be similar to those of the ns and np atomic orbitals (figure 2.1).

In particular, the addition of the hydrogen 1s functions will cause the spherical distribution of the heavy atom A(ns) orbital to contract in the directions of the A-H bonds. The combination with the A(np) orbitals will generally shrink the momentum density (as the P-space MOs are now larger), and, whenever the symmetry of the new molecular orbital is lower than the original atomic np

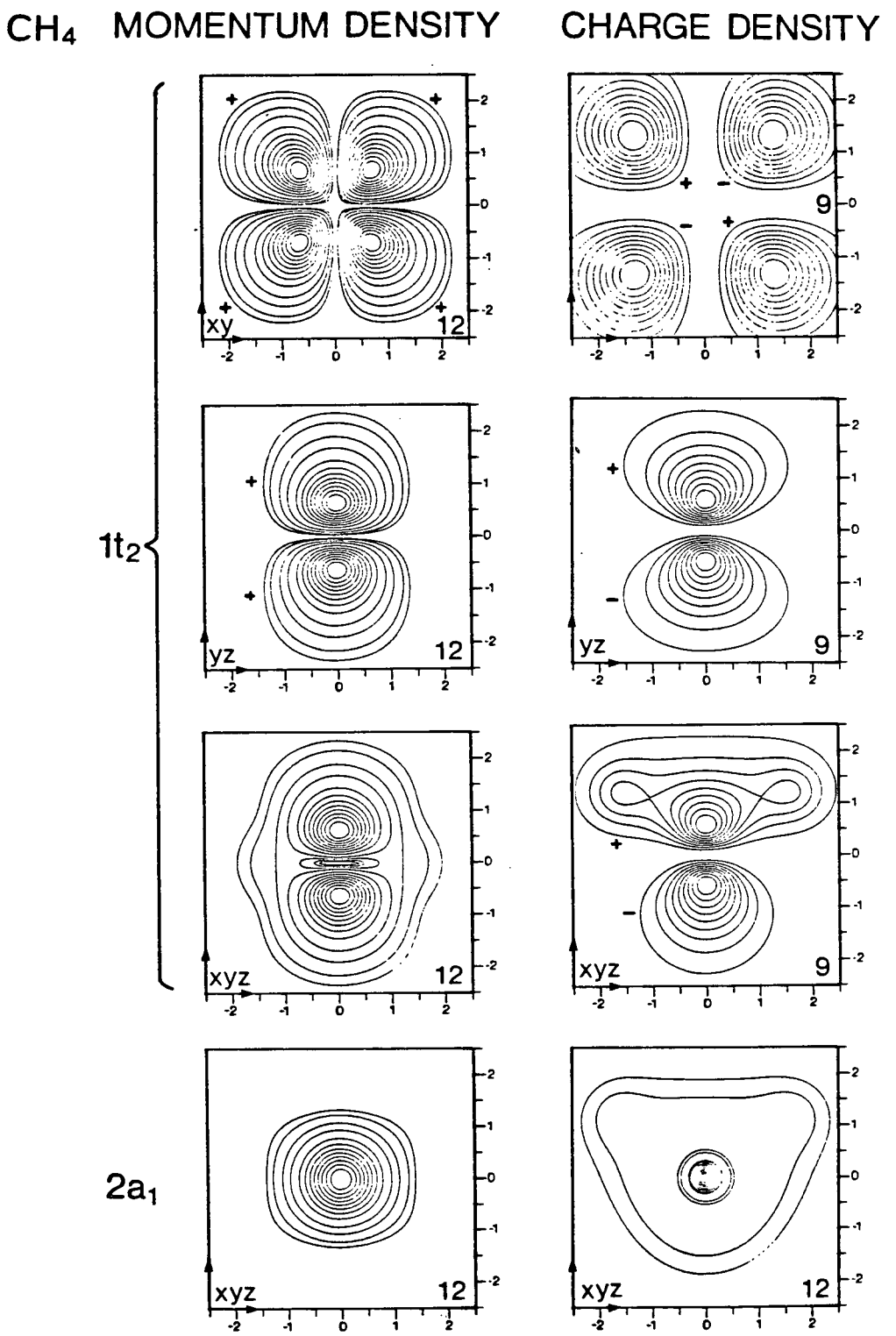

Figure 2.3 CH_4 momentum and charge density maps.

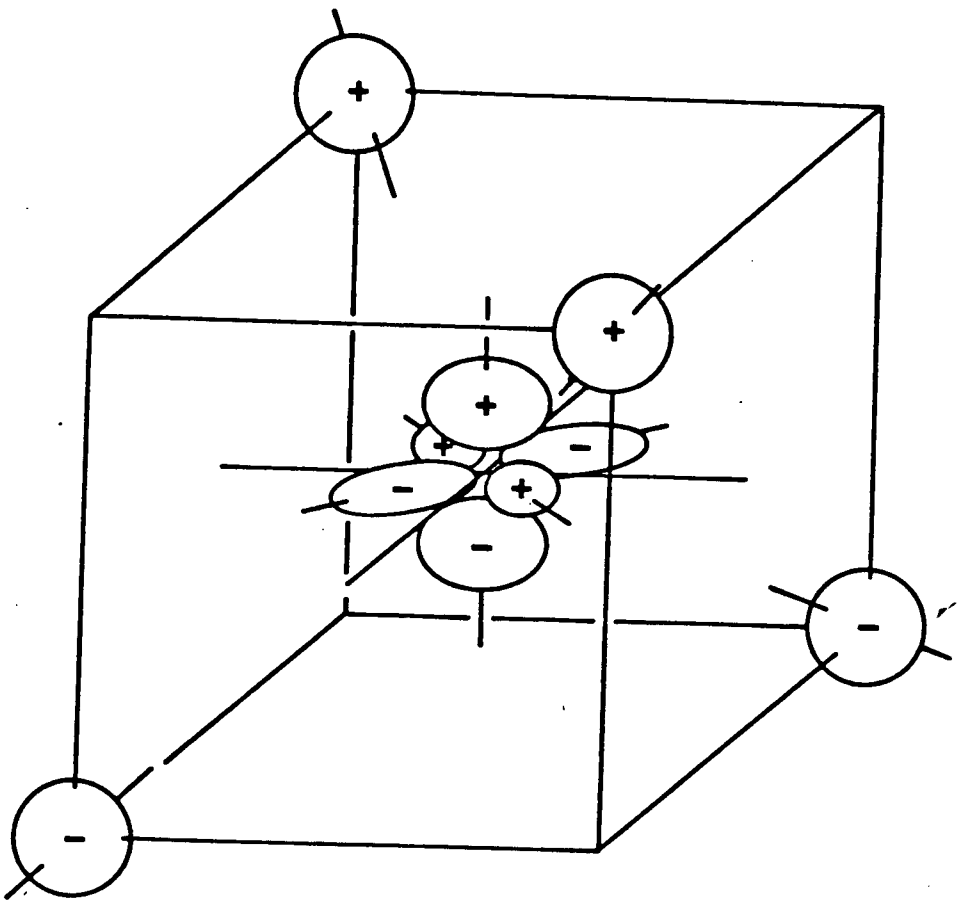

Figure 2.4 Schematic diagram of the constituent atomic orbitals of the CH_4 $1t_2$ MO.

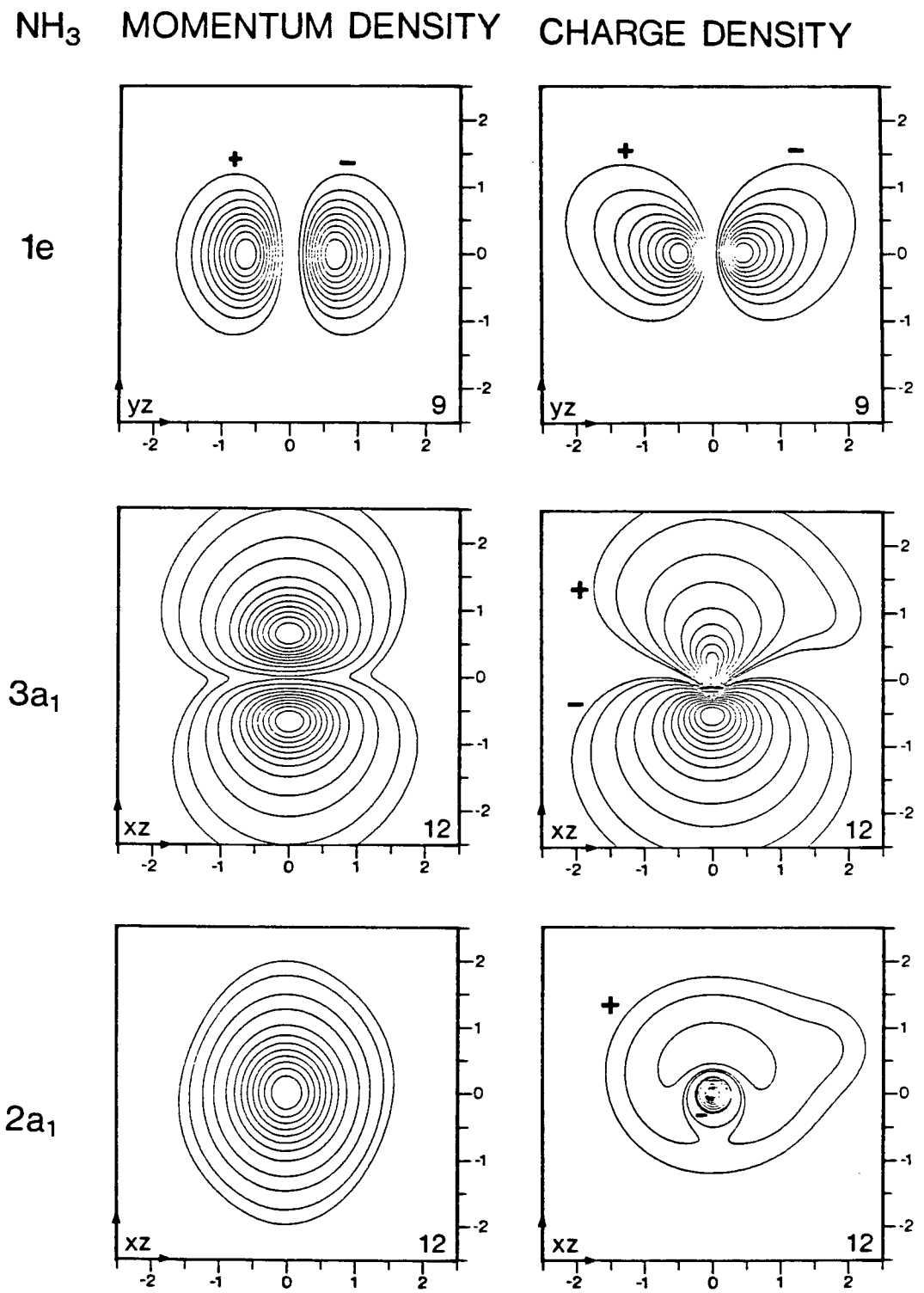

Figure 2.5 NH_3 momentum and charge density maps.

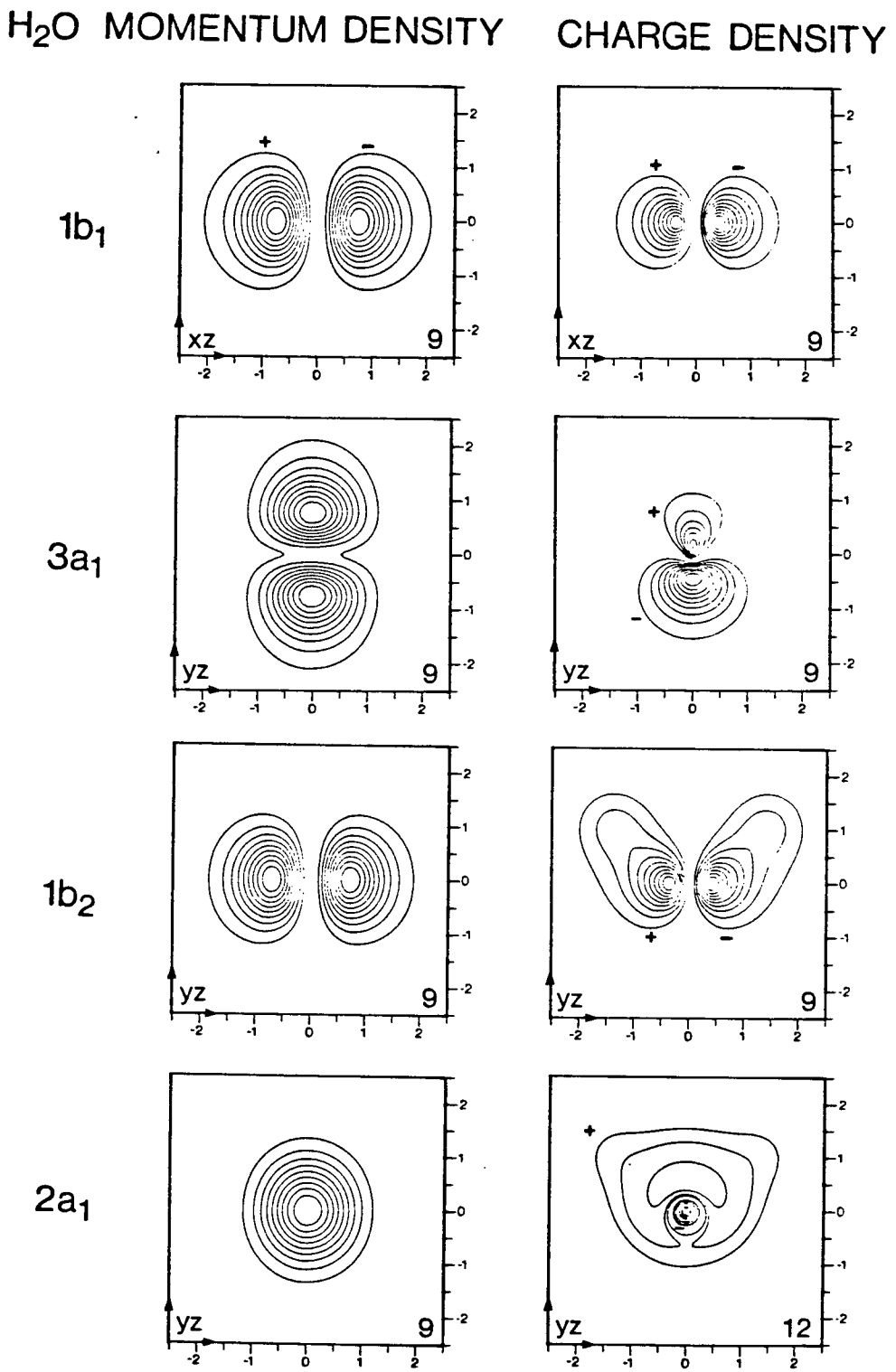

Figure 2.6 H_2O momentum and charge density maps.

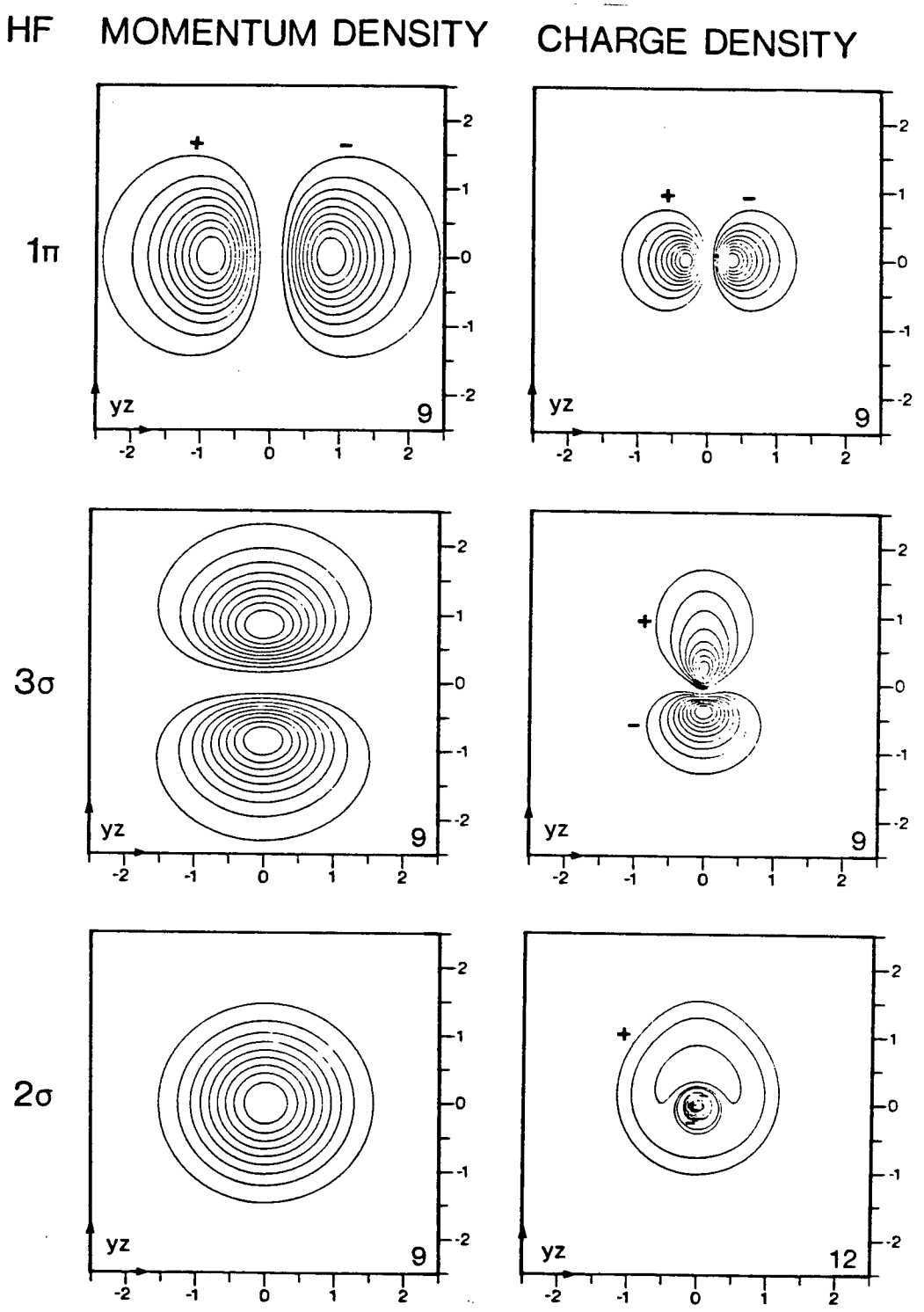

Figure 2.7 HF momentum and charge density maps.

orbital, the P-space nodal plane will be filled in to some extent. Illustrative density maps for first row hydrides are given in figure 2.3, and 2.5-2.7, and for H_2S in figure 4.5. The inner s-type a_1 MOs ($A(2s)+H_1(1s)+H_2(1s)$) are all Class I. The higher p-type orbitals are Class IIi if the nodal plane is still present, or Class IIa if it has degenerated to a nodal surface.

The methane $1t_2$ orbital shows an interesting difference from the momentals of the other first row hydrides. The latter either preserve or destroy the nodal plane in forming the molecular orbital. The methane $1t_2$ momentum density falls in between: it has two nodal lines (lines on which the density is zero) which bisect the H-C-H angle between H atom 1s functions of opposite sign. Momentum contour surfaces for this orbital will look like a round balloon which has been poked in on four sides (figure 2.3). It was a gratifying exercise to work out what the $1t_2$ density map must look like according to the above principles and the Q projections in section 2.4, and then to confirm it by computing the density maps. This orbital is Class $IIIi_1$ in the direction joining two H-atoms with 1s AOs of like sign (see the schematic representation of the $1t_2$ MO, figure 2.4) and Class IIi in the direction of the central carbon 2p atomic orbital.

2.5.2 Diatomic molecules (A_2,AX)

This section is illustrated with the wavefunctions of H_2 and CO {Basch (1972)} and N_2 {Kunz}.

Going back to basic chemistry, one describes the simplest case of a σ bonding orbital between two identical atoms, A, separated by distance R, as having occurred when electron density moves from its atomic distribution around the nuclei into the bonding region between the nuclei, depicted in figure 2.8. Generally this produces a molecular orbital centered midway between the atoms and is elongated along, and constricted perpendicular to, the bond axis: in fact, the familiar 'lozenge-shaped' σ bonding orbital. Therefore, by the Reciprocity principle, the P-space density will also be more or less s-type but dilated perpendicular to the bond axis and contracted parallel to the bond direction. This is illustrated by the $1\sigma\{g\}$ orbital of the H_2 electron density map (figure 2.9) where the σ MO is formed from the gerade combination of two 1s atomic orbitals, and, to a lesser extent, in the $2\sigma\{g\}$ orbital of N_2 (figure 2.10). Such orbitals project as Class I (section 2.4.2).

Higher σ-bonding orbitals such as the N_2 $3\sigma\{g\}$ (figure 2.10) do not display such contractions. They have a significant contribution of 2p atomic orbitals which puts density into the antibonding regions and increases the

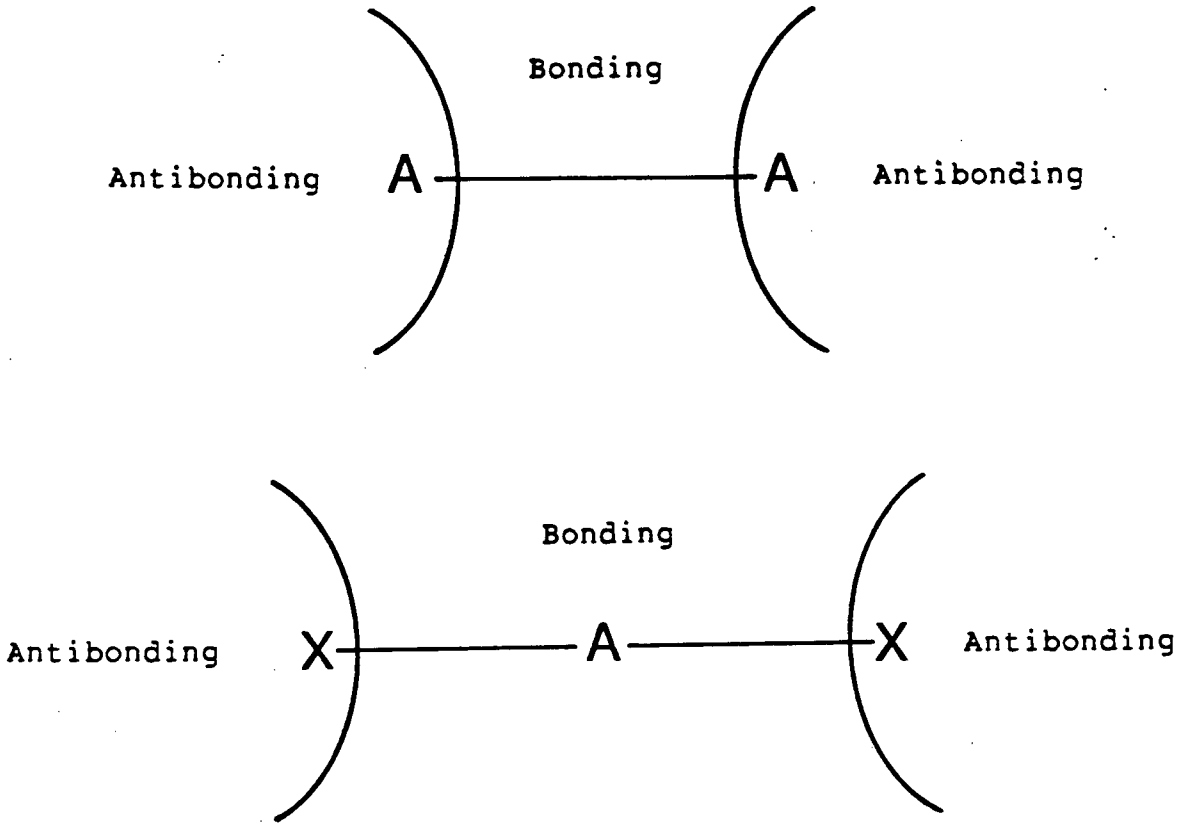

Figure 2.8 Bonding and antibonding regions in diatomic (A_2, AX) and triatomic (AX_2, AXY) molecules.

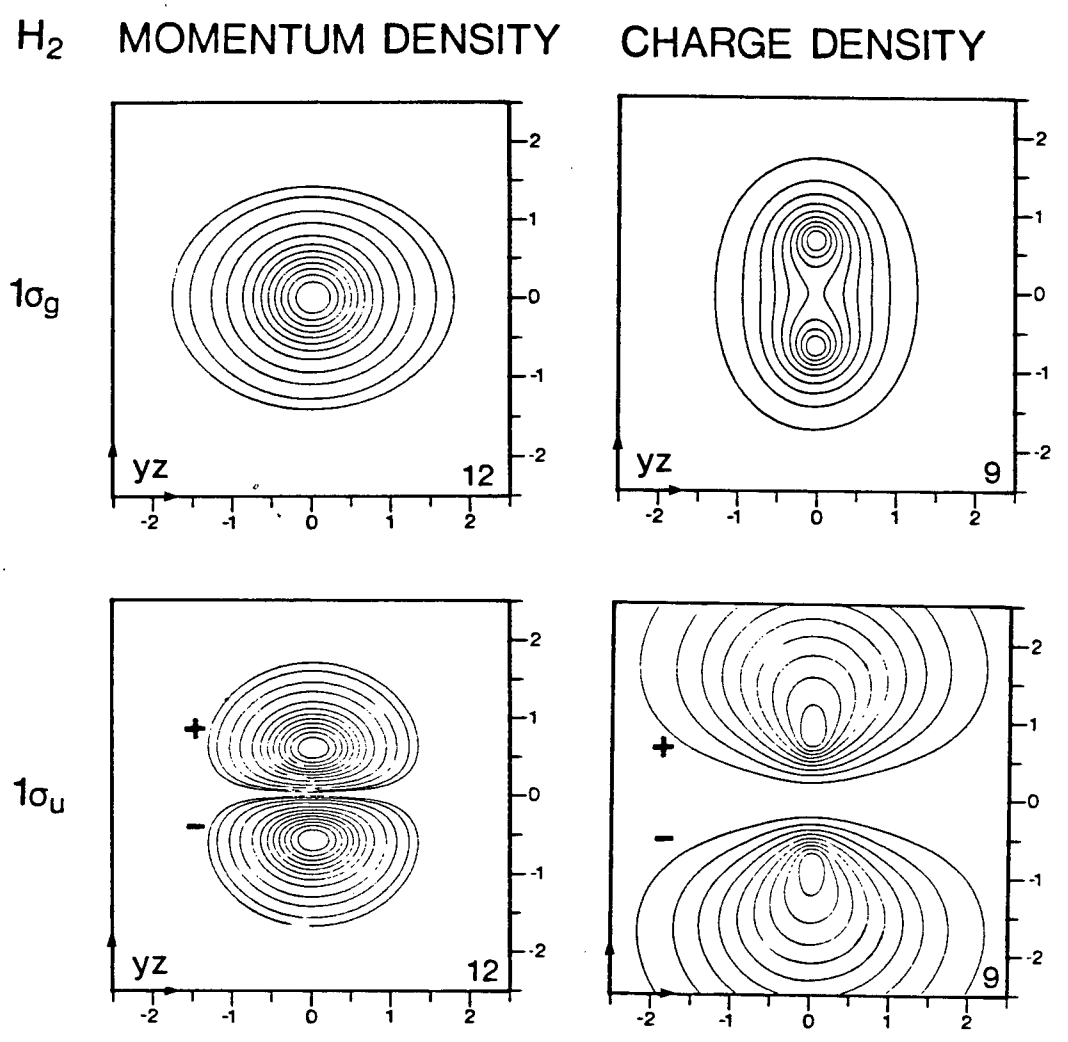

Figure 2.9 H_2 momentum and charge density maps for the $1\sigma\{g\}$ and the (unoccupied) $1\sigma\{u\}$ MOs.

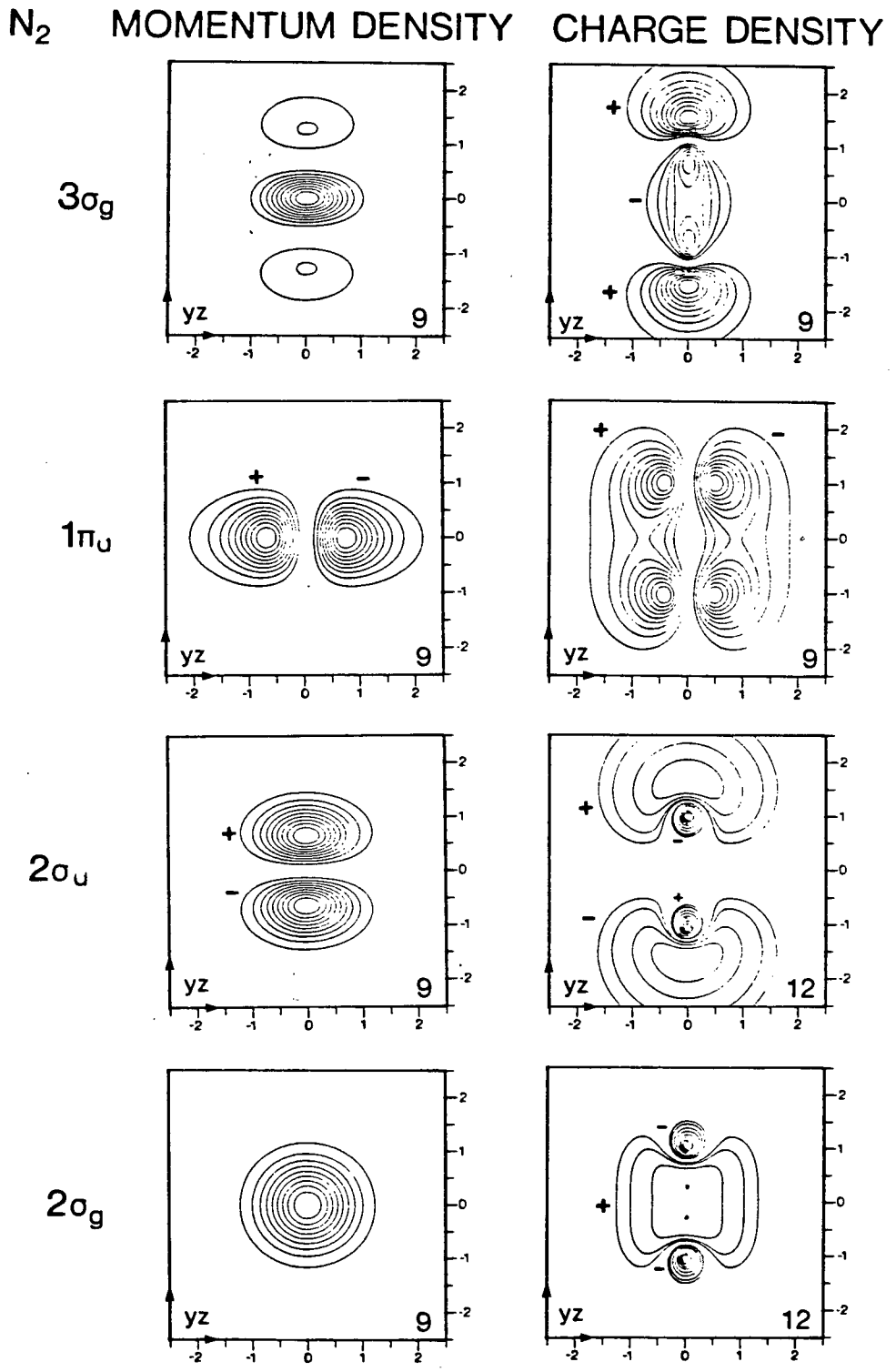

Figure 2.10 N_2 momentum and charge density maps for the valence MOs.

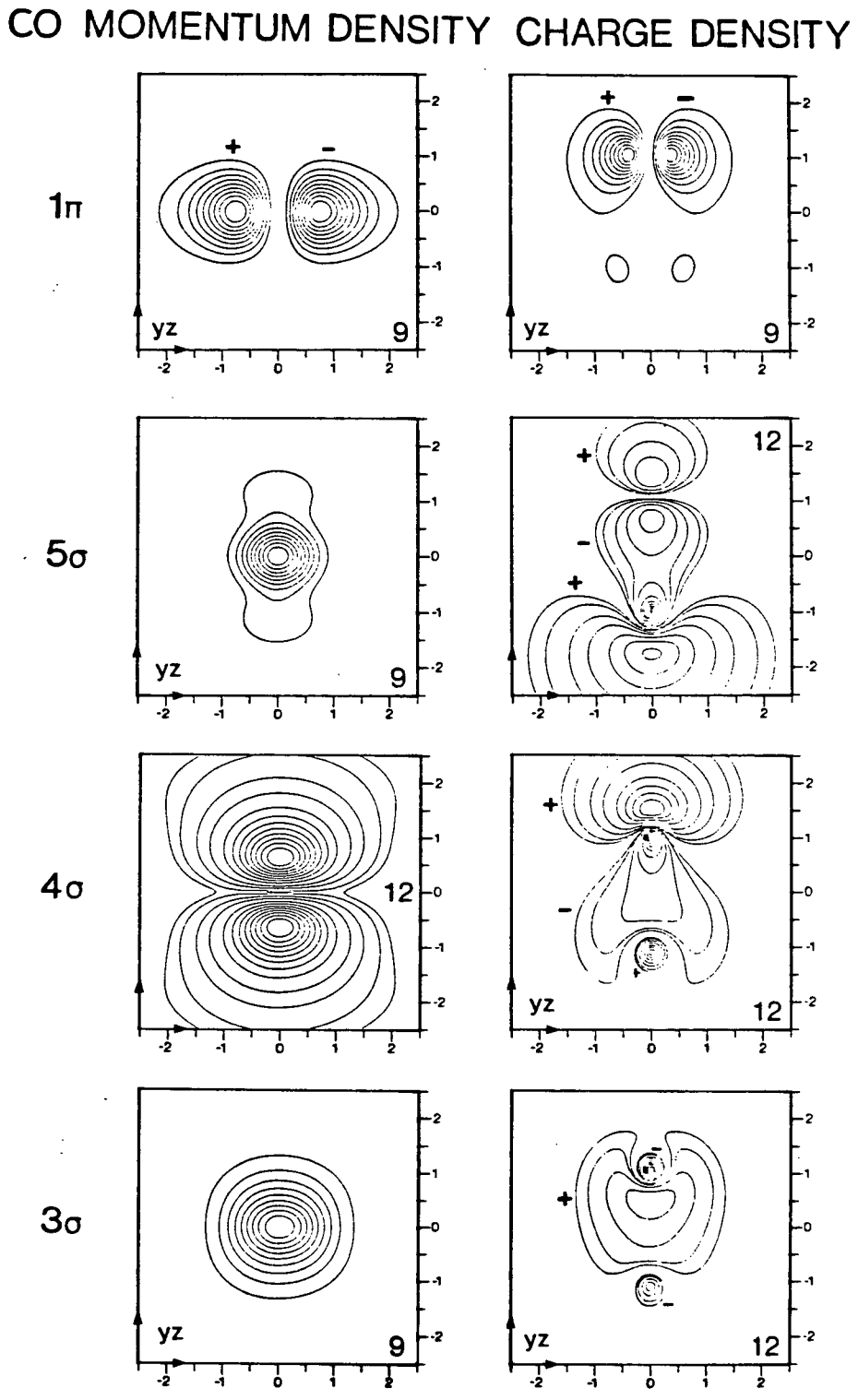

Figure 2.11 CO momentum and charge density maps.

'pseudo-angular' momentum (see definition below). The wavefunction is now a three-lobed structure with nodal surfaces near the nitrogen atoms, which overlaps destructively with FT waves of a period approximately twice the internuclear spacing, and constructively with FT waves of somewhat shorter period. This gives rise to the two nodal surfaces in the N_2 $3\sigma\{g\}$ momentum density map at about $p||=\pm 0.7a_0^{-1}$ and the areas of momentum density at $p||=\pm 1.4a_0^{-1}$. This high $p||$ density is a result of the increased antibonding character and decreased bonding character of the $3\sigma\{g\}$ orbital relative to the $2\sigma\{g\}$. The N_2 $3\sigma\{g\}$ orbital falls into Class $IIIi_2$.

The next case is the π-bonding MO, as exemplified in the N_2 $1\pi\{u\}$ orbital. Everyone is familiar (figure 2.10) with the two banana-shaped lobes of this orbital, formed from the ungerade combination of N $2p\{x\}$ and $2p\{y\}$ atomic orbitals. This orbital looks like an atomic p orbital that has been stretched in the bond direction. Again therefore, by the Reciprocity principle, the P-space representation of this orbital should, in comparison with the atomic N2p orbital, show almost the same density distribution perpendicular to the bond, but with a contraction in the distribution parallel to the bond, which in fact it does. The $1\pi\{u\}$ wavefunction is projection class IIi.

Antibonding orbitals arise with the combination of like atomic orbitals of opposite sign, such that a nodal plane is

introduced between the two centres, pushing electron density out of the bonding region. The molecular orbital has a 'pseudo-angular momentum' greater than the individual atomic orbitals: i.e. if the AOs are two s-orbitals, the ungerade combination produces an MO which looks like a p-orbital. On going to momentum space the nodal plane is preserved, and we get a p-type P-space orbital whose radial extent is inversely related to the bond length of the molecule. Thus the characteristic of $\sigma^*(2s)$ antibonding orbitals is the complete removal of density from the perpendicular momentum direction, and a p||{max} which reflects a convolution of the internuclear distance and the radial extent of the constituent atomic momentum density. This is an instance where the nuclear geometry information is apparent in the P-space density function, though in an obscure form. The N_2 2σ{u} orbital is in Class IIi.

I have introduced a concept 'pseudo-angular momentum' here, which is a hand-waving idea at best: what I am trying to refer to is the increasing complexity of the nodal plane or nodal surface structure of molecular orbitals, going from the inner MOs to the outer ones. This tendency has parallels in the nodal structure of atomic orbitals which becomes more intricate with increasing principal quantum number, however the analogy is not exact because, by definition, molecules have more than one centre, and the term 'pseudo-angular momentum' to represent this concept is the best that can be

devised. For example, the difference between the $2\sigma\{g\}$, $2\sigma\{u\}$ and $3\sigma\{g\}$ MOs of N_2 (figure 2.10) is mainly one of 'pseudo-angular momentum'; the number of nodal surfaces is increasing from none, to one, to two.

A non-bonding orbital (that is not non-bonding by virtue of equal amounts of bonding and antibonding character) is a trivial case in P-space as in R-space: the density will be very close to that of the constituent atomic orbital, modified only by bond oscillation effects in the case of degenerate non-bonding orbitals on two or more centres (see section 2.6).

In between these two extremes of bonding and antibonding lie the molecular orbitals of heteronuclear diatomic molecules where the molecular orbitals are constituted from dissimilar atomic orbitals. σ- and π-bonding MOs are now constituted from unequal amounts of dissimilar atomic orbitals with the result that they have some non-bonding character, and resemble more closely their constituent atomic orbitals. This means there is a reduction in the bonding effects described for the homonuclear MOs above:

(1) Bonding orbitals that are mainly σ(2s) or π(2p) show less contraction in the bond axis direction. Examples are the 3σ (class I) and 1π (class IIi) orbitals of CO (figure 2.11) and NO (figures 7.2 and 7.3);

(2) σ-antibonding orbitals that are essentially of $\sigma^*(2s)$ character now have the $p||=0$ nodal plane filled in a little. This is seen in the 4σ orbitals of CO and NO which are Class IIa in the bond direction and Class I in the perpendicular direction. The reason for the $p=0$ intensity is that there are no longer equal positive and negative parts of the R-space wavefunction, and so the overlap with the zero-frequency FT wave is not exactly zero;

(3) σ-bonding orbitals that are predominantly $\sigma(2p)$ no longer show nodal surfaces in P-space for the same reason as the $\sigma^*(2s)$ case. Examples are again found in the 5σ MOs of CO and NO.

The final generalization for bonding effects in homo- and heteronuclear diatomics may be stated as follows:

(1) The bonding region in R-space is the interatomic region; bonding character is indicated by increased density in this region. The antibonding region is at the ends of the molecule: antibonding character is likewise indicated by density in these regions;

(2) The bonding direction in P-space is the plane perpendicular to the bond axis; bonding effects are indicated by a contraction of density toward this plane, relative to the atomic density. Antibonding effects are indicated by a displacement of density from this plane to higher $p||$ regions.

The discussion of $\pi^*(2p)$ MOs is deferred to Chapter 7.

2.5.3 Linear symmetric triatomics (AX_2)

The situation for these heavy atom triatomics is more complicated than for the previous systems, because of the increased number of valence electrons.

The bonding regions (figure 2.8) are now the two areas between the atoms, and the antibonding regions are outside the end atoms of the molecule; an orbital which places density on the end atoms and none on the middle atom may be considered mostly non-bonding, since the end atoms are far enough apart as to have little interaction. The R-space wavefunctions of such systems have symmetry 'gerade', or 'ungerade', depending on whether they change sign on inversion through the central atom coordinates, and are σ or π depending on whether they change sign on reflection in a $\sigma\{v\}$ plane.

The understanding of bonding in AX_2 systems hinges on the fact that the momentum density function for an LCAO wavefunction can be broken up into one-center and two-center parts:

$$(2.11)\quad \rho\{i\}(\underline{p}) = \rho_1(\underline{p}) + \rho_2(\underline{p})$$

The explicit form for these is given in Appendix B. The one-center part is just the sum of the individual basis set

P-space density functions and is everywhere positive. For an AX_2 system aligned in the z-direction the one-centre part will be a combination of 2s and 2p{z} density, leading to a roughly spherical momentum density function, but elongated in the p|| direction and centred at the P-space origin. The two-center part is the sum of all the interference terms between two atomic centers, and is not restricted to positive sign. As with any interference effect, there are constructive and destructive components which vary as a function of frequency and interatomic separation. Therefore, electron amplitude at two (or more) areas separated by $\underline{r}$ reinforces the atomic one-center momentum density near point $\underline{p}=2n\pi/\underline{r}$ (n=0,1,2...) in P-space if the areas are of the same sign, or near point $\underline{p}=(2n+1)\pi/\underline{r}$ (n=0,1,2...) if these areas are of oscillating sign (i.e. +|-|+|- and so on). The atomic density is likewise reduced near $\underline{p}=(2n+1)\pi/\underline{r}$ where there is electron density of the same wavefunction sign separated by $\underline{r}$, and near $\underline{p}=2n\pi/\underline{r}$ for oscillating signs. This is illustrated schematically in figure 2.6 and summarised in Table 2.2.

Referring again to the Reciprocity principle, if the R-space bonding regions are on the bond axis to either side of the central atom, and the antibonding regions are outside either end of the molecule, then in P-space antibonding density will reinforce low momentum regions, and bonding density reinforces high momentum regions. Non-bonding

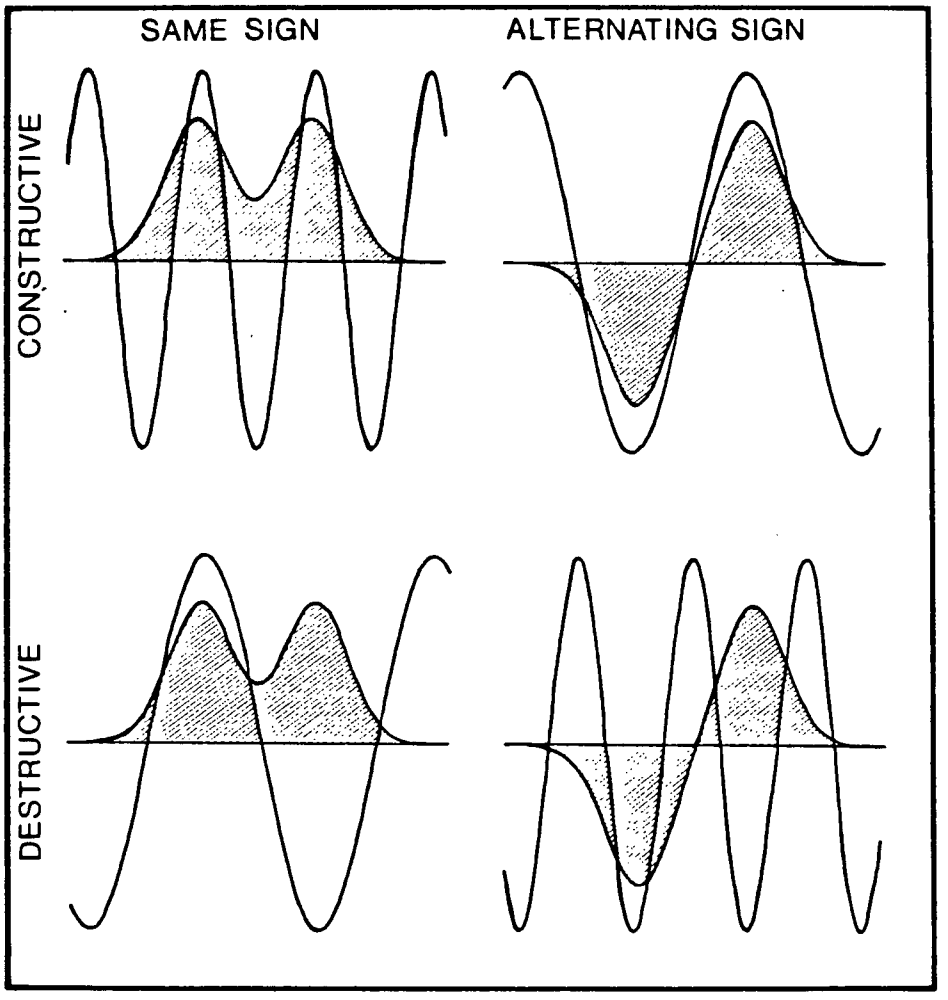

Figure 2.12 Schematic diagrams of the overlap of different frequency components of the Fourier Transform with wavefunctions of different character.

Table 2.2 Constructive and destructive interference

	Same sign	Oscillating sign
Constructive	$\underline{p}=2n\pi/\underline{r}$	$\underline{p}=(2n+1)\pi/\underline{r}$
Destructive	$\underline{p}=(2n+1)\pi/\underline{r}$	$\underline{p}=2n\pi/\underline{r}$
	$n=0,1,2...$	

Table 2.2 Constructive and destructive interference

density will fall somewhere in between.

In the case of symmetric AX_2 systems the destructive parts of the interference term can be strong enough to exactly cancel the one-centre part at certain values of p||, resulting in nodal planes. However, in asymmetric AXY systems this will no longer occur (a situation similar to homonuclear and heteronuclear diatomics), and the only nodal planes will be those in the π orbitals.

The exact values of momentum can be worked out knowing the symmetry of the orbital and the geometry of the molecule. The detailed case for CO_2 is presented in section 6.5.

It might be noted that these arguments can also be applied to the bonding in diatomic molecules, to rationalize the shape of the P-space density in the $3\sigma\{g\}$ orbitals of N_2 and O_2.

2.6 Bond Oscillation

Further development of the idea of charge separation reinforcing certain components of the FT wave leads to the concept of bond oscillation {Levin (1975), Coulson (1944)}. The momentum distribution will, as a result of the four

situations in Table 2.2, have weak fringes going out to large p, separated by $2\pi/\underline{R}$ where $\underline{R}$ is the vector between two nuclei. This produces a sinusoidal modulation of the FT amplitude in the $\underline{R}$ direction. This effect is analogous to optical interference fringes in the well-known double slit experiment. The sinusoidal modulation arises from the factor $\exp(i\underline{p}.\underline{R}\{AJ\})$ between pairs of atoms A,J (see equation B.8).

Bond oscillation effects are most noticeable when the two areas of charge density are well-localised and distinct from each other. Excellent examples are the core MOs of homonuclear diatomics (see example N_2 $1\sigma\{g\}$, $1\sigma\{u\}$ {Kunz}, figure 2.13). Here the magnitude of the oscillation is as large as the p=0 density. In valence MOs where a large part of the density is located in the bonding region, the modulations due to bond oscillation are much weaker, and may only be seen by plotting MD maps with very low contour values out to large momenta (e.g. figure 2.14). Valence bond oscillations may become stronger if there are several atoms at similar interatomic spacings, whereupon several oscillations of the FT wave are reinforced, with consequential increase in modulating amplitude.

The nuclear geometry is preserved in the P-space representation in the presence of bond oscillations since the spacing between successive peaks of the bond oscillation density is inversely proportional to the interatomic distance of the two centres. In a polyatomic system each

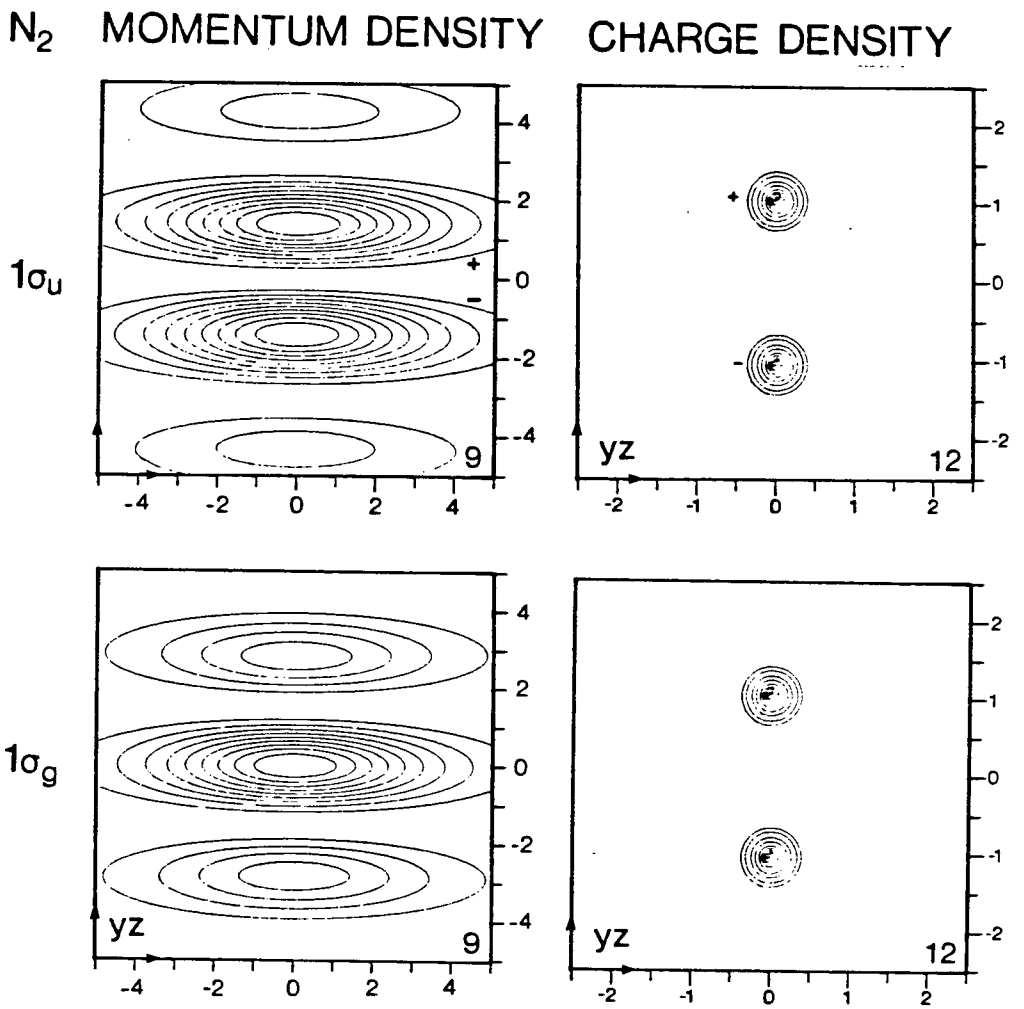

Figure 2.13 N_2 inner shell $1\sigma\{g\}$ and $1\sigma\{u\}$ momentum and charge density maps, showing bond oscillation.

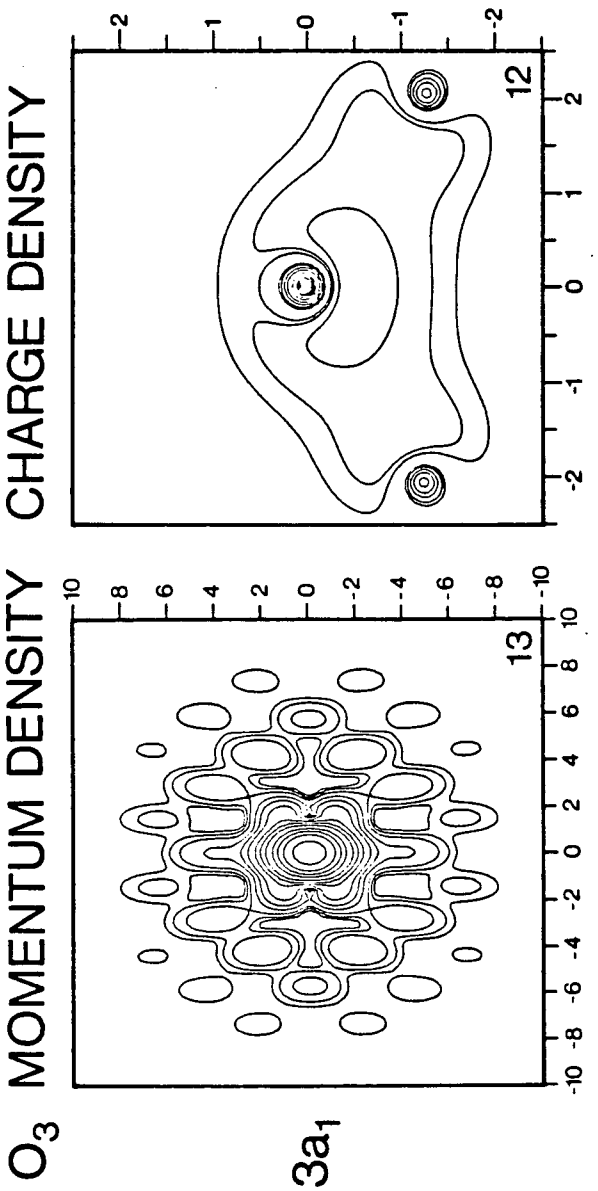

Figure 2.14 O_3 $3a_1$ orbital momentum and charge density maps showing extensive bond oscillation. There are 13 contours in the P-space map at fractions .5, .2, .1, .05, .02, and so on down to .00005 of the maximum density.

pair of atoms will give rise to its own bond oscillation series, and so the nuclear geometry is apparent in much the same way as the crystal structure is apparent from an X-ray crystallography study. An example of this is the $3a_1$ MO of O_3 (ozone) {Basch (1972)} shown in figure 2.14.

It will be noted that a side effect of the bond oscillation phenomenon is an apparent elongation of the P-density perpendicular to the bond axis. This effect does not indicate that the MO in question necessarily has significant bonding character. An extreme example is N_2 $\sigma\{1s\}$ orbital: we know this core MO to be non-bonding, but there appears to be a very strong elongation indicating bonding. However, the overall density is still more or less spherically distributed about the P-space origin, indicating a non-bonding MO.

2.7 The Spherical Average

As gaseous targets are used in the binary (e,2e) experiment a spherical average of the three-dimensional momentum density is observed on account of the rotational motion of the target molecules. This naturally obscures information in the momentum density, but this is not such a handicap as might be thought since the obscured angular form

is often dictated by the symmetry of the orbital and we can oftentimes work out what that angular form must be.

The spherical average does tend to distort the relative amounts of various angular momentum components of the total density function in favour of the lower l contributions. An example of this is the 4σ orbital of NO (see figures 7.2 and 7.3) where the momentum density map shows a mainly p-type $\sigma^*(2s)$ orbital with a small amount of density (<10 per cent of the maximum) at p=0: the spherically-averaged momentum distribution (figure 7.1) shows much more intensity at q=0, relative to the maximum.

The spherical average also tends to distort the depth of minima in nodal areas: a nodal or near-nodal surface in a linear molecule at for example $p_{||}=0.5$ will be filled in to some extent by density at $p_{\perp}>0.5$ when the spherical average is taken. A good example of this is the $3\sigma\{g\}$ MO of O_2 (figure 7.2c).

CHAPTER 3 EXPERIMENTAL

...they did not understand or like
machines more complicated than a
forge bellows, a water mill, or a hand loom...

This chapter describes the physical construction of the spectrometer, the vacuum support systems, the electronics of the spectrometer control and signal processing and data acquisition systems, operating and calibration procedures, and data analysis. The basic system has been reported in the literature {Hood (1977)}. Further modifications incorporated during the present work are indicated in the following text.

3.1 The Vacuum System

As with all electron spectrometers the instrument can only function in high vacuum ($<10^{-4}$torr; 1torr=1mmHg). Accordingly, the spectrometer is housed in a vacuum chamber of about $0.1m^3$ volume. This chamber is pumped by a 6-inch Varian VHS-4 oil diffusion pump to attain a base pressure of

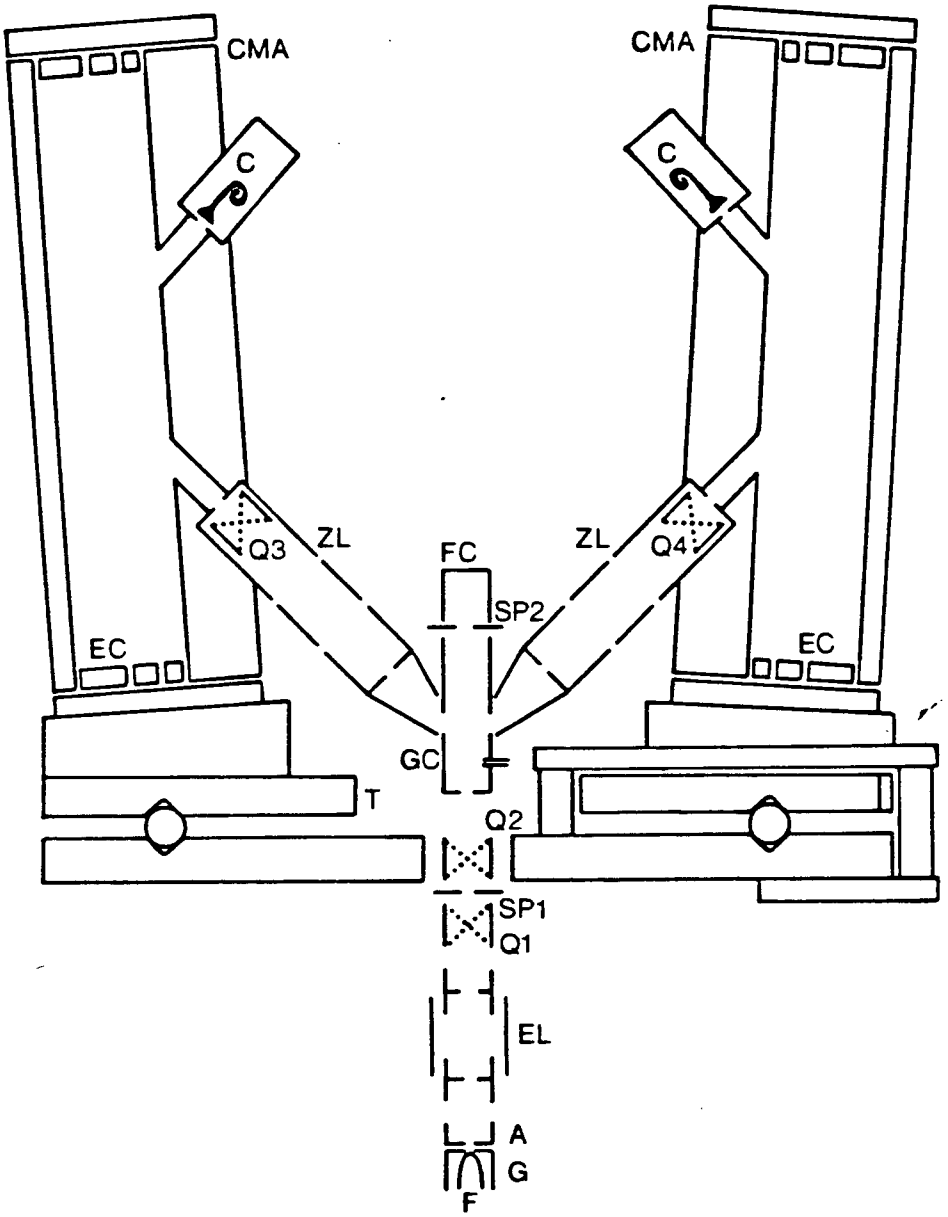

Figure 3.1 Schematic diagram of the binary (e,2e) spectrometer used to obtain most of the experimental results in this thesis.

Legend:

CMA	Cylindrical mirror analyser segment	SP2	Spray plate 2
C	Channeltron	GC	Gas cell
ZL	Electrostatic zoom lens	Q	Quad electron deflectors
FC	Faraday cup beam dump	EL	Einzel lens
T	Turntable	A	Anode
EC	End correctors	G	Grid
		F	Filament

about $5x10^{-7}$torr; Convalex diffusion pump oil is used. The diffusion pump exhaust is pumped away by a Welch Duo-seal 1402 rotary mechanical pump. The system can be pumped down to operating pressure in about 3 hours, but it is customary to wait overnight before commencing operation, to allow the chamber walls and spectrometer surfaces to outgas. The ambient pressure is measured by a Veeco ionization gauge mounted on the top of the spectrometer chamber. The port leading to the gauge is shielded with a metal plate to eliminate interference from the large numbers of electrons produced by the ion gauge filament. All mechanical joints in the vacuum housing are sealed with Viton O-ring gaskets, or else soldered or welded permanently. Two plexiglas-covered viewing ports on the side and top of the vacuum chamber allow observation of the spectrometer in operation.

3.2 The Spectrometer

The spectrometer itself (figure 3.1) consists of an electron beam source, a beam steering unit, a gas cell, and two electron analysers each made up of a three-element electron lens and a cylindrical mirror segment electron energy analyser with channeltron electron detectors, and a mechanical angle-scanning system.

3.2.1 The electron gun

The electron gun used for most of this work is a Cliftronics CE5AH unit designed to supply an electron beam of intermediate energy (100-2000eV). The gun consists of several elements:

(1) A thermionic emitter, usually a tungsten wire hairpin or ribbon loop;

(2) A grid, immediately next to the filament, with a small aperture (0.5mm) through which the extracted electrons pass;

(3) An anode 1mm from the grid, of similar construction;

(4) A three-element einzel lens after the anode.

The filament is electrically heated with a DC current to its operating temperature (1000-1500°C) at which point electrons can be extracted easily by an electric field. This extraction field is defined by the small apertures in the grid and anode, and by the relative electric potential on the three elements. Normally the filament is maintained at $-E_0$ volts (i.e. if a 400eV beam is desired then the filament is set to -400 volts with respect to the gas cell which is at ground potential). The grid is usually set to a potential close to that of the filament. The filament/grid configuration now defines a relatively field-free region at the tip of the filament where a space charge or 'cloud' of free electrons builds up. The anode is set several hundred

volts positive with respect to the grid and, because of the small size of the apertures in the grid and anode, this defines a very sharp needle-shaped extraction field into which the space charge flows. The sharper this extraction field can be made, the more collimated will be the resulting electron beam. The physical line-up and voltages of the filament/grid/anode assembly is crucial to the production of a good beam. By 'good' here I mean a well-collimated beam, with high flux and of small energy spread. The filament-grid spacing is especially critical: by trial and error a separation of 0.2-0.3mm was found to give good, reproducible results. The einzel lens in the gun allows the operator to correct any small divergences in the beam emanating from the anode. In three-element einzel lenses the first and last elements are at the same potential (in this case, at ground potential) and the middle element potential is adjusted so as to obtain the desired focussing effect.

With tungsten ribbon loop filaments depending on the gas pressure and type of gas used, 400eV beams of 20-100μA could be obtained, collimated so well that 98 per cent of the beam flux would pass through a 2mm aperture in a spray plate 20cm removed from the gun. With thoriated tungsten wire hairpin filaments the beam was less good (10-50μA, 90-95 per cent focussed through the spray plate) but tended to last 50-100 per cent longer before burning out. Factors tending to prolong the life of the filament are:

(1) Running at lower temperatures (i.e. lower filament currents);

(2) Using tungsten wire filament material

(3) Using relatively inert gases at low pressures.

Factors which tend to shorten the filament life are:

(1) Poor physical line-up of the filament or high flux requirements which necessitate high filament temperatures;

(2) Using tungsten ribbon filament material;

(3) Running reactive or corrosive gases at high pressures.

The beam produced by the gun will have a finite energy spread. This is due to the Boltzmann distribution of electron energies in the filament material which is heated to high temperature, and to the characteristics of the space charge generated between the filament and the grid. Factors tending to reduce the energy spread of the electron beam are:

(1) Lower filament temperatures;

(2) Having the filament and the grid at similar potentials.

Factors affecting the beam flux, energy and collimation are complex and interrelated, so it is not a straightforward matter to discuss these in any simple way.

Recently it has been found that for 1200eV operation a

hairpin tungsten filament mounted so that the tip protrudes into the grid-anode space gives good beams up to 100μA. In this mode of operation the electrons emerging from the anode is quite divergent, and one relies on the einzel lens to collimate the beam.

The electron gun is surrounded by a loose wire mesh which is biased at the cathode (filament) potential. The mesh prevents unwanted electrons pouring out of the back of the gun from straying near the analysers.

3.2.2 The beam steering unit

The beam steering unit is intended to correct for residual magnetic fields and mechanical misalignment as the beam travels from the gun to the gas cell. The unit consists of two spray plates, a Faraday cup beam dump, and two sets of electrostatic beam deflectors, all mounted coaxially with the electron gun. Spray plates are simply plates with small apertures through which the beam passes, connected to a microammeter. If any part of the beam, through magnetic field deflection or poor alignment or focussing, should strike the spray plate, then the resulting current can be observed and the beam characteristics corrected. Since there is one spray plate before the gas cell and one after, it is possible to ensure that the beam passes down the axis of the gas cell in spite of residual magnetic fields which may tend to deflect it. The Faraday cup serves to collect the

unscattered beam and prevents it from causing interference in penetrating the analysers. The Faraday cup is also connected to the microammeter so the total incident beam current can be monitored.

3.2.3 The gas cell

The gas cell itself is simply a tube blocked off at both ends, mounted coaxially with the electron gun. Apertures are made in the ends for the beam to pass through, and slots are cut around the middle for the scattered electrons to pass out of the cell. Where the slots are open to the vacuum chamber these open areas are covered with sliding metal shim blinds. This again is intended to prevent noise from stray electrons and to make the cell more nearly gas-tight. A small hole is made to admit the gas. The gas cell permits a local increase in the gas density in the scattering region, without having to flood the whole vacuum chamber to achieve the desired target density. It has been estimated {Hood (1977)} that the gas pressure inside the cell is approximately one to two orders of magnitude greater than the ambient vacuum chamber pressure.

3.2.4 The electron lenses

The three-element electron lenses which transport the electrons from the scattering region to the analysers have two functions:

(1) To focus those scattered particles with the correct energy and trajectory on to the analyser entrance aperture;

(2) To retard the energies of the scattered particles by some fixed adjustable amount E{retard}.

Three-element zoom lenses have the property that different retard ratios may be obtained without altering the focal positions of the lens. Each lens has a beam deflection unit immediately before the analyser entrance aperture to correct for residual magnetic field and mechanical misalignment effects. Each lens has an entrance aperture which serves as an angular stop preventing the entrance of a large number of unwanted electrons. The lenses are mounted at a polar angle of 45°. This particular angle is chosen for two reasons:

(1) Binary encounter theory dictates that the closest e-e collision produces scattered electrons at approximately this polar angle;

(2) More particularly, it is possible to measure down to lowest q only near a 45° polar angle. To be precise, the lowest measurable q for an incident energy of 400eV and a representative binding energy of 15 eV is $0.1a_0^{-1}$, and occurs at $\phi=0°$ and $\theta=44.6°$. The

measured q rises rapidly if the polar angle is changed even slightly (see figures 3.8 and 3.9). This topic is treated more fully in section 3.5.

3.2.5 The cylindrical mirror segment analysers

The electron analysers are cylindrical mirror analyser (CMA) segments. A cylindrical mirror analyser is defined as two infinitely long coaxial metal cylinders (figure 3.2). They have the property that charged particles emanating from a point (A) within the inner cylinder can, if they are of the correct energy and trajectory, be focussed on another point (B) within the inner cylinder by correctly applying electric potentials to the two elements. Inasmuch as infinitely long cylinders are unattainable by mere mortals, the usual practice is to truncate the cylinders somewhere beyond points A and B, and place correcting elements in the ends of the cylinders to maintain the original electric field. Since in the present application it is also impractical to have fully cylindrical analysers, they have also been truncated in the azimuthal direction to allow room for the gas cell and lenses: hence the name CMA segments. Elements are also provided to correct for the azimuthal truncation. One of the analysers is fixed, and the other is mounted on a rotating turntable to permit the variation of the azimuthal scattering angle ϕ. As shown by equation 1.16 and figures 3.8 and 3.9 this is closely related to

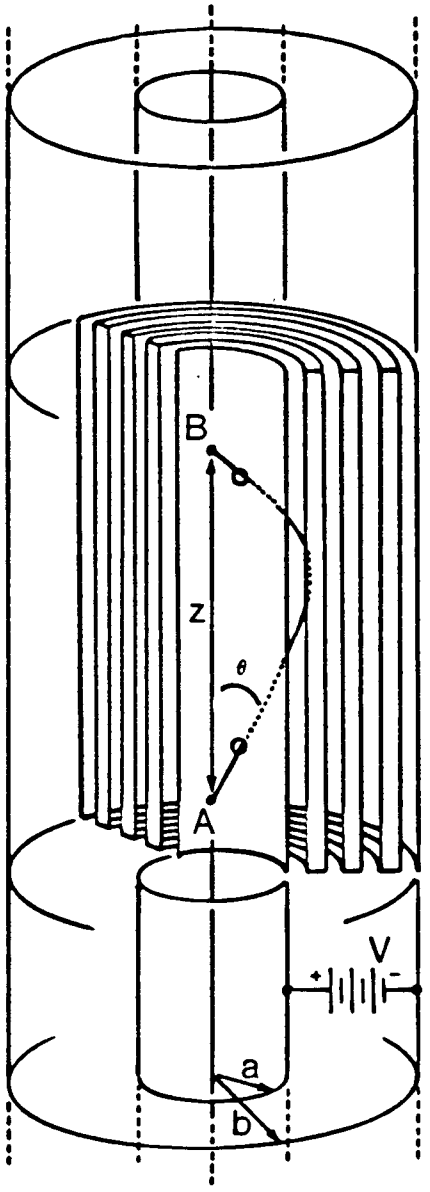

Figure 3.2 Schematic diagram of a cylindrical mirror segment analyser and trajectory of an analysed electron.

scanning q.

Because particles must have the correct energy to pass from point A to point B the CMAs serve as energy selectors. The correct energy of the electrons to pass through the analyser is termed the pass energy, E{pass}. Correct operation of the spectrometer requires that:

(3.1) $E_1 = E_2 = \frac{1}{2}(E_0 - \epsilon) = E\{retard\} + E\{pass\}$

The necessary voltages are supplied by various DC power supplies, adjustable by the operator.

The analysers are designed to have first and second order focussing:

(3.2) $\frac{dz}{d\theta} = \frac{d^2z}{d\theta^2} = 0$

where θ is now the analyser entrance angle, and z is the axial component of the distance between points A and B (figure 3.2). Since these points were chosen to be on the axis of the analyser, the entrance angle must be 42.3° to obtain second order focussing (explaining the 2.7° tilt to the analysers seen in figure 3.1) according to theoretical calculations of CMA parameters {Risley (1972)}. These calculations also give the dispersion for such a case as:

(3.3) $D = E\{pass\} \frac{dz}{dE\{pass\}} = 5.6$

(in units of the inner cylinder radius). If the entrance and

exit apertures are both of 1mm diameter, this means a resolution of:

$$(3.4)\quad R = \frac{\Delta E\{pass\}}{E\{pass\}} = 0.01$$

Therefore, for a pass energy of 50eV, and an energy spread of about 0.8eV for the incident electrons (from elastic scattering measurements), the overall resolution for the spectrometer should be:

$$R = (.5^2 + .5^2 + .8^2)^{1/2} = 1.07$$

(The result of the convolution of several Gaussian peaks together is another Gaussian whose width (FWHM) is the square root of the sum of the squares of the individual widths.) In actual fact the resolution is generally slightly worse than this, generally between 1.2-1.6eV depending on the filament, because the figure R=0.01 does not take into account the spread in entrance angles, which, although the analyser has second order focussing, does have an effect on the energy resolution. It might be noted here that the best energy resolution attained in a binary (e,2e) experiment is a 0.06eV FWHM measurement on argon {Williams (1978)} but this required long acquisition times.

With the electron lenses as trajectory selectors we now have a system which will characterize the positions and momenta of the scattered particles emerging from the gas

cell to within some experimental error. Since the energy and trajectory of the incident beam is also known, this experimental arrangement permits the measurement of the binary (e,2e) cross-section, as a function of binding energy (ϵ) and momentum (q).

3.2.6 The channeltrons

Electrons which successfully pass through the analyser are collected in the channeltrons (channeltron = channel electron multiplier). These are semiconducting glass tubes with a secondary emission coefficient significantly greater than unity. A bias of several thousand volts is applied over the length of the tube. When an electron from the analyser strikes the inner surface of the tube it releases a shower of several secondary electrons from the glass. Because of the bias on the tube these secondary electrons are accelerated toward the positive end of the tube and eventually they in turn strike the walls of the tube releasing many more showers of electrons. Since each electron produces more than one secondary electron there is a net amplification of the single incident electron into a pulse of 10^7-10^8 electrons at the other end of the tube. This pulse can now be amplified and processed by conventional electronic circuits. The pulse has the following characteristics:

(1) -10 to -50mV pulse amplitude when capacitatively

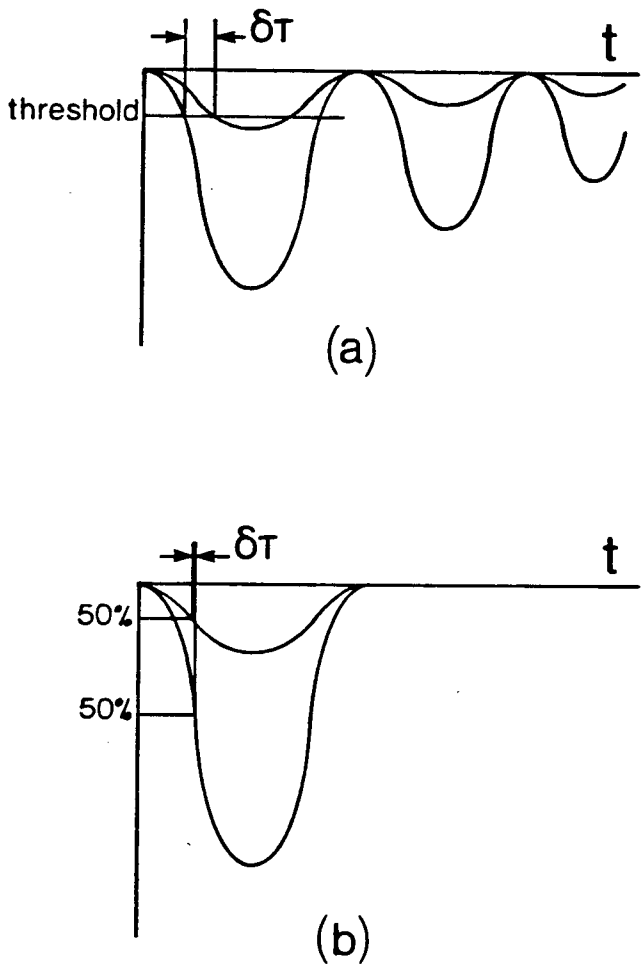

Figure 3.3 Schematic diagram of channeltron pulse shapes and different types of discriminator responses:
(a) Poor termination of cables resulting in ringing on the signal, and threshold-crossing discrimination with attendant timing uncertainty.
(b) Clean channeltron signal and accurate timing from constant fraction discrimination.

coupled (0.05μF) into a 50Ω load. Noise on this signal is less than 5mV.

(2) Near-Gaussian pulse shape - 10ns FWHM.

The channeltron is housed inside a metal shield to prevent interference from stray electrons. Care is taken to prevent arcing of the high voltage (3.5-4kV) channeltron bias to nearby low-voltage points.

Channeltrons are usually curved to prevent secondary ion feedback. A gas molecule which happens to be ionized by a collision with a secondary electron would be accelerated towards the entrance of the channeltron, where it could trigger another burst of secondary electrons. Curving the channeltron means that the ion strikes the wall well before it reaches the entrance.

The channeltron electron multiplier detectors (originally Mullard B419AL) have been replaced by a similar but smaller set (Mullard B318AL). This replacement, combined with closer impedance matching at the pulse pickoff point on the channeltron output, has improved the timing resolution from about 12ns to 7-8ns (FWHM). With somewhat longer data acquisition times (3-4 days per orbital) than had previously been used, and improved timing, a significant improvement in the overall signal-to-noise ratio was obtained, compared with work previous to the H_2S results.

3.2.7 The angle-scanning system

An electromechanical servo loop system is used to set the angle of the moving analyser. The servo amplifier compares a reference voltage from the data acquisition control system with a scan voltage from a potentiometer mechanically linked to the analyser turntable, and generates an AC motor-driving output with the correct phase to turn the motor in the direction which makes the difference between the reference and scan voltages less. Once the two voltages are the same the servo amplifier output drops to zero and the motor stops.

Considerable effort was expended to make this system reliable and accurate. Presently the angle is resettable to $\pm 0.2^{\circ}$ A special silencer unit was devised to turn off the motor once the angle was set. Previously, chatter in the motor was very noisy, and caused loosening and wear in the mechanical parts of the system.

3.3 Construction and Materials

The spectrometer is constructed almost entirely out of brass and aluminum because magnetic fields must be reduced to a minimum, and because these materials are cheap, and easy to machine. The vacuum housing is surrounded by a

μ-metal shield (a material of high permeability) to reduce the effects of the earth's magnetic field. Where high temperatures or mechanical strength require it, stainless steel is sometimes used: if brass is heated to high temperatures the zinc in it will evaporate. Electrical insulation is achieved with sapphire balls, Teflon, ceramic, and Macor (a machinable ceramic). Electrical connections through the vacuum housing are provided by octal (Varian Eimac) and HV-BNC (Ceramaseal) sealed feedthroughs soldered into brass flanges which in turn are bolted onto the baseplate and sealed with O-rings. All surfaces (except for the electron gun) which define an electric potential directing the motion of electrons within the spectrometer are coated with benzene soot. This is simply a form of amorphous carbon and helps to:

(1) Maintain an equal potential over the entire surface of a given spectrometer element;

(2) Reduce the secondary emission coefficient of the surface material so that electrons which strike the surfaces do not bounce off or produce further secondary electrons which contribute to noise in the spectrometer.

Apertures in the electron lens and in the spray plates are made of molybdenum, which also has a low secondary emission coefficient, further reducing noise within the system.

3.4 Signal Processing

The following sections describe the processing of the raw channeltron pulses, in order to extract the (e,2e) event rate. Fairly sophisticated electronic circuitry is required to process the channeltron signals, and to detect true coincidences (i.e. two channeltron pulses triggered by scattered electrons from the same (e,2e) event).

3.4.1 Channeltron coupling

The channeltron pulses are capacitatively decoupled from the high voltage bias and transmitted to the first stage of amplification by 50Ω coaxial cable (RG58/U, RG174/U) (see figure 3.4). This amplification stage is done by ORTEC 9301 Fast Pulse Preamplifiers (FPP). It is very important that the signal cable be properly terminated in order to ensure that the signal quality is not degraded due to impedance mismatches which cause 'ringing' (figure 3.3). Several circuits have been tried out, and the most used ones are shown in figure 3.4. Circuit A has the advantage that only two feedthroughs and two lengths of cable are required, but has the disadvantage that the lines are not properly terminated, and hence generates a large amount of ringing on the pulses.

Best results are obtained with circuit B. All four ends of the two signal cables are terminated in 50Ω resistive

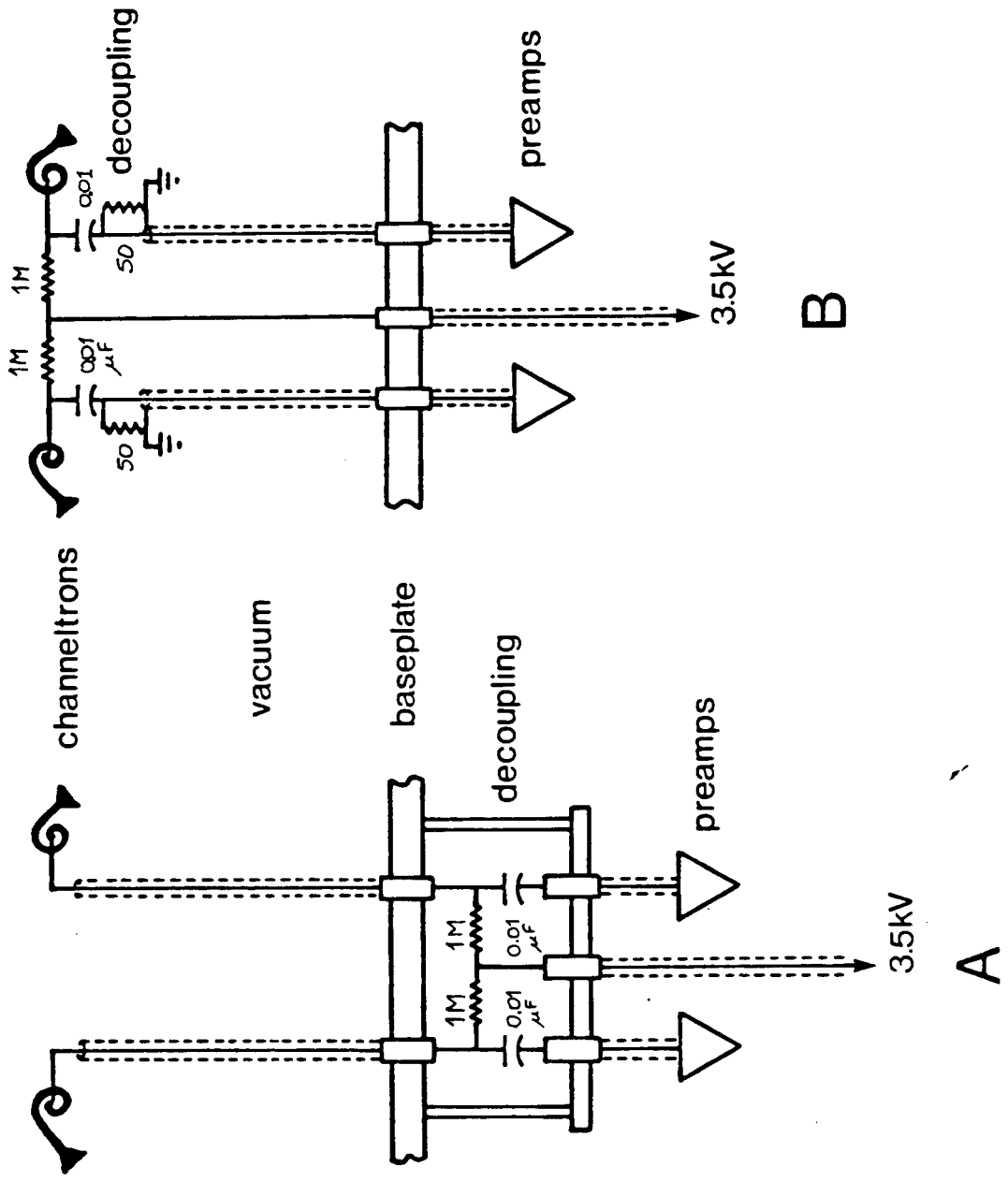

Figure 3.4 Channeltron pulse decoupling circuits:
(a) Circuit A: improper termination of cables
(b) Circuit B: correct termination of cables

loads, and all four ends of the outer shield elements are carefully grounded to reduce pickup from external sources of electrical noise, and from the other channeltrons. (It should be noted that a pulse is transmitted equally well when applied to either the inner element or the outer shield of a coaxial cable. Thus if the outer shield is not grounded at both ends it will act as an excellent antenna.) The time constant of the terminator resistor and decoupling capacitor is chosen to be much longer than the channeltron pulse: this means that the signal will not be distorted by capacitative differentiation to any significant extent.

3.4.2 Pulse amplification and discrimination

A schematic diagram of the signal processing electronics is given in figure 3.5.

The first stage of amplification is done by the FPPs: these in a sense are simply glorified fuses because they isolate the expensive and sensitive main electronics from the destructive effects of very high voltage transients which result from breakdown of the channeltron bias voltage inside the spectrometer. It is cheaper and quicker to replace components in the preamps than in main amplifiers, in the event of arc-overs. They also serve as line drivers for the coaxial cables leading to the main amplifiers: the weak signal from the channeltrons requires amplification before it can be transmitted without interference from

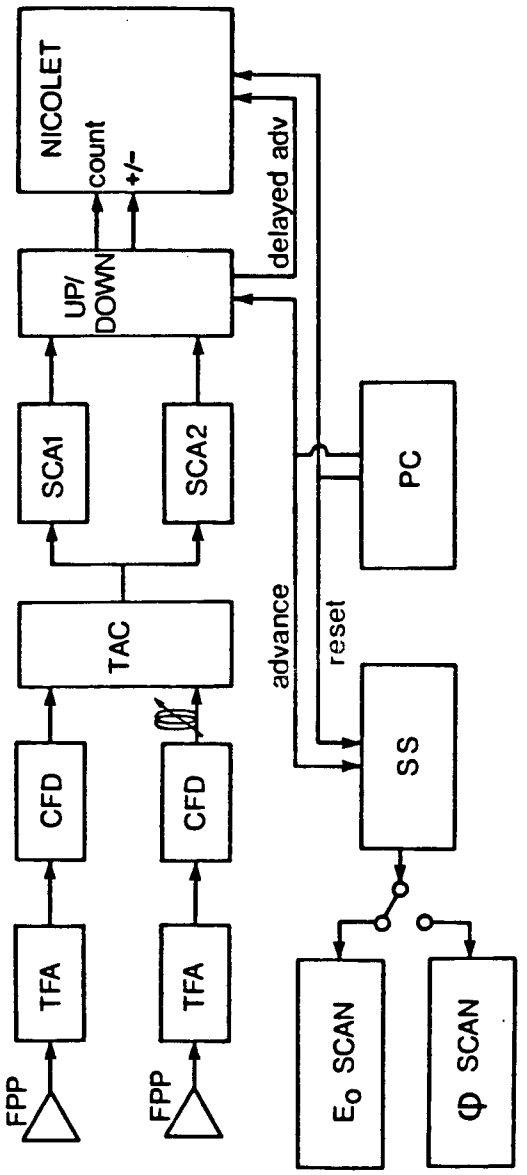

Figure 3.5 Schematic diagram of signal-processing electronics

Legend:

FPP Fast pulse preamps
TFA Timing filter amps
CFD Constant fraction discriminator
TAC Time to amplitude converter
SCA Single-channel analyser
SS Spectrum scanner
PC Program Control

ground loops or pickup over cables that may be up to 3m long. This way the cable length from the channeltrons to the first amplification stage is only about 30cm.

The main stage of amplification is done by ORTEC 454 Timing Filter Amplifiers (TFA). These are fast rise time 50Ω amplifiers with adjustable gain up to 20:1. The gain of each amplifier is set so that the pulse height distributions of each channel at the amplifier output are roughly equal, compensating for unequal channeltron gains. They are also equipped with active filter networks to adjust the rise and fall time constants of the output pulse, but these are usually not used as it is desirable to keep the pulse as sharp as possible. A lot of ringing or oscillation on the pulse may be reduced by adjusting the fall time constant, but this is a 'bandaid' solution at best, and it is advisable to locate and eliminate the source of the problem.

The main amplifiers are followed by ORTEC 463 Constant Fraction Discriminators (CFD). The function of these units is to provide a very sharp, uniformly timed and shaped output pulse whenever there is a valid input pulse. 'Valid' in this case means that the input pulse amplitude must exceed a certain adjustable threshold before the unit will respond and produce an output pulse. This threshold feature is used to reject noise below a certain level. The timing of the output pulse is critical to this experiment in providing a precise indication of the relative times of the pulses on

each line. Simple threshold-crossing discrimination is not adequate for this application, as inspection of figure 3.2 will show: production of the output pulse is initiated when amplitude of the input pulse crosses a given threshold voltage. It is seen that the relative timing of the output pulse is sensitive to the amplitude of the input pulse. If the rise time of the pulse is 4-5ns this means an uncertainty in the timing of the output pulse of a similar amount. The only way to reduce this uncertainty is to set the threshold close to zero, but then low-level noise starts to trigger the discriminator.

Constant fraction discrimination is the method chosen to solve this problem. In this technique the output pulse is produced when the input waveform reaches a fixed fraction of the total pulse height. This gives the timing result shown in figure 3.3, and is nearly independent of the pulse height.

3.4.3 Coincidence detection

The main task of the signal processing electronics is to detect coincidences in the two streams of electrons entering the channeltrons. A valid (e,2e) event produces two electrons which reach the channeltrons at the same time ($t_1=t_2$, or $\Delta t=0$) and therefore initiates two simultaneous pulses in the CFD output lines. However there is another scattering event which produces an identical response in the

channeltrons. This can happen if two unrelated electrons in the incident beam simultaneously collide with two gas molecules within the collision volume producing (by some process of inelastic scattering or ionization, etc.) two unrelated scattered electrons: one has the necessary momentum $\underline{k}_1$ to pass through one analyser, and the other electron $\underline{k}_2$ through the other analyser. Obviously this accidental coincidence signal at the channeltrons will be indistinguishable from a true coincidence which signifies a real (e,2e) event. The problem then is how to remove the background of accidental coincidences and measure only the true coincidence rate.

The answer lies in the fact that the accidental coincidence rate is only the special case where the timing of the two incident electrons is simultaneous ($\Delta t=t_1-t_2=0$). The rate for the observation of two random channeltron pulses having a non-zero time separation ($\Delta t=\tau$) must be the same as the $\Delta t=0$ rate. Also, the rate of non-(e,2e) coincidences is not a function of binding energy or azimuthal scattering angle. Therefore, if the rate of observation of pulse pairs of time separation $\Delta t=0$ and $\Delta t=\tau$ can both be measured, it follows that the true (e,2e) rate is given by:

(3.5) $\text{Rate}\{e,2e\} = \text{Rate}\{\Delta t=0\} - \text{Rate}\{\Delta t=\tau\}$

Rate{e,2e} is termed the 'true coincidence rate', Rate{$\Delta t=0$}

is called the 'total coincidence rate', and Rate{$\Delta t=\tau$} is the rate of random pulse pairs. 'Accidental coincidence rate' refers to those coincidences where $\Delta t=0$, but the two electrons do not come from a valid (e,2e) event.

The rejection of accidental coincidences is done electronically with a time-to-amplitude converter (ORTEC TAC 467), two single channel analysers (ORTEC SCA 406), a coaxial cable delay line, and a logic circuit or computer software (figure 3.5). A TAC has two inputs, START and STOP: one CFD is connected to the START input and the other CFD through the delay line to the STOP input. A valid pulse at the START input starts an internal clock in the TAC at time t_1. A subsequent pulse at the STOP input stops this clock at time t_2 and triggers the conversion of this internal measured time into an output pulse whose amplitude is proportional to the time separation Δt. The true coincidences do not all occur exactly at $\Delta t=0$, but rather there is a finite time width, $\delta\tau$, associated with this signal due to slight changes in propagation times of the signals through the spectrometer and electronics; a delay is used in the STOP line to shift the true coincidence signal completely into the range of the TAC, otherwise true coincidences where the STOP pulse comes slightly before the START pulse will not be detected by the TAC. With Mullard B318AL channeltrons $\delta\tau$ is about 6-8ns.

A histogram of the TAC output is shown in figure 3.6. A

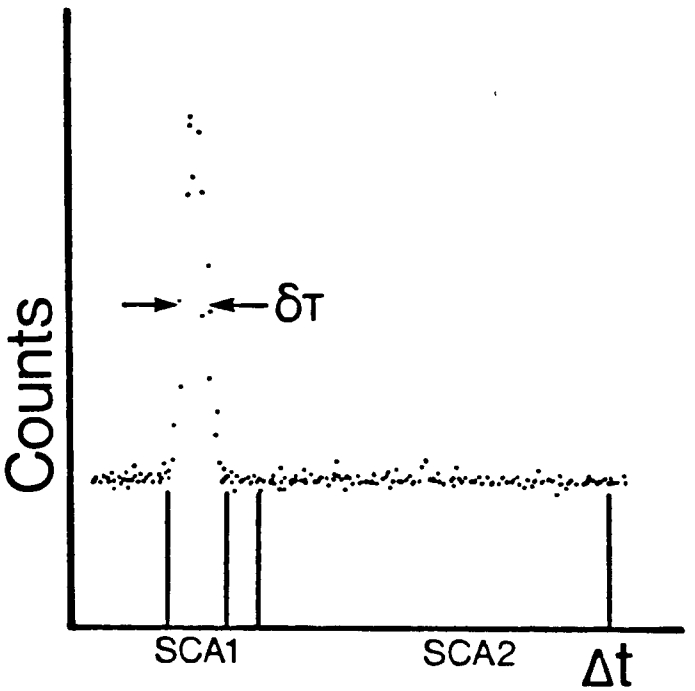

Figure 3.6 Typical time spectrum showing placement of SCA windows.

flat background is observed, due to the random pulse pairs, and superimposed on this is a peak due to the true coincidence signal. The position of this peak is related to the cumulative differences in propagation times of the two signals. The width of the peak is a function of the timing spread due to the dispersion of particles in the analysers, noise in the system, and jitter in the CFDs.

The TAC output pulse is fed to the two SCAs. An SCA generates an output pulse only if the input pulse has an amplitude within a voltage window with adjustable upper and lower bounds. One SCA is set to span the coincidence peak, and the other has the same width, but is positioned on the flat background (see figure 3.6). The data acquisition system is arranged so that a pulse from SCA1 will increment a counter register, and a pulse from SCA2 will decrement the counter. This is how equation 3.5 is implemented in the data acquisition electronics: it can be seen that the time-averaged pulse rate from SCA2 cancels off the accidental coincidence rate in SCA1 so that only the true coincidences accumulate in the counter.

In fact, as figure 3.6 shows, the ratio of the SCA window widths need not be unity, but can be some integer n greater than unity, as long as an equal count n is added to the spectrum upon receipt of an SCA1 pulse. This modification improves the statistical accuracy of the spectrum since more measurements of Rate$\{\Delta t=\tau\}$ are made. The

statistical accuracy of the final spectrum is:

$$(3.6)\quad \sigma = \left[N\{\Delta t=0\} + \frac{N\{\Delta t=\tau\}}{n} \right]^{1/2}$$

where $N\{\Delta t=0\}$ is the number of counts from SCA1, $N\{\Delta t=\tau\}$ is the number of counts from SCA2, and n is the ratio of the window widths. Clearly, increasing n reduces σ. For most of the measurements in this thesis, n was set to 15.

3.4.4 Signal-averaging data acquisition system

Two data acquisition systems were used: the first is a combination of a specially built 16-bit up/down counter register, a commercial Nicolet 1072 signal averager, and ORTEC scan control units (this system was already in place at the beginning of the work for this thesis); the second was designed during the thesis work around a PDP LSI11/03 microcomputer.

The data acquisition system must perform several functions:

(1) Storage space for a multi-channel histogram must be provided;

(2) There must be an active channel where the total count can be incremented by n on receipt of a pulse from SCA1, or decremented in the case of a pulse from SCA2;

(3) There must be provision whereby the active channel

can be stepped through the histogram and reset, concurrently with stepping and resetting a reference voltage which is used to control the scanned parameter;

(4) The contents of the histogram must be displayed graphically for observation, and there should be a method for making permanent graphical and numerical records of the data.

The term 'signal averaging' denotes the process of repetitive accumulated scanning of a spectrum, where the results of a scan are added to the previous scans. This is done for two reasons:

(1) If the signal intensity is comparable with, or less than the noise in a measurement, the noise will cancel out over many scans because it is a random phenomenon, but the signal, though weak, is present all the time, and should reinforce itself with every scan. With a long enough collection time it will eventually be visible over the noise;

(2) Although there might be a large change in the signal rate with time over the course of a run, this will not affect the final spectrum since during any single scan the change in intensity will be insignificant.

The Nicolet 1072 signal averager is a data acquisition and storage device with the features described above. It has

a hardware memory of 1024x16-bit words, divided into 4x256-word segments. There is a pulse counting circuitry and external channel advance and reset lines. Outputs are provided for a continuous X-Y oscilloscope display, point plotter, and teletype.

The up/down counter interfaces between the two SCAs and the Nicolet. The internal 16-bit register is incremented by a pulse from SCA1 and decremented by a pulse from SCA2. Receipt of a channel advance pulse indicates the end of the data collection period for a given active channel and triggers the readout of the final contents of the internal register into the Nicolet and clears the register. This readout takes the form of a serial pulse train to the Nicolet pulse input line, and a simultaneous hi/lo logic level into the Nicolet add/subtract line. The number of pulses is equal to the absolute magnitude of the accumulated count, and the state of the add/subtract line gives the sign. This result is added to the accumulated count. Then a delayed version of the channel advance pulse steps the Nicolet to the next channel.

The Nicolet 1072 is capable of functioning (via plug-in units) as a pulse height analyser as well as a signal averager. In this mode the TAC output is converted to a histogram of frequency vs pulse height. The Nicolet also provides some primitive data reduction facilities to add and smooth spectra, subtract backgrounds, and so on.

The microcomputer-based data acquisition system is described in detail in Chapter 8. All that need be said here is that all the basic functions of the Nicolet system are emulated, and, due to the versatility and powerful software of a computer system, many tedious data reduction and analysis procedures are automated. Data is semi-permanently stored on floppy diskette medium, along with all parameters pertinent to the run. Permanent graphical and textual records are made on a graphics printer. The computer-based system allows more flexibility in data acquisition. For instance it is possible, since the computer can control both incident energy and scattering angle simultaneously, to record several binding energy spectra and momentum distributions concurrently and so maintain the correct relative absolute intensity of a given structure with respect to its fellows.

3.5 The Instrumental Response Function

The spectrometer is sensitive only to those electrons emerging from the gas cell which have particular properties. We do not observe an ideal (e,2e) cross-section of a single molecule, but rather some result which also has convoluted in a resolution function with several dimensionalities:

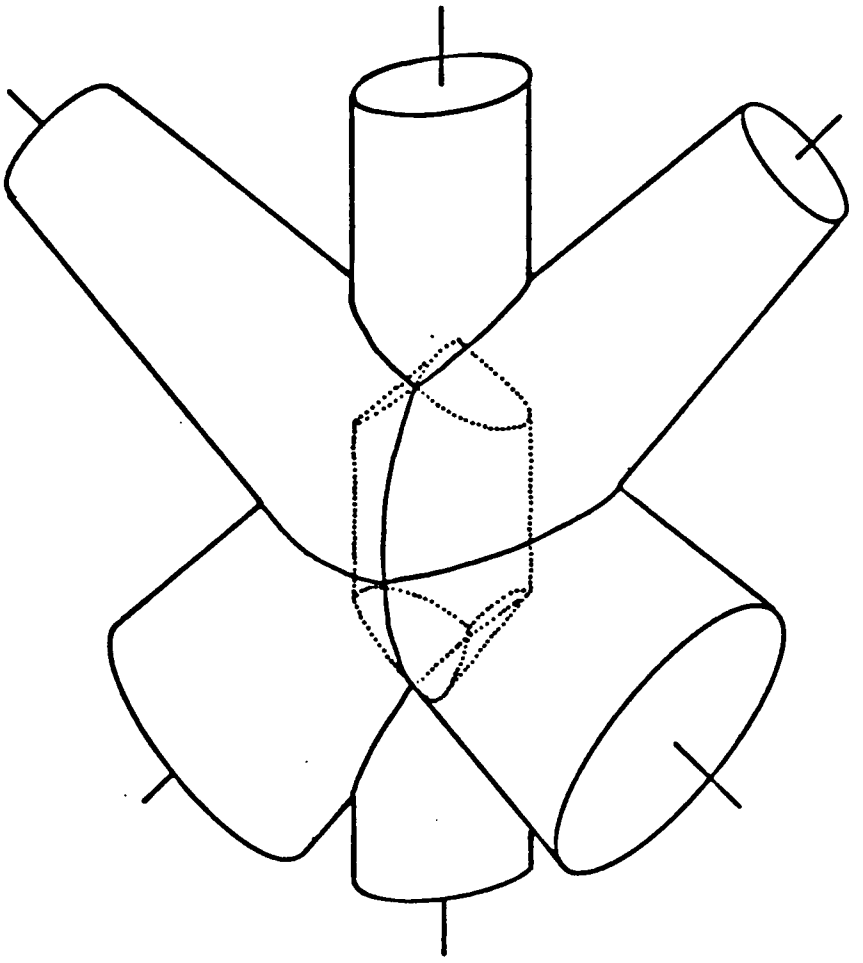

Figure 3.7 The collision volume resulting from the overlap of hypothetical cylinders and cones representing the incident beam volume and the acceptance cones of the lenses.

(1) The spatial collision volume as defined by the overlap of the incident electron beam, and the acceptance cones of the lenses (figure 3.7). This overlap determines the mean θ and ϕ angles, and the effective θ and ϕ resolution. It is very important to understand that this volume is not necessarily a constant function of the azimuthal scattering angle. The question will be elaborated below;

(2) The finite energy resolution which is a function of the energy spread of the incident beam, and the dispersion of the two analysers;

(3) The overall timing uncertainty which arises from differences in analyser transit times, channeltron response, and electronic processing delays; This does not normally enter into the response function since one effectively integrates over Δt by setting SCA1 to span the entire coincidence peak;

(4) Incident beam flux: this is almost never an absolutely constant function of incident energy;

(5) Gas density: it is assumed that the sample gas is homogeneously distributed throughout the gas cell;

(6) Lens/analyser transmission function: this is not necessarily perfectly constant as a function of azimuthal angle.

The optimization of the spectrometer operation must take into account the following points (numbered to refer to

the same topics as above):

(1) In order to ensure that the collision volume does not alter significantly with azimuthal scattering angle the mean diameter of the electron beam (it probably has a semi-Gaussian cross-section) must be made significanly less than the diameter of the lens acceptance cones at their intersection. If this is done then the collision volume will be a thin cylinder whose shape changes only very slightly at the ends, as the moving analyser revolves. Also, if there is any drift in the position of the beam, the acceptance cone of the moving lens, or misalignment in the physical construction of the spectrometer, such things will have little effect on the collision volume. The only disadvantage to this type of operation is that a fairly large θ angle is subtended over the length of the collision volume, which must be taken into account in comparing theoretical momentum distributions with experiment. If however, in the interests of good θ- and ϕ-resolution, the acceptance cones are made very sharp then several problems will result: it will be difficult to keep the moving lens acceptance cone centred on the beam; the alignment of the lenses in the θ-dimension is also now more critical; changing collision volume with ϕ-angle will be unavoidable, unless higher incident energy is used to compress the distribution into a small ϕ-range, whereupon the

relative ϕ-resolution is back to where it was before; and finally, the data rate will be diminished. With the optimized collision volume the θ-resolution will be worse than the ϕ-resolution. This will have the greatest effect in p-type distributions near q=0, where the sharp minimum will be filled in to some extent. Because there is uncertainty in this resolution factor, and also because of the uncertainty in the mean θ value arising from the use of the deflectors in the lenses, I am unwilling to draw firm conclusions about the shape of the distribution or its agreement with theory in the region $q<0.4a_0^{-1}$;

(2) Where the binding energy spectrum is simple enough (i.e. the peaks are few and well-separated) it is desirable to degrade the energy resolution to the point where the binding energy peaks begin to merge together. This will afford the highest possible data rate, yet still allow the momentum distributions to be determined without overlap from other states. For complex binding energy spectra one can try to resolve the outer valence peaks, but in the present state of the art, it is not practical to try to resolve the inner valence region as this is almost always very intricate. In any case, it is not practical to try to improve the overall energy resolution to much beyond a factor 1.5 times the incident beam energy spread. The energy response function is optimized by reducing the

incident beam energy from $E_0+\epsilon$ to E_1 and observing the energy distribution of elastically scattered electrons in each analyser. The lens focus control and the lens deflectors were used to make this distribution as sharp and as nearly symmetric as possible, but it is now realised that the use of the deflectors in the vertical plane distorts the effective θ angle. It is recommended that these two elements be short-circuited to the analyser inner element;

(3) It is desirable to reduce the overall timing spread so as to be able to increase the ratio of the widths of the SCA1 and SCA2 windows, and improve the statistics of the measurement. This can be done by the following: narrowing the acceptance cone of the electron lenses and raising the pass energy in the analysers (where feasible) so that the dispersion is less and the lens/analyser transit time spread is thereby reduced; using smaller channeltrons with sharper pulse outputs; and improving the quality of the signal decoupling and transmission between the channeltrons and the preamps so that only a bare minimum of noise and ringing is imposed on the signal. It is important to check from time to time that the coincidence peak has not drifted out of the SCA1 window;

(4,5) Changes in the incident beam flux, as a function of energy, and gas density, as a function of time, can

be accounted for by normalizing the scan time to the singles scattering rate in the moving analyser, and by the signal-averaging data acquisition method. One must be careful when using normalization as it can obscure poorly-optimized factors in the instrumental response function: for instance, drifts in the collision volume due to poorly-tuned beam and lenses, magnetic field changes, or charging effects; or changing background count rates due to anisotropic stray electrons;

(6) The lens/analyser transmission function is an unlikely source of trouble, but it can change slightly if magnetic field fluctuations cannot be rigorously eliminated. The moving analyser is especially susceptible to this, and also to a varying background of stray electrons within the vacuum chamber. This is why μ-metal shielding must be used, and measures taken to control or eliminate all sources of stray electrons. While such stray electrons do not affect the coincidence count rate since they do not arise from (e,2e) events, they can give rise to a sloping background by altering the random pulse-pair rate as a function of angle.

3.5.1 The q-θ-ϕ surface

Figures 3.8 and 3.9 shows a representation of equation 1.17 where q is plotted as a function of the θ and ϕ scattering angles for E_0 values of 400 eV and 1200 eV. A hypothetical binding energy of 15eV is used.

It is seen that at 1200eV the momentum distribution is compressed to lower ϕ-angle and also that q is a sharper function of θ, than at 400eV. Therefore at the higher energy it is relatively more important to know precisely the effective mean θ and ϕ angles in converting the ϕ-scale to the q-scale, and the θ- and q-resolution in comparing experiment with theory.

For all of the work in this thesis a resolution convolution program was used to fold the experimental angular resolution and Mott scattering factor into the theoretical momentum distribution. This program (written by Drs. A. Hammett and S.T. Hood) approximates the finite angular acceptance cone of the lens with an average over several rays of slightly differing θ- and ϕ-angle. The number and direction of these rays were determined empirically by comparison of a good theoretical wavefunction with experiment for helium. Unfortunately, the helium 1s momentum distribution is not very sensitive to the angular resolution, and the parameterization should also have been done on the argon 3p momentum distribution. Judging by the

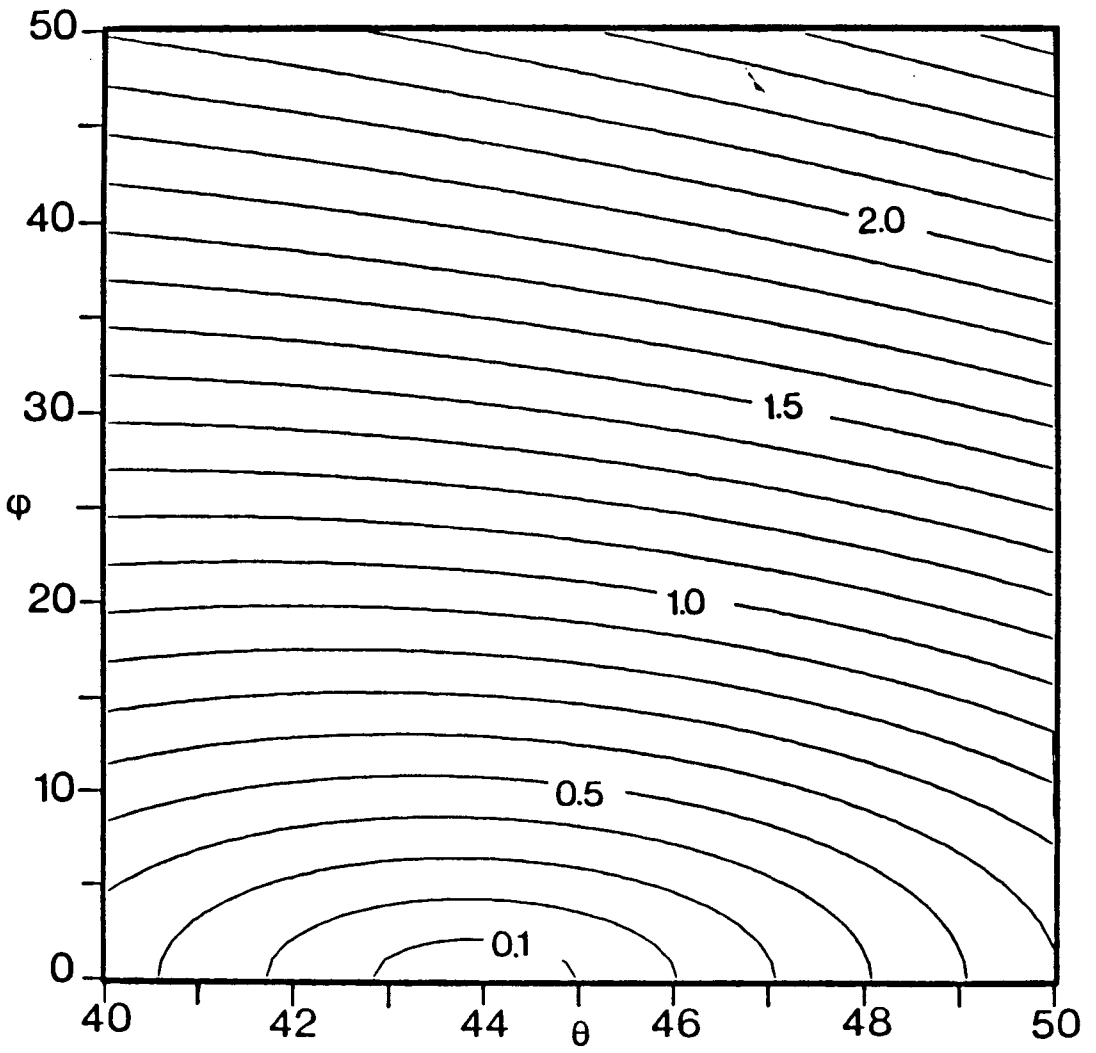

Figure 3.8 Contour map of q as a function of θ and ϕ at E_0=400eV and ϵ=15eV. Contours are at intervals of $0.1a_0^{-1}$.

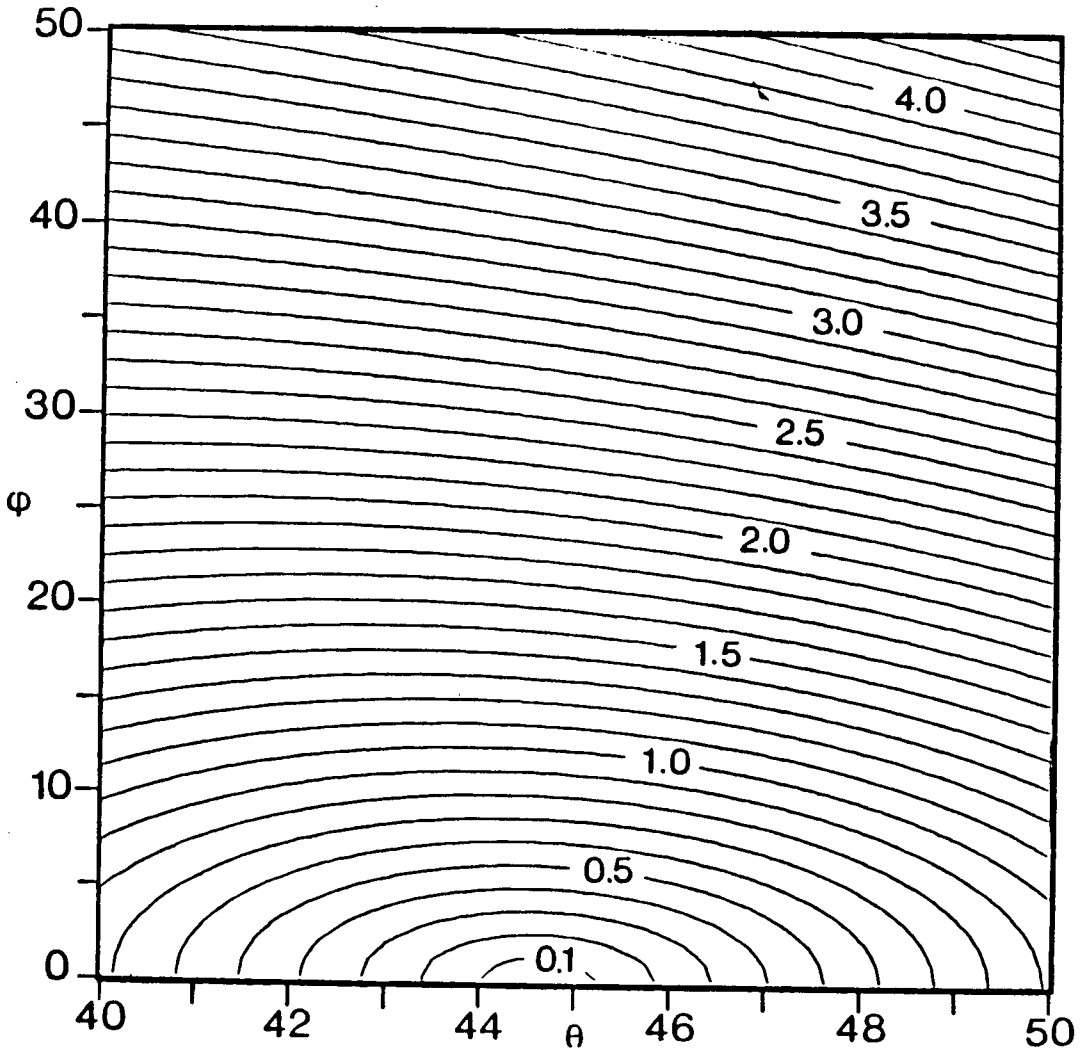

Figure 3.9 Contour map of q as a function of θ and ϕ at E_0=1200eV and ϵ=15eV. Contours are at intervals of $0.1a_0^{-1}$.

H_2S results the estimated angular resolution is probably worse than it really is: the experimental p-type momentum distributions are consistently sharper than calculation; however, the opposite seems to be the case for CO_2.

3.5.2 Comparison of 400eV vs 1200eV operation

The choice of incident energy E_0 is an important factor in running the spectrometer. The several arguments for preferring 400eV or 1200eV operation are given here:

(1) Signal/noise ratio: the binary (e,2e) cross-section falls off as $E^{-3/2}$ with increasing energy (see equations 1.18 and 1.19), whereas the inelastic scattering cross-section for production of single particles of energy $E_1=E_2=\frac{1}{2}(E_0-\epsilon)$ {Inokuti (1971)} falls off faster as E^{-2}. For this reason it is desirable to operate at higher energy so as to increase the signal/noise ratio. This does mean a lower data rate, but this can be improved by increasing the collision rate (i.e. higher beam flux and gas density);

(2) Angular resolution: as demonstrated in the previous section, the angular resolution must be improved going to higher energy, in order to maintain the equivalent q-resolution. As with any type of resolution improvement this goes hand-in-hand with a loss in data rate. A loss in relative angular

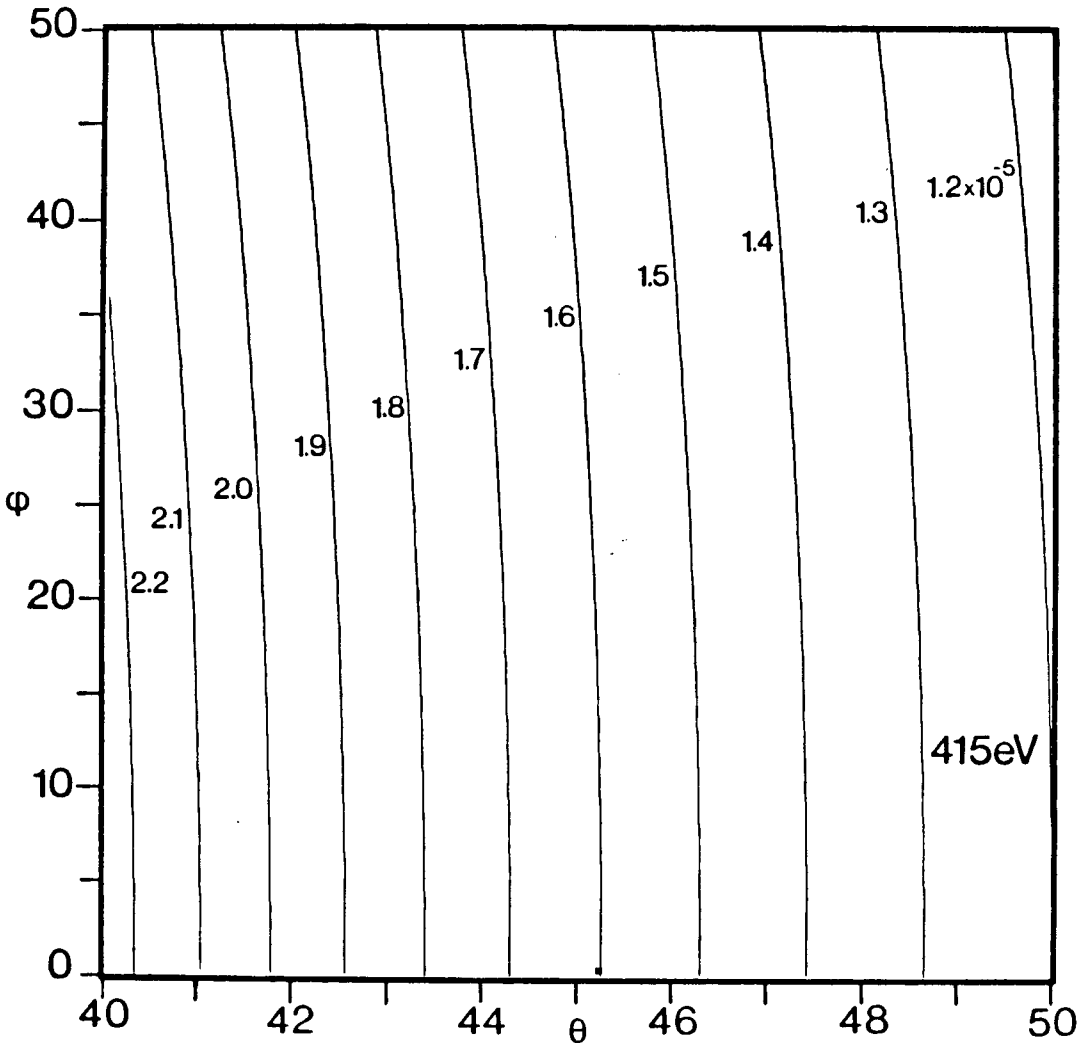

Figure 3.10 Contour map of $\sigma\{Mott\}$ as a function of θ and ϕ at E_0=400eV and ϵ=15eV. Contour values are labelled on the diagram.

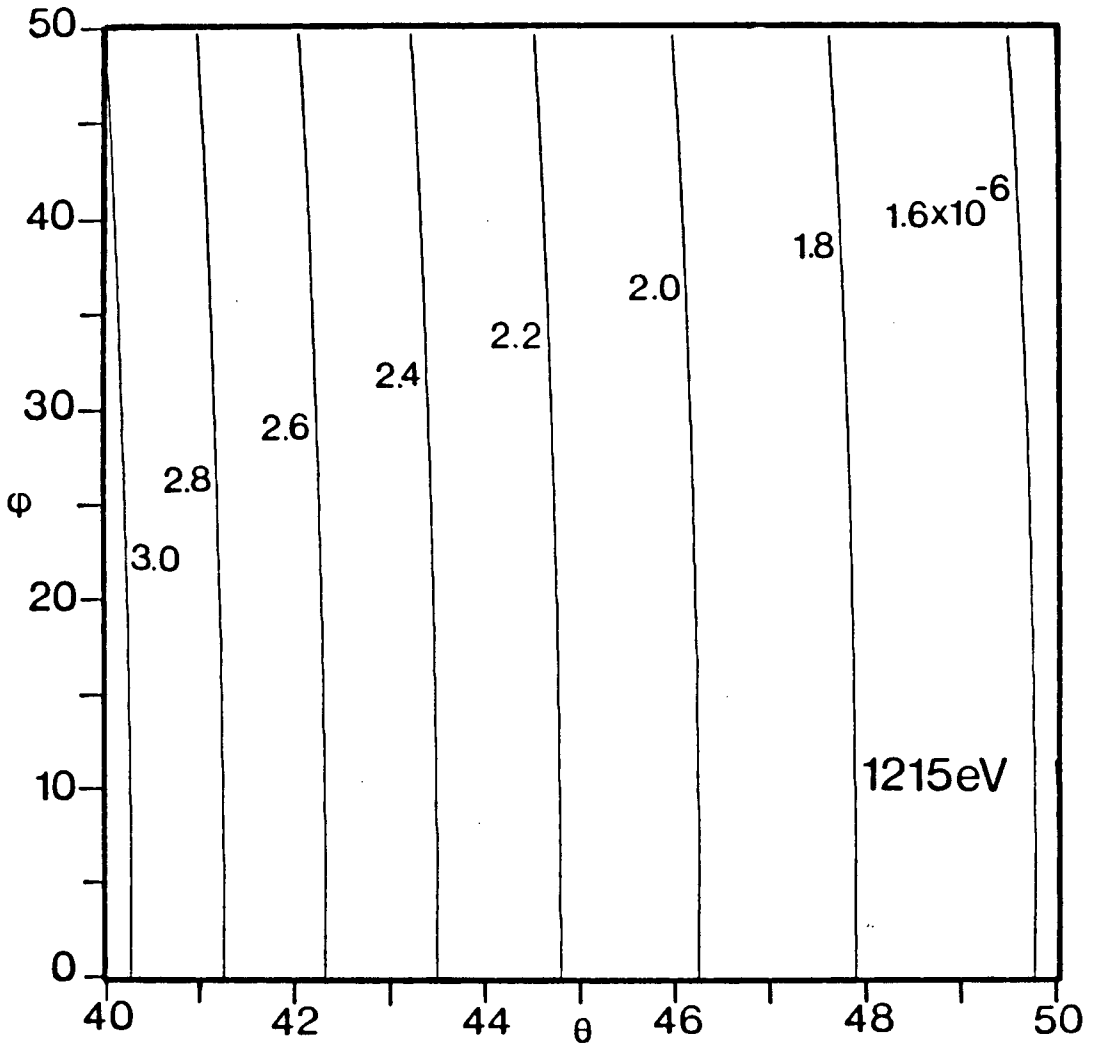

Figure 3.11 Contour map of $\sigma\{Mott\}$ as a function of θ and ϕ at E_0=1200eV and ϵ=15eV. Contour values are labelled on the diagram.

resolution affects primarily the determination of p-type momentum distributions near q=0, and makes it difficult to tell the s/p character of the distribution. This s/p character is sometimes very revealing as to the asymmetry of the molecular orbital, and the obscuring of this region is significant loss of information;

(3) Electron beam and lens effects: it is much easier to extract and control a 1200eV beam than a 400eV one, and for this reason one can prolong the filament life by running it cooler. It is , however, harder for the lens to decelerate 600ev electrons down to the pass energy, compared to 200eV electrons, without loss of signal. The lens magnification may also change with different deceleration ratios;

(4) The Mott scattering factor becomes more nearly constant as a function of ϕ-angle with higher incident energy E_0. While this is not a problem at either energy because this factor is exactly known, it means the measured distribution at higher energy (assuming perfect resolution for the moment) is a slightly closer reflection of the spherically-averaged momentum density;

(5) The PWIA is a better approximation of the actual scattering process at 1200eV, than at 400eV, and relative intensities will be more accurate at the higher energy.

All these considerations suggest that with limited angular resolution perhaps a good compromise would be operation at 800eV.

3.6 Data Analysis

The raw data provided by the spectrometer usually needs very little in the way of manipulation before it is presentable. Data is collected in one of three modes:

(1) A time spectrum (figure 3.6) is a histogram of the count of TAC pulses separated into bins (Nicolet memory channels) according to their amplitude, which is directly proportional to the pulse-pair time separation Δt. No further processing is necessary, except to put the points on the correct time scale;

(2) A binding energy spectrum can be obtained as a spectrum of the true (e,2e) event count as a function of the separation energy ϵ at which the counts were accumulated, with fixed ϕ angle.

(3) An angular correlation is the spectrum of the true (e,2e) event count over a range of azimuthal scattering angles with fixed binding energy.

Binding energy spectra may also be presented as they are recorded, except to calibrate the energy scale (usually

against accurate PES spectra). The data may be three-point smoothed, which is a process of generating a new spectrum from the old, where the count in the ith channel of the new spectrum is a weighted average of the ith channel in the old spectrum and the two channels on either side of it. This reduces the scatter of the points and makes structure easier to see, but it should be used carefully as where the statistics are very poor, or the number of points in a given structure is small, it may distort peak heights or introduce artifacts into the data.

Angular correlations must be calibrated to the correct ϕ scattering angle, checked that they are symmetric about $\phi=0°$ (as they should be in the symmetric non-coplanar geometry according to equation 1.17) and then converted to the q-scale. This type of data may also be three-point smoothed if the structure is weak and the statistical error large. Generally if the SCA windows are set correctly there should be no background on the signal, but if there is, it is permissible to subtract off a background only when it is absolutely certain where the true zero of intensity is.

When the final ion state energies are too close to be resolved experimentally it is not possible to measure the angular correlation directly as there will be some contribution from other peaks close by. In such a case the angular correlations must be found by deconvoluting (using some sort of peak-fitting algorithm) the areas of peaks from

several binding energy spectra made at different ϕ angles. Knowing the relative peak areas of all the peaks and the angular correlation of at least one well-separated peak one can generate the other angular correlations. This method is used in the study on CO_2 (Chapter 6).

CHAPTER 4 HYDROGEN SULPHIDE

Sam sniffed the air.
'Ugh! That smell!' he said.
'It's getting stronger and stronger.'

Binary (e,2e) studies are now available on many Group IV-VII hydrides, and on the isoelectronic rare gases. Studies include CH_4 {Weigold (1976)}, NH_3 {Hood (1976a)}, PH_3 {Hamnett (1977)}, H_2O {Hood (1977), Dixon (1977)}, the present work on H_2S {Brion (1978b), Cook (1979), Cook (1980)}, HF and HCl {Brion (1979), Suzuki (1980a), Brion (1980)}, HBr and HI {Brion}, and the rare gases He, Ne, Ar, Kr, and Xe {Weigold (1973), McCarthy (1976a), McCarthy (1976b), Weigold (1975)}.

The present experimental and computational work on H_2S was carried out with the following objectives:

(1) To obtain the binary (e,2e) binding energy spectrum and the momentum distributions of the valence shell molecular orbitals of H_2S;

(2) To obtain a representative set of calculations ranging in quality from the simplest approximate methods to those giving results near the Hartree-Fock

limit, in order to investigate the requirements necessary for a basis set which can not only give acceptable energies but also adequately reproduce the valence molecular orbital momentum distributions. In this aspect of the study the importance of d-orbitals, a subject of considerable controversy in recent years, will be assessed;

(3) To study any MFS structure in an attempt to understand its origin. In view of theoretical many-body effect predictions {Domcke (1978)} this involves investigation of the binding energy spectrum up to at least 32eV. Previous studies have not looked above about 25eV;

(4) To compare and contrast the results for H_2S with those for other hydrides and related systems.

4.1 Experimental Results

The incident energy used was 400eV and the overall FWHM energy resolution is about 1.6eV. The maximum true coincidence count rate on peak 1 ($2b_1$) is approximately $0.1s^{-1}$. The H_2S sample gas was purchased from the Matheson Co. and was used without further purification. No evidence of impurities is seen in the binding energy spectra.

The H_2S binding energy spectra are presented in figure 4.1. The lower energy portion from 8-18eV was recorded at ϕ=12°. The remaining segments spanning 18-34eV were recorded at three different azimuthal angles (ϕ=0,5,11°) and have each been three-point smoothed once. A brief exploration above 34eV showed no observable structure. The energy scale was calibrated on the 10.48eV $2b_1$ peak of the high-resolution photoelectron spectrum {Turner (1970), Karlsson (1976)}. The 18-34eV region is compared with the result of many-body calculations in figure 4.2 (see following discussion). The data shows three well-defined peaks below 18eV (1,2,3 in figure 4.1, Table 4.1). These were determined to have p-type momentum distributions. Above this point the quality of the data drops due to the low intensity of the structure and the limited statistical accuracy. Nonetheless it is possible to identify a very weak peak (4) at 19.4eV which was determined to have an s-type momentum distribution by measuring the relative (e,2e) cross section at three azimuthal angles (ϕ=0,12,24°). Two partially resolved peaks (5,6) of moderate intensity were observed at 22.0 and 23.4eV, having s-type momentum distributions (again checked at three azimuthal angles ϕ=0,12,24°). Finally a broad, low intensity structure was observed spanning 25-34eV and is considered to contain four or more major peaks (7,8,9,10). Measurements of the binding energy spectrum at three angles (figure 4.1) and of the angular correlations at three energies (figure 4.3) show

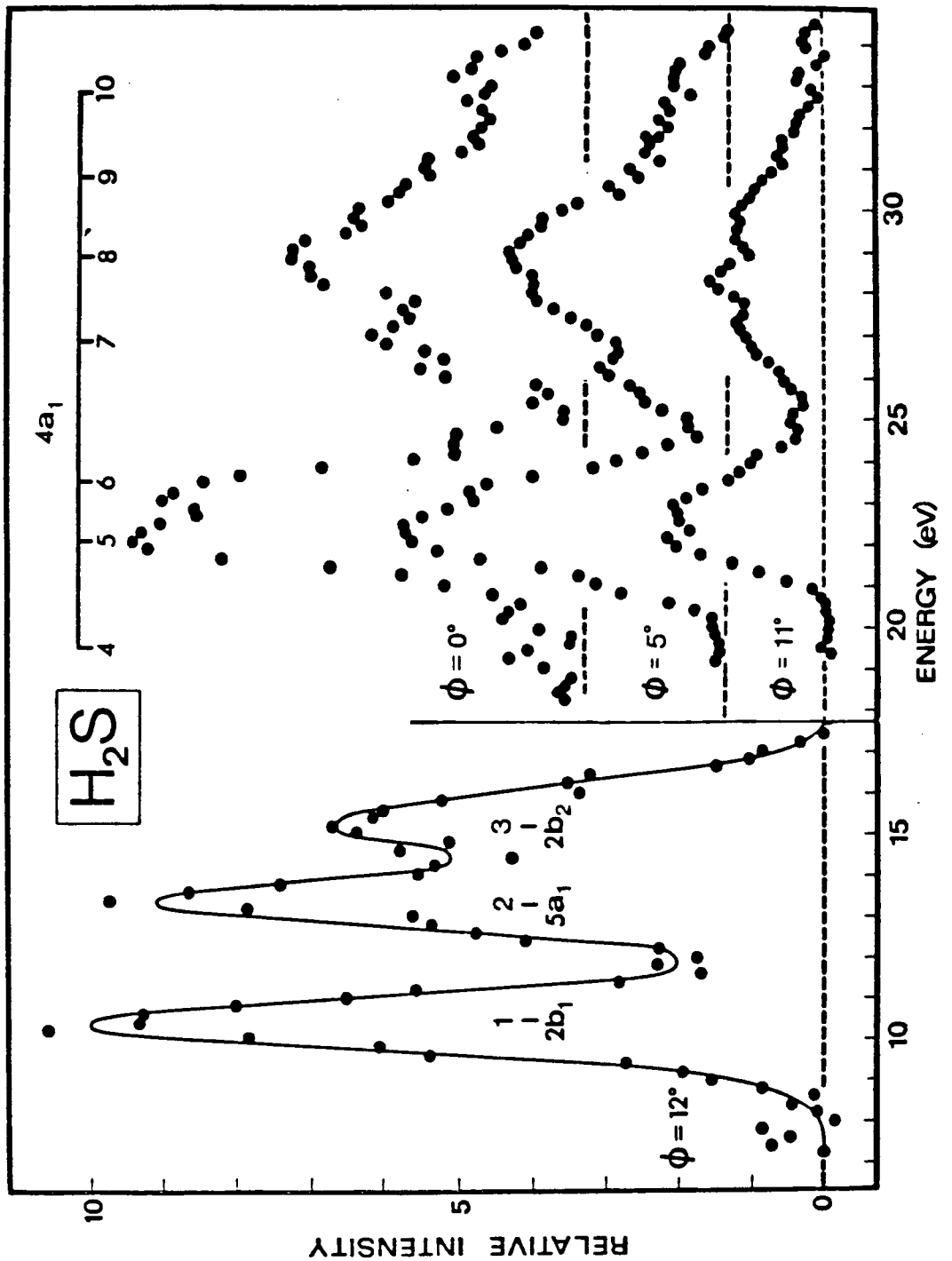

Figure 4.1 Binding energy spectrum of H_2S

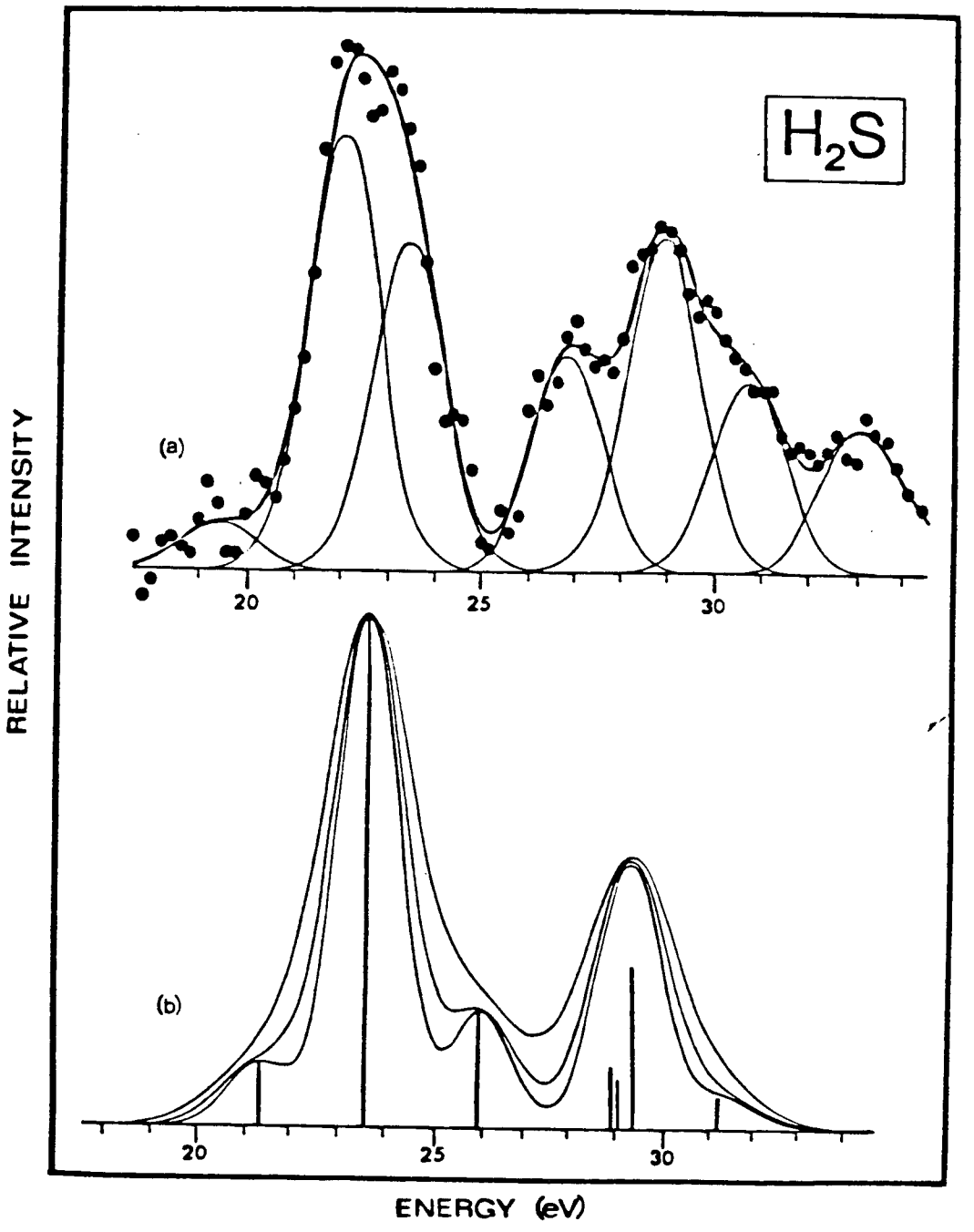

Figure 4.1 Binding energy spectra of H_2S.

Figure 4.2 (a) Binding energy spectrum of the MFS region of H_2S at $\phi=0°$. A least-squares fit of seven Gaussian peaks is shown:
(b) Green's function calculation of the MFS structure, with 0.7eV added to the theoretical energies. The theoretical lines are convoluted with Gaussian peaks of 1.7, 2.0, and 2.5eV FWHM.

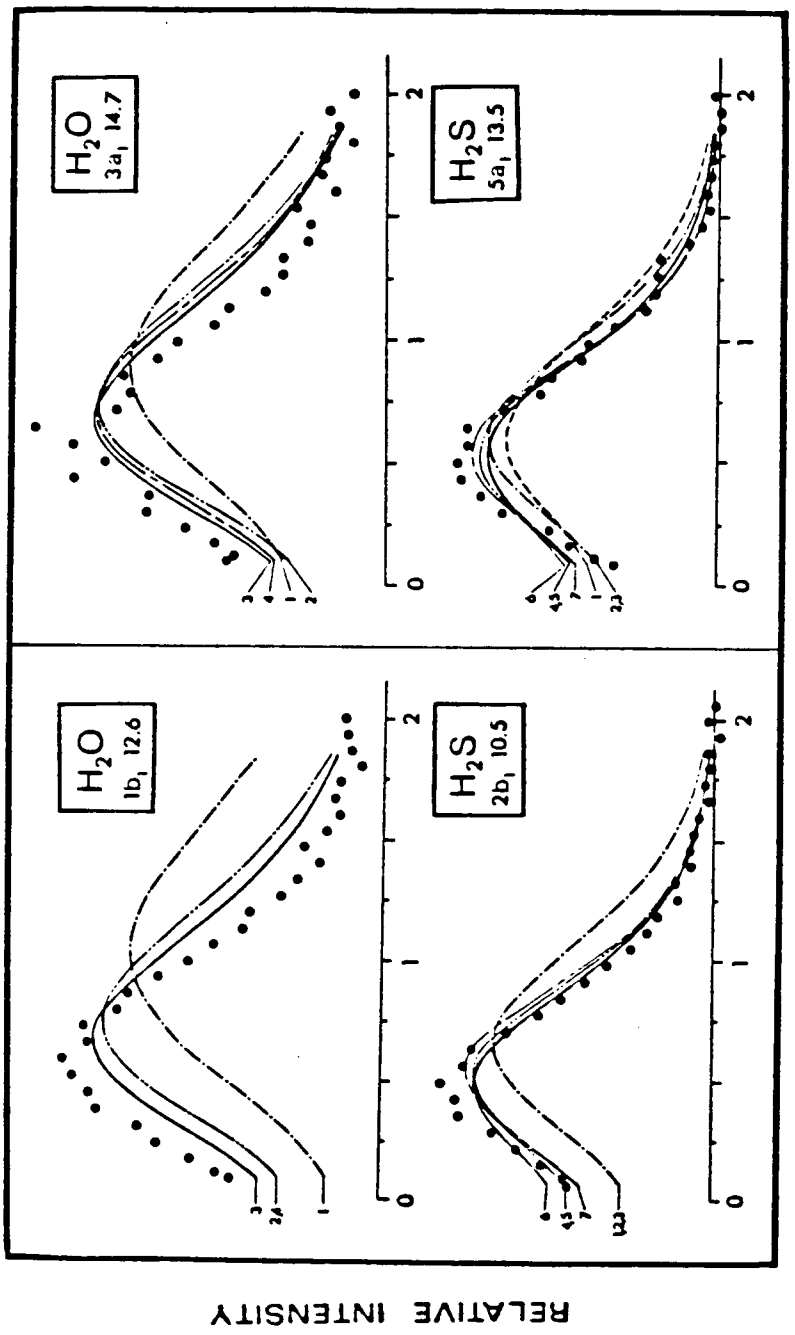

Figure 4.3 Momentum distributions of the valence orbitals of H_2O and H_2S. The molecule name, orbital label and experimental energy for each measurement are given in the box. Theoretical momentum distributions for H_2O are: (1) SZ; (2) $1\frac{1}{2}Z$; (3) HF; (4) DG; and for H_2S are: (1) CNDO; (2) SZ; (3) SZ+3d; (4) DZ; (5) DZ+3d; (6) HF; (7) DG.

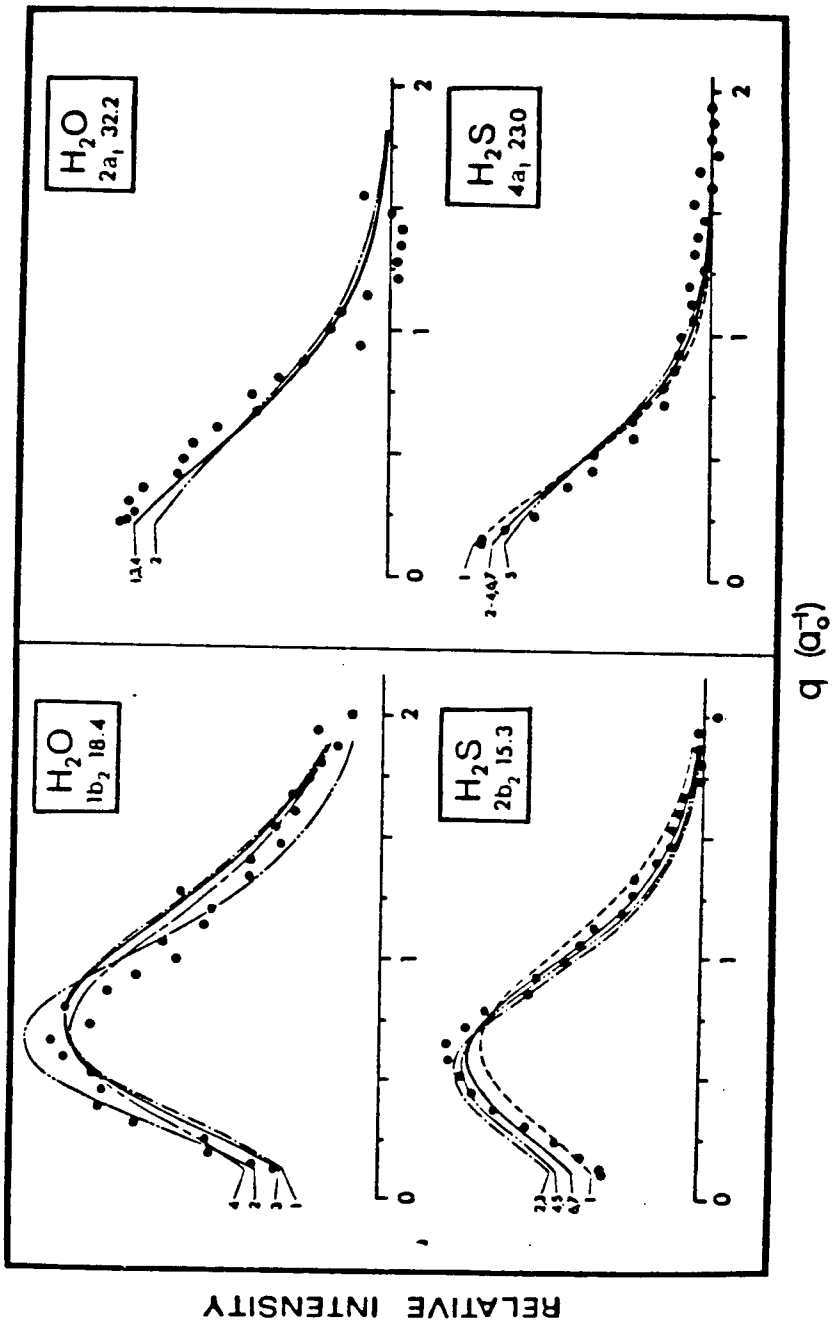

Figure 4.3 continued

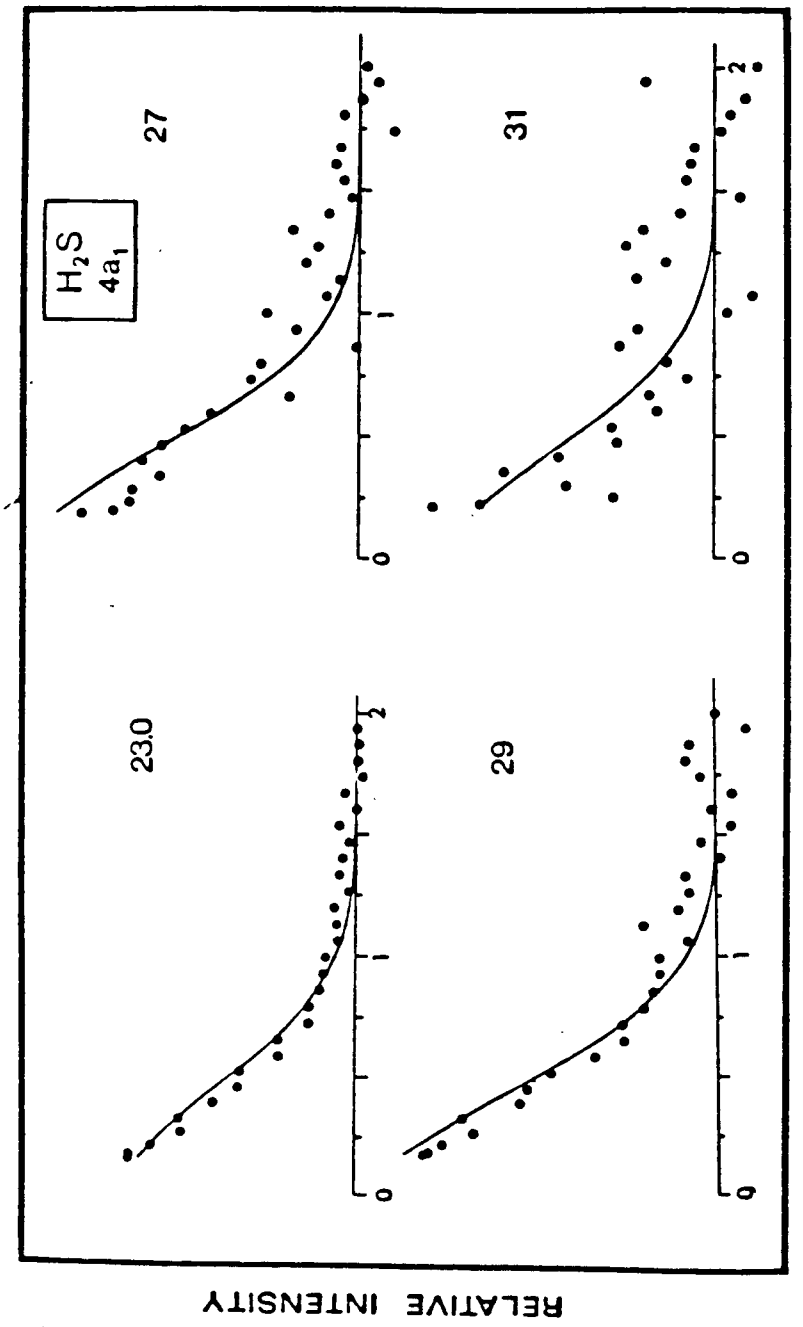

Figure 4.3 continued

(within the limits of the statistics) that this structure is predominantly s-type. The angular correlations were measured over a range of azimuthal angles +45 to -20° in steps of 1.5°.

The displayed momentum distributions (figure 4.3) are shown least-squares normalized to the calculated momentum distributions which have had the experimental angular resolution folded in. It should be noted that the low momentum regions of the calculated momentum distributions are particularly sensitive to the values of the angular resolution chosen for the folding-in procedure. Therefore, in comparing calculation and experiment, attention is particularly focussed on the region above $q=0.4a_0^{-1}$. This includes the position of the maximum of the distribution (in the case of p-type distributions) and the behaviour of the curve above about $q=0.4a_0^{-1}$.

In figure 4.3 the results of previous work on H_2O {Hood (1977)} are presented in the same format as that used for H_2S in order to facilitate comparisons between results for the two molecules later in the discussion.

Figure 4.3 also shows the experimental results for the multiple final state structure in H_2S above 19eV. Since all calculated distributions are almost identical, only the results of calculation H_2S-HF are shown (for details see following section). The statistics are poor on distributions

7 and 9 because these peaks are very weak in the binding energy spectrum.

4.2 Calculations

The calculations on H_2S (shown in figure 4.3) either carried out by us or obtained from the literature and other sources are listed here:

(1) CNDO: a simple CNDO/2 calculation using a minimal basis set of Slater-type orbitals (STOs), augmented by d-functions. The 3s, 3p, and 3d functions all have the same exponent;

(2) SZ: a single-zeta ab-initio calculation using STOs {Clementi (1963)}. This computation was done with the ATMOL/2 package at Oxford University;

(3) SZ+3d: a single-zeta ab initio calculation but augmented with diffuse d-functions {Hillier (1970)} , also done on the ATMOL/2 package;

(4,5) DZ, DZ+3d: similar to SZ and SZ +3d except that the basis set used was of double-zeta quality in all but the d-functions {Clementi (1964)};

(6) HF: an accurate calculation approaching the Hartree-Fock limit using a triple-zeta equivalent GTO basis including d-functions {Guest (1976)};

(7) DG: a calculation using a basis set of Gaussian

functions (GTOs), not including d-functions, but incorporating some very diffuse low-exponent functions {Zeiss}. The exponents were obtained by least-squares fitting of the GTO set to the results of atomic calculations. These atomic calculations were done with a double-zeta quality basis set, and four GTOs were fitted to each atomic orbital, but without the usual r^{-1} weighting of the fitting function. The absence of the r^{-1} weighting means the GTO basis is more accurate in duplicating the double-zeta result in the outer spatial regions of the atomic orbitals.

The calculations for H_2O described in a previous paper are summarized here for reference {Hood (1977)}.

(1) SZ: a single-zeta basis calculation with STO functions, of the same quality as H_2S-SZ, called 'basis 1' in {Hood (1977)};

(2) 1½Z: a mixed basis calculation; with oxygen 2p levels described by double-zeta functions, and remaining atomic orbitals by single-zeta functions, labelled 'basis 2' in {Hood (1977)};

(3) HF: a full double-zeta calculation augmented by 3d functions on oxygen, and 2s, and 2p polarization functions on hydrogen. The oxygen 2p levels are described by triple-zeta functions, called 'basis 4' in {Hood (1977)};

(4) DG: a GTO basis calculation similar to that of

H_2S-DG {Zeiss}.

4.3 Discussion

The molecular orbital theory electronic configuration for H_2S is:

$(1a_1)^2(2a_1)^2(1b_2)^2(3a_1)^2(1b_1)^2(4a_1)^2(2b_2)^2(5a_1)^2(2b_1)^2$

with the last four orbitals constituting the valence shell.

4.3.1 Binding energy spectra of H_2S

The binding energy spectrum of H_2S has already been partially investigated by PES methods using both UV {Turner (1970)} and X-ray {Siegbahn (1972)} light sources. These studies all show consistent results for the binding energies of the electrons in the three outermost orbitals. The first band in the He-I photoelectron spectrum reported by Turner with a vertical IP of 10.48eV has a vibrational envelope characteristic of the removal of a non-bonding electron, and may be unequivocally assigned to the $2b_1$ (lone-pair) orbital on sulphur. LCAO-MO-SCF calculations give this orbital almost exclusively sulphur 3p{x} (out-of-plane) character (see geometry diagram, Appendix C). The next band with a vertical IP of 13.25eV is clearly

Table 4.1 Calculated and experimental H_2S binding energies.

Peak	Expt[1]	Expt[2]	Expt[3]
1 $2b_1$	10.5	-	10.48
2 $5a_1$	13.5	-	13.35
3 $2b_2$	15.3	-	15.25
4	19.4	19.4	-
5	22.0	22.0	-
6	23.4	23.4	-
7 $4a_1$[11]	27	-	-
8	29	-	-
9	31	-	-
10	33	-	-

Peak	SZ[4]	SZ+3d[5]	DZ[6]	DZ+3d[7]	HF[8]	DG[9]	MBGF[10]
1 $2b_1$	10.33	9.95	10.75	10.46	10.49	12.60	9.61
2 $5a_1$	12.87	13.05	13.42	13.70	13.65	15.12	12.39
3 $2b_2$	15.74	15.57	16.22	16.20	16.21	17.57	15.44
4							21.33
5							23.65
6							26.11
7 $4a_1$	26.71	26.05	27.38	26.72	26.87	30.33	29.00
8							29.16
9							29.45
10							31.34

1 Present work: centroid of MFS structure is at 25eV.
2 High-resolution He-II PES
3 He-I PES
4-10 These results are described in section 4.4.
11 Energies for these levels in the present work are from the fitted results.

strongly bonding, as evidenced by its vibrational envelope which exhibits a long progression in the ν_2 or bending normal mode. Calculations for this $5a_1$ orbital put electron density largely in the central region between the three atoms, thus accounting for the angle-stabilizing nature of this MO. This orbital is constituted of basically the sulphur 3p{z} orbital (in-plane, along the C{∞v} axis) together with major contributions of the required symmetry (a_1) from the hydrogens. The third orbital, designated $2b_2$, with a vertical IP of 15.3eV is perhaps the most strongly bonding of all. Its vibrational envelope is extensive, and corresponds to stimulation of the ν_1, or symmetric stretching mode. This correlates well with calculations which give this orbital mainly S-H σ-bonding character brought about by overlap of the lobes of a sulphur 3p{y} orbital (in-plane, parallel to hydrogen atoms) with each hydrogen 1s. Therefore electron density is placed along the bonds.

Few PES measurements have been made of the binding energy of the deepest valence shell MO ($4a_1$) since it lies beyond the range of the He-I line. A low-resolution He-II spectrum has been reported {Rabalais (1977)} which shows a broad peak in the region of 22eV with little discernible vibrational structure, but unfortunately the binding energy scale does not extend above 25eV. The valence shell XPS spectrum of H_2S {Siegbahn (1972)} also shows a peak at 22eV,

with some possible indication of structure above 22eV, which the authors did not consider significant. A peak at 19eV ascribed to a nitrogen impurity is also shown. However, in view of the width of the 19eV peak, the impurity assignment is questionable. The situation has been partially clarified by the high-resolution He-II spectrum of H_2S {Maier, Brion (1978b), Domcke (1978)}. This spectrum shows that the broad peak at 22eV is in fact composed of two major peaks at 22.0 and 23.4eV. A very broad low intensity peak is also indicated at 19.4eV. This 19.4eV feature is too broad and also too far removed from the 18.6eV $2s\sigma\{u\}$ band of nitrogen to be ascribable to a nitrogen impurity. This peak at 19.4eV is of relatively low intensity and therefore cannot be seen at the sensitivity of the low-resolution He-II spectrum. The $4a_1$ orbital is not strongly bonding as indicated by calculation which ascribe to it mainly sulphur 3s character with only a small a_1 symmetry contribution from the hydrogens. Thus the $4a_1$ MO has considerable atomic character. A recently-reported dipole (e,2e) binding energy spectrum of H_2S {Brion (1978b)} has indicated broad peaks centered around 22.5 and 29 eV.

Recently there has been a growing realization of the important role of many-body effects in the ionization of inner valence orbitals. There have been some attempts to predict theoretically the multiple final state, or shake-up, structure of H_2S. A recent calculation using rather limited

VB-SCF-CI methods {Chipman (1978)} incorporating only four excited configurations plus the ground state, claims to reproduce the energies of the experimentally observed 19.4 and 22.0eV peaks. At the time this calculation was carried out the extent of the shake-up structure in H_2S was not fully realized, and, in view of the results to be presented later in this paper, the limited total wavefunction chosen for the work is probably inadequate to describe all the structure we have now observed. Nevertheless with this in mind the relative energies predicted are more reasonable when one considers that the experimental XPS peak at 22eV discussed by Chipman is in fact two peaks as shown by this work and the He-II spectrum. The predicted spacing of 4.5eV is consistent with the assignment of the 23.4 peak as the 'parent', rather than the one at 22.0eV, even though the latter is more intense. The Green's function theoretical technique is more comprehensive in the sense that there are not the restrictions on the calculation that are imposed by the method of Chipman, and furthermore in that a more flexible basis set is used. The MBGF calculation predicts three major well-separated peaks in the region 21-26eV, with extensive lower intensity structure extending up to around 32eV (figure 4.2b). All of the peaks above 19eV are predicted to be associated with ionization from the $4a_1$ molecular orbital and therefore would be expected to show the same momentum distribution. The three peaks between 21-26eV are nicely reflected in the high-resolution He-II

spectrum {Domcke (1978)} if one allows a shift of about 1eV to lower energy in the theoretical energy scale. The calculations also give reasonable estimates of the relative intensities of these three peaks.

Peaks 1,2 and 3 of the binary (e,2e) H_2S binding energy spectrum (figure 4.1) show reasonable agreement of peak positions with previous He-I PES work {Turner (1970), Goddard (1978)}. The relative intensities of these three lowest energy peaks are similar to those in H_2O {Hood (1977)}. In the region of 19-25eV this work shows close agreement with the low-resolution He-II spectrum with respect to peak energies, intensities and line shapes. Both spectra bear out the MBGF predictions of three peaks in this energy range, as discussed above and shown in figure 4.2. Finally, the first evidence for extensive MFS structure in the region 25-34eV is reported. Again, the Green's function calculations have predicted structure in this region which seems to show some correlations with the present work (figure 4.2), but it should be noted that the calculations are quite sensitive to basis set changes. I have enumerated several bands (7,8,9,10, figure 4.1) in this region, where there appear to be at least four major peaks. It is possible (see figure 4.2a) to obtain a good least-squares fit of four Gaussian peak shapes (1.7eV FWHM) to this structure, though this should not be taken as the only possible deconvolution of the data. The assignment of peaks in this region is

difficult to make out due to the relatively poor energy resolution and the low intensity of this structure. The results are conclusive only in that they confirm the MBGF prediction of some sort of extensive MFS structure of a_1 symmetry. Clearly higher resolution work is required here for comparison with the many-body Green's function calculations.

4.3.2 Momentum distributions

The momentum distributions are shown in figure 4.3.

For the $2b_1$ and $5a_1$ MOs of H_2S the greatest improvement in the fit of calculated curves occurs in going from a single-zeta to a double-zeta quality basis set. The addition of d-functions to either the SZ or the DZ calculation produced no significant changes in the distribution and for this reason these results were not displayed in the figures. Significant improvement over the DZ result is only obtained with the HF limit calculation, but this does not produce as great a change as going from SZ to DZ.

The SZ and DZ results on the $2b_2$ MO show very similar distributions, in contrast to the previous two MOs and here the HF limit calculation gives the greatest improvement over both SZ and DZ in the fit to experiment. Both SZ and DZ bases predict a distribution somewhat more spatially extended than is in fact measured. The fact that in H_2S and

H_2O the HF limit calculation is superior to either SZ or DZ may be due to the presence of hydrogen 2p polarization functions. As described in section 4.1 the b_2 MO is primarily an S-H (or O-H) bonding orbital with density distributed along the bond axes. Therefore the ability of the hydrogen polarization functions to direct density into these regions and improve the overlap with the sulphur 3p{y} (or oxygen 2p{y}) atomic orbital should be particularly marked in this MO.

There has been considerable controversy during the past few years over the role that S-3d orbitals play in the bonding in sulphur compounds. Hartree-Fock calculations of the binding energies of these d-orbitals in atomic excited states such as $s^2p^3d(^5D)$ suggested that the d-orbital energy was far too high for it to play a significant role. However, an increasing body of experimental evidence {Cruikshank (1968)} has pointed to an active involvement of these d-orbitals in the bonding under certain circumstances. The most clear-cut cases arise when highly electronegative elements are bonded to sulphur and an extensive series of calculations on SO_2 {Rothenberg (1970)} showed that unless S-3d orbitals were included, quantitatively reasonable results could not be obtained. In the case of SO_2, further evidence is provided by the photoelectron spectrum. One combination of O-2p orbitals transforms as a_2 and should therefore be accurately non-bonding if S-3d orbitals are

unimportant {Ratner (1971)}. In fact, as the spectrum shows, the $^2A_2$ bond exhibits considerable bonding character {Hillier (1971)}.

The position with regard to H_2S is less clear. By comparing the contributions of d-orbitals to the bond strengths in SO_2 and H_2S, it was concluded {Rothenberg (1970)} that they were an order of magnitude less important in the latter case. Support for this conclusion has come from some recent calculations {Von Niessen (1977)} who found that only very diffuse d-orbitals had any impact on the orbital energy.

It has been suggested that if the s and p bases are exhaustively described, no d-orbital contribution will be important in any molecule. Aside from the evidence of the SO_2 spectrum quoted above, this statement also can be questioned on the basis of its corollary. If a very poor basis is selected, we should expect substantial improvement in the orbital description by employing d-orbitals. In fact, the results of our present work suggest that, at least for H_2S, this is not so. The poor description of the $2b_1$ orbital found in a minimum basis set calculation is not significantly improved by the addition of d-orbitals to the sulphur atom but is bettered by making the s/p basis more flexible. Where the s/p basis is not extensive, but d-orbitals have been included, one should not necessarily assign any intrinsic chemical importance to the effect of

the d-functions {Kwart (1977)}. Rather, any changes here are due to the slight additional flexibility which these functions introduce into the basis used in modelling the molecular orbital wavefunction.

Changes in total electron density in H_2O and H_2S as a result of adjusting the basis set have been studied {Bicerano (1977)}. In their calculations the density difference plots on H_2S show the greatest changes between the single-zeta and double-zeta basis sets. Smaller changes occur on gradually improving the basis through addition of successively extra s- and p- functions, then d-functions, then hydrogen 2p-functions, and finally extra polarization functions to give a near-HF limit result. Calculation of the density difference plots on H_2O using analogous basis sets shows that the effect of d-functions, though relatively small in both cases, is as large or even greater in H_2O than in H_2S. Certainly d-orbitals in H_2O can have virtually no explicit chemical importance and their effect in H_2O and H_2S seems only to make the s/p basis slightly more flexible. These results, together with those of the present work, suggest that reasonable wavefunctions for H_2O require a very extensive, carefully chosen s/p basis, and for H_2S an s/p basis somewhat less flexible. If this is done no d-functions need be included.

Examination of Table 4.1 shows that addition of d-functions produces no significant systematic changes in

the orbital energies. The small changes seen here are not meaningful, but result only from allowing the SCF calculation more 'space' within which to variationally minimize the total energy. One should not therefore conclude that the wavefunction in the bonding region has automatically been improved on addition of extra functions, without looking for systematic changes in orbital energies, lowering of the total energy, or significant alterations of density plots or momentum distributions.

Of particular note is the performance of the diffuse Gaussian basis (DG) calculation in reproducing the experimental distribution in both H_2O and H_2S. The fit of the curves is consistently as good as, and sometimes marginally better than the double-zeta results. The method of optimizing Gaussian exponents, as described above, has been used with some success to calculate other quantities, such as dipole moments and polarizabilities {Zeiss (1979)} which are more critically dependent on the spatial distribution of charge. The advantage of the diffuse basis calculation lies in the fact that although it is essentially single-zeta in complexity, it is effectively double-zeta in the quality of its description of the atomic orbital wavefunctions. The computation is therefore simplified. Due to the linear weighting and incorporation of very diffuse functions it is flexible in the (e,2e)-sensitive bonding regions, but on the other hand, it is fairly rigid near the

nuclear centres, and so will not reproduce orbital energies very accurately.

4.3.3 MFS structure

All major structures in the H_2S binding energy spectrum beyond the three outer valence IPs have been shown experimentally (see figure 4.3) to exhibit s-type momentum distributions, confirming the Green's function predictions that all MFS structure is associated with ionization of the $4a_1$ MO. The different SCF calculations of the $4a_1$ momentum distribution are all virtually identical (with the exception of the very poor CNDO result) and for this reason only the HF limit result is shown in figure 4.3. This ease of description indicates the large atomic character of the $4a_1$ MO. Some attempt was initially made, on empirical and semi-quantitative grounds, to assign the MFS structure to a combination of discrete ionizations and excitations, as has been done for inner shell XPS spectra {Allan (1972)}, but no convincing argument could be made for any such assignment. This supports the view that this structure involves, in the valence shell, a complex rearrangement or mixing of states which are not related to the occupied and unoccupied levels of the ground state in any simple way. Therefore no ion state can be singled out as 'parent' on the basis that its electronic structure is very similar, except for one missing valence electron, to the ground state structure. In the

configuration interaction picture this would mean that the wavefunction for each final ion state contains a number of important configurations, none of which dominate strongly over the others. For these reasons I have generally used the term 'multiple final state' (MFS) to describe the structure associated with the inner valence orbitals, rather than terms such as 'shake-up' and 'shake-down' or 'satellite structure'. These terms can still be used in the discussion of inner shell spectra as measured by ESCA or XPS techniques from which they originally arose. Because of the large separation in energy between the inner shell hole and the valence levels, there is very little mixing of states, and the picture incorporated in the 'sudden' approximation theory {Aberg (1967)} is likely to be more reasonable.

4.3.4 Trends in the AXn hydrides and rare gases

The valence electronic structure of the group V-VII hydrides (AHn) is grossly similar in that there exists a p-type mainly non-bonding, low-energy 'lone-pair' orbital, followed by one or two sometimes degenerate higher-energy, mainly bonding p-type MOs, and one still higher s-type MO of essentially atomic character.

In order to study the relationships among experimental MDs of the various hydride molecules and rare gas atoms I have made correlation diagrams (figure 4.4) of the values of q{max} and q{½max} against $IP^{1/2}$. q{max} is the momentum at

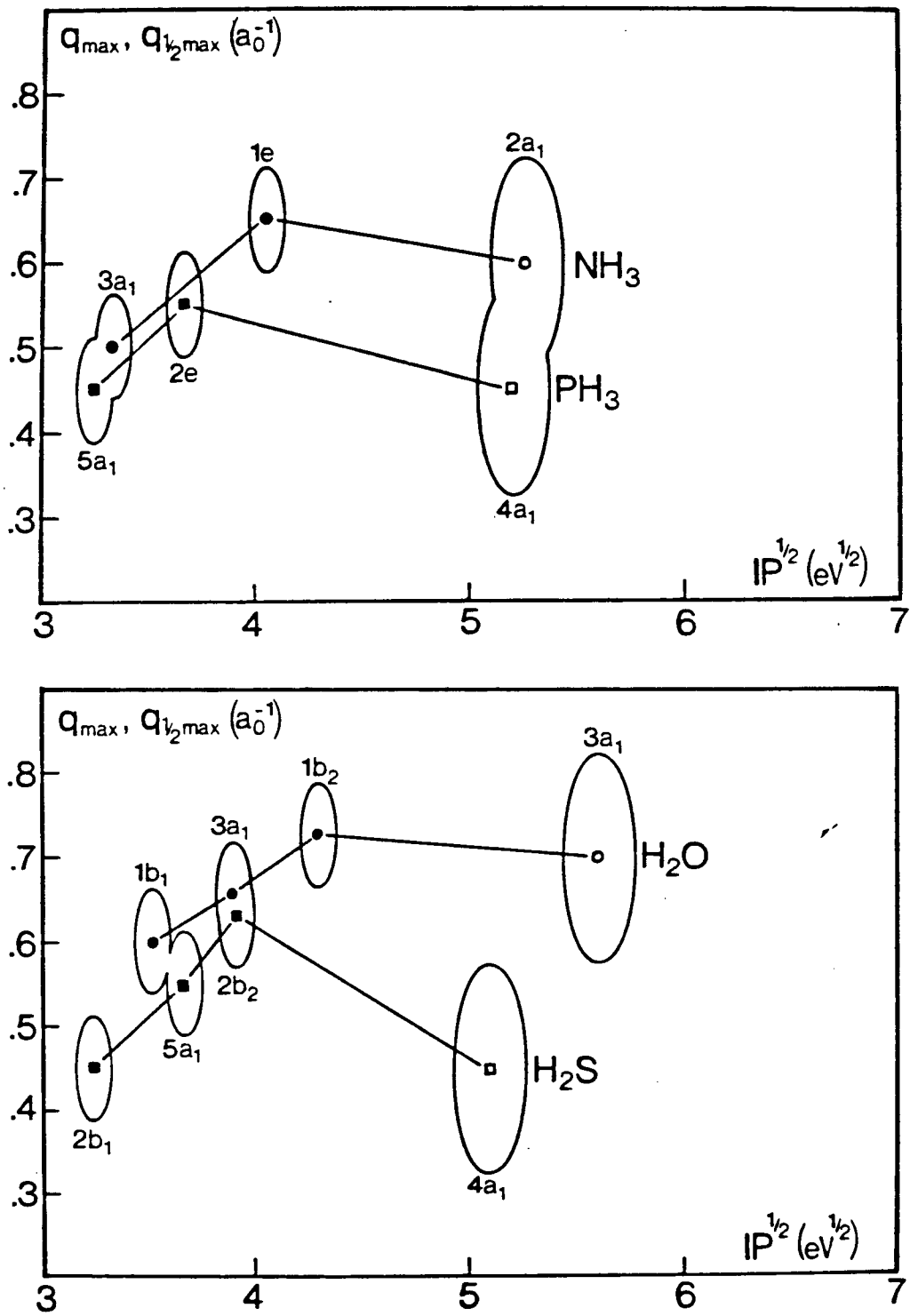

Figure 4.4 Correlation diagrams of q{max} and q{½max} against $IP^{1/2}$. Solid symbols denote q{max} and open ones give q{½max}. Solid lines join the points of the same molecule, and error estimates are given by the ellipses.

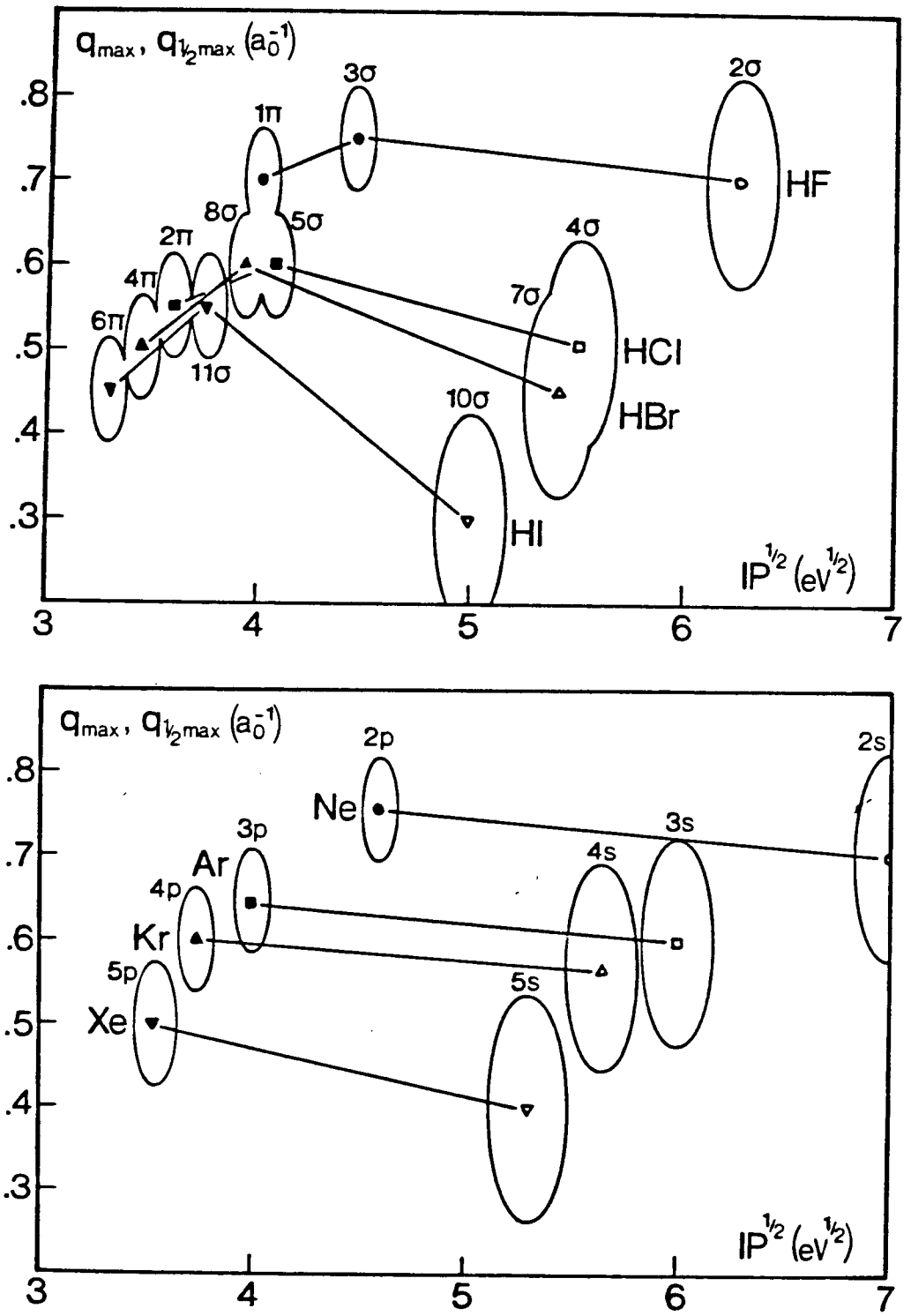

Figure 4.4 continued

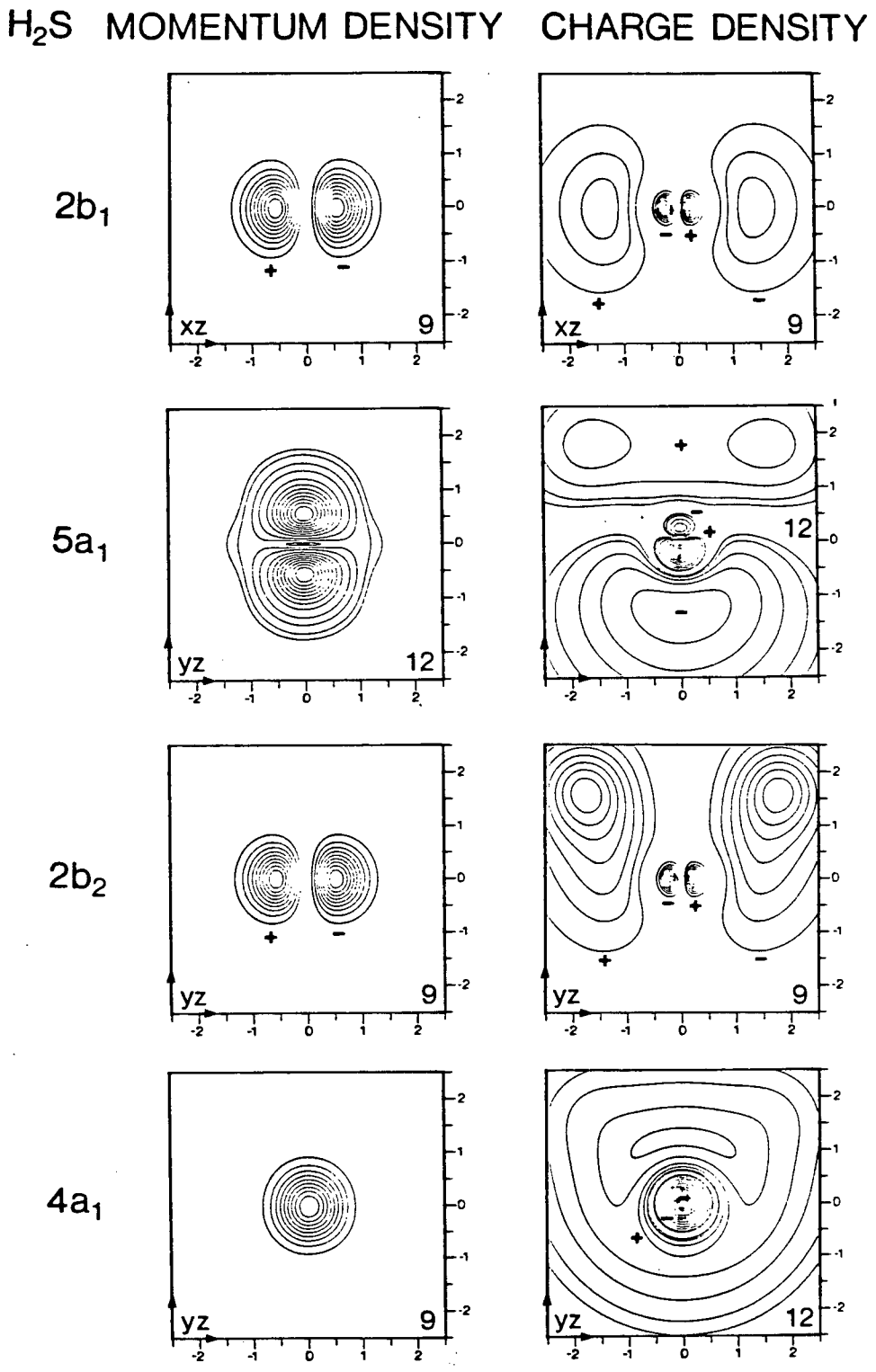

Figure 4.5 Momentum and charge density maps for H_2S from the H_2S-DG wavefunction.

Table 4.2 Energies and values[1] of q{max} and q½{max} for the hydride molecule momentum distributions. H_2S results are from this work. Sources for the other molecules are given at the beginning of Chapter 4.

(Molecule)
(Orbital q{max}/q{½max} IP)

CH_4			NH_3			H_2O			HF			Ne		
$1t_2$	.6	14.2	$3a_1$	.50	11.0	$1b_1$	.59	12.6	1π	.70	16.1	2p	.75	22
			1e	.68	16.5	$3a_1$	.66	14.7	3σ	.75	19.9			
						$1b_2$	.72	18.4						
$2a_1$	.5	24	$2a_1$	.7	32	$2a_1$	.7	32	2σ	.7	39.7	2s	.7	49
			PH_3			H_2S			HCl			Ar		
			$5a_1$	.45	10.6	$2b_1$	.45	10.5	2π	.55	12.8	3p	.65	15.8
			2e	.55	13.4	$5a_1$	.52	13.5	5σ	.6	16.5			
						$2b_2$	.63	15.3						
			$4a_1$	.45	27	$4a_1$	.45	26	4σ	.5	30	3s	.6	36
									HBr			Kr		
									4π	.5	11.8	4p	.6	14.2
									8σ	.6	15.6			
									7σ	.45	29	4s	.55	32
									HI			Xe		
									6π	.45	10.8	5p	.5	12.3
									11σ	.55	14.2			
									10σ	.3	25	5s	.4	28

1 It is only the innermost, highest energy orbital of a given molecule in this table which is s-type and for which q{½max} values are given. All others are q{max} values for p-type MDs.

which the MD reaches its maximum in a p-type distribution (solid symbols, figure 4.4); q{½max} is the momentum at which an s-type distribution has fallen to half its q=0 intensity (open symbols, figure 4.4). Ideally one would like to plot the expectation value <q>, but the combination of angular resolution effects, statistical uncertainty and an insufficiency of points at high q do not permit the extraction of <q> by integration over q of momentum distributions so far presented in the literature. q{max} and q{½max} are proportional to <q> but with different constants of proportionality. Also this proportionality may be expected to change slightly with small changes in the s/p character of the momentum distribution.

The plots are made against $IP^{1/2}$ since one has in Koopmans' theorem:

$$-IP = \epsilon = T + V$$

$$T = \langle p^2 \rangle / 2$$

where T is the kinetic energy of the electron. It is not unreasonable to suppose that the potential energy felt by electrons in each of the three outer p-type MOs of a given system is approximately the same and so a roughly linear relation between <q> (as reflected by q{max}) and $IP^{1/2}$ would not be surprising. This relation would not carry over to the inner s-type orbital as the potential energy of this orbital is different, and q{½max} reflects <q> differently.

Due to statistical uncertainty and angular resolution effects in the momentum distributions, and to the necessity of extrapolating s-type distributions back to q=0, there is significant possibility for error in ascertaining the values of q{max} and q{½max}. Values of $IP^{1/2}$ are more precise, except where the centroid of an MFS band must be computed in order to estimate the one-electron IP. A conservative estimate of these errors is indicated by ellipses in figure 4.4. Values of q{max}, q{½max} and IP are listed in Table 4.2.

Several trends in these correlation diagrams may be discerned:

(1) As expected from the discussion above the points for the outer p-type MOs of a given molecule (where they are not degenerate) generally fall on a line which has very nearly the same slope in all the hydrides. This indicates that the behaviour of the potential energy of these orbitals is, if not a constant in each molecule, at least following a systematic trend in different MOs of different molecules;

(2) The points generally move to higher energy going from left to right along the rows. This is in accordance with the increasing charge of the heavy atom nucleus;

(3) Similarly, and for the same reason, the points move up going right along the rows, reflecting the increased P-space radial extent, and hence, by the Reciprocity principle, the decreasing spatial size of the MOs. This is also seen in the atomic orbitals of the heavy atoms in figure 2.1;

(4) Points for the second row hydrides and rare gases (and subsequent rows in groups VII and VIII) are always below and to the left of the corresponding points in the preceding row. Again this reflects the increased size and lowered energy expected when the valence shell is made up of atomic orbitals whose principle quantum number is increasing.

These trends show a nice consistency in all the systems presently studied. The only exceptions are the HCl 5σ and Xe 5s points, which appear to be out of line with the corresponding points of the other systems in those groups. No explanation if offered for these discrepancies apart from the errors inherent in the determinations as described above.

In the case of certain hydrides (NH_3, H_2O, HF, PH_3, H_2S and HCl) the momentum distributions have been computed from wavefunctions of varying quality of basis sets. Again, several trends may be noted:

(1) The inner s-type MD of all these hydrides is

well-approximated by even the simplest basis set calculations. This indicates the essentially atomic character of these orbitals;

(2) Of the outer p-type MDs it is always the outermost, lowest-energy MD which is hardest to calculate. In the second row hydrides a wavefunction approaching the HF limit is required to fit the data closely, and in the first row hydrides even this is not adequate. In all cases the calculations predict an MD extended to higher q than is actually measured: the true electron density is therefore spatially more extended than is predicted theoretically;

(3) The remaining higher-energy p-type MDs require a near-HF limit wavefunction to correctly approximate their shape in the first row hydrides, while their second row counterparts can be closely fitted with a double-zeta wavefunction.

That a given quality basis set performs better for second row hydrides than for their first row counterparts is likely due to two factors: first of all, a given quality basis set is more flexible in the second row simply because there are more functions, and second, the shift in electron density during molecule formation is less extreme in the second row and less flexibility is required of the basis set. By this argument it might be supposed the HF, with the greatest electronegativity difference between the

constituent atoms, would show the greatest discrepancy between experimental and theoretical MDs, and so it would if the number of hydrogen atoms were the same for all the hydrides. However H_2O, though having less electronegativity difference between the atoms, does have two H atoms which requires that the basis set have more polarization functions to direct density into the bonding regions, whereas HF, with only one H atom, does not have this requirement. This probably accounts for the observation that the H_2O $2b_1$ MD shows the greatest discrepancy between experiment and theory.

The extent of the MFS structure associated with the inner a_1 or s orbital in all the systems discussed in this section increases going down the groups. The first row hydrides and neon show no MFS structure beyond a slight asymmetry of the single binding energy peak. With subsequent rows the amount of structure increases until in HI and Xe this structure spans 20-30eV. This trend arises out of the increasing availability of low-lying virtual states (which reduces the energy denominator in the formula {Cederbaum (1977), Chong (1974)} for the intensity of these lines), and there is also a greater density of such virtual states of different l quantum number to which excitations may occur. This intuitive rationalization also explains the existence of MFS structure in the first row diatomic {Schirmer (1977)}: there is now a low-lying π^* virtual level

which is not present in the hydrides.

4.4 H_2S Density Maps

Density maps computed from the H_2S-DG wavefunction are shown in figure 4.5. Several things are immediately obvious about these maps. The effect of the sulphur atom constituency is seen in the large size of the R-space density maps compared to the H_2O maps (figure 2.6) and in the presence of nodal surfaces between the n=2 subshell and the n=3 valence shell. By the Reciprocity principle the H_2S momentum density maps therefore show a less extended function than do the H_2O maps. The n=2 subshell is not seen in the momentum density maps as it would appear at very large p, again according to the Reciprocity principle, and has little effect in the $p<2.5a_0^{-1}$ valence region.

The H_2S $2b_1$ orbital shows the familiar p-type density function and is unremarkable except for the characteristics noted in the previous paragraph. The $2b_1$ wavefunction falls into Q-class IIi.

The $S3p\{z\}+H_1 1s+H_2 1s$ constituency of the $5a_1$ orbital means the nodal plane in this orbital is reduced to a nodal surface. The Q-projection taken in the y-axiz direction falls into Class $IIIa_1$ (figure 2.2) and explains the

structure of the P-space density on the p{x} axis. In the z-direction the projection is Class IIa and gives rise to the partial p-type character of the MD.

The $2b_2$ orbital maintains the σ{v} plane of symmetry, and so retains the p{y}=0 nodal plane, and falls into class IIi. The presence of the hydrogen 1s functions extends the R-space density, and so by the Reciprocity principle shrinks the momentum density. A careful examination of the $2b_1$ and $2b_2$ P-space density maps will show the latter is slightly smaller than the former.

Finally, the $4a_1$ orbital maps show that this MO is mainly of sulphur 3s character (class I), as it is very nearly spherical. The effect of the H1s functions is only to slightly distort this sphericity.

4.5 Conclusions

The results indicate that, in order to reproduce reasonably well the momentum distributions (and therefore the spatially extended part of the wavefunction) in first and second row hydrides, the incorporation of d-functions into the basis set for Hartree-Fock calculations is much less important than the provision of a sufficiently flexible set of s and p functions. For first row hydrides this set

should be of at least triple-zeta quality and for the second row at least double-zeta with perhaps extra s and p functions in the valence shell of the heavy atom. If d-functions are to be added the s/p basis should first be essentially complete. In other words, a single-zeta basis with d-functions is not likely to give meaningful results.

The binary (e,2e) measurements of both binding energy spectra and momentum distributions have provided new and definite evidence of strong electron correlations effects in the ionization of the $4a_1$ inner valence orbital of H_2S. These findings strongly support recent theoretical predictions using the many-body Green's function technique. An intense group of multiple final ion state peaks was predicted to arise from $4a_1$ ionization, as has now been observed. Furthermore, the measured momentum distributions confirm the origin of the multiple final state structure.

CHAPTER 5 CARBONYL SULPHIDE

'Thank you, Sam' he said in a cracked whisper.
'How far is there to go?'

5.1 Introduction

In this chapter four studies on the COS valence shell binding energy spectrum are considered:

(1) The theoretical spectrum, as computed by the 2ph-TDA many body Green's function technique;

(2) The valence X-ray photoelectron (ESCA) spectrum (1254eV), previously reported {Allan (1972)};

(3) The binary (e,2e) spectrum, obtained at two azimuthal angles (ϕ=0° and ϕ=15°) {Cook (1981)};

(4) The dipole (e,2e) spectrum at an equivalent 'photon' energy of 40eV {White (1980)}.

The ESCA and dipole (e,2e) experimental spectra both give intensities proportional to the optical oscillator

strengths for the transitions at their respective photon energies. The difference between them is that the dipole (e,2e) work uses low energy 'virtual photons', whereas the ESCA result was obtained with high energy X-radiation. The calculation yields a spectrum of pole strengths which do not include the dipole matrix element, and should therefore only be compared with photoelectron spectra at the high energy limit where the dipole matrix element is effectively constant. At the lower 'photon' energies used in the dipole (e,2e) work the dipole matrix element is expected to show strong energy dependence over the range of binding energies studied.

Intensities in the binary (e,2e) spectrum are proportional to the momentum density in the ground state molecular orbital from which ionization occurred, at the particular values of energy and momentum set by the experimental conditions. The intensity distribution in the overall binding energy spectrum will therefore be in general quite different from that obtained in photoelectron spectroscopy (which generally probes much higher momentum components).

The many-body Green's function technique is described in Chapter 1. The initial ab-initio wavefunction for COS used for the C and O atoms a (9s5p/4s2p) double-zeta basis set {Huzinaga (1965)}, augmented by a set of d-functions with $\alpha\{d\}(C)=0.6$, $\alpha\{d\}(O)=0.8$, and for the S atom the

(12s9p/6s4p) basis set of Veillard {Veillard (1968)}, augmented by a set of d-functions with $\alpha\{d\}(S)=0.5$. The total SCF energy resulting from this ab-initio calculation done at the experimental equilibrium geometry using the program system MUNICH {Diercksen, Diercksen (1974)} was -510.1140au. In the 2ph-TDA calculation the occupied valence orbitals and the 11 virtual orbitals lowest in energy were included. The results of the many-body calculations are given in Table 5.1.

5.2 Results and Discussion

The electronic configuration of COS is:

$$\{core\}^{14}\ (6\sigma)^2(7\sigma)^2(8\sigma)^2(9\sigma)^2(2\pi)^4(3\pi)^4$$

of which the 6σ and 7σ levels are called the inner valence orbitals, and the 8σ,9σ,2π and 3π levels the outer valence orbitals, by reason of their distinctly different ionization behaviour which will be elaborated upon below.

The calculated pole strengths are shown in figure 5.2, while more detailed information is shown in Table 5.1. Definitions of terms were given in section 1.4.1. Figure 5.1 shows a comparison of the various experimental spectra with the calculation. To facilitate this comparison the

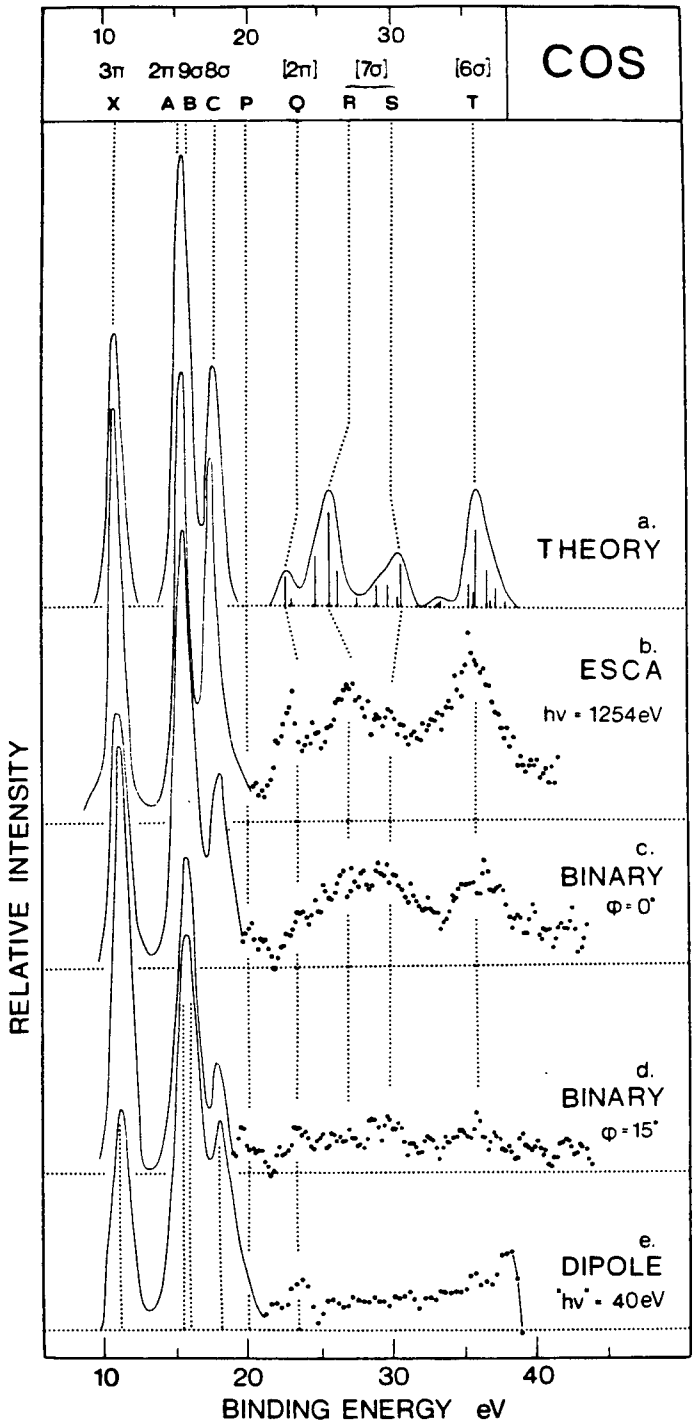

Figure 5.1 Binding energy spectra of COS:
(a) Theoretical spectrum via the Green's function technique
(b) the ESCA spectrum (c) binary (e,2e) spectrum at $\phi=0°$
(d) binary (e,2e) spectrum at $\phi=15°$
(e) dipole (e,2e) spectrum at 40eV energy loss

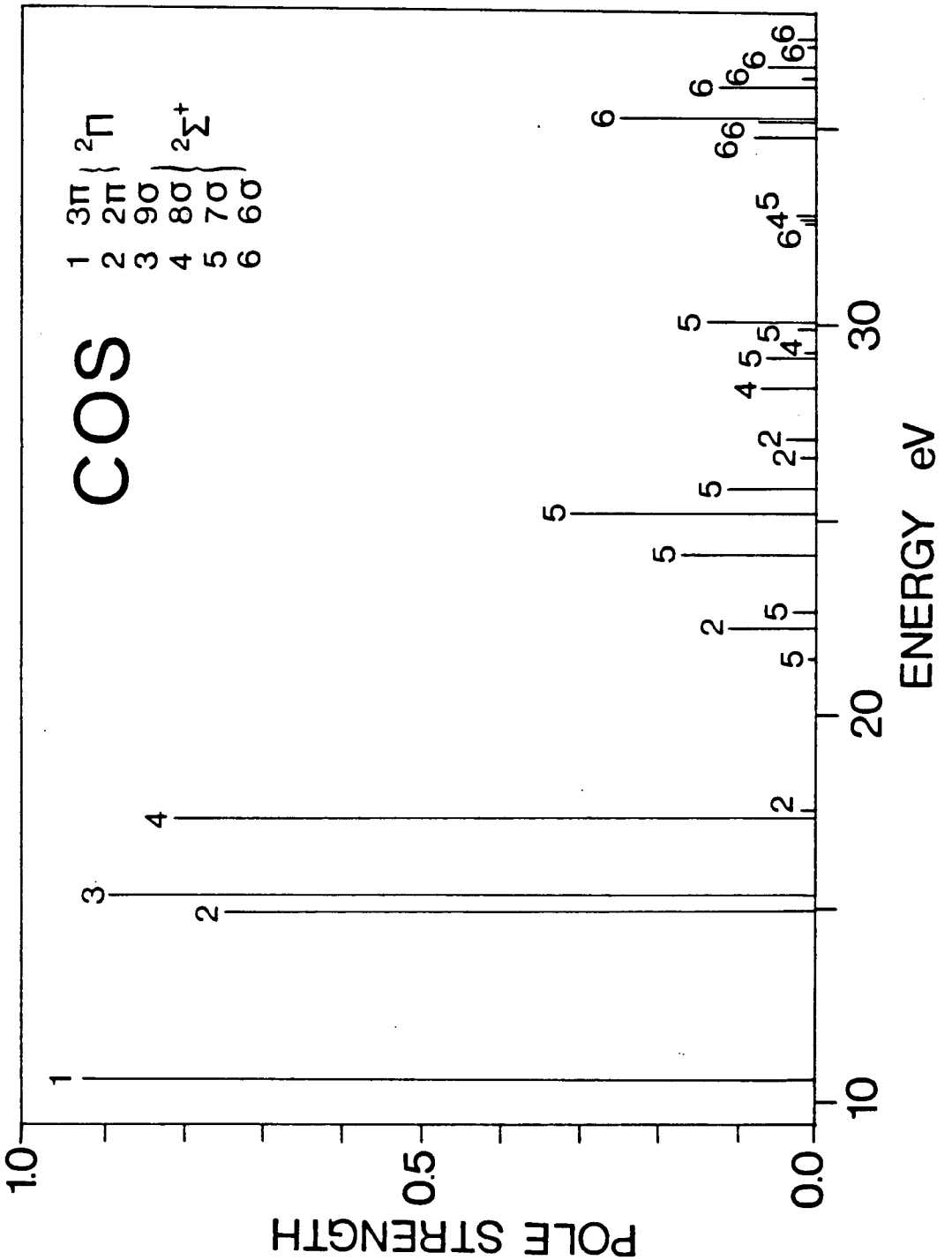

Figure 5.2 Results of the Green's function calculation of the COS ionization potentials and pole strengths.

Table 5.1 Vertical IPs, hole state intensities, and pole strengths for COS.

Final state	IP[1] (spectral feature)	Hole state intensity				Pole[2] strength p{n}
$^2\Pi$		$\|x\{2p\}\|^2$	$\|x\{3p\}\|^2$			
	(X) 10.53	0.004	0.920			0.924
	(A) 14.89	0.745	0.004			0.749
	17.46	0.015	0.002			0.017
	(Q) 22.22	0.070	0.003			0.073
	26.55	0.016	0.004			0.020
	27.15	0.035	0.001			0.036
$^2\Sigma^+$		$\|x\{6s\}\|^2$	$\|x\{7s\}\|^2$	$\|x\{8s\}\|^2$	$\|x\{9s\}\|^2$	
	(B) 15.31	-	-	0.015	0.876	0.891
	(C) 17.29	-	-	0.795	0.016	0.811
	21.35	-	0.030	0.001	0.004	0.035
	22.64	-	0.014	0.011	0.003	0.028
	24.11	0.001	0.099	-	0.006	0.106
	25.24	-	0.313	-	-	0.313
	25.84	0.002	0.105	0.001	0.001	0.109
	(R, 28.36	0.007	0.016	0.048	0.004	0.071
	S) 29.17	-	0.060	0.005	0.001	0.065
	29.27	-	0.006	0.011	0.004	0.021
	29.91	-	0.019	0.004	0.001	0.024
	30.12	0.001	0.135	-	0.001	0.140
	32.57	0.009	0.003	0.001	0.001	0.014
	32.70	0.005	0.004	0.006	0.001	0.016
	32.80	-	0.022	0.001	0.001	0.024
	34.83	0.074	0.002	-	-	0.076
	35.17	0.066	0.002	-	0.001	0.069
	35.30	0.248	-	0.001	-	0.249
	36.13	0.116	0.002	0.008	0.001	0.127
	36.34	0.018	0.001	0.001	-	0.020
	36.55	0.049	0.005	0.002	-	0.056
	(T) 37.11	0.010	0.002	-	-	0.012
	37.34	0.016	0.010	0.001	0.005	0.023
	37.96	0.001	0.011	-	-	0.012
	38.63	-	0.002	0.008	0.003	0.013
	38.86	0.046	-	-	-	0.046
	39.75	0.056	0.002	0.001	0.001	0.060
	39.95	0.011	-	-	0.005	0.016

1 Labelling as in figure 5.2
2 The values of p{n} are shown in figure 5.1 and are defined as the sum of the hole state intensities according to equations 1.28 and 1.29.

calculated pole strength spectrum has been convoluted with a 1.3eV FWHM Gaussian peak shape, and 0.7eV has been added to all calculated energies to align the spectra. The dipole and binary (e,2e) spectra have each been three-point smoothed once.

All four experimental spectra show three strong peaks in the range 10-20eV (X,A,B,C), and a weak series of broad structures extending over the range 20-45eV (P,Q,R,S,T). The calculated spectrum is in good agreement with this: Table 5.1 shows that the one-electron picture holds quite well for ionization from the 8σ,9σ,2π and 3π outer valence orbitals, leading to the strong peaks between 10 and 20eV, the $9\sigma^{-1}$ and $2\pi^{-1}$ states being unresolved. The intensity associated with ionization from each of these orbitals is largely concentrated in one line, and only 10-20 per cent of the intensity is spread over satellite lines. For the 6σ and 7σ inner valence orbitals, on the other hand, a different behaviour is found, both experimentally and theoretically: the theoretical intensity from these orbitals is spread over numerous lines, and this is reflected in the weak, extended structure between 20 and 45eV in the experimental spectra. No single line carries more than 30 per cent of the intensity associated with a single orbital, and one is faced with a complete breakdown of the molecular orbital picture of ionization {Domcke (1979), Schirmer (1977), Cederbaum (1978), Cederbaum (1980)}. From figures 5.1 and

5.2, the basic difference between the outer valence part (10-20eV) and the inner valence part (20-45eV) is evident.

The results for the $^2\Sigma^+$ symmetry ion states ($6\sigma^{-1}$,$7\sigma^{-1}$,$8\sigma^{-1}$,$9\sigma^{-1}$) exhibit a remarkably mixed character in most of the final ion states (Table 5.1) - most of the states derive their intensity from more than one ground state orbital. Even the two outermost $^2\Sigma^+$ states representing the 8σ and 9σ orbitals are not pure. The satellite lines of these outer valence orbitals are seen (figure 5.1) to be intermingled with the inner valence lines. One can no longer distinguish between outer valence satellite lines and 'CI-states' representing the inner valence orbitals. The mixed character of the $^2\Sigma^+$ states leads to variations in the intensity of individual lines with varying photon energy. This effect is clearly seen in the variable 'photon' energy dipole (e,2e) spectra of COS {White (1980)}.

The ϕ=0° and ϕ=15° binary (e,2e) results show a general diminution of intensity over the whole 20-45eV MFS region, with increasing ϕ. This indicates that the whole structure arises from ground state orbitals that have predominantly s-character, thus ruling out major contributions from the 2π and 3π orbitals which would be largely 'p-type'. However, on closer inspection one sees that the shapes of the two spectra are not identical in this region, which means that there is some weak 'p-type' character in the structure: in

particular there is a feature at 23.5eV (Q) seen in all the spectra which is relatively stronger at ϕ=15° than at ϕ=0° compared to the rest of the MFS structure. This is in excellent agreement with the theoretical prediction of a fairly strong 'p-type' 2π satellite at 22.22eV (22.92eV in figure 5.2, since 0.7eV is added to the theoretical energy scale). A similar effect is predicted in CS_2, N_2O and (to a lesser extent) in CO_2 {Domcke (1979)}. The existence of a low-lying and localized π^* orbital is responsible for this effect. However, the large relative intensity of feature Q in the ESCA spectrum suggests that it may involve a superposition of π- and σ-type lines, due to the low π/σ intensity ratios predicted by calculation {Allan (1972)}.

On the basis of the theoretical spectrum we can assign three regions of the MFS structure: the first is the 23.5eV peak (Q) due to a 2π satellite, mentioned above; the second is a broad band from 25 to 33eV (R,S) which the calculation indicates to be primarily 7σ in origin, though with a small admixture from the 8σ orbital which may account for the slight difference in the shape of this band between ϕ values of 0° and 15°; the third region (T) is another broad band (33-40eV) due almost exclusively to ion states originating in the 6σ orbital. The calculation does not predict the very weak shoulder at 20.5eV (P) which seems to be present in all the experimental spectra. A consideration of relative intensities in the binary (e,2e) spectra suggests some

p-type character for this structure (see figure 5.1).

What is intriguing about this MFS structure is that the relative intensities at $\phi=0°$ and $\phi=15°$ for the 6σ and 7σ bands suggest that they have similar momentum distributions, as mentioned above - mainly s-type. From the atomic orbital composition {Basch (1972)} and from the calculated momentum distribution {Giardini (1977)} of the $2\sigma\{u\}$ molecular orbital in CO_2 (see {Giardini (1977)} and also section 6.5) one might expect the analogous 7σ orbital in COS to have appreciable p-character. Apparently changing one oxygen atom to a sulphur, thus reducing the $D\{\infty h\}$ symmetry to $C\{\infty v\}$, is enough to introduce appreciable s-character into the orbital. This argument is supported by an analysis of the pole strengths in Table 5.1 which shows the 7σ mixing with the other σ orbitals. An alternative explanation of course is that the 6σ and 7σ lines are not separated into two fairly distinct bands as suggested by the calculation, but rather that they intermingle so extensively that only the sum of the 6σ and 7σ momentum distributions can be detected.

Making the rough approximation that the dipole matrix element factor in the peak intensities may be considered constant in the valence region under discussion, the ESCA spectral intensities may be compared directly with the theoretical pole strengths (which do not include the dipole matrix element). Five regions of intensity can be identified in the ESCA spectrum, centered at 20.5 (P), 23.5 (Q),

27 (R), 30 (S) and 36eV (T). The latter four are reproduced in the (0.7eV shifted) theoretical spectrum with only small differences of energies and intensities.

The correct way to compare the binary (e,2e) spectra in the MFS region with the theoretical work would be to integrate the binding energy spectrum over momentum before comparison. However, as in the MFS region the shape of the spectrum is fairly constant with azimuthal angle, there is some justification for comparing the relatively more intense $\phi=0^{\circ}$ spectrum with the calculation and the ESCA spectrum. Doing so, one sees essentially the same five bands (P,Q,R,S,T) as in the ESCA spectrum and this is also compatible with the theoretical predictions. The large difference in the relative intensity of the 23.5eV feature (Q) is due to its significant 'p-type' character, as explained earlier.

The binary (e,2e) spectra extend to higher energy than the other experimental data and beyond the highest calculated final states shown in figure 5.1 and Table 5.1. Appreciable MFS intensity is present beyond 40eV. Although the calculation indicates some intensity in this region, no quantitative predictions can be made due to limitations in the method {Cederbaum (1980)}, as stated earlier.

The dipole (e,2e) spectrum serves to confirm the presence of dense structure extending up to at least 40eV;

however, as explained earlier, the intensities are not related in any simple way to the other spectra. The spectrum also confirms the presence of the peaks at 20.5 (P) and 23.5eV (Q), but does not, of course, show structure above 40eV since this is the limit of the equivalent photon energy.

5.3 Conclusions

Experimental measurements of the electron binding energy spectrum once again confirm the Green's function technique predictions of complete breakdown of the one-electron picture of ionization in the inner valence region. The intensity of ionization from the 6σ and 7σ MOs is spread over a wide energy range from 22 to 45eV, with no clearly identifiable main peaks.

CHAPTER 6 CARBON DIOXIDE

He looked back, and then he looked up;
and he was amazed to see how far his
last effort had brought him.

6.1 Introduction

Carbon dioxide is a 22-electron molecule of D{∞h} symmetry. The electronic structure is:

$$(\text{core})^6(3\sigma\{g\})^2(2\sigma\{u\})^2(4\sigma\{g\})^2(3\sigma\{u\})^2(1\pi\{u\})^4(1\pi\{g\})^4$$

The correspondence between the various notations used in this chapter is given in Table 6.1.

The binding energy spectrum of CO_2 is well known in the PES He-I region {Turner (1970)} where the four outer valence states appear at 13.8eV (X), 17.6eV (A), 18.1eV (B) and 19.4eV (C).

The inner states have previously been observed using

XPS {Allan (1972)}, dipole (e,2e) spectroscopy {Domcke (1979)}, and binary (e,2e) spectroscopy {Giardini (1977)}: a broad band is seen in the range 30-42eV in all cases. Both the $2\sigma\{u\}$ and the $3\sigma\{g\}$ states contribute to the intensity in this region, which is distributed over many lines, with no clearly identifiable main peak for either state. This broad spectrum of final ion states arising from the two inner valence orbitals has been predicted using many-body Green's functions calculations {Domcke (1979)}, and is a common feature of the binding energy spectra of many small molecules beyond 20eV.

The previous binary (e,2e) study {Giardini (1977)} was done at 1200eV impact energy with an energy resolution (2.5eV FWHM) somewhat lower than in this work, and an angular resolution considerably better. Due to the limited energy resolution the A, B, and C peaks were not separated, and only the momentum distribution of the X-state was obtained directly.

6.2 Experimental

The incident energy in the present study is 400eV and the experimental energy resolution is 1.2eV (FWHM). Wide range binding energy scans including the inner valence

regions are shown in figure 6.1. With this energy resolution we are able to partially resolve the A, B, and C peaks to an extent that allows us to estimate the angular correlations for the separate orbitals by deconvolution of the binding energy spectra. These were obtained over the range 10 to 25eV at a series of azimuthal angles (ϕ=0-48°) and are shown in figure 6.2. The deconvolution was done with a least-squares Gaussian peak fitting program. First the X-state peak alone in a given binding energy spectrum was fitted, to obtain the experimental energy resolution for that spectrum. Then the full spectrum was fitted using fixed peak widths and fixed peak separations. The fixed peak widths were calculated from the X-state experimental result and the Franck-Condon envelopes obtained from high resolution PES measurements {Turner (1970)}. (Typical binding energy spectra used in the deconvolution are shown in figure 6.2.). Once the relative peak areas of the four peaks were found, the A, B, and C angular correlations were generated by multiplying the X-state angular correlations by the peak area ratios (A/X, B/X, C/X). The results of the deconvolution are given in figure 6.3. The directly-measured angular correlations for the inner valence region are given in figure 6.4.

Table 6.1 State and orbital nomenclature in CO_2.

State number	Ground state MO	Ion state label	Ion hole state
1	$1\pi\{g\}$	X	$(1\pi\{g\})^{-1}$
2	$1\pi\{u\}$	A	$(1\pi\{u\})^{-1}$
3	$3\sigma\{u\}$	B	$(3\sigma\{u\})^{-1}$
4	$4\sigma\{g\}$	C	$(4\sigma\{g\})^{-1}$
5	$2\sigma\{u\}$	MFS	$(2\sigma\{u\})^{-1}$
6	$3\sigma\{g\}$	MFS	$(3\sigma\{g\})^{-1}$

Table 6.2 Bonding, non-bonding and antibonding regions in CO_2 (atomic units) (see also Table 2.2).

	R-space region	P-space region	
		$\pi\{u\}$ $\sigma\{g\}$	$\pi\{g\}$ $\sigma\{u\}$
Bonding	2-3	2-3	1-1.5
Non-bonding	4.5	1.4	0.7
Antibonding	6	1.0	0.5

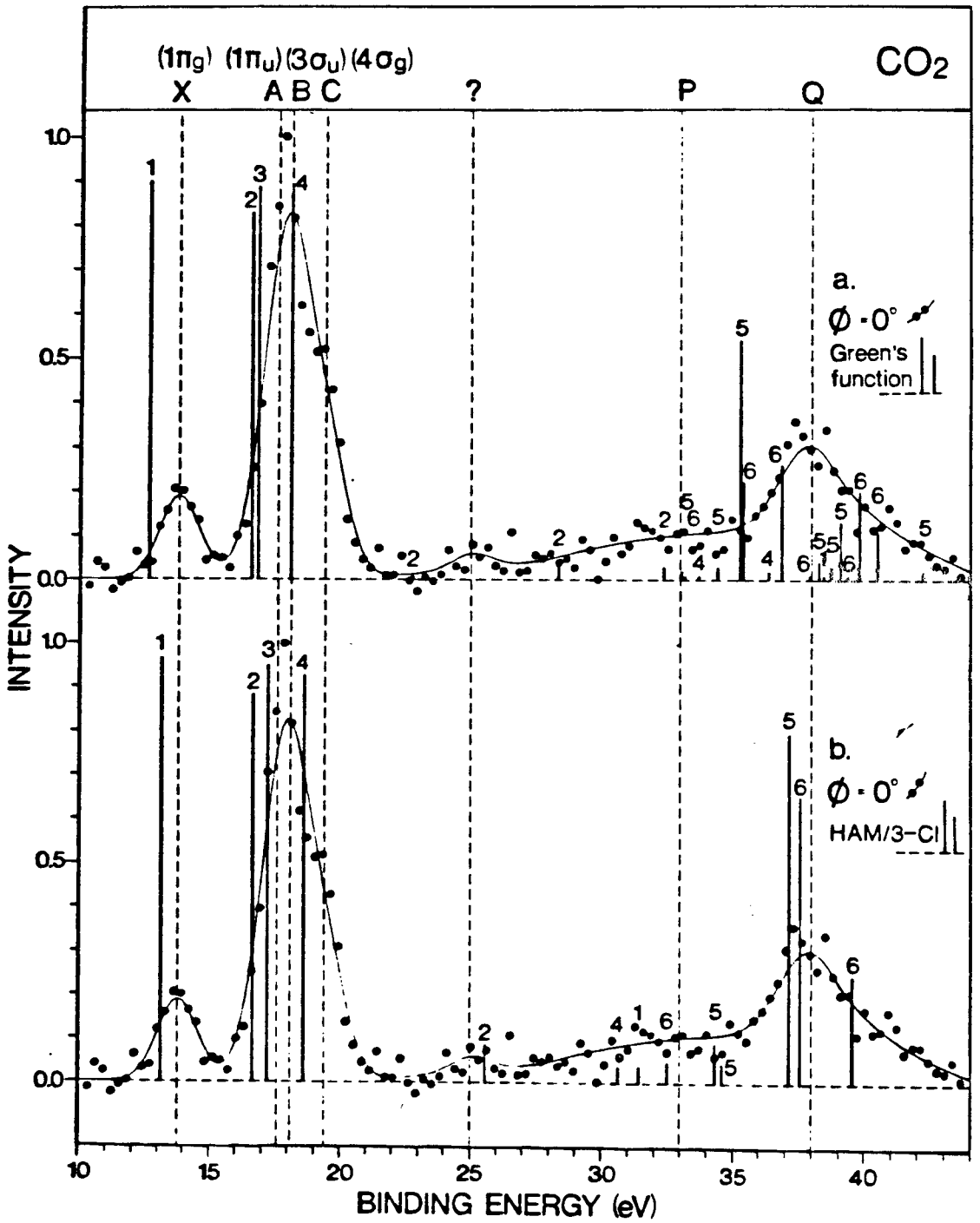

Figure 6.1 Full CO_2 binding energy spectrum at ϕ=0°:
(a) including results of MBGF calculation
(b) including results of HAM/3-CI calculation

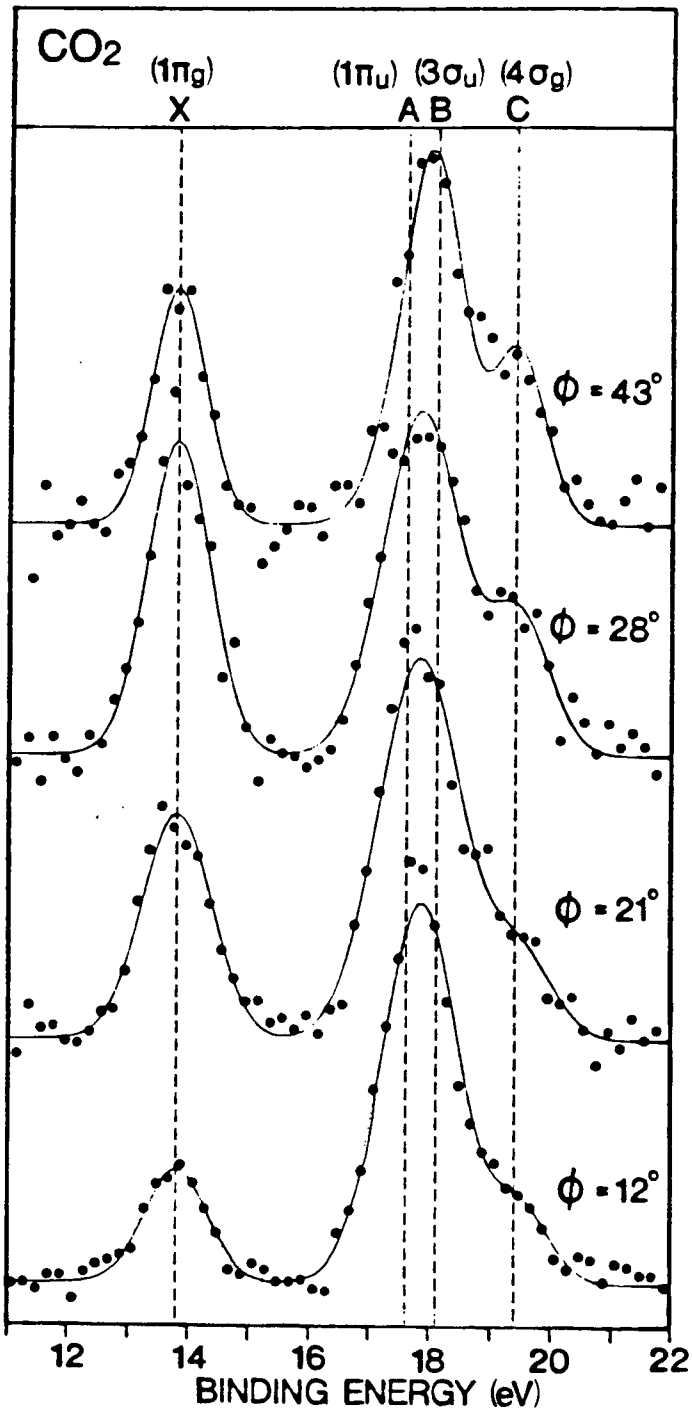

Figure 6.2 Typical binding energy spectra used in the deconvolution procedure.

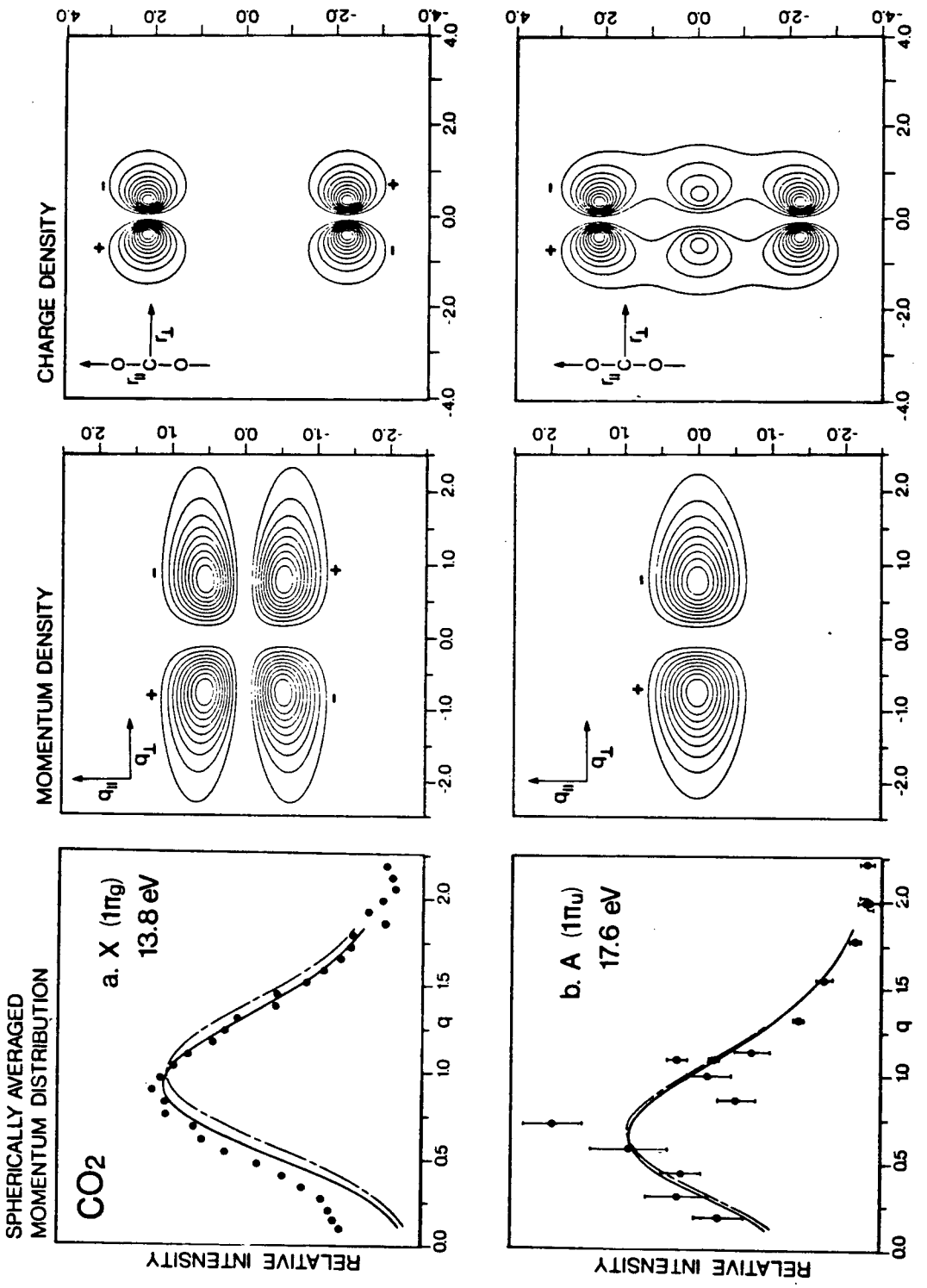

Figure 6.3 Experimental and theoretical momentum distributions, and theoretical momentum and charge density maps for CO_2. Solid lines are the DZ+3d-G76 results and the dashed lines are the DZ-SB results.

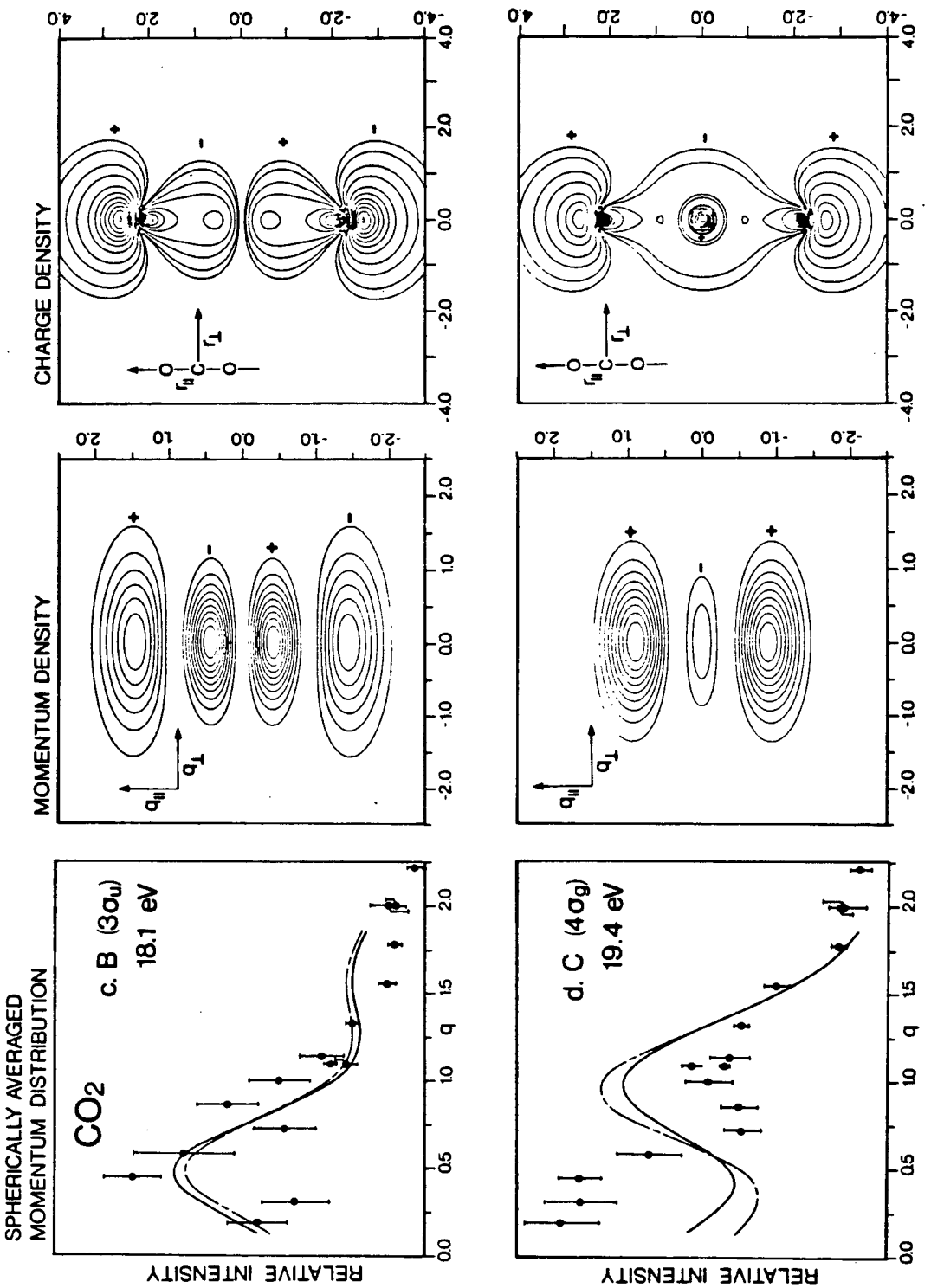

Figure 6.3 continued

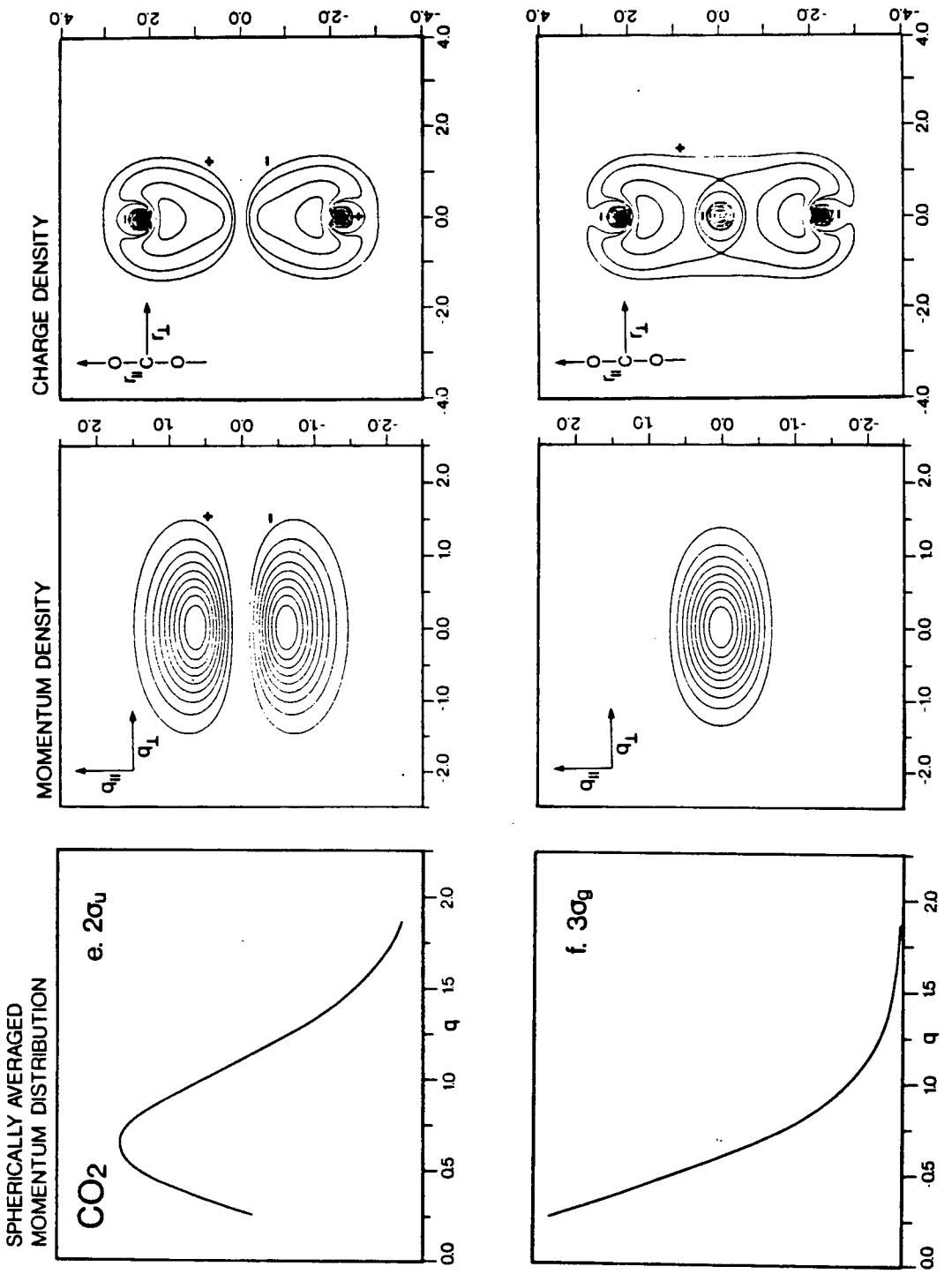

Figure 6.3 continued

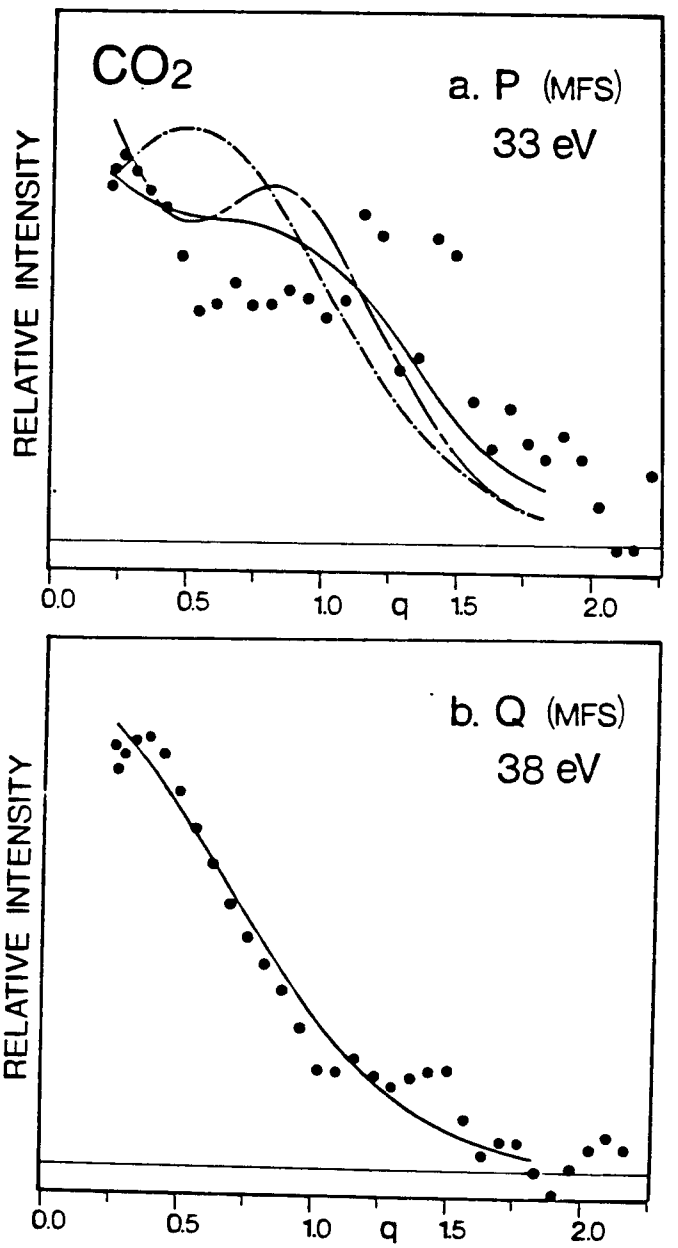

Figure 6.4 Experimental and theoretical momentum distributions at 33eV and 38eV in the MFS region.

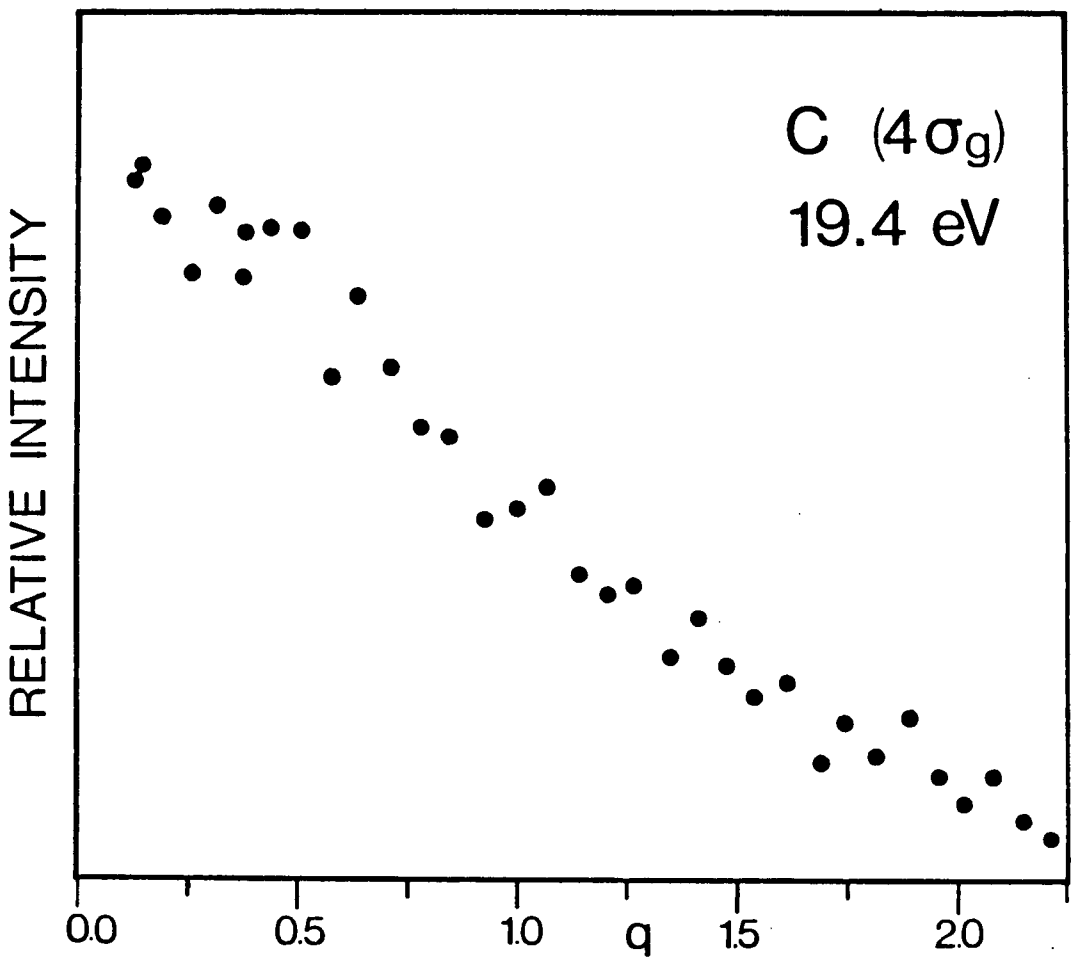

Figure 6.5 Directly-measured momentum distribution at 19.4eV.

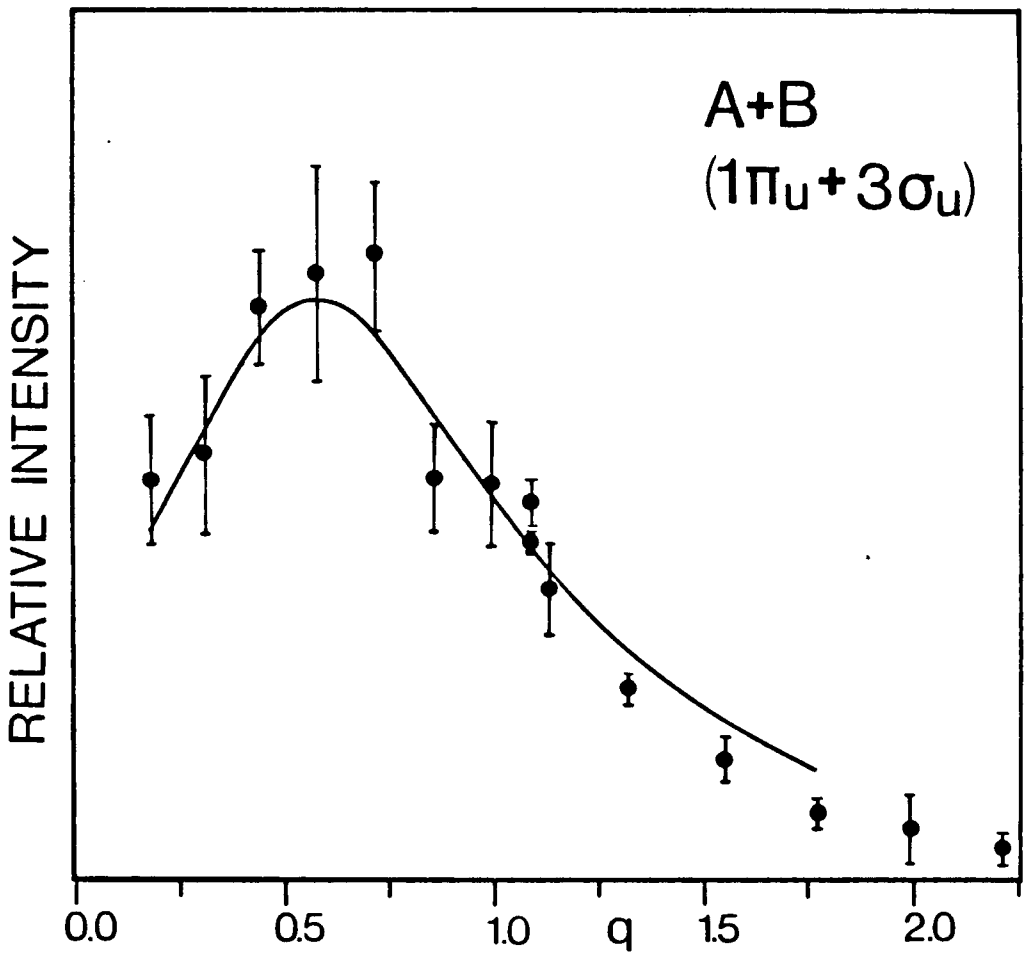

Figure 6.6 The summed A+B experimental and theoretical momentum distributions.

6.3 Calculations

Calculations of the binding energy spectrum of CO_2 have been done with:

(1) MBGF: the 2ph-TDA many-body Green's function method {Domcke (1979)};

(2) HAM/3-CI: the semi-empirical HAM/3-CI method {Chong}.

The Green's function method is described briefly in section 1.4.1. This method includes extensive final state correlation but not ground state correlation.

The HAM/3 calculation is based on the transition-state of ½-occupation method {Asbrink (1977)}. The method relies on extensive parameterization from many PES measurements on small molecules. Configuration interaction has been incorporated by Chong and co-workers, and in this case includes the 84 lowest energy singly- and doubly-excited states above the ground ionic state. The method accounts for extensive ground state and final state correlation.

Note that these two theoretical models give (apart from the binding energies) only the spectroscopic factor of the final ion state in question and do not include other factors in the dipole or binary (e,2e) cross-section formulae. This must be remembered when comparing calculations with experimental spectra. The results are shown in figure 6.1;

note that the occupation number has not been included in the theoretical lines.

Two HF-SCF calculations were chosen to compare with the experimental work on the momentum distributions:

(1) DZ-SB: an LCAO-MO-SCF calculation {Basch (1972)} of essentially double-zeta quality;

(2) DZ+3d-G76: a similar calculation done with the Gaussian 76 package using the 4-31G* standard basis set, including d-functions.

Experimental and theoretical momentum distributions, and theoretical momentum and position density maps from the DZ-SB calculation are shown in figures 6.3 and 6.4. In all cases shown in these figures, the plane of the diagram contains the axis of the molecule oriented along the vertical axis of the diagram.

6.4 MFS Structure of CO_2

The present results agree well with the previous binary (e,2e) study {Giardini (1977)} on the valence binding energy spectrum of CO_2 when the large difference in energy resolution is taken into account, and also with previous XPS {Allan (1972)} and dipole (e,2e) work {Domcke (1979)} in respect of peak energies. It has been noted before

(section 5.2) that although the intensities in binary (e,2e) spectroscopy and X-ray spectroscopy are governed by different relationships, the relative shapes of the MFS structure (30-42eV) are quite similar. This is reasonable since the dipole matrix element in the XPS cross-section is almost constant with binding energy and if, coincidentally, the $2\sigma\{u\}$ and $3\sigma\{g\}$ orbitals have similar magnitudes of the dipole matrix element and binary (e,2e) form factor at their respective scattering kinematics then the spectra should be similar. The binary and dipole (e,2e) cross-sections are also different but similarities are not necessarily expected between the MFS structure in these two cases since dipole (e,2e) spectroscopy is done closer to threshold where the dipole matrix element goes through large variations with binding energy. Even so there is still a rough correspondence between the two spectra except around 27eV. Here the dipole spectrum shows two moderately intense peaks (features I,II of figure 1 in {Domcke (1979)}) which appear only very weakly in the binary and XPS spectra. These are predicted to be $1\pi\{u\}$ satellites by both calculations but it is not possible to check this assignment by measuring the binary (e,2e) angular correlation as the structure is too weak.

The calculations give fairly good results in the outer valence region, except that the lines are all too low by about 1.2eV in the MBGF result and by about 0.6eV in the

HAM/3-CI result. In figure 6.1 the theoretical energies have not been shifted, unlike figures 4.2 and 5.1.

Both calculations on the binding energy spectrum of CO_2 predict that the bulk of the MFS structure (30-42eV) arises mainly from the two inner valence orbitals ($2\sigma\{u\}$,$3\sigma\{g\}$) with a small admixture from the outer valence states, and that the several final ion state peaks from each inner valence orbital are so extensively intermingled that there is at present no possibility of resolving them. This is in contrast to the case of COS (see Chapter 5) where the four orbitals mix significantly in the MFS region but there are broad bands of the structure which are predicted to be from mainly one orbital or another. Of these two calculations on CO_2 the HAM/3 method gives considerably better agreement (figure 6.1) which is not surprising, as this method is extensively parameterized, whereas the MBGF calculation is completely ab-initio. Indeed such is the excellence of the agreement in this and other cases that, in view of the very low cost, one might consider abandoning the far more expensive Green's function method were it not for the fact that at this time the parameterization has only been done for the atoms of the first row (up to Z=10). In comparison the Green's function method is general for all atoms. It must also of course be realized that there is a large hidden cost in the HAM/3 parameterization procedure, which is likely to be difficult for the more complex second row

atoms.

6.5 Momentum Distributions and Bonding in CO_2

This section carries on the ideas introduced in section 2.5.3 on AX_2 molecules.

The two calculations used to compute momentum distributions give very similar shapes for the MDs, with the possible exception of the $4\sigma\{g\}$ orbital. The inclusion of d-functions in the DZ+3d-G76 calculation has little effect on the wavefunction (the coefficients are all less than 10 per cent of the s- and p-function coefficients). As was suggested in Chapter 4, improvements to these wavefunctions should first be concerned with the flexibility of the s/p basis, and then with including d-functions.

The momentum distributions computed from the moderately sophisticated double-zeta wavefunctions are all good approximations to the experimental fact (with the possible exception of the $4\sigma\{g\}$ orbital discussed below). Some of the success of these wavefunctions is due to the fact that the geometry of the molecule, which is accurately known, dictates the form of the wavefunction to a greater extent than in simpler molecules like the hydrides (Chapter 2,4). Table 6.2 summarizes the location of the bonding (and

non-bonding and antibonding) regions of the CO_2 molecule and indicates where P-space density might be expected to arise. As this table and figure 6.3 demonstrate, the bonding regions are localised in certain known regions governed by the CO_2 geometry, and the momentum distribution must reflect closely the separation distances of these regions. Therefore it could have been predicted, before doing any calculations, that the momentum distributions will have intensity, or the absence of intensity, at certain values of q, simply because CO_2 has three atoms, spaced at $2.25a_0$, and therefore its bonding and antibonding regions are separated by certain distances; the only degree of freedom then left to the SCF calculation is the estimation of the amount of density to appear in those regions, and they are clearly doing a fairly good job of this also (with the possible exception of the $3\sigma\{g\}$ and $2\sigma\{u\}$ orbitals which cannot be observed directly, and the $4\sigma\{g\}$ orbital which will be discussed below). This accounts for the fact that the peak positions (q{max}) of all the experimental momentum distributions are quite accurately predicted by the calculations, as is not the case for the hydrides.

6.5.1 The $3\sigma\{g\}$ and $2\sigma\{u\}$ orbitals

The density maps in figure 6.3f shows that the innermost orbital is $\sigma\{g\}$ symmetry (no nodal plane at $p||=0$; class I) and the strong contraction in the $p||$ direction indicates that it extends over the whole molecule, and is therefore bonding. This cannot be confirmed experimentally as it is not yet possible to observe vibrational structure in the inner valence region. (There is one exception to this that I know of: a weak satellite of the $C^2\Sigma^+\{u\}$ state of N_2^+ around 25eV has an obvious vibrational series which has been observed {Asbrink (1974)} with He-II PES and calculated {Domcke (1975)} by the Green's function technique.)

The $\sigma\{u\}$ nature of the next orbital is indicated in the presence of the nodal plane $p||=0$. The momentum density is class IIi and peaks at $p||\{max\}=0.6$ indicating non-bonding character (Table 6.1) but there is also significant density at $p||>0.7$ which suggests some overall bonding character. Again, unfortunately, it is not possible to test this supposition against the shape of the Franck-Condon envelope. An estimation of this structure via a potential energy surface calculation would be useful here, and also in the $3\sigma\{g\}$ case.

Both theoretical calculations of these two orbitals give very nearly the same result: this is why only one curve is shown in their MDs in figure 6.3e,f.

The momentum distribution of the large peak at 38eV is predicted by both calculations to be due to ionization from the $3\sigma\{g\}$ and $2\sigma\{u\}$ states in roughly equal proportions, (figure 6.1), and in fact a least squares fit of the $3\sigma\{g\}$ and $2\sigma\{u\}$ theoretical momentum distributions to the experimental points yields a good fit in the ratio of 1:1.3.

The momentum distribution measured at 33eV however shows (figure 6.4) considerable intensity at large q which cannot be accounted for by a combination of $3\sigma\{g\}$ and $2\sigma\{u\}$ alone. Several least-squares fits of combinations of theoretical MDs to the experimental points are shown in figure 6.4 (only the DZ+3d-G76 result is shown, as the other result is similar): a combination of $3\sigma\{g\}$ and $2\sigma\{u\}$ in the ratio 1:5.7 (short-dashed line) clearly does not account for the large q intensity; a combination of the $3\sigma\{g\}$ and $4\sigma\{g\}$ orbitals in the ratio 1:4.9 fits a little better (long-dashed line) as the $4\sigma\{g\}$ orbital has considerable intensity around q=1.0, but still does not account for all the intensity above this point; a better result still comes with a least-squares fit of the $3\sigma\{g\}$ and $1\pi\{g\}$ theoretical distributions in the ratio 1:3.2 (solid line), which is in disagreement with the MBGF calculations which predict very little intensity due to the $1\pi\{g\}$ or $4\sigma\{g\}$ orbitals, but is in excellent agreement with the HAM/3-CI prediction (see figure 6.1). Other combinations of theoretical momentum distributions were fitted to this measurement, but as they

resulted in negative coefficients, they are patently not valid.

6.5.2 The $4\sigma\{g\}$ orbital

The experimental momentum distributions for the first three outer valence orbitals were obtained by the deconvolution procedure described in the experimental section. This procedure was difficult due to the close spacing of the binding energy peaks and the results are correspondingly of rather limited statistical accuracy particularly in the case of the separate A and B momentum distributions. However they do permit certain conclusions to be drawn.

In figure 6.5 is also shown the experimental and theoretical momentum distributions for the $1\pi\{u\}$ and $3\sigma\{g\}$ orbitals summed together. It is seen that the experimental points form a relatively smooth curve for this combination, as do the points in the separate $4\sigma\{g\}$ distribution. This is some indication that the deconvolution procedure gives reasonably good results in separating the $4\sigma\{g\}$ state peak from the envelope and that the modulation feature observed in this orbital is genuine. The statistical accuracy of the separated $1\pi\{u\}$ and $3\sigma\{u\}$ momentum distributions is significantly lower than for the $4\sigma\{g\}$ distribution, as is to be expected considering their binding energies.

The $4\sigma\{g\}$ orbital is an outer valence orbital where it is possible to check the bonding character deduced from the density maps against the experimental Franck-Condon envelopes. The $\sigma\{g\}$ symmetry of this orbital (class $IIIi_2$) is seen in the density at $p||=0$, and indicates (in this case) some bonding character. The large density in the lobes at $p||\{max\}=0.9$ indicates also a significant antibonding contribution from the charge density outside the oxygen atoms. These two contributions tend to balance each other out, leaving a mainly non-bonding orbital, as confirmed by the absence of vibrational structure on the He-I PES binding energy peak {Turner 1970)}.

The theoretical momentum distribution only agrees with experiment to the extent that the positions of the maxima are predicted correctly, but the intensities of these features are not. There may be several reasons why this is so: the deconvolution of the three peaks may not be accurate in the low q region, allowing some intensity from peak B to leak into the peak C, but in view of the good agreement of the other two deconvoluted MDs with theory this probably does not account for all the q=0 intensity; there may also be ground state correlation between the $4\sigma\{g\}$ and the $3\sigma\{g\}$ which would tend to augment the q=0 intensity; or it may just be a failure of the double-zeta basis that the SCF procedure cannot properly estimate two MO wavefunctions when they are of the same symmetry. Measurements on O_2

{Suzuki (1980b)} indicate there is significant correlation in the analogous case of the $3\sigma\{g\}$ and $2\sigma\{g\}$ orbitals, which is in support of the second argument above. An attempt was made to measure the $4\sigma\{g\}$ momentum distribution directly, but this proved inconclusive; the result shows (figure 6.5) an s-type distribution with no evidence of the hump at q=1.0. Very likely the B state is filling in the q=0.6 region. Finally, it may be possible that the CO_2 $4\sigma\{g\}$ is just a difficult orbital wavefunction to calculate with the limited flexibility of these basis sets - there is a significant difference between the two theoretical curves, even though the basis sets are quite similar.

6.5.3 The $3\sigma\{u\}$ and $1\pi\{u\}$ orbitals

The $3\sigma\{u\}$ orbital is interesting in that its MD shows a q{max} at 0.4 - surprisingly low considering that the atomic C2p and O2p orbitals have their p{max} at 0.6 and 0.8 respectively (figure 2.1). The reason for this is neatly explained by the antibonding density at p||=0.4 (Table 6.2) seen in the momentum density maps (class IVi).

The $3\sigma\{u\}$ orbital is another situation where the bonding and antibonding contributions roughly cancel, leaving little vibrational structure in the PES spectrum {Turner 1970)}. There is probably some small net antibonding tendency from this orbital.

The greater part of the momentum density in the $1\pi\{u\}$ orbital (class IIi) is in the $p||=0$ plane, indicating that the π orbital extends over the whole molecule, as is obvious from the charge density map. This orbital is responsible for the major part of the bonding in CO_2 and the PES spectrum shows an extensive Franck-Condon envelope for this peak.

The agreement between experiment and theory is good on both these orbitals, especially in respect of the q{max} values. In the $3\sigma\{u\}$ the smaller modulation around q=1.5 in the theoretical curve is not seen in the experimental points. Here again the explanation of this discrepancy may lie in the inadequacy of the basis sets, or in correlation between the $3\sigma\{u\}$ and $2\sigma\{u\}$ orbitals.

For a time there was some uncertainty in the energies of the $1\pi\{u\}$ and $3\sigma\{g\}$ states in CO_2 {Turner (1970)}: different calculations predicted different ordering of these states. The problem was resolved when the PES spectrum was found to show that the higher energy state (17.6eV) must be the $1\pi\{u\}$ orbital because of its extended vibrational envelope. The present CO_2 results are in agreement with this assignment: the experimental momentum distributions plainly show the q{max} for the $1\pi\{u\}$ MD at 0.7 is higher than that for the $3\sigma\{g\}$ MD at 0.4, which is in agreement with the calculations. That this good agreement is seen is evidence of the success of the deconvolution procedure, and some encouragement to suppose that the $4\sigma\{g\}$ q=0 intensity is not

an experimental artifact.

6.5.4 The 1π{g} orbital

Because CO_2 has enough electrons to populate a π{g} level, unlike any of the systems studied so far in this thesis, an interesting feature is seen in the momentum distribution of this outermost orbital: q{max} is at the unusually high value of 0.9. The reason for this is obvious on inspection of the momentum density map (class $IIIi_1$): the gerade combination of 2p{x} and 2p{y} oxygen atomic orbitals means there are two perpendicular nodal planes which push q{max} from its atomic position of $0.7a_0^{-1}$ along the p⊥ axis, out to 0.9 between the nodal planes. This effect will be seen in all orbitals which have this 'pseudo d-orbital' symmetry: for instance the NO 2π and O_2 1π{g} orbitals where p{max} occurs at 0.8 and $0.9a_0^{-1}$ respectively (Chapter 7). In other words, an antibonding π*-orbital is essentially of similar angular form as an atomic d-orbital situated on the bond midpoint (see section 2.5.1 on 'pseudo-angular momentum'). This case also has parallels with the π-system of trans-butadiene (C_4H_6) {Tossell (1981)}. The C_4H_6 1a{u} and 1b{g} molecular orbitals have some similar characteristics to the CO_2 1π{u} and 1π{g} molecular orbitals respectively. All four molecular orbitals have a nodal plane containing the atom centres which characterizes π-systems. The 1π{g} and 1b{g} molecular orbitals have

another nodal plane in the middle of the molecule and perpendicular to the atomic backbone. The most probable momenta are $0.6a_0^{-1}$ and $0.8a_0^{-1}$ for the C_4H_6 1a{u} and 1b{g} molecular orbitals respectively. The CO_2 1π{g} most probable momentum (0.9) is greater than that for C_4H_6 1b{g} because the CO_2 molecule is one atom shorter than C_4H_6. By the Reciprocity principle this means a momentum density of proportionally greater extent in the bond axis dimension in CO_2. Similarly the CO_2 1π{u} q{max} (0.7) is higher than that of the C_4H_6 1a{u} orbital.

This emphasizes that one must exercise caution in associating the energy of an orbital directly with the most probable momentum of the distribution. It is not necessarily true that one should expect the momentum distribution to move to higher values of q as one goes deeper into the valence shell of the molecule (i.e. to higher binding energy). It is seen here that it is possible for an electron to have a momentum distribution at higher most probable q, but still be at a lower binding energy than another orbital. Of course the balance of the electron's energy is in the Coulomb potential interactions with the other particles in the system, and since the 1π{g} is an antibonding orbital it may be expected to have strong Coulomb repulsion terms which raise its energy.

p||{max} is at 0.6 for this orbital indicating non-bonding character. Because the momentum density falls

off steeply with increasing p|| there is little bonding character, unlike the $2\sigma\{u\}$ orbital, explaining why the PES binding energy peak has no vibrational structure. The experimental MD for this orbital shows intensity near q=0 which is in disagreement with that expected from the symmetry of the orbital (pseudo-d). This intensity is not likely to be real, and is probably an artifact due to the combined effects of angular resolution, statistical error, and uncertainty in the exact mean θ scattering angle.

6.6 Conclusions

CO_2 shows interesting variety in its molecular orbitals and momentum distributions. The geometry of the molecule has a strong effect on the shapes of the MDs (these are quite different from the MDs of atomic carbon and oxygen), and this shape can be used to estimate roughly the relative bonding, non-bonding, and antibonding character of the orbitals. The use of momentum and charge density maps is very revealing in this study.

The calculation of the CO_2 MO wavefunctions does not benefit greatly from the addition of d-functions, as was also found for H_2S, and in fact, can be done fairly successfully with only a double-zeta basis, although there

is some error in the estimation of the $4\sigma\{g\}$ orbital.

The HAM/3-CI method of calculating binding energy structure has been shown to give excellent results for the case of CO_2.

CHAPTER 7 NITRIC OXIDE AND OXYGEN

'This matter winds itself ever in new riddles!'

Binary (e,2e) studies have been carried out on NO and O_2 by the Flinders University (e,2e) group. To complement the experimental results {Brion}, the momentum distributions, momentum density maps and charge density maps from several theoretical molecular wavefunctions have been computed here at UBC.

7.1 Nitric Oxide

The NO electronic configuration (not including spin) is:

$$(\text{core})^4(3\sigma)^2(4\sigma)^2(5\sigma)^2(1\pi)^4(2\pi)^1$$

Experimental results for the NO molecule were done at 1200eV incident energy. Binding energy spectra at two angles

were recorded, as well as angular correlations at energies 9.5, 21, and 40.5eV: these energies correspond to the $2\pi^{-1}$, $4\sigma^{-1}$, and $3\sigma^{-1}$ orbital vacancy ion states. Angular correlations for the other peaks could not be recorded since they are spaced too closely to be resolved energetically.

The NO wavefunction is notoriously difficult to calculate. Two theoretical wavefunctions were studied for NO:

(1) DZ-NSO-CI: a double-zeta, natural spin orbital, restricted CI calculation {Kouba (1971)};

(2) GTO-UHF: a (9s5p/4s3p) contracted GTO basis, unrestricted Hartree-Fock, single-configuration calculation {Kunz}.

The total energies of these wavefunctions are (Hartrees): -129.2599 (DZ-NSO-CI), and -129.2065 (GTO-UHF). The limiting Hartree-Fock energy has been estimated to be -129.3443 Hartrees {Sinanoglu (1966)}. The first calculation assumed the experimental internuclear distance of $2.1747a_0$, and the second places the atoms $2.25a_0$ apart.

The experimental and theoretical MDs are shown in figure 7.1. The computed density maps are shown in figure 7.2 and 7.3. Since the alpha and beta MOs of the DZ-NSO-CI work are very similar (except for the 2π), only the alpha ones are shown. It was assumed that the tabulated basis function coefficients in the DZ-NSO-CI wavefunction refer to a basis set where the positive lobe of the axial 2p basis

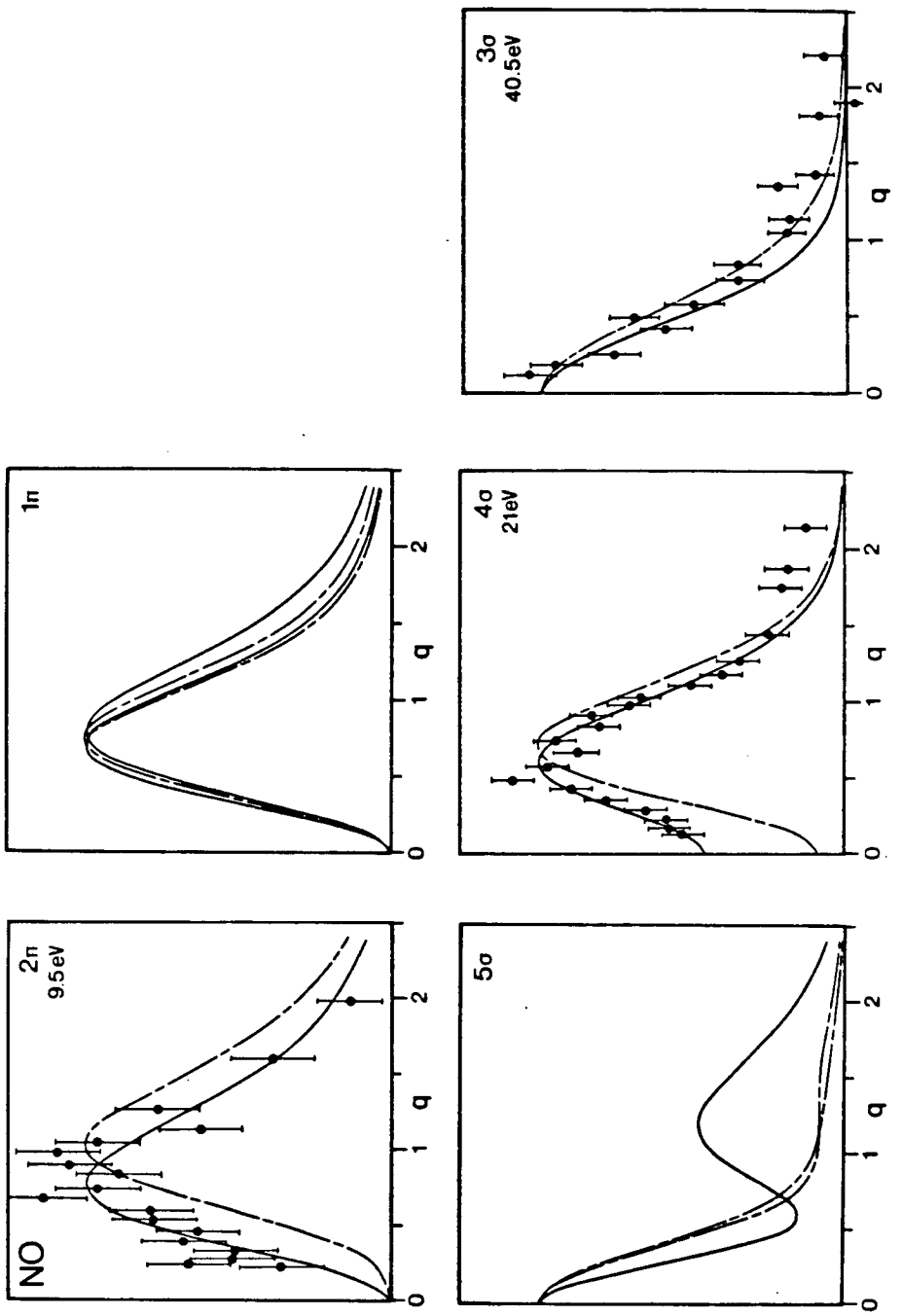

Figure 7.1 Experimental and theoretical momentum distributions of NO. Solid lines are the DZ-NSO-CI results and dashed lines are the GTO-UHF results.

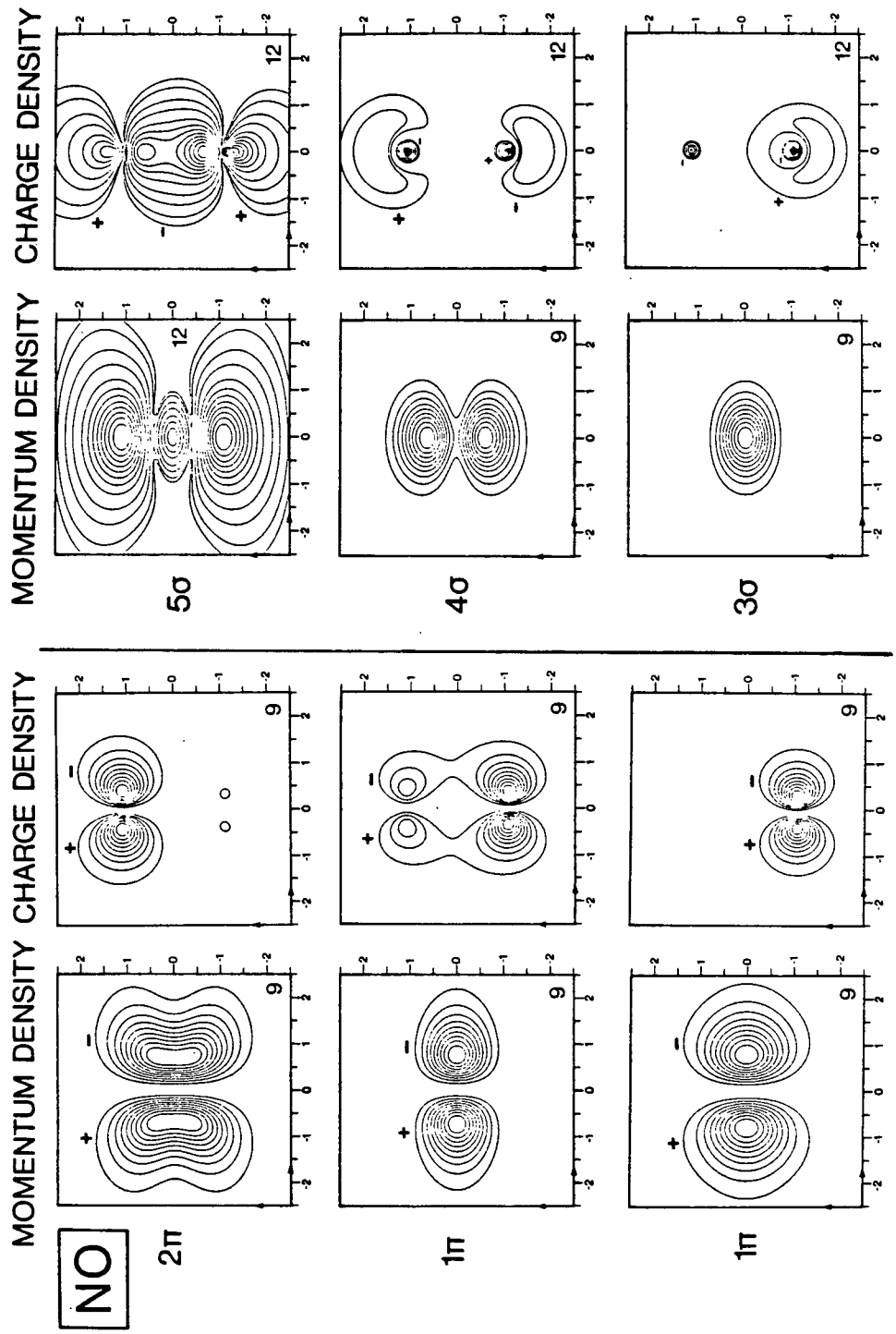

Figure 7.2 Momentum and charge density maps from the DZ-NSO-CI wavefunction (spin α parts only).

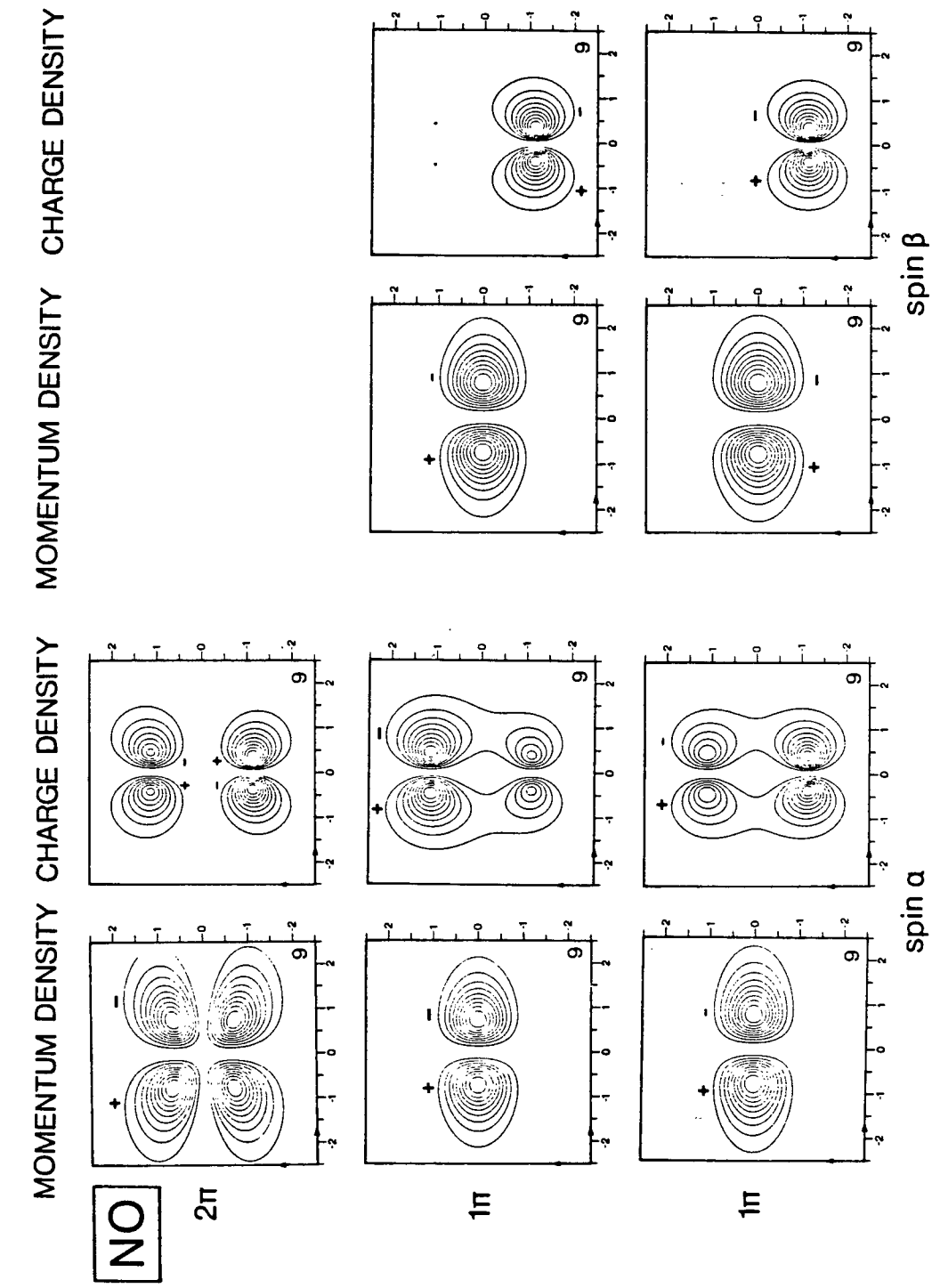

Figure 7.3 Momentum and charge density maps from the GTO-UHF wavefunction.

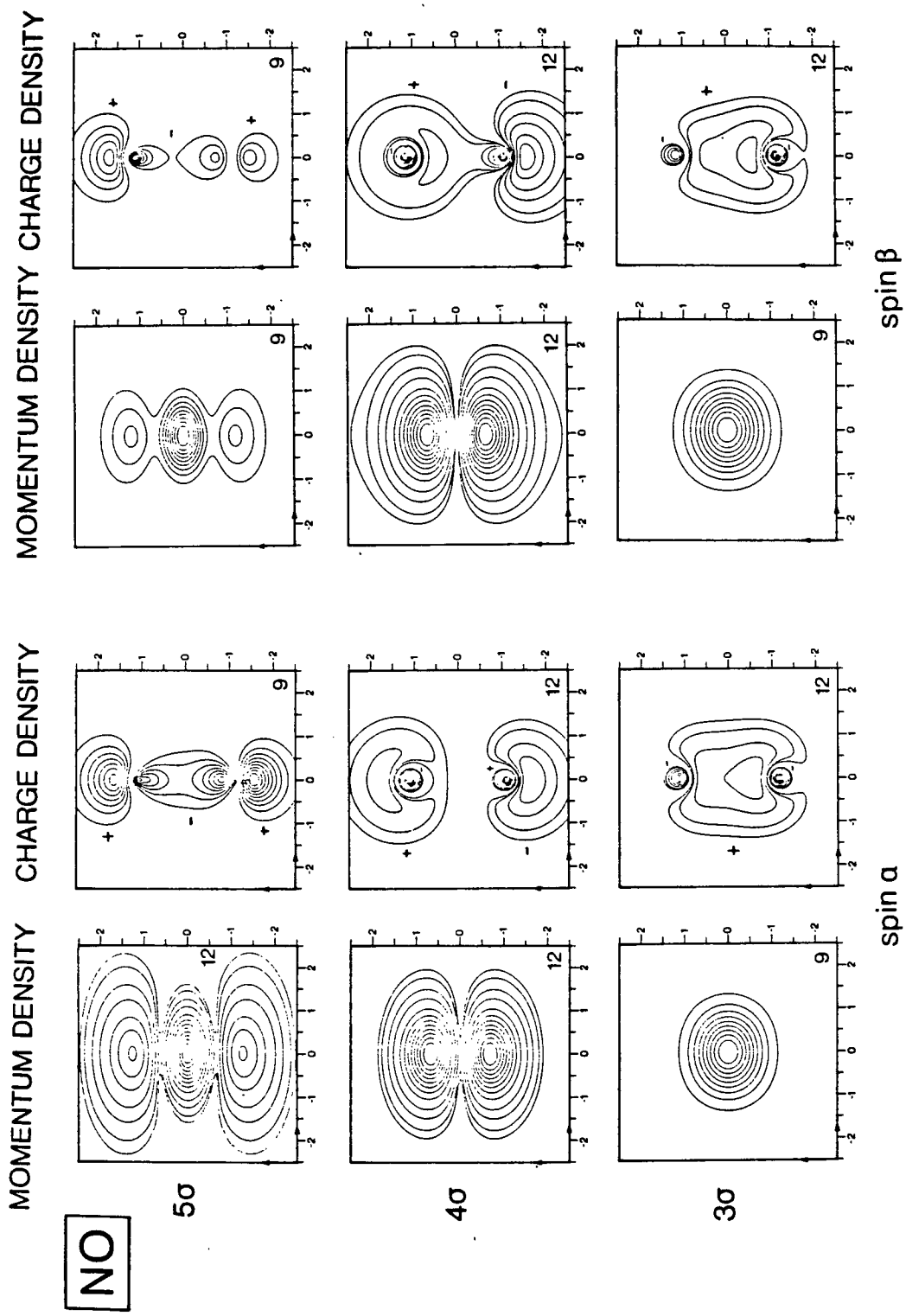

Figure 7.3 continued

functions and the oxygen atom are toward the same end of the molecule; the orientation of the 2p functions is not explicitly stated in the paper, though I am assured by the authors and by other authorities that this assumption is probably correct.

7.1.1 The NO inner valence orbitals

The DZ-NSO-CI calculation suggests the innermost 3σ orbital has some bonding character, (witness the contraction in the bond direction of the momentum density map) while the other calculation show non-bonding attributes (the contour lines are nearly circular). The momentum distributions indicate that this estimation of bonding character in the DZ-NSO-CI calculation is probably not correct, as the fit between calculation and theory is not quite as good as in the GTO-UHF calculation. Our chemical intuition is in accord with this: we conceive of the inner valence orbitals as being 'atomic-like' and showing little bonding or antibonding tendency.

The situation is reversed in the 4σ orbital, where the DZ-NSO-CI MD clearly fits better than the GTO-UHF: the former indicates that the orbital, though nominally antibonding, has some nonbonding character as seen in the density around p=0, while the latter have almost no density at low q, in disagreement with the experimental result.

The momentum density for the 3σ orbital can be constructed mainly from class I Q-projections. The 4σ momentum density is class IIa in the bond direction, and the differences between the two calculations is due to the varying asymmetric contribution of 2s functions on each centre.

7.1.2 The NO outer valence orbitals

The outermost 2π orbital is an excellent example of the selectivity of binary (e,2e) in judging the quality of wavefunctions which, examined under other criteria - energy, for instance, or dipole moment, may have little to distinguish them. The two calculations estimate differently the character of this MO as almost non-bonding (DZ-NSO-CI) or nearly full antibonding (GTO-UHF). The important feature is the amount of density in the $p_{||}=0$ plane: if this is not large then the position of p{max} in the MD will move to larger p compared with the atomic orbitals, which is the case for the GTO-UHF calculation. The DZ-NSO-CI calculation, on the other hand, does put considerable density in the $p_{\perp}$ plane, with the result that the value of p{max} does not change as much compared with the atomic orbitals (figure 2.1). This kind of orbital falls somewhere between class IIi and class $IIIi_2$ in the bond axis direction (see section 2.4) depending on whether it is more nearly non-bonding or antibonding respectively.

Next consider the spherically-averaged momentum distributions from the two calculations: both distributions will be p-type because of the nodal plane, but due to its significant non-bonding character, the DZ-NSO-CI calculation has the lowest p{max}, with the GTO-UHF result significantly higher. The experimental result shows in a very gratifying manner that the DZ-NSO-CI result is correct, and the other definitely in error.

Another explanation has been advanced {Suzuki (1980b)} to account for the large p{max} in the outermost MO of NO and O_2, which rests on the fact that in both cases it is singly-occupied. For both O_2 and NO this MO is a π^* orbital occupied by a single (unpaired) electron (the doubly degenerate π^* orbitals are each singly occupied in O_2). In that discussion {Suzuki (1980b)} of the O_2 results it was suggested that the higher most probable momentum might be the result (via the Reciprocity principle) of less spatial extension of the orbital arising from the absence of intra-orbital electron-electron repulsion. The fact that a correspondingly large most probable momentum has also been observed for the doubly-occupied outermost π^* orbital of CO_2 suggests that this effect is primarily due to the 'd-like' pseudo-angular momentum of the antibonding (π^*) orbitals in all three molecules. Intra-orbital correlation effects can for the most part be ruled out as a direct contributing factor on two counts:

(1) Correlation effects are generally quite small in the ground state, accounting for about 1eV of the total energy. This is not enough to cause such a large shift directly;

(2) 'Intra-orbital' versus 'inter-orbital' correlation is only a convenient artificial partitioning of the total correlation between all the electrons, and to single out the former as the cause of a specific effect in one orbital is not valid.

That the DZ-NSO-CI wavefunction does do a better job than the GTO-UHF wavefunction must be due mostly (as the basis sets are similar) to the natural-spin-orbital configuration-interaction technique wherein correlation is properly accounted for in the whole molecule (which in turn affects the SCF potential and the shape of the 2π NSO), rather than solely because the 2π intra-orbital correlation is removed.

The remaining theoretical molecular orbitals, while they have not been checked experimentally due to the close spacing of their final ion state energies, are of academic interest as a demonstration of bonding in heteronuclear diatomics. The calculations both predict bonding π-orbitals between the two atoms, and non-bonding π-orbitals centred mainly on the oxygen. The bonding character is reflected in the amount of contraction of the momentum density in the bond direction. This in turn affects the

spherically-averaged MDs: a contraction of the density in the p|| direction means the MD shifts to lower q, as may be seen comparing figure 7.1 with figures 7.2 and 7.3 (not all the 1π MDs are shown in figure 7.1 as they are often very similar).

The greatest difference in the DZ-NSO-CI and GTO-UHF results is in the 5σ MO: the DZ-NSO-CI result predicts roughly equal bonding and antibonding contributions that give rise to MD intensity around q=0 and q=1.2. The GTO-UHF calculation predicts somewhat more antibonding character which increases the totally symmetric component in this orbital and so augments the q=0 intensity at the expense of the q=1.2 region. It has been suggested {Kouba (1971)} that the 5σ orbital probably accounts for most of the bonding in this molecule, but examination of the charge density maps indicates that this is perhaps incorrect in light of the argument above, and that the bonding arises mainly from the 1π molecular orbital.

7.2 Oxygen

The electronic MO configuration of the 16-electron O_2 molecule is:

$$(\text{core})^4(2\sigma\{g\})^2(2\sigma\{u\})^2(3\sigma\{g\})^2(1\pi\{g\}^4(1\pi\{u\})^2$$

A calculation on oxygen {Kunz} similar to the GTO-UHF calculation on NO is displayed in the form of charge and momentum density maps, and momentum distributions in comparison with experimental binary (e,2e) results {Suzuki (1980b)} in figure 7.4. The theoretical momentum distribution is shown with a solid line. Solid circles indicate 1200eV experimental data, and open circles 400eV data. The angular resolution in the momentum distribution measurements is claimed to be sufficiently good that it is unnecessary to fold in experimental resolution factors into the calculated momentum distributions, and in figure 7.4 no such factors have been included.

The agreement between experimental and theoretical momentum distributions is, in general, very good for all MOs within the statistical accuracy of the measurements.

7.2.1 The O_2 σ{g} orbitals

There seems to be extensive correlation, in either the initial ground state or final ion states or both, involving the 2σ{g} and 3σ{g} O_2 orbitals. This produces at least four binding energy peaks which all exhibit an s-type momentum distribution, but have varying degrees of 'kink' at $q=0.6a_0^{-1}$. Of these four momentum distributions I have chosen the lowest and highest in energy to compare with theory, as these are likely to be 'purer' in one state or the other, as indeed figures 7.4c and 7.4e show: the

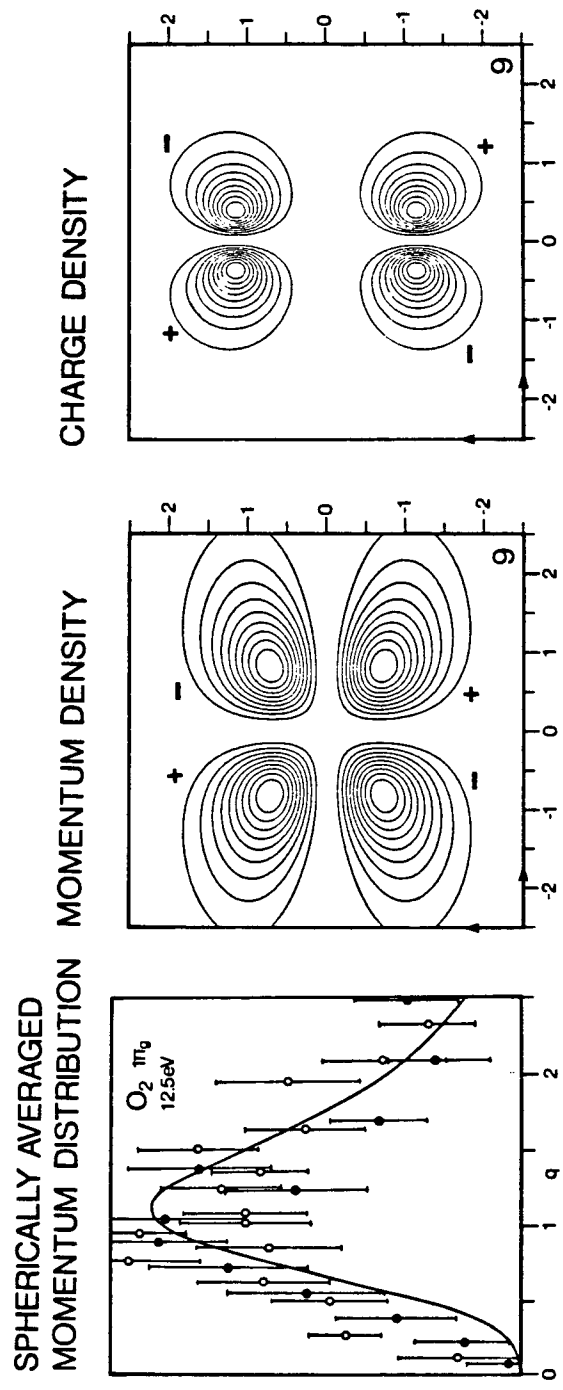

Figure 7.4a Momentum distributions and momentum and charge density maps for O_2: the $1\pi\{g\}$ orbital.

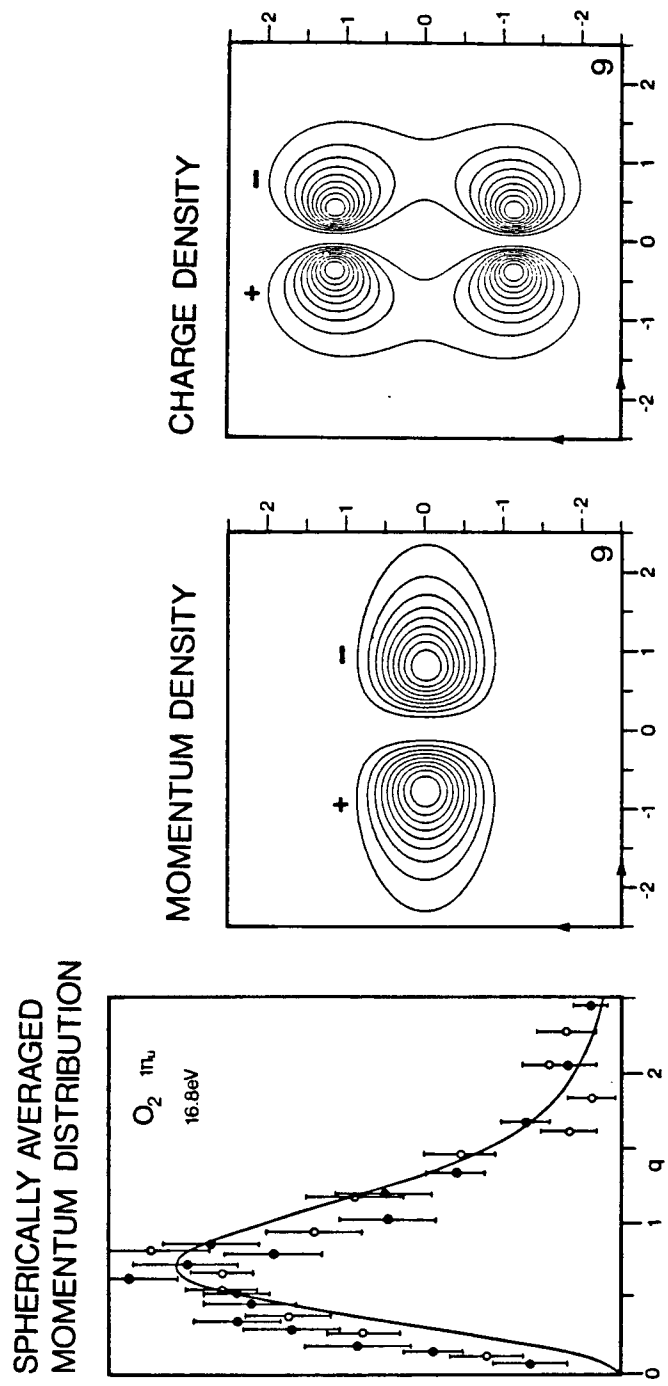

Figure 7.4b Momentum distributions and momentum and charge density maps for O_2: the $1\pi\{u\}$ orbital.

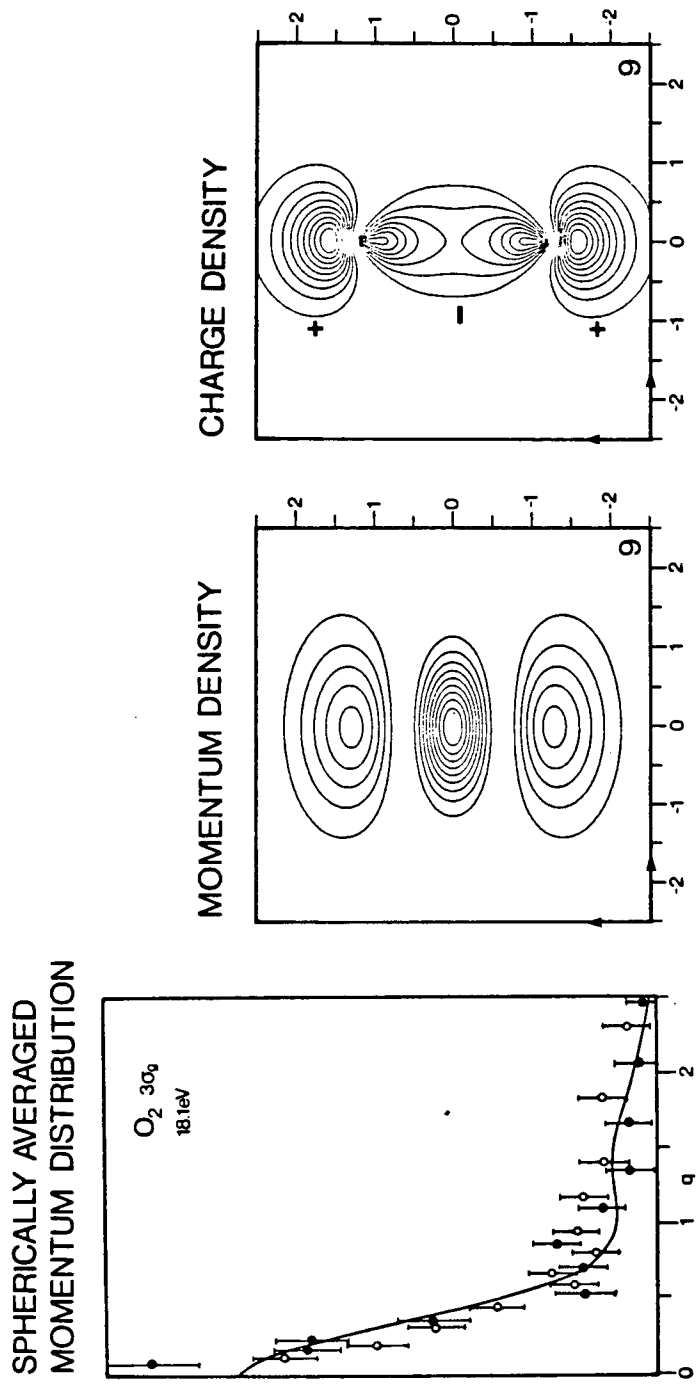

Figure 7.4c Momentum distributions and momentum and charge density maps for O_2: the $3\sigma\{g\}$ orbital.

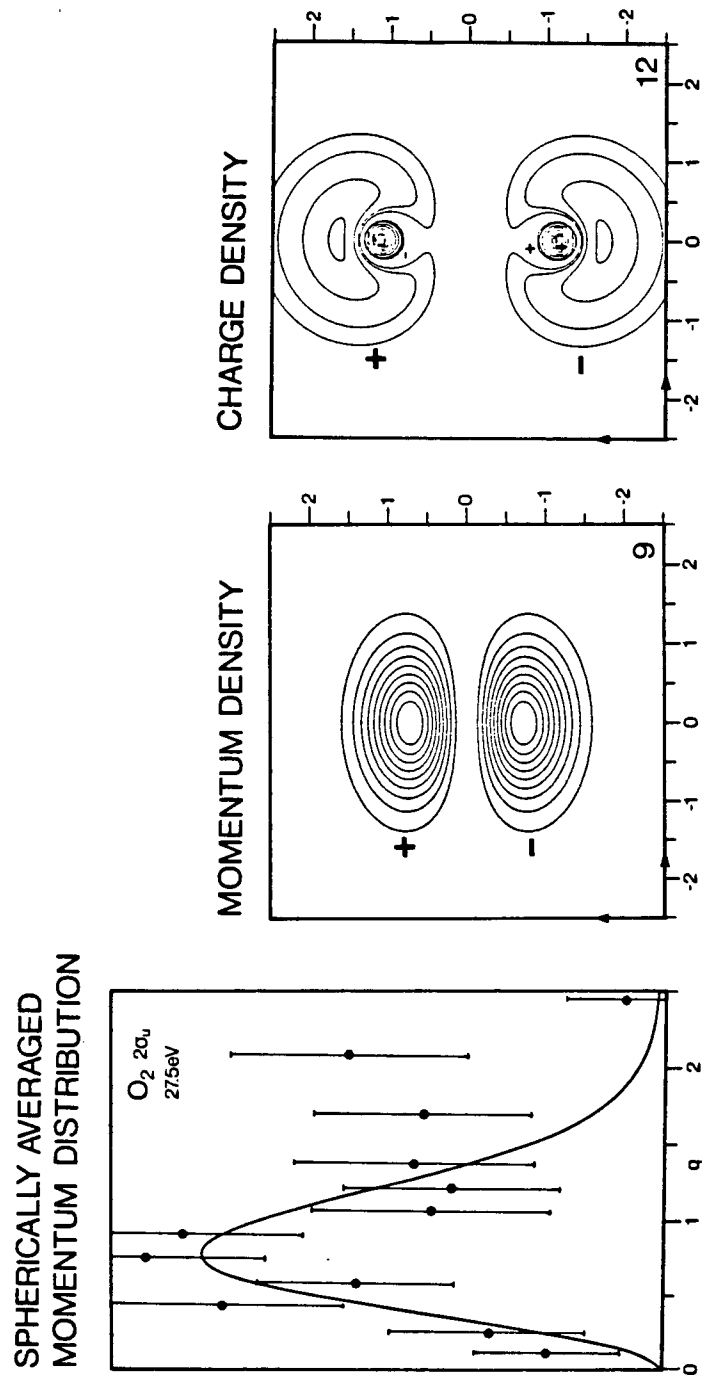

Figure 7.4d Momentum distributions and momentum and charge density maps for O_2: the $2\sigma\{u\}$ orbital.

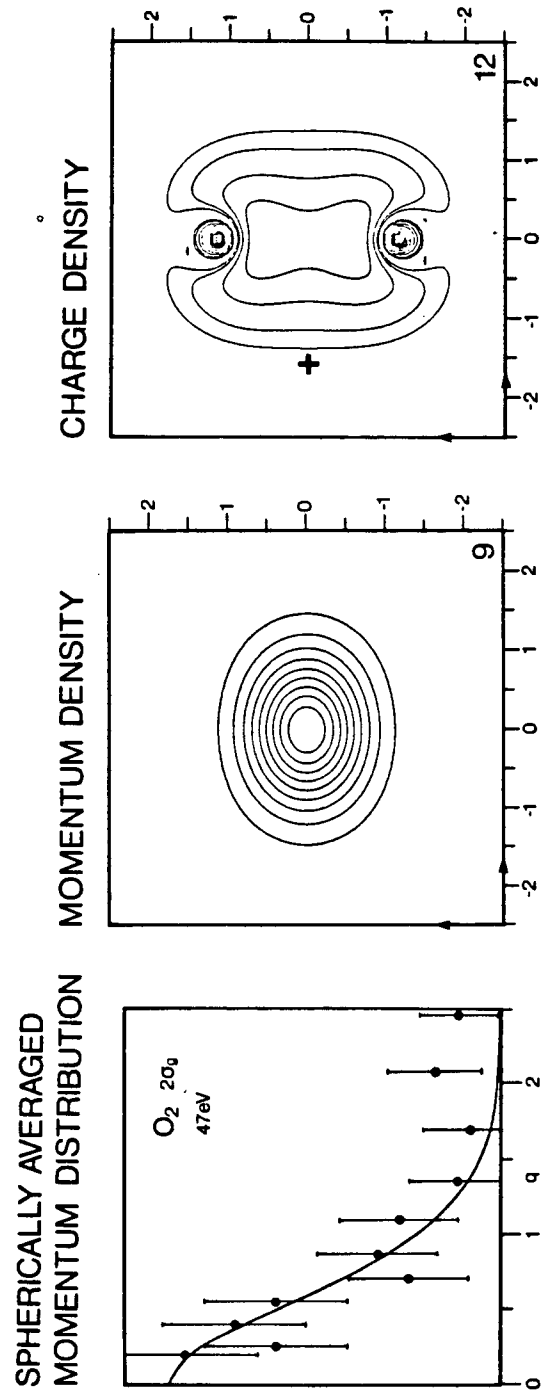

Figure 7.4e Momentum distributions and momentum and charge density maps for O_2: the $2\sigma\{g\}$ orbital.

agreement is excellent, with the small exception of the position of the 'kink' which the calculation puts rather higher than the measurement. The position of the kink is determined by the location of the P-space nodal surfaces, which is in turn determined by the ratio of s/p character in the orbital: if there is in fact some extra 2s character coming in from the $2\sigma\{g\}$ orbital this may account for the discrepancy.

7.2.2 The $2\sigma\{u\}$ orbital

Insofar as may be judged, the agreement between theory and experiment is satisfactory, within the statistical accuracy of the measurement. This orbital is of antibonding character and is described by the Class IIi Q-projection.

7.2.3 The $1\pi\{u\}$ and $1\pi\{g\}$ orbitals

As has been mentioned earlier, oxygen is another example of the situation where p{max} increases as ϵ decreases, for two π orbitals. Again, the reason for the large p{max} ($0.9a_0^{-1}$) in the $1\pi\{g\}$, compared to the $1\pi\{u\}$ ($0.7a_0^{-1}$) is the second nodal plane, $p_{||}=0$, which pushes momentum density to larger p, although $p_{\perp}$ is almost the same. The reason why the calculation agrees well with experiment here, in contrast with the NO 2π, is that the O_2 $1\pi\{g\}$ is a pure antibonding orbital, in a homonuclear molecule, with no possibility of non-bonding character

coming in. Therefore, the coefficient of the atomic 2p orbitals on one oxygen with respect to the other is exactly the same (to within a sign), fixed by the symmetry of the system, whereas in the NO 2π MO the relative amounts of 2p AOs on each centre (and hence the relative non-bonding/antibonding character, and the position of p{max}) is a variable, and likely very sensitive to the quality of the basis set and the method of calculation to boot.

This situation should be reflected in the comparison of the outer CO_2 1π{u} and 1π{g} MOs with the corresponding COS 2π and 3π orbitals: theoretical wavefunctions for the CO_2 orbitals are good, but I predict that the COs 3π q{max} will be lower than the CO_2 1π{g} and also difficult to calculate. In general, where symmetry is lowered by changing an atom but maintaining similar structure (as in O_2 to NO, N_2 to HCN, CO_2 to COS), we may expect calculated results using similar quality basis sets to be less good in the less symmetric case.

In both these cases the agreement of measurement and theory is good: the only discrepancy is that the theoretical momentum distributions are at very slightly higher momentum compared to the experimental points (ignoring the low q region where the discrepancy may be due partly to residual angular resolution effects). This has been noted before in the outer valence orbitals of other systems, and again means

that the (9s6p/5s3p) basis set, while accurate for inner, more atomic-like MOs, fails to account completely for the electron density shift in the outer MOs when forming the molecule.

7.3 Conclusions

Charge and momentum density maps have been used to refute previous suppositions as to the origin of the high q{max} in the NO 2π and O_2 1π{g} orbital momentum distributions. This feature arises mainly out of the π^* antibonding character of these orbitals and not directly from the absence of intra-orbital correlation.

The double-zeta wavefunction of Kunz has been shown to give good results in the estimation of the O_2 MDs, but in the case of NO a correlated wavefunction is necessary to account for the electron density shifts in forming this molecule.

CHAPTER 8 THE NEW MCP SPECTROMETER

They make no beautiful things,
but they make many clever ones...
It is not unlikely that they have
invented some of the machines that
have since troubled the world...

8.1 Introduction

Until recently spectrometers of almost all descriptions included in some part of their works a slit or aperture followed by a particle detector of some sort. These detectors respond only to the presence or absence of specific kinds of particles in the active region of the detector. Therefore in order to detect a spectrum as a function of some parameter x one must have a device to physically disperse the particles in proportion to their x value. If a slit is placed in the dispersion plane, then this defines a system which is sensitive to a particular value of the parameter x, and can be scanned through a range

of x by moving the slit.

The unfortunate aspect of this system is that the great part of the signal that does not pass through the slit is simply thrown away. This is tremendously inefficient since the process which is producing the particles is for the most part generating unused signal.

Some spectrometers have been built {Moore (1978)} to make more efficient use of the signal. These usually involve using arrays of detectors and multiple slits. However it rapidly becomes prohibitive in terms of cost and signal processing to use such methods, and perhaps only one order of magnitude increased efficiency can be attained.

8.2 MCPs (Multichannel plate arrays)

With the advent of MCP technology it now becomes possible to have a slitless detector and detect all the signal all the time. This device can be used to detect charged particles which can be dispersed in a plane as a function of some parameter x.

The reader may get a picture of the physical construction of an MCP by imagining thousands of drinking straws standing on end, packed tightly side by side, glued

together to form a disk or rectangle, and shrunk by a factor of 200. Next transmutate the straws into the special semiconducting glass used in channeltrons and the glue to ordinary glass and spray both faces with nickel or gold to make electrical contact: the result is an MCP.

Of course these devices are not made by this fanciful method, but rather by sophisticated new techniques of glass drawing and doping, which accounts for their high cost.

An MCP works by essentially the same principle as a channeltron (section 3.2.6). The difference is that an incident particle stimulates only one of the very tiny channels in the devices. The device output is therefore localised at the same place as the incident particle, except that there are now 10^3-10^4 output electrons for each incident particle. This is still too few electrons to be detected electronically, so the usual practice is to cascade two MCPs in series, giving 10^6-10^7 electrons output.

MCPs were originally developed as image intensifiers for use in military night-vision binoculars and in low light television tubes. At first production was limited to fairly small 25mm diameter disks, but with improved techniques 50 and 70mm diameter disks are now available. Indeed so useful are these devices that one or two companies are marketing MCP assemblies complete with mounting hardware and electronic signal processing units.

MCPs find a use in spectroscopy wherever charged particles can be dispersed as a function of scattering angle, energy, mass etc. There are even MCPs now which will detect photons of sufficient energy (UV or greater). The most common use to date of these devices in research is in electron spectrometers. An MCP is placed in the dispersion plane of the electrostatic analyser, so that electrons of a large range of energies can be detected concurrently.

8.3 Position-sensitive Signal Collection

Apart from their construction, the most difficult problem encountered in the use of MCPs is how to convert the position of the output pulse into an electronic signal which can be processed to reveal the spectrum. There are probably almost as many ways of doing this as there are spectrometers using the devices. Most applications use one of the following methods:

(1) Multiple discrete anodes: a collector plate divided up into small electrically-separate metal anodes is placed next to the output face of the MCP. Each collector anode is connected to its own preamp/amplifier/discrimator electronics. Position is decoded to within the area of one anode by the-

presence of a pulse on one of the output lines. Resolution is limited to the size of the anodes;

(2) Charge-coupled diode CCD: the output electron shower is converted via a phosphor screen to a burst of photons which are optically focussed onto an array of photosensitive diodes. The diodes build up a charge according to how much light falls on them over a given time period. At the end of the sample period the diode array is read out serially into some sort of storage device. Resolution limited by the number of elements in the photodiode array. Coincidence experiments cannot be done with this device; neither can individual events be accessed;

(3) Charge division: a collector made of a continuous resistive strip, or of discrete collector elements connected in series with capacitors or resistors is placed next to the MCP output face. Leads are attached to the ends of the strip and two charge preamps connected to these leads. The output pulse lands on the strip and sees two parallel paths to ground. The current down one side of the strip and through each preamp is inversely proportional to the impedance of that path to ground. The preamp output amplitude V is proportional to the total charge presented at the input. If the length of the strip is L and the pulse lands a distance l from one end, then that distance is obtained from the preamp pulse amplitudes by taking:

$$(8.1)\quad l = \frac{Lv}{v+v'}$$

This can be done by analogue divider circuits or by digitizing the pulse amplitudes and doing the calculation with a digital processor. An advantage of this method is that the resolution with a resistive strip collector is theoretically infinite and only limited by the size of the pores in the MCPs, and by the resolution of the digitizer. If a capacitor string is used then the resolution is normally limited to the size of the discrete elements; however, it is possible to obtain higher resolution if the output pulse is allowed to defocus slightly and span two elements of the discrete anode chain. This tends to smooth out what would otherwise be a staircase-like response function. Another advantage of this method over the CCD method is that the final computed l is not sensitive to variations in channel gain across the face of the MCP. The amplitude of the MCP output pulse would appear in both the numerator and the denominator of equation 8.1 and so cancels out.

I have chosen the third method, charge division through a capacitor string, for implementation in the new spectrometer. This is a proven technique {Van Hoof (1980)} and seemed to be the one which was both simple in concept and fairly cheap in execution. It is also the one which can

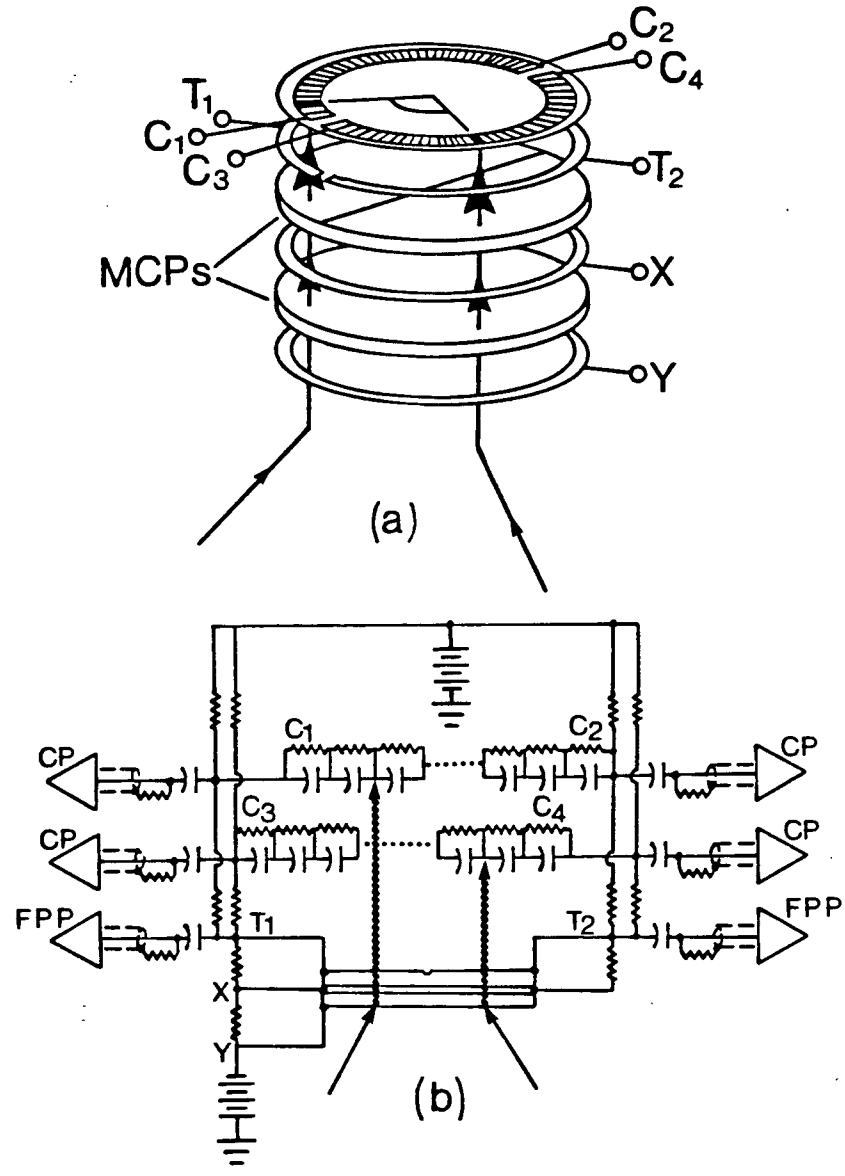

Figure 8.1(a) Exploded view of the MCP assembly.
(b) Schematic diagram of the MCP circuit.

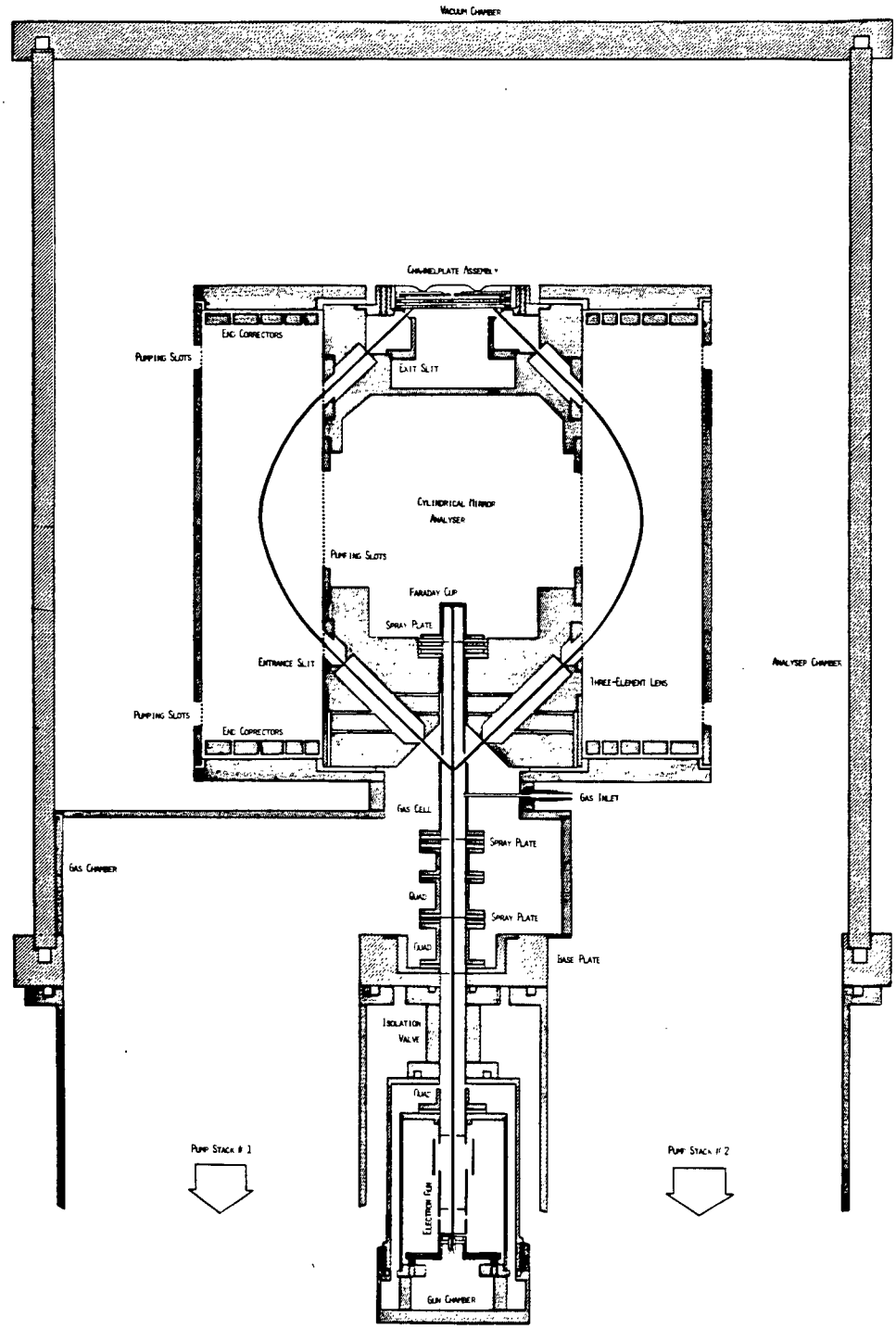

Figure 8.2 Schematic diagram (to scale) of the new binary (e,2e) spectrometer.

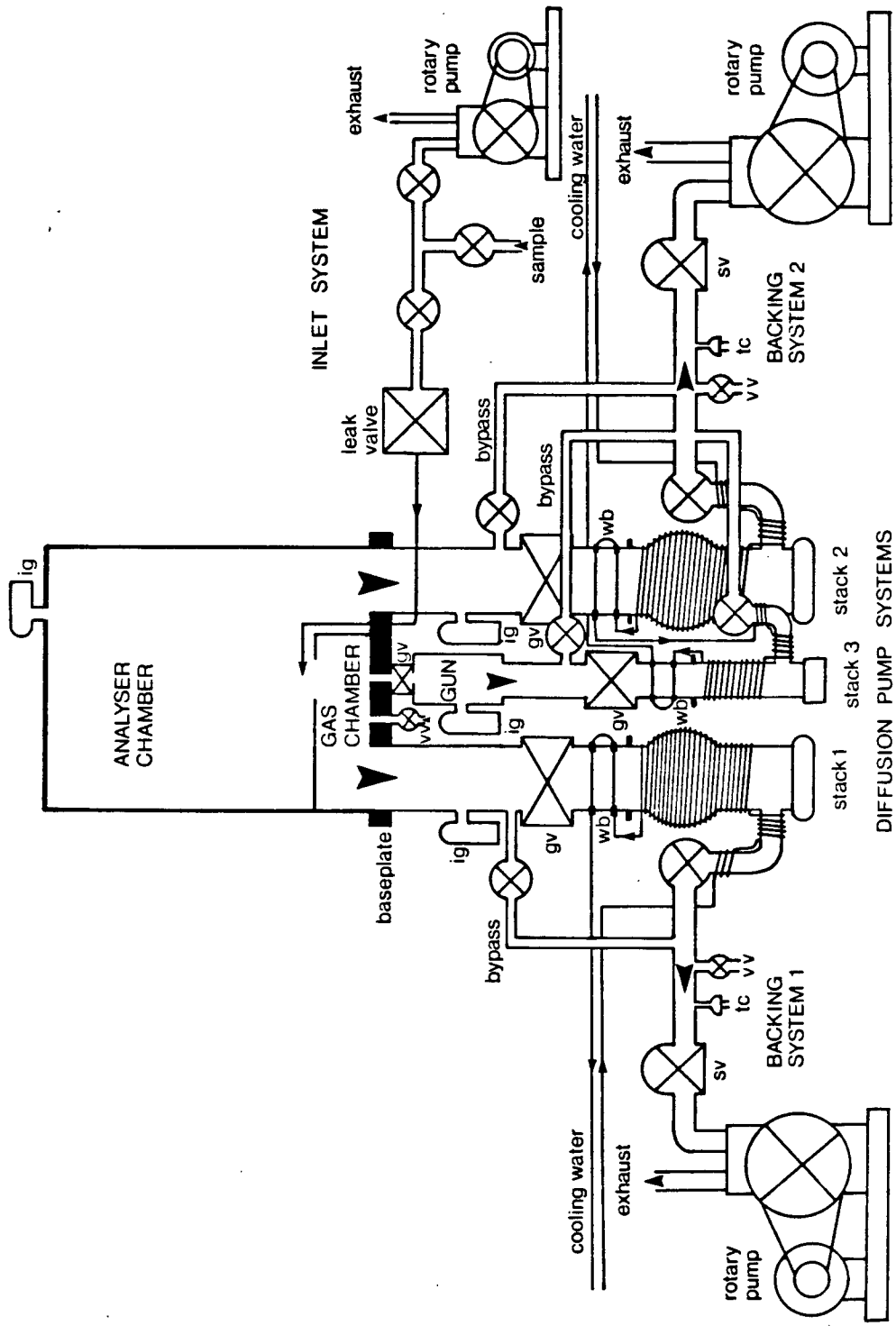

Figure 8.3 Schematic diagram of the vacuum support system for the new binary (e,2e) spectrometer.

Legend:

IG ionization gauge
VV vent valve
GV gate valve
SV solenoid valve
TC thermocouple gauge
WB water baffle

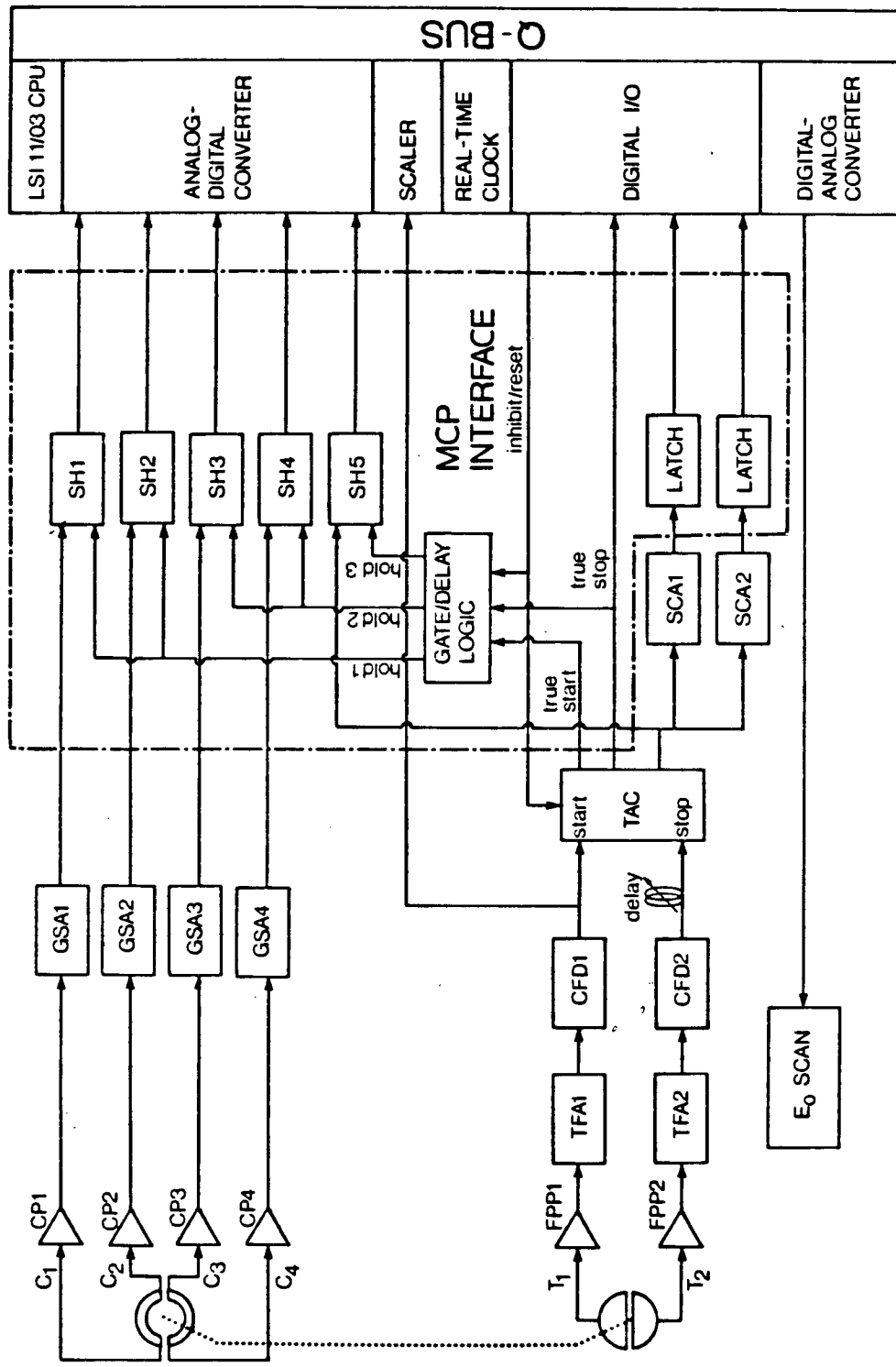

Figure 8.4 Block diagram of the signal-processing and computer electronics for the MCP outputs.

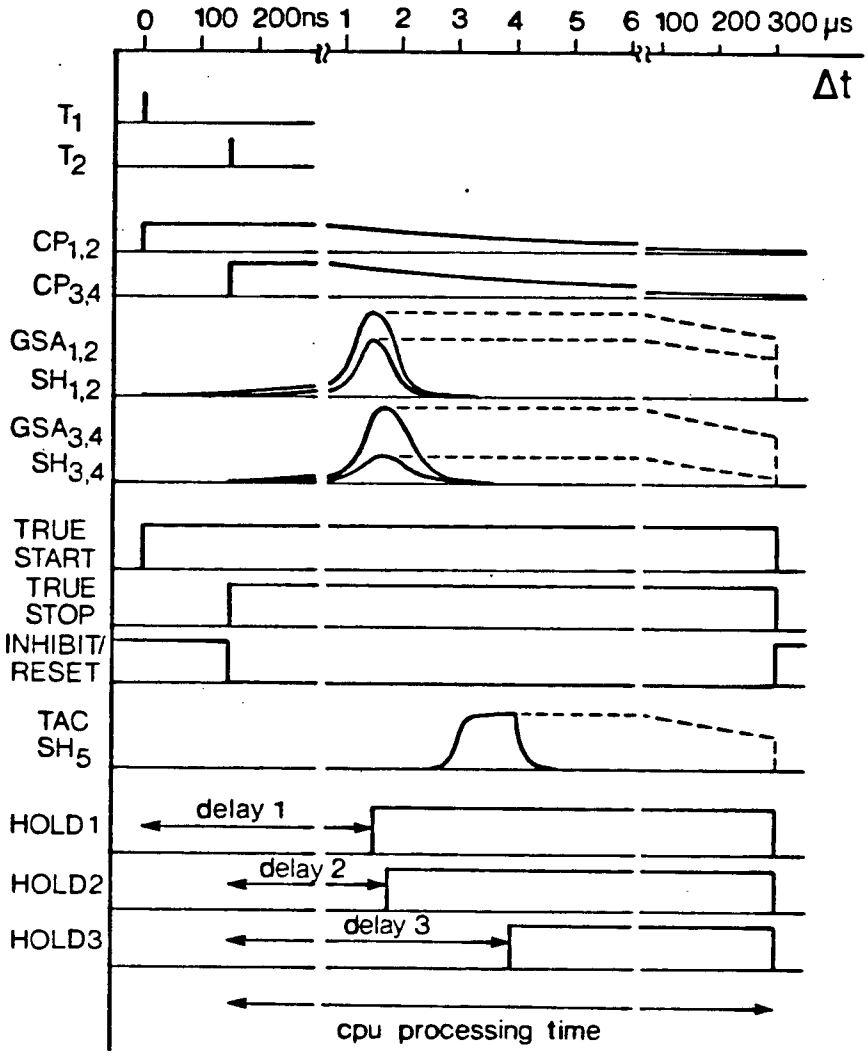

Figure 8.5 Timing diagram for the signals in the processing circuits.

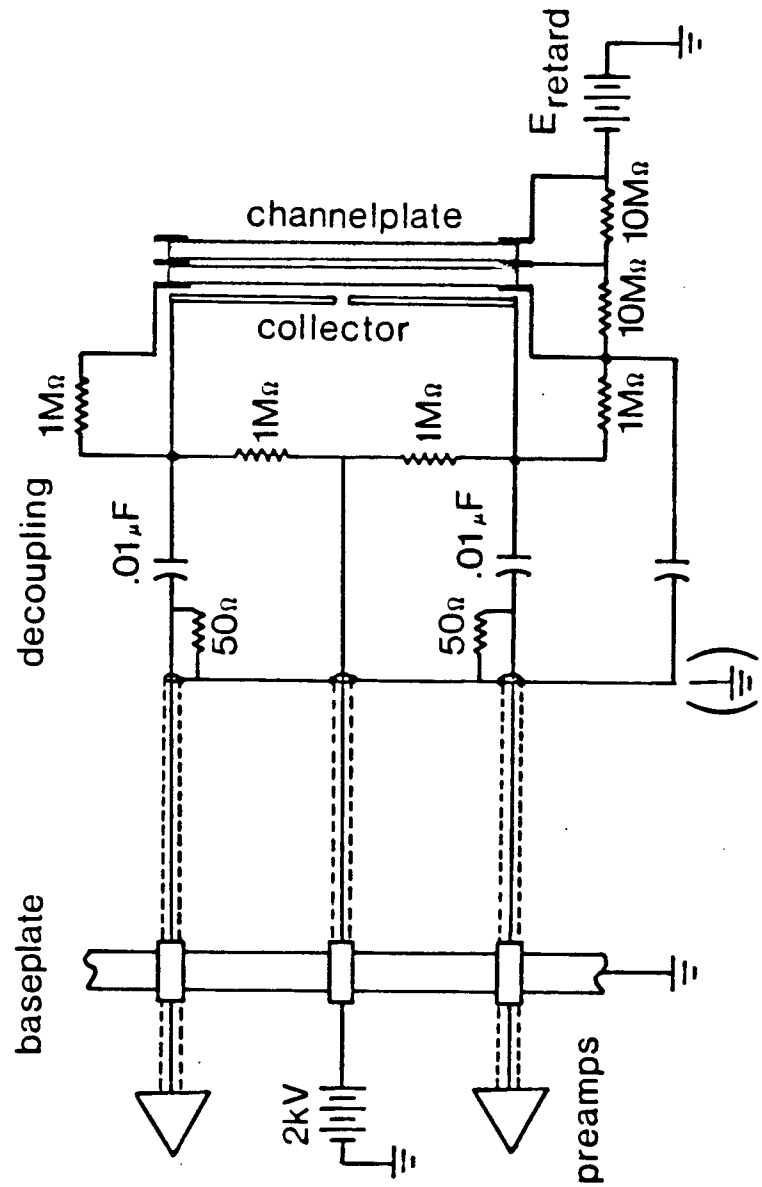

Figure 8.6 Initial test circuit for the MCP.

Table 8.1 MCP interface control lines

Device Bit	Name/Function
DRV11	Parallel 16-bit digital I/O
DRVCSR0	MCP interface inhibit/reset
DRVCSR1	BNC9010 remote/local
DRVCSR6	Enable interrupts
DRVCSR7	External event interrupt flag (TAC TRUE STOP)
DRVCSR2-5,8-15	not used
DRVIN0	SCA1 event
DRVIN1	SCA2 event
DRVIN2-15	not used
DRVOUT0	BNC9010 pulse/DC
DRVOUT1	X-Y plotter pen up/down
DRVOUT2,3	not used
DRVOUT4-15	BNC9010 digital amplitude word (BCD)
ADV11-A	16-channel 12-bit multiplexed analog/digital converter
ADVCSR0	Go bit - start conversion
ADVCSR6	Enable interrupt on conversion completion
ADVCSR7	Conversion complete
ADVCSR8-11	Channel select $0\text{-}17_8$
ADVCSR14	Enable error interrupt
ADVCSR15	Error flag
ADVCSR1-5,12,13	not used
ADVBUF0-11	12-bit signed conversion result
AAV11-A	4-channel 12-bit digital to analog converter
DACA0-15	Reference voltage for incident energy E_0 power supply
DACB,C0-15	X and Y deflections for scope display
DACD0-15	Reference voltage for angle scanning servo loop
KWV11-A	Real-time clock
KWVCSR0	Go bit - start timer
KWVCSR1,2	Mode
KWVCSR3-5	Clock rate
KWVCSR6	Interrupt on overflow
KWVCSR7	Clock overflow
KWVCSR8-15	not used
KWVBUF0-15	Clock count

easily be combined with the necessary coincidence detection circuitry.

8.4 The New Spectrometer Design

The design requirements for the new spectrometer, the vacuum system, the electronics and the computer system are given in the following sections.

8.4.1 The vacuum system

Triple differential pumping was a primary requirement for the new machine. The reasons are:

(1) The sensitivity of the MCP to noxious gases which can degrade the special semiconducting glass, and to high pressures of any gas which can lead to arc-overs through the very fine channels;

(2) If reactive gases are excluded from the region of the electron gun then oxide cathodes can be used instead of tungsten filaments.

Oxide cathodes are thin layers of barium oxides on a metal contact, indirectly heated. These electron emitters run cooler than tungsten filaments, and so the energy spread of the resultant electron beam is less. Where a tungsten filament might have a ΔE of 0.7-0.9eV oxide cathodes have

0.3-0.5eV. Differential pumping refers to the technique of dividing a vacuum chamber into several compartments with only a small aperture connecting them. If a pumping stack is attached to each compartment then one can maintain pressure differentials across the apertures of up to an order of magnitude. This allows three compartments: one with the gas all at relative high pressure, and the other two with the MCP and electron gun at low pressure.

The gas chamber and the analyser chamber both have 5-inch pumping throats leading to Varian VHS-4 diffusion pumps (the same type as on the old machine). The gun chamber has a 2½-inch tube leading to a small 3-inch diffusion pump. All three pumping stacks have gate valves and water traps. LN_2 cold traps are not necessary in the diffusion pump stacks. A ½-inch gate valve between the gun chamber and the gas chamber allows access to the electron gun, while still keeping the rest of the system pumped down.

The diffusion pumps are backed by two large rotary pumps: one for the analyser and gun pumps, and one for the gas chamber pump. Four ports are provided for ion gauges: one on each pumping stack and one on top of the chamber.

8.4.2 The electron gun

The same type of gun body is used in the new machine as in the old (Cliftronics CE5AH), except that a mounting for oxide cathodes has been substituted for tungsten filaments. The beams from this gun are not as good as the other in the old machine (10-30μA, 90 per cent focussed) but this is partly due to the longer distance the beam must travel, and the fact that it must pass through a ½-inch gate valve.

8.4.3 The beam steering unit

This unit is similar in all respects to the one in the old machine, except that an extra set of deflectors has been installed between the gun and the gate valve. The first spray plate after the gate valve defines the aperture for differential pumping between the gas chamber and the gun chamber. The last spray plate and the Faraday cup are mounted in the lens.

8.4.4 The gas cell

Again, similar in most respects to the one in the old machine, the new gas cell is made in two parts: the lower half is fixed to the top of the beam steering unit, and the upper half to the lens. The gap between the two halves allows the scattered electrons to pass into the lens. The gas cell defines a field free scattering region, and permits

a local buildup of gas density.

8.4.5 The cylindrical mirror analyser

In this spectrometer the analyser is a full CMA mounted coaxially with the gas cell and the conical lens. This analyser has almost perfect cylindrical symmetry, so all scattered electrons emerging from the collision volume at $\theta=45°$ and with energy E=E{retard}+E{pass} will pass through the exit slit of the analyser regardless of azimuthal angle. (The only lapses from perfect cylindrical symmetry are in some small support columns in the inner cylinder, and pumping slots cut in the inner and outer cylinders. These pumping slots have been covered with a 99 per cent transparent copper mesh to preserve the electric field.) This means that (e,2e) electrons of all azimuthal angles will be transmitted to the detector, and that all orientations of a given azimuthal angle will also be transmitted. This gives an upper limit to the improvement in efficiency over the old machine of a factor of about 500 (assuming an acceptance half-angle for the old spectrometer lenses {Hood (1977)} of about 4°). Such an increase in the data rate means that data acquisition can be cut from a period of days down to hours. The scattered electron trajectories through the lens and analyser describe a surface which is similar to that of a football (American-style). This image may be helpful in visualizing

the workings of this spectrometer.

It is not possible to achieve even perfect first order focussing (let alone second order focussing) due to various physical constraints in the design of the spectrometer; however, as is explained in the next section, good focussing attributes are not necessarily a high priority in this application. Since the analyser entrance angle must be 45° (the same as the θ scattering angle), this requires that the sum of the radial components of the distances from the source and image foci to the inner cylinder be 3.4, and the axial component of the distance between the foci be 9.2, both in units of the inner cylinder radius {Risley (1972)}. Due to the size of the conical lens and the MCP detector assembly, the minimum radius of the inner cylinder is 2.5 inches, which means that the height of the analyser would have to be at least 20 inches, and the radius of the outer cylinder about 25 inches, which is too large for our machine shops to handle.

Electrons of the correct energy are transmitted from an annular entrance slit 2cm inside the inner cylinder to an annular exit slit 10cm above the entrance slit and 3cm inside the inner cylinder. The radius of the inner cylinder is 2.5 inches, and the outer cylinder 5 inches. These proportions for the CMA mean that it will have approximately 0.5 per cent resolution, i.e. $\Delta E\{pass\}/E\{pass\}=0.005$ {Risley (1972)}; since the MCP detector is expected to

improve the data rate so much, there is no reason not to try for better energy resolution. The design of the CMA means that the particle beam will pass approximately half way between the elements of the CMA at the point of largest radius: this helps to make the electrons insensitive to surface effects near the analyser elements. The choice of the position of the output slit is intended to allow the analysed electrons to diverge slightly before striking the MCP. This ensures that the count rate per unit area of the MCP will not exceed 1 count per channel per second. Above this rate the device starts to saturate.

8.4.6 The conical lens

There is nothing in the literature on the design of an electrostatic lens to focus an object from a point on the beam axis to an annular image around the beam axis, where image and object define a 45° cone. Lacking the skills to calculate the structure of such a beast, and for want of any better ideas, it was decided to build a three-element conical lens in the same proportions as the old spectrometer lenses. This device would have some sort of transport properties (certainly not the same as the old lenses) which could be optimized by suitably adjusting the voltage applied to the middle element. It was not understood until after it was built, however, that this sort of lens would also deflect the scattered electrons into a slightly steeper or

shallower cone. Consider: the electric field gradient at the lens gaps will not be the same in the top and bottom halves of the lens assembly (see figure 8.1) because the volume elements near the upper and lower gaps are different; the radial distances and polar angles from the central axis are slightly different. This implies that the action of the resulting electric field will not be that of a pure lens (as in three element tubular lenses) but will also behave partly like a prism, deflecting the scattered electrons away from their original trajectory in the θ dimension. In order to compensate for this, the upper and lower parts of the middle lens element have been wired into a circuit similar to those supplying the beam deflector voltages; there is one potentiometer to set the potential midway between the two elements, and another to set a positive and negative offset with respect to the center potential, which is to be applied directly to the elements. In this way it should be possible to correct for deflection introduced by the lens.

In my view the best solution to the lens problem (see also section 3.5) for this and other (e,2e) spectrometers would be to use a spherical retarding field for the scattered electrons, with no lens magnification effect or polar angle deflection. Such a field could be established with concentric shells or grids. When there are no electron optical effects the angular acceptance and the effective θ angle would be defined by the physical construction alone,

without having to worry about lens magnification or focussing effects. (It would be important to reduce magnetic fields in such a device, in order to be able to do without deflectors in the lens.)

Retarding lenses serve a purpose which is, in fact, partly contradictory to our intent in binary (e,2e) spectroscopy. In other types of spectroscopy lenses were intended to retard scattered electrons from their scattered energy down to a lower energy where they could then be analysed with higher resolution. They also enabled one to focus scattered electrons from a large volume of space on to the small entrance aperture of the lens; the larger the collision volume, the greater the signal rate (gas and beam density being equal) which is almost always a desirable thing. In such types of spectroscopy it is usually inconsequential that this large collision volume implies indeterminate scattering angles, as angular resolution was not a priority. However, in binary (e,2e) it is very important that the polar scattering angle be sharply restricted around $\theta=45^\circ$ in order to accurately determine q at low azimuthal scattering angles (see figure 3.7), and it is also important to have good ϕ resolution. This is why one really only needs a retarding device to improve energy resolution, and not a focussing device with its inherent magnification of the image. In this respect the University of Maryland spectrometer design {Moore (1978)} is an

improvement, as it has no lenses. However, neither does it have a retarding device, so energy resolution may be limited.

8.5 The New Binary (e,2e) MCP Detector

8.5.1 Construction

The MCP assembly design is shown in exploded view in figure 8.1. Two 52cm MCPs (Mullard G25-501A) are used in chevron formation, spaced 0.010 inches apart, followed by the collector spaced 0.010 inches from the output face of the second plate. The microchannels are not exactly perpendicular to the face of the plate, but are canted slightly. Chevron formation means that the two plates are mounted so that the channels of one plate slope in the opposite direction to the other. This attempts to prevent secondary ion feedback, in imitation of the curvature of channeltrons. Electrical contacts to the plates are made with silver rings, and insulation is done with nylon or Teflon. The whole assembly is gently sandwiched together and secured with a spring clip.

The detector must be electrically divided in two in order to perform the coincidence determination between the

scattered electrons. One scattered electron strikes one half of the detector and the second strikes the other side. With a fine sandblaster, the nickel plating of the output face of the second plate was carefully removed along a diameter to electrically separate the two sides. Contacts T_1 and T_2 are made to each half: when an electron triggers the detector this produces as a momentary depletion of charge at one of the nickel contacts and hence a positive pulse in one of the T_1 or T_2 lines.

The collector is to be a ring of discrete anodes (figure 8.1) designed to line up with the intersection of the trajectories of the electrons leaving the analyser with the input face of the MCP detector. The anodes are connected with capacitors in series to form two half-circle strings. Connections C_1,C_2,C_3, and C_4 are made to the four ends. The two collector strings are also aligned physically with the two halves of the MCP output face. Each capacitor has a resistor wired in parallel to slowly drain away accumulated charge. The values of the capacitors are 100 pF and the resistors 10^6 ohms, giving a time constant of RC/n=2.5ms with n=40 discrete anodes per strip. This is well in excess of the initial processing time of the collector pulses, so no degradation of the signal should occur.

The collector is to be made from a suitably etched, two-sided fiberglass printed circuit board. The discrete anodes would be on the MCP side of the PC board, and the

resistor and capacitors on the other. Sundry components for providing the MCP high voltage bias, and for decoupling the timing and collector signals will also be mounted here.

8.5.2 Signal processing

The MCP assembly produces six pulses when there is a coincidence: T_1, T_2, C_1, C_2, C_3 and C_4. The T_1 and T_2 lines carry sharp positive pulses for the coincidence determination which is done using the same TAC/SCA method as in the old machine (see section 3.4.3). Lines C_1-C_4 carry an amount of charge which depends on where the two electrons land. If one can digitize the amount of these charges then the azimuthal angle between the two electrons can be computed as:

$$(8.2)\quad \phi \propto \frac{C_1}{C_1+C_2} + \frac{C_3}{C_3+C_4}$$

This result can be used as a pointer to a storage location. The accumulated count at that location is then incremented or decremented according to whether the coincidence determination has shown a true coincidence or a random pulse pair. In this way a spectrum of the azimuthal distribution of signal is obtained. It will be necessary to multiply this spectrum by a ramp of the form:

$$(8.3)\quad \frac{180^\circ}{180^\circ-\phi}$$

since there is the possibility which increases with ϕ that the two (e,2e) electrons might both land on the same half of the MCP detector, and so would not be detected.

The signal processing for the C_1-C_4 outputs is to consist of four sets ORTEC 142AH charge preamps (CP) followed by ORTEC 485 Gaussian Shaping Amplifiers (GSA). A charge pulse appearing at the CP input is capacitatively decoupled from the high voltage line and integrated. The CP output is a pulse with a rise time of the width of the input charge pulse and a fall time of about 500μs. Data rates of more than $(500\mu s)^{-1}=2000s^{-1}$ are not a problem since CP output pulses may pile up with no loss of signal.

The GSAs contain special shaping networks which respond to steps in the input voltage, such as are provided by the CPs. The GSA output is a smooth, uniformly shaped semi-Gaussian pulse 3μs wide whose amplitude is directly proportional to the size of the input step. The use of the GSA means that the system should be insensitive to any change in the preamp output rise time due to changing widths of the charge pulse, or distortion of the charge pulse as it travels down the capacitor chain, and the shape and uniformity of the output pulse allow it to be precisely digitized.

8.5.3 MCP/computer interface

The interfacing of the six signal lines plus many data and control lines between the spectrometer and the computer is done with a custom built unit (MCP Interface) designed and constructed in the UBC shops to my specifications. A block diagram for the interface is given in figure 8.4.

The MCP Interface data acquisition logic is idle until it is 'woken up' by the presence of a high logic level simultaneously in the TAC TRUE START and TRUE STOP outputs. These two signals indicate that the TAC has detected a coincidence on the T_1 and T_2 lines, and that the computer may expect valid signals on the C_1-C_4 lines. The interface then does several things:

(1) An interrupt flag is set in one of the computer's digital I/O registers. This flag interrupts the CPU and transfers control to a software routine to process the (e,2e) event;

(2) The TAC is inhibited from processing any more START and STOP signals until the interface is reset by the computer;

(3) An internal 'valid event' logic level is set high, which allows the five sample/hold units to sample the TAC and GSA output pulses when three internal timers indicate these pulses have reached their peak.

The interface logic must supply a 'hold' signal to the

sample and hold (SH) circuits at the precise instant that the TAC and 485 pulses reach their peak. Normally the SH output 'tracks' the input, but when a 'hold' signal is received, the output is held constant at the value of the input at that instant (see figures 8.5 and 8.6). The TAC TRUE START output leading edge is used to start an internal clock K_1, which measures out a fixed time interval. This interval can be adjusted to span the time the C_1 and C_2 GSA output pulses take to rise to their peaks. At the end of this time a 'hold' logic line is set high, and if the 'valid event' line is also high the SH circuits SH_1 and SH_2 are switched from 'track' to 'hold'. Similarly, internal clock K_2 times from the TRUE STOP leading edge to the peak of the C_3 and C_4 GSA outputs, providing the 'hold' signal for SH circuits SH_3 and SH_4. The 'hold' signal for SH_5 (the TAC output SH circuit) is also timed by K_3 from the TRUE STOP leading edge. The reason for having several timers is that the T_1 and T_2 pulses are separated in time by an amount Δt from zero up to the range of the TAC, which may be several hundred nanoseconds. This is enough time for the GSA output to be significantly below its peak value. The TAC output pulse of course has a different offset from T_1 and T_2 than the GSA outputs, so it must have its own timer.

The outputs of the five SH units are connected to a 16-channel, multiplexed, 12-bit voltage digitizer board in the computer, which would be controlled by a software

interrupt service routine.

The SCA output pulses latched by two flip-flops in the interface and the resulting logic levels are connected to two input lines of a 16-bit digital I/O board in the computer.

The entire logic system in the MCP Interface can be reset by clearing a special bit in the digital I/O board, and can then be enabled by asserting this bit. The logic system is reset and enabled after every interrupt.

In addition to signal and data lines there are control lines for setting the voltage of the incident energy power supply, for setting the angle (of the angle scan system in the old machine) and for producing a display of spectra on an X-Y oscilloscope. These four voltages are supplied by a four-channel digital-to-analog converter (DAC) from 12-bit numbers loaded into the DAC registers by the computer.

The channel advance and reset functions of the old ORTEC 4610 Program Control Unit are emulated in the computer-based system in software, using a real-time clock device. A fixed time base will be available, and also a feature allowing the operator to tie the dwell time per channel to the total singles rate in the two T_1 and T_2 channels.

Sundry other output lines on the digital I/O board

include a plotter pen up/down bit and several lines to control the output amplitude of a remote-programmable pulse generator (Berkeley Nucleonics 9010). Such a pulse generator could be used (among its myriad other uses) to do computerized self-test and self-calibration of the MCP position decoding system. There is also unused space in the digital I/O board which could be used to read in a number from a digital voltmeter and so provide self-calibration of the incident energy power supply. The function of all the lines in the computer interfacing is summarized in Table 8.1.

The MCP interface has been in operation satisfactorily on both spectrometers using all its functions except the C_1-C_4 digitizing lines.

8.5.4 The computer system

The computer system is based on a PDP LSI11/03 processor manufactured by the Digital Corp. The system peripherals include the DEC VT100 video terminal, the MDB DSD-440 dual floppy diskette drive mass-memory, and an IDS-460 graphics impact printer and all the interface boards described above. The system was purchased from the Transduction Co. (Toronto), with the exception of the printer. The software runs under the DEC RT-11 operating system: this provides a foreground/background environment for user programs in which it is possible to have a

foreground job (controlling the spectrometer and performing data acquisition) running concurrently with a background job (which could be performing, for instance, data analysis or a variety of other functions). This operating system was a major factor in the choice of the LSI11/03 computer system, and means that the computer, which represents a sizeable investment, is not completely tied up when it is acquiring data, unavailable for anything else.

RT-11 includes a complete set of utilities for creating, maintaining, and manipulating files on disk, plus compilers for the FORTRAN and BASIC high level languages and the MACRO assembly language. A portfolio of specialized programs has been written for binary (e,2e) applications: these include an extensive library of plot subroutines for the graphics printer, a foreground (e,2e) data acquisition program, a background program which allows communication with the foreground and manipulation of data files, data plotting programs, etc. This computer is not suitable, however, for the programs which compute momentum distributions, density maps and Gaussian least-square peak fits: these require a high-speed, large memory, number-crunching processor to be convenient, for which the Amdahl V7 in the UBC Computing Centre is entirely appropriate. It is possible to transfer data between the lab and the Computing Centre on 8-inch floppy diskettes conforming to the IBM standard.

Binary (e,2e) data files stored on diskette are structured in four 256x16-word blocks: the first block contains labels and spectrometer parameters pertinent to the run; the second and third blocks contain the values of the independent spectrum variable (voltage, angle or time) as 32-bit floating point numbers; the fourth block contains the accumulated data. The operator is able to specify the type of scan, and all the fixed scan parameters interactively at the video terminal. At present only the true coincidence rate is recorded in the data file, and only a single operating mode at a time is available (i.e. binding energy spectrum, angular correlation, time spectrum or single (e,e) scattering), but plans are afoot to modify the data acquisition program so that the true and accidental coincidence rate and the random pulse pair rate are recorded separately (to allow the calculation of the statistical accuracy of the measurement), and to allow concurrent data acquisition in all modes. The advantage of the latter modification is in maintaining the proper relative absolute intensity of each binary (e,2e) structure with respect to its fellows, rather than having to compute renormalization factors from binding energy spectra after the data is recorded.

8.6 Preliminary Testing

8.6.1 The vacuum system

After tracking down one or two leaks the base pressure measured on the large pump stacks was $7x10^{-8}$torr, measured at the gun chamber it is $1x10^{-6}$torr and on the top of the chamber it is $5x10^{-7}$torr. When enough gas is admitted to raise the ambient pressure one order of magnitude in the gas chamber, the analyser and the gun chamber pressures only go up one-tenth this amount, indicating that the differential pumping is working satisfactorily.

8.6.2 The electron gun

The installation described in section 8.4.2 gives an adequate beam at 400 eV (10-20μA, 90 per cent focussed). At 1200eV it improves to 20-30μA and 95 per cent focussed. The gate valve isolating the gun is a great convenience: since oxide cathodes must not be exposed to air once they are activated it is possible to open the main chamber but still keep the gun under high vacuum.

8.6.3 The analyser

Initial testing of the analyser was done with two Mullard B318AL channeltrons mounted at the analyser exit slit at an azimuthal angle of 11°. The MCPs were wired into a circuit similar to figure 3.4b. E{retard} was set to zero to eliminate problems with deflection of the scattered electron by the lens. The spectrum of 200eV electrons scattered elastically from helium with 200eV pass energy set in the analyser gave an elastic peak of 0.5eV FWHM which is a significant improvement in resolution over the 0.8-1.0eV FWHM obtainable on the old machine. It cannot be established with this method whether or not the analyser transmission is isotropic as a function of ϕ.

8.6.4 MCP testing

The first tests with the MCP were made with a simplified collector consisting of two brass half-disks mounted so as to line up with the dividing strip on the MCP output face. The brass disks should collect all the signal in each half of the spectrometer, essentially yielding a binding energy spectrum integrated over angle. The first test circuit with this collector is shown in figure 8.5.

In an attempt to improve the characteristics of the MCP pulses at the preamp T_1 and T_2 inputs, a novel signal feedthrough arrangement was devised. Individual

metal/ceramic BNC feedthroughs were dispensed with, and single lengths of coaxial cable were used instead, running without a break straight through a flange on the baseplate. Vacuum integrity was maintained by carefully sealing the cables in the flange with high-quality, low vapour pressure epoxy resin glue. Combined with careful impedance matching and cable termination, this arrangement virtually eliminates all ringing on the signal. It is not necessary to use an impedance-matched collector anode, as has been devised by other groups.

This circuit did, however, give huge coupling problems, between the T_1 and T_2 signals. This was not understood for a long time, and many different modifications were tried in the attempt to eliminate this problem. It was finally realized that the MCP output face was only at virtualAC ground, not a true AC ground, and also that coax cables do not transmit the voltage applied to the central conductor alone, but rather they transmit the difference voltage between the inner and outer conductors. It is seen from figure 8.6 that the positive pulse generated on the MCP output face at the instant the electron shower leaves is capacitively coupled to both coax shields, and so produces a negative pulse at the preamp inputs which is indistinguishable from the normal MCP output pulse.

The remedy was painfully simple: the coax shields must be grounded at both ends, and the MCP output face must be

tied to the AC signal ground potential. That the new feedthrough arrangement and signal decoupling works was established by a seven-second observation of the preamp output pulse shape on an oscilloscope. Then the high voltage started breaking down, and the resulting transients destroyed the preamp transistors. Subsequent examination of the spectrometer showed that the breakdown had occurred in several of the MCP channels, rendering the device at least temporarily and probably permanently inoperative. The only way to resuscitate the device is to disconnect the faulty channels electrically from the rest of the device and this necessitates removing the nickel contact film from those channels - a ticklish business at best.

It has been learned through painful experience that these MCP devices are not as rugged as had been thought. It is recommended that extreme care be taken in handling, storing, and operating these devices. It should be noted that the shelf-life of MCP devices is not infinite at atmospheric pressure, even when stored with dessicant. Unidentified crystalline growths which could not be removed by solvent appeared on the faces of our device after being stored for about a year. It is likely that the presence of these growths in combination with fine dust particles caused the breakdowns.

Measures taken in the care of these devices must include:

(1) Storage for long periods of time should be in a hydrocarbon-free vacuum system (i.e. a container with O-ring seals which can be evacuated by a pump with traps for oil vapours, and then closed off);

(2) Contact with ordinary dust-laden laboratory air should be avoided as much as possible. The device and its mounting can be cleaned and remounted under dry nitrogen using glove box techniques. High purity solvent (n-propanol) is recommended for cleaning, and a dry nitrogen gas jet can be used to blow any remaining dust away;

(3) Once installed in the spectrometer the system should be pumped down for several days in order to remove adsorbed water vapour from the MCP channels. The walls of the channels represent a considerable surface area, and pumping within the channels is constricted due to their extremely small diameter.

CHAPTER 9 CLOSING REMARKS

'Have you thought of an ending?'
'Yes, several, and all are dark and unpleasant,' said Frodo.

The value of binary (e,2e) spectroscopy both in itself in providing fascinating and instructive insights into the electronic structure of molecules, and as a yardstick for judging the quality of theoretical wavefunctions has been demonstrated in this thesis. It has been shown that the binary (e,2e) technique is capable of making fine distinctions in the shape of valence orbitals of small molecules, and can be used to great advantage in testing the quality of calculated wavefunctions, where it is seen that the test of calculated energies against experimental ones cannot always be relied on as an accurate indication of improvement in the wavefunction. The technique is yet in its infancy, with much molecular structure still unexplored.

The work on H_2S, CO_2, NO, and O_2 shows that the momentum distribution, while obscuring some information because it is a spherical average, nevertheless reveals more about the nature or character of the electrons of the

molecule than does any other experimental probe. It sharply delineates the differences between the many types of molecular orbitals: non-bonding, atomic-like MOs, valence σ-, π-, and π*- bonding MOs in diatomics, π*-antibonding MOs in triatomic CO_2, and so on, and also the difference between results of various methods of calculating the wavefunctions for these systems.

The technique has revealed hitherto unsuspected structure in the ionization of inner valence electrons (Chapters 4, 5 and 6) and has gratifyingly confirmed the theoretical predictions of the many-body Green's function method put forward by L.S. Cederbaum and coworkers. Owing to the complexity of this structure it is evident that accurate calculations intended to predict this structure should in future utilize similar techniques going well beyond the Hartree-Fock limit. This sort of data is less easily obtained from PES or XPS, and also, when obtained, is less informative, lacking the momentum distribution information which is the signature of the originating orbital.

The limitations of the technique are threefold:

(1) Energy resolution restricts the determination of momentum distributions to those orbitals which can be resolved in the binding energy spectrum, or deconvoluted with adequate precision.

(2) Angular uncertainty and resolution effects distort or obscure the momentum distribution near θ=45°, near

ϕ=0°, and where there is sharply changing intensity. This makes it difficult to observe accurately one of the more interesting regions of the momentum distribution around q=0.

(3) Targets must be gaseous and stable, and in fairly plentiful supply. This rules out very reactive gases, and ones where large quantities cannot be produced at once. It also limits the measurement of the MDs of transient species.

It is hoped that the new MCP spectrometer (Chapter 8), when completed, will reduce these limitations. Since this spectrometer is vastly more efficient it will be feasible to sacrifice signal for better energy resolution. The detector has, in principle, infinite angular resolution, and so it remains only to ensure that the polar scattering angle is accurately known. The differential pumping should allow the use of noxious gases as targets, but even so it is unlikely that measurements on transient species will be viable for some time.

There is a wide range of molecules not yet studied. It would be interesting to carry out binary (e,2e) studies on the following:

(1) Some transition metal compounds, to look at genuine d-electrons. VCl_4 and $TiCl_4$ would be feasible, and perhap some of the simple transition-metal carbonyls ($Fe(CO)_6$, etc.), as the d-orbital is well

separated energetically from the other orbitals. It would be interesting to see whether here the outermost d-type MO is as hard to treat theoretically as is the outermost orbital in the first-row hydrides;

(2) Systems where there is more complex nodal structure than just π^*-antibonding orbitals. Some of the higher unsaturated molecules, or systems with more group VI and VII atoms to populate higher levels may fit the bill here;

(3) Systems with a higher degree of asymmetry;

(4) Systems where there might be a possibility of observing bond oscillation, for instance C_3O_2.

In addition to studying more interesting targets, we need to look more closely at the information the momentum distribution carries. This has been started with the auto-correlation function B(r) developed by the Maryland research group {Tossell (1981)}, and with the q{max} and q{½max} vs $IP^{1/2}$ plots in this thesis.

It should be possible to measure $\langle q \rangle$ and $\langle q^2 \rangle$ by integrating the measured momentum distributions directly:

$$(9.1)\quad \left\langle q^{n} \right\rangle = \frac{\int dq\; q^{n+2}\; F\{i\}(q)}{\int dq\; q^{2}\; F\{i\}(q)}$$

assuming that σ\{Mott\} had little effect, and that the resolution-sensitive q=0 region would be weighted out by the

q^2dq volume element factor. This would then enable one to obtain (in the HF limit and under Koopmans' approximation) the kinetic and potential parts of the orbital total energy as:

$$T = \langle p^2 \rangle / 2$$

$$\epsilon = -IP \tag{9.2}$$

$$V = \epsilon - T$$

which should afford further insight into molecular electronic structure.

A recent accurate determination of the momentum distribution of atomic hydrogen {Lohmann} where the wavefunction is exactly known affords the opportunity to test this proposition. The measurement, done at incident energies of 400, 800, and 1200eV in the range $0<q<1.5a_0^{-1}$, shows an excellent fit to the curve $(1+q^2)^{-4}$, which is the functional form one expects from the $\psi=\exp(-r)$ hydrogen atom wavefunction. The expectation value of the nth power of p in this wavefunction is given by:

$$\left\langle p^n \right\rangle = \frac{\Gamma\left(\frac{n+3}{2}\right)\Gamma\left(\frac{5-n}{2}\right)}{\Gamma\left(\frac{3}{2}\right)\Gamma\left(\frac{5}{2}\right)} \tag{9.3}$$

which predicts $\langle p \rangle = 8/3\pi = 0.85$ and $\langle p^2 \rangle = 1$. Numerical evaluation by trapezoid integration of equation 9.1 with the experimental data gives the result $\langle q \rangle = 0.86$ and $\langle q^2 \rangle = 0.98$.

To reach this result it was necessary to add a tail to the experimental data beyond q=1.5 of the form $(1+q^2)^{-4}$. As was found in previous work {Tossell (1981)} it is necessary to have highly accurate data up to at least q=4.0 in order to get meaningful results from integrations of this kind.

Measurements of adsorbed gases on surfaces have recently gained a lot of attention and one naturally wonders if binary (e,2e) could be adapted to such targets. An indeed fascinating and valuable ability would be the observation of how the orbitals of a gas molecule distort when in contact with a metal surface. However, in my opinion, it is not likely that we shall soon be able to sufficiently distinguish energetically the valence electrons of the adsorbed gas molecule, or atom, from the conduction electrons of the metal substrate. This leaves us with the core electrons: it may be possible to estimate the surface geometry of the adsorbed atoms by looking for the strong bond oscillations that will be seen in an extended, ordered array of adsorbed atom core orbitals. The plane wave approximation however is certain to be inadequate for core orbitals if the usual scattering conditions are used, and it will be necessary to go to very high incident energy (which will lead to angular resolution problems) or else somehow account theoretically for the distortion of the free-electron waves, in order to obtain meaningful data. Multiple scattering effects may also be a problem. The great

advantage of the binary (e,2e) technique over some other surface methods, it must be remembered, is that of orbital selectivity, which means that the actual scatterer is a much simpler thing than in, for instance, LEED (low energy election diffraction) studies, where whole atoms are the scatterers. The only other comparable techniques are SEXAFS (surface extended X-ray aborption fine structure), and these require an elaborate data analysis procedure. It may be that the advantage of orbital selectivity will be found to outweigh the difficulties.

Finally, I hope that this work has been instrumental in introducing momentum space chemistry (Chapter 2) to the ordinary chemist, and that, with some practice we will gain some ease and familiarity with momentum densities and momentum distributions. The use of position and momentum density maps has been shown to be of great help in understanding the shapes of momentum distributions.

> They found him all alone in his little room. It was littered with papers and pens and pencils; but Bilbo was sitting in a chair before a small bright fire. He looked very old, but peaceful, and sleepy.

Leaves 265 and 266 missed in page numbering

APPENDIX A GLOSSARY

> Hobbits delighted in such things, if they were accurate: they liked to have books filled with things they already knew, set out fair and square with no contradictions.

A.1 Symbols and Units

α Exponent of a Gaussian basis function, proportionality

$\delta(x-x_0)$ Delta function

$\delta\tau$ FWHM of the (e,2e) coincidence peak in a time spectrum, uncertainty in time

$\delta\{mn\}$ Kronecker delta

Δt Time difference

ϵ Binding energy

κ Momentum vector in centre of mass coordinates

μs Microseconds

ν Frequency, vibrational quantum number

ω Energy parameter of the Green's function

Ω Units of electrical resistance (ohms)

$\Omega(\underline{r})$ Polar angles of the vector $\underline{r}$

ϕ Azimuthal scattering angle, azimuthal coordinate

$\phi\{Jj\}(\underline{r}), \phi\{Jj\}(\underline{p})$ The jth basis function on atom J in R- and P-space

Φ The final state of the entire scattering system

$\psi\{i\}(\underline{r}), \psi\{i\}(\underline{p})$ The ith molecular orbital in R- and P-scace

Ψ The initial state of the entire scattering system

$\Psi_0(N)$ Target initial N-electron ground state (Slater determinant)

$\rho\{i\}(\underline{r}), \rho\{i\}(\underline{p})$ Probability density of the ith molecular orbital in R- and P-space

Σ Summation

$\underline{\underline{\Sigma}}(\omega)$
Self-energy part in the energy representation

τ Time, dipole matrix element

θ Polar scattering angle, polar coordinate

$\Phi\{i,N-1\}$
Target final N-1 electron excited state (one electron missing from orbital i)

$\underline{\nabla}$ Grad

$^{\circ}$ Degrees

* Complex conjugate

a Index of atom

a_0 Distance in atomic units

a_0^{-1}
Momentum in atomic units

a*{i}
Creation operator of a particle in state i

a{i}
Annihilation operator of particle in state i

au Atomic units

b Basis function index in summations

c Speed of light in vacuum

c{iJj}
LCAO coefficient of the jth basis function on atom J in the ith molecular orbital

e 2.718281828..., charge on the electron

$\hbar$ Planck's constant/2π

i Inversion symmetry element, square root -1, molecular orbital index

j Basis function index in summations

j{l}(pr)
Spherical Bessel function

$\underline{k}_0$ Momentum vector of the incident (e,2e) electron

$\underline{k}_1, \underline{k}_2$
Momentum vectors of the two exit (e,2e) electrons

l Angular quantum number, length

m Electron mass, metres

mm Millimeters

n Principal quantum number

n{A}
Number of basis functions on atom A

nm Nanometres

ns Nanoseconds

p|| Component of momentum parallel to the bond direction

p||{max}
Maximum probable momentum in the direction parallel to the bond

$p\underline{|}$ Component of momentum perpendicular to the bond direction

$p_{\perp}\{max\}$
Maximum probable momentum in the direction perpendicular to the bond

p,θ,ϕ
Momentum-space spherical polar coordinates

$\underline{p},p$ Momentum vector and magnitude

$p\{max\}$
Most probable momentum

$p\{x\},p\{y\},p\{z\}$
Momentum-space Cartesian coordinates

$\underline{q},q$ Momentum vector and magnitude

$q\{\frac{1}{2}max\}$
Momentum at which the experimental MD has fallen to half its q=0 intensity in an s-type distribution

$q\{max\}$
Most probable momentum (in an experimental distribution)

r,θ,ϕ
Position-space spherical polar coordinates

$\underline{r},r$ Position vector and magnitude

s Seconds

t Time

torr
Unit of pressure. 1torr=1mmHg

x,y,z
Position-space Cartesian coordinates

$x\{i,n\}$
Hole state amplitudes of the Green's function

A Atom index in summations, antisymmetrization operator

C Overlap of non-interacting orbitals in a transition probability

E Energy loss

$E(M^{*+})$
Total energy of the target ion M^{*+}

E(M)
Total energy of the target molcule M

E_0 Energy of the incident binary (e,2e) electron

E_1,E_2
Energies of the two exit (e,2e) electrons

E{pass}
Energy an electron must have to pass through on electrostatic analyser

E{retard}
The reduction in energy of an electron passing through an electron lens

$F\{i\}(q)$
Binary (e,2e) form factor

$G(\omega)$
Green's function of energy

J Atom index in summations

L Length

M (e,2e) scattering amplitude, target molecule before (e,2e) collision

M*+ Target ion after collision

N Number of atoms, number of electrons, normalization factor

$\underline{P}$ Momentum operator

P{nl}(p)
Radial part of a P-space atomic orbital wavefunction

Q(r),Q(p)
One-dimensional wavefunction projection

R{nl}(r)
Radial part of an R-space atomic orbital wavefunction

S{i}
Intensity factors in the binary (e,2e) cross-section

$T(\underline{k}_1,\underline{k}_2;\epsilon,\underline{k}_0)$, $T(\underline{r}_1,\underline{r}_2;\underline{r},\underline{r}_0)$
Mott scattering amplitude

$X_0(\underline{k}_0,\underline{r})$
Free (e,2e) incident electron wavefunction

Y{lm}(θ,φ)
Complex spherical harmonic functions

$\underline{\underline{1}}$ Unit matrix

A.2 Abbreviations

ADC Analog to digital converter

AO Atomic orbital

CFD Constant fraction discriminator

CI Configuration interaction

CP Charge preamplifer

DAC Digital to analog converter

DZ Double-zeta

FPP Fast pulse preamplifier

GSA Gaussian shaping amplifer

GTO Gaussian-type orbital

HF Hartree-Fock

LCAO Linear combination of atomic orbitals

MBGF Many-body Green's function

MCP Multichannel plate

MD Momentum distribution

MO Molecular orbital

NSO Natural spin orbital

PWIA Plane-wave impulse approximation

RHF Restricted Hartree-Fock

SCA Single channel analyser

SCF Self-consistent field

SH Sample and hold

STO Slater-type orbital

SZ Single-zeta

TAC Time to amplitude converter

TFA Timing filter amplifier

UHF Unrestricted Hartree-Fock

2ph-TDA Two-particle-one-hole Tamm-Dancoff approximation

A.3 Terms

Angular correlation
: The raw binary (e,2e) data as a function of scattering angles θ or ϕ.

Bond oscillation
: The manifestation of the molecular geometry in P-space: at large p the momentum density is tends to a pure sinusoidal oscillation, with a period inversely proportional to the bond length.

Bonding principle
: A set of axioms which describe the manifestations of bonding, non-bonding and antibonding character in an MO in R-space and P-space.

Coincidence
: The occurence of two events within a certain time interval.

Electron density
: The distribution of the probability of finding an electron at a point in R-space.

Form factor
: Binary (e,2e) form factor describing the distribution of intensity as a function of scattering angle.

Green's function
: A function that describes the propagation in space and time of a system of particles. The energy representation of the Green's function has poles at the energies of the particles.

Inner valence electrons
: Those valence electrons which, when ionized, lead to several final ion states with no particular main parent peak, distributed in energy above about 20eV.

Momentum density
: The distribution of the probability of finding an electron with a certain (vector) momentum.

Momentum distribution
: The experimental angular correlation obtained in the symmetric non-coplanar scattering geometry, plotted against q; also the spherically-averaged theoretical momentum density.

Mott scattering
The scattering of two identical particles in the Coulomb potential, including effects of exchange.

MFS structure
That structure in a binding energy spectrum, usually above 20eV, which arises because ionization of one inner valence orbital leads to multiple final ion states of different energies.

Nodal plane
A plane of symmetry where the wavefunction amplitude and density is zero.

Nodal surface
A surface of any shape where the wavefunction amplitude and density is zero.

Outer valence electrons
Those valence electrons which, when ionized, lead to one strong peak in the separation energy spectrum, generally below 20eV, and perhaps some very weak peaks at higher energy.

Plane wave
The wavefunction of a free particle $\exp(i\underline{k}.\underline{r})$.

Pole strength
The intensity of poles in the N-particle Green's function, a factor in the binary (e,2e) intensity.

Reciprocity principle
That attribute of the Fourier Transform where a dilatation of a dimension in R-space leads to a contraction of the dimension in P-space, and vice versa

Relative absolute intensity
Similar to 'relative intensity' (q.v.) but the scale bears some known relation to other similar plots.

Relative intensity
The ordinate of a plot of the measured signal rate against some scanned parameter. The scale bears no relationship to anything else.

Self-energy
The alteration in the energy of an ideal particle when it exerts a disturbing influence on surrounding ideal particles which in turn react back on the first particle to change its energy and convert it into a quasiparticle.

Symmetric coplanar
: The binary (e,2e) scattering geometry where the azimuthal scattering angle is fixed at 0° and the polar angle is scanned.

Symmetric non-coplanar
: The binary (e,2e) scattering geometry where the polar angle is fixed at $\theta=45^{\circ}$ and the azimuthal angle is scanned. This method gives the momentum distribution directly.

Wavefunction
: The mathematical function describing the amplitude of a particle or system of particles in space and time.

APPENDIX B DEFINITIONS AND DERIVATIONS

'Are you still awake?' Sam whispered.

B.1 Momentum Density Maps from LCAO-MO Wavefunctions

The wavefunction for the ith molecular orbital is expressed as a linear combination of Slater-type basis functions or of Gaussian primitives, thus:

$$\psi\{i\}(\underline{r}) = \sum_{J}^{N} \sum_{j}^{n\{J\}} c\{iJj\}\ \phi\{Jj\}(\underline{r}\{J\}) \qquad \text{(B.1)}$$

where $\phi\{Jj\}(\underline{r}\{J\})$ is the jth basis function on centre J, N is the number of atoms and n{J} is the number of functions on atom J. c{iJj} is the coefficient of the jth basis function on atom J in the ith molecular orbital, and the coordinate vector $\underline{r}\{J\}$ is referred to atom J, not the origin of R-space. The Fourier transform of this is:

$$\psi\{i\}(\underline{p}) = (2\pi)^{-3/2} \int d\underline{r}\ e^{-i\underline{p}.\underline{r}}\ \psi\{i\}(\underline{r}) \qquad \text{(B.2)}$$

If we define $\underline{r}=\underline{R}\{J\}+\underline{r}\{J\}$ where $\underline{R}\{J\}$ is the position vector

of centre J where the jth atomic orbital is situated, then:

$$\psi\{i\}(\underline{p}) = (2\pi)^{-3/2} \sum_{J}^{N} \sum_{j}^{n\{J\}} c\{iJj\}\, e^{-i\underline{p}.\underline{R}\{J\}} \times \int d\underline{r}\{J\}\, e^{-i\underline{p}.\underline{r}\{J\}}\, \phi\{Jj\}(\underline{r}\{J\})$$

$$= \sum_{J}^{N} \sum_{j}^{n\{J\}} c\{iJj\}\, e^{-i\underline{p}.\underline{R}\{J\}}\, \underline{\phi}\{Jj\}(\underline{p}) \qquad \text{(B.3)}$$

The integral is just the Fourier transform of the position space atomic orbital wavefunction. It is seen that the momentum space molecular orbital is a linear combination of atomic momentals, but the nuclear geometry information is removed from the atomic orbital and now appears in a phase factor exp(-ip.R{J}). If the basis functions are defined as:

$$\phi\{Jj\}(\underline{r}) = N\{j\}\, R\{n\{j\},l\{j\}\}\, Y\{l\{j\},m\{j\}\}(\Omega\{\underline{r}\}) \qquad \text{(B.4)}$$

with n=1,2,3...; l=0,1...n-1; m=-l...+l

and the following identity is used {Messiah (1958)}:

$$e^{-i\underline{p}.\underline{r}} = 4\pi \sum_{l=0}^{\infty} \sum_{m=-l}^{+l} (-i)^{l}\, j\{l\}(pr) \times Y\{lm\}(\Omega\{\underline{p}\})\, Y^{*}\{lm\}(\Omega\{\underline{r}\}) \qquad \text{(B.5)}$$

then the integral in equation B.3 becomes:

$$(B.6)\quad \sum_{l=0}^{\infty}\sum_{m=-l}^{+l}(-i)^{l}\sqrt{\frac{2}{\pi}}\int r^2dr\; j\{l\}(pr)\; R\{n\{j\},l\{j\}\}$$

$$\times\quad Y\{lm\}(\Omega\{\underline{p}\})\underbrace{\int d\Omega\{\underline{r}\}\; Y^*\{lm\}(\Omega\{\underline{r}\})\; Y\{l\{j\},m\{j\}\}(\Omega\{\underline{r}\})}_{=\delta\{l,l\{j\}\}\;\delta\{m,m\{j\}\}}$$

$$= N\{j\}\; P\{n\{j\},l\{j\}\}(p)\; Y\{l\{j\},m\{j\}\}(\Omega\{\underline{p}\})$$

where $P\{nl\} = (-i)^{l}\sqrt{\frac{2}{\pi}}\int r^2dr\; j\{l\}(pr)\; R\{nl\}(r)$

A contour plot of the momentum density may be generated directly from the wavefunction as $\rho\{i\}(\underline{p}) = \psi^*\{i\}(\underline{p})\psi\{i\}(\underline{p})$, which is the more straightforward way, and, in terms of computing considerations faster and less costly. It is also possible to expand the summation and partition the density into a sum of one-centre and two-centre contributions as follows:

$$(B.7)\quad \rho\{i\}(\underline{p}) = \left[\sum_{A}^{N}\sum_{a}^{n\{A\}} c\{iAa\}\; e^{-i\underline{p}.\underline{R}\{A\}}\; \phi\{Aa\}(\underline{p})\right]^*$$

$$\times\quad \left[\sum_{J}^{N}\sum_{j}^{n\{J\}} c\{iJj\}\; e^{-\underline{p}.\underline{R}\{J\}}\; \phi\{Jj\}(\underline{p})\right]$$

The one-centre part is:

$$(B.8a)\quad \rho_1\{i\}(\underline{p}) = \sum_{A}^{N} \sum_{a}^{n\{A\}} \sum_{b}^{n\{A\}} c^*\{iAa\}\, c\{iAb\} \times \phi^*\{Aa\}(\underline{p})\, \phi\{Ab\}(\underline{p})$$

The two-centre part is:

$$(B.8b)\quad \rho_2\{i\}(\underline{p}) = 2Re \sum_{\substack{A\,J \\ A<J}}^{N\,N} \sum_{a}^{n\{A\}} \sum_{j}^{n\{J\}} c^*\{iAa\}\, c\{iJj\}\, e^{i\underline{p}.\underline{R}\{AJ\}} \times \phi^*\{Aa\}(\underline{p})\, \phi\{Jj\}(\underline{p})$$

where $\underline{R}\{AJ\}=\underline{R}\{A\}-\underline{R}\{J\}$ is the R-space vector from atom A to atom J. The momentum density plots were generated by evaluation of either function over a mesh of 100x100 points in a plane in the molecule. Equation B.8 is general for any molecule. A similar derivation presented in the literature {Camilloni (1979)} for linear diatomic molecules contains an error in equation 16 of that reference: the sign of the exponent $i\underline{p}.\underline{R}\{AJ\}$ is given incorrectly.

B.2 Momentum Distributions from LCAO-MO Wavefunctions

In order to compare the theoretical density with experiment, equation B.8 must first be spherically averaged:

$$(B.9)\quad F\{i\}(p) = (4\pi)^{-1} \int d\Omega\, \rho\{i\}(\underline{p})$$

This gives the result {Levin (1975), Dey (1977)} used to

compute momentum distributions from theoretical LCAO-MO wavefunctions:

$$(B.10)\quad F\{i\}(q) = F\{at\} + F\{int\}$$

where

$$(B.11a)\quad F\{at\} = (4\pi)^{-1} \sum_{A}^{N} \sum_{a}^{n\{A\}} \sum_{b}^{n\{A\}} N\{a\}\, N\{b\}\, c^*\{iAa\}\, c\{iAb\}$$
$$\times\ P\{n\{a\}l\{a\}\}(p)\ P\{n\{b\}l\{b\}\}(p)$$
$$\times\ \delta\{l\{a\}l\{b\}\}\delta\{m\{a\}m\{b\}\}$$

and, using identity B.4 again:

$$(B.11b)\quad F\{int\} = 2\mathrm{Re} \sum_{A}^{N} \sum_{J}^{N} \sum_{a}^{n\{A\}} \sum_{j}^{n\{J\}} N\{a\}\, N\{j\}\, c^*\{iAa\}\, c\{iJj\}$$
$$A<J$$
$$\times\ P\{n\{a\}l\{a\}\}(p)\ P\{n\{j\}l\{j\}\}(p)$$
$$\times\ \sum_{lm}^{\infty} i^{l}\, j\{l\}(pR\{AJ\})\, Y\{lm\}(\Omega\{\underline{R}\{AJ\}\})$$
$$\times \int d\Omega\{\underline{p}\}\, Y^*\{lm\}(\Omega\{\underline{p}\})\, Y^*\{l\{a\}m\{a\}\}(\Omega\{\underline{p}\})\, Y\{l\{j\}m\{j\}\}(\Omega\{\underline{p}\}$$

The integral over three angular momenta gives:

$$(B.11c)\quad (-)^{m\{a\}} \left[\frac{(2l+1)(2l\{a\}+1)(2l\{j\}+1)}{4\pi}\right]^{1/2}$$
$$\times \begin{pmatrix} l & l\{a\} & l\{j\} \\ -m & m\{a\} & m\{j\} \end{pmatrix} \begin{pmatrix} l & l\{a\} & l\{j\} \\ 0 & 0 & 0 \end{pmatrix}$$

In computed momentum distributions in this thesis the

summation $l=0-\infty$ is truncated after convergence at $l=5$.

The analytical forms of the radial functions P{nl}(p) used in the computations are found by solution of the spherical Bessel transform {Levin (1975), Komarov (1976), Kaijser (1977), Epstein (1971)} and are given in Table B.1. The forms of the spherical harmonics are given in Table B.2.

The matrix to transform cartesian spherical harmonics, in which literature wavefunctions are usually expressed, into complex spherical harmonics, which are required in equations B.6 and B.11, is the following:

(B.12)

$$
\begin{bmatrix} Y\{s\} \\ Y\{x\} \\ Y\{y\} \\ Y\{z\} \\ Y\{x^2\} \\ Y\{y^2\} \\ Y\{z^2\} \\ Y\{xy\} \\ Y\{xz\} \\ Y\{yz\} \end{bmatrix} = \begin{bmatrix} 1 & 0 & 0 & 0 & 0 & 0 & 0 & 0 & 0 \\ 0 & 0 & \frac{-1}{\sqrt{2}} & \frac{1}{\sqrt{2}} & 0 & 0 & 0 & 0 & 0 \\ 0 & 0 & \frac{i}{\sqrt{2}} & \frac{i}{\sqrt{2}} & 0 & 0 & 0 & 0 & 0 \\ 0 & 1 & 0 & 0 & 0 & 0 & 0 & 0 & 0 \\ \frac{\sqrt{5}}{3} & 0 & 0 & 0 & \frac{-1}{3} & 0 & 0 & \frac{1}{\sqrt{6}} & \frac{1}{\sqrt{6}} \\ \frac{\sqrt{5}}{3} & 0 & 0 & 0 & \frac{-1}{3} & 0 & 0 & \frac{-1}{\sqrt{6}} & \frac{-1}{\sqrt{6}} \\ \frac{\sqrt{5}}{3} & 0 & 0 & 0 & \frac{2}{3} & 0 & 0 & 0 & 0 \\ 0 & 0 & 0 & 0 & 0 & 0 & 0 & \frac{-i}{\sqrt{2}} & \frac{i}{\sqrt{2}} \\ 0 & 0 & 0 & 0 & 0 & \frac{-1}{\sqrt{2}} & \frac{1}{\sqrt{2}} & 0 & 0 \\ 0 & 0 & 0 & 0 & 0 & \frac{i}{\sqrt{2}} & \frac{i}{\sqrt{2}} & 0 & 0 \end{bmatrix} \begin{bmatrix} Y_0^0 \\ Y_1^0 \\ Y_1^1 \\ Y_1^{-1} \\ Y_2^0 \\ Y_2^1 \\ Y_2^{-1} \\ Y_2^2 \\ Y_2^{-2} \end{bmatrix}
$$

Table B.1 Radial functions R{nl}(r) and P{nl}(p)

STOs

$$P\{1s\} = 2^{5/2}\,\pi^{-1/2}\,\zeta^{5/2}\,(p^2+\zeta^2)^{-2}$$

$$P\{2s\} = 2^{5/2}\,3^{1/2}\,\pi^{-1/2}\,\zeta^{5/2}\,(1-\tfrac{4}{3}p^2(p^2+\zeta^2)^{-1})\,(p^2+\zeta^2)^{-2}$$

$$P\{2p\} = i\,2^{9/2}\,3^{-1/2}\,\pi^{-1/2}\,\zeta^{7/2}\,(p^2+\zeta^2)^{-3}$$

$$P\{3s\} = 2^5\,5^{-1/2}\,\pi^{-1/2}\,\zeta^{9/2}\,(2\zeta^2(p^2+\zeta^2)^{-3/2}-(p^2+\zeta^2)^{-1/2})\,(p^2+\zeta^2)^{-5/2}$$

$$P\{3p\} = i\,2^5\,3^{-1}\,5^{1/2}\,\pi^{-1/2}\,\zeta^{7/2}\,(1-\tfrac{6}{5}p^2(p^2+\zeta^2)^{-1})\,(p^2+\zeta^2)^{-3}$$

$$P\{3d\} = -2^6\,5^{-1/2}\,\pi^{-1/2}\,\zeta p^2(p^2+\zeta^2)^{-4}$$

$$R\{1s\} = 2\,\zeta^{3/2}\,e^{-\zeta r}$$

$$R\{2s\},R\{2p\} = 2\,3^{-1/2}\,\zeta^{5/2}\,re^{-\zeta r}$$

$$R\{3s\},R\{3p\},R\{3d\} = 2^{3/2}\,3^{-1}\,5^{-1/2}\,\zeta^{7/2}\,r^2e^{-\zeta r}$$

GTOs

$$P\{1s\} = 2^{1/4}\,\pi^{-3/4}\,\alpha^{-1/4}\,e^{-p^2/4\alpha}$$

$$P\{2p\} = i\,2^{1/4}\,3^{-1/2}\,\pi^{-3/4}\,\alpha^{-3/4}\,pe^{-p^2/4\alpha}$$

$$R\{1s\} = 2^{7/4}\,\pi^{-3/4}\,\alpha^{3/4}\,e^{-\alpha r^2}$$

$$R\{2p\} = 2^{13/4}\,\pi^{-3/4}\,\alpha^{5/4}\,re^{-\alpha r^2}$$

Table B.2 Spherical harmonics

Complex spherical harmonics	Cartesian spherical harmonics
$Y_0^0 = (4\pi)^{-1/2}$	$Y\{s\} = (4\pi)^{-1/2}$
$Y_1^0 = \sqrt{\frac{3}{4\pi}}\,\frac{z}{r}$	$Y\{x\} = \sqrt{\frac{3}{4\pi}}\,\frac{x}{r}$
$Y_1^1 = -\sqrt{\frac{3}{8\pi}}\,\frac{x+iy}{r}$	$Y\{y\} = \sqrt{\frac{3}{4\pi}}\,\frac{y}{r}$
$Y_1^{-1} = \sqrt{\frac{3}{8\pi}}\,\frac{x-iy}{r}$	$Y\{z\} = \sqrt{\frac{3}{4\pi}}\,\frac{z}{r}$

APPENDIX C MISCELLANEOUS

'Mercy!' cried Gandalf...
'What more do you want to know?'
'The names of all the stars, and of all living things,
and the whole history of Middle-earth and Over-heaven
and of the Sundering Seas,' laughed Pippin.

Table C.1 Valence molecular orbital electronic structure. MOs are ordered by energy; occupancy is shown by the superscript; a bar separates outer valence from inner valence MOs where there is a sharp distinction; the symmetry is given underneath the name.

He	$(1s)^2$	Ne	$(2p)^6$ $(2s)^2$	Ar	$\frac{(3p)^6}{(3s)^2}$	Kr	$\frac{(4p)^6}{(4s)^2}$	Xe	$\frac{(5p)^6}{(5s)^2}$		
CH_4 T{d}	$(1t_2)^6$ $(2a_1)^2$	NH_3 C{3v}	$(3a_1)^2$ $(1e)^4$ $(2a_1)^2$	H_2O C{2v}	$(1b_1)^2$ $(3a_1)^2$ $(1b_2)^2$ $(2a_1)^2$	HF C{∞v}	$(1\pi)^4$ $(3\sigma)^2$ $(2\sigma)^2$				
				H_2S C{2v}	$(2b_1)^2$ $(5a_1)^2$ $\frac{(2b_2)^2}{(4a_1)^2}$	HCl C{∞v}	$(2\pi)^4$ $\frac{(5\sigma)^2}{(4\sigma)^2}$				
						HBr C{∞v}	$(4\pi)^4$ $\frac{(8\sigma)^2}{(7\sigma)^2}$				
						HI C{∞v}	$(6\pi)^4$ $\frac{(11\sigma)^2}{(10\sigma)^2}$				
H_2 D{∞h}	$(1s\{g\})^2$	N_2 D{∞h}	$(3\sigma\{g\})^2$ $(1\pi\{u\})^4$ $\frac{}{(2\sigma\{u\})^2}$ $(2\sigma\{g\})^2$	O_2 D{∞h}	$(1\pi\{g\})^2$ $(1\pi\{u\})^4$ $\frac{(3\sigma\{g\})^2}{(2\sigma\{u\})^2}$ $(2\sigma\{g\})^2$	CO_2 D{∞h}	$(1\pi\{g\})^4$ $(1\pi\{u\})^4$ $(3\sigma\{u\})^2$ $\frac{(4\sigma\{g\})^2}{(2\sigma\{u\})^2}$ $(3\sigma\{g\})^2$				
		CO C{∞v}	$(5\sigma)^2$ $(1\pi)^4$ $\frac{}{(4\sigma)^2}$ $(3\sigma)^2$	NO C{∞v}	$(2\pi)^1$ $(1\pi)^4$ $\frac{(5\sigma)^2}{(4\sigma)^2}$ $(3\sigma)^2$	COS C{∞v}	$(3\pi)^4$ $(2\pi)^4$ $(9\sigma)^2$ $\frac{(8\sigma)^2}{(7\sigma)^2}$ $(6\sigma)^2$				

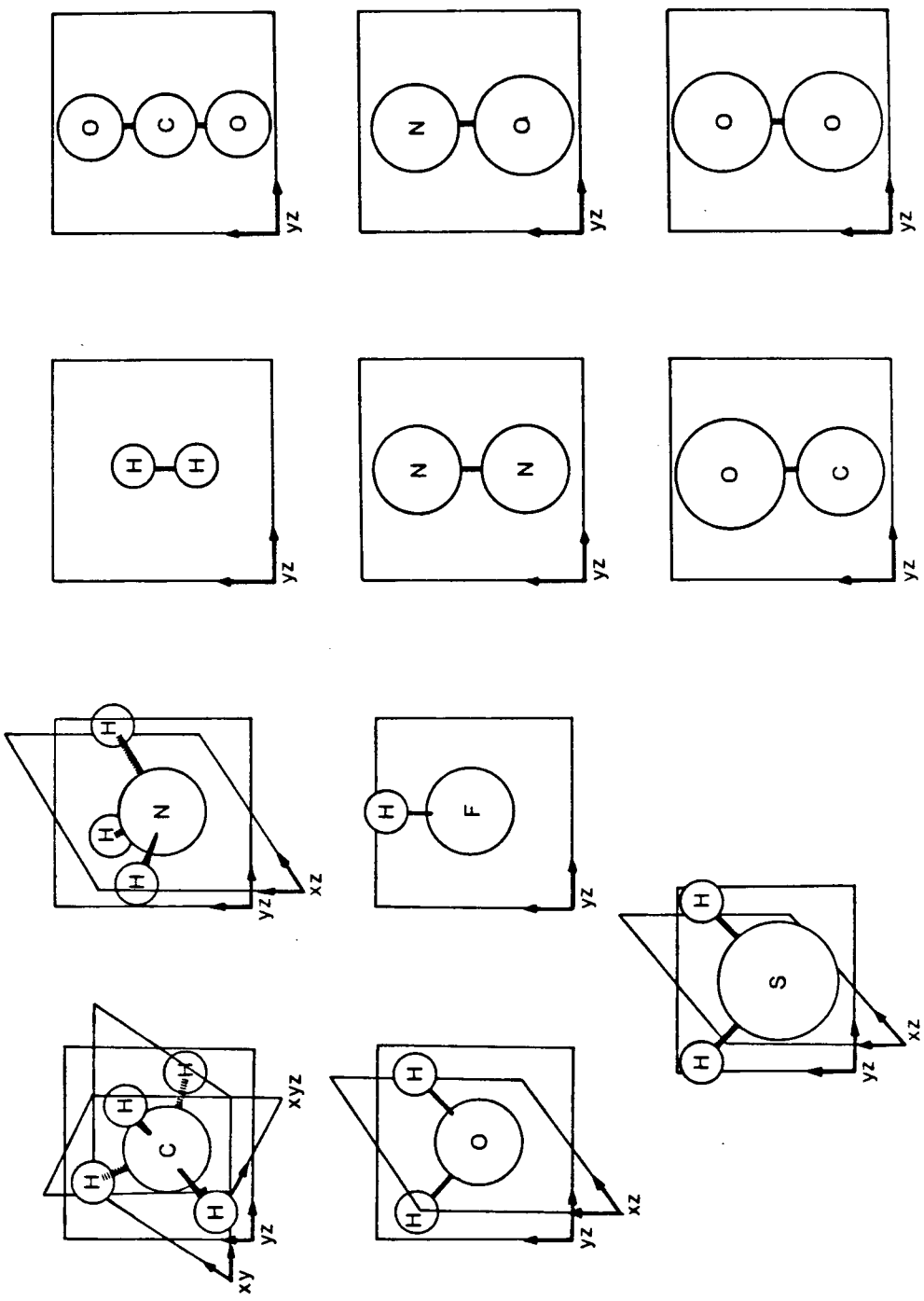

Figure C.1 Geometry and contour map planes for selected molecules.

APPENDIX D REFERENCES

...there lie in his hoards many records that few can now read, even of the lore-masters, for their scripts and tongues have become dark to later men.

Literature references to journal articles are given as:

Principle author surname (year) thesis pages
Full names of all authors
Journal name volume page

References to books are given as:

Principle author surname (year) thesis pages
Full names of all authors
Title
Publisher

Aberg (1967) 148
T Aberg
Phys Rev 156 35

Allan (1972) 147,161,169,174,187
CJ Allan U Gelius DA Allison G Johansson H Siegbahn and K Siegbahn
J El Spect 1 131

Asbrink (1974) 192
L Asbrink and C Fridh
Phys Scr 9 338

Asbrink (1977) 186
L Asbrink C Fridh and E Lindholm
Chem Phys Letters 52 63

Basch (1972) 51,58,75,170,187
H Basch and LC Snyder
Molecular Wave Functions and Properties
Wiley New York

Bicerano (1977) 145
J Bicerano DS Marynick and WN Lipscomb
J Am Chem Soc 100 732

Bradshaw (1980) 29
AM Bradshaw W Eberhardt HJ Levinson W Domcke and LS Cederbaum
Chem Phys Lett 70 36

Brion 125,202
CE Brion
private communication

Brion (1975) 19
CE Brion
Radiat Res 64 37

Brion (1977) 19
CE Brion A Hamnett GR Wight and MJ van der Wiel
J El Spect 12 323

Brion (1978a) 19
CE Brion and KH Tan
Chem Phys 34 141

Brion (1978b) 14,125,139
CE Brion JPD Cook and KH Tan
Chem Phys Letters 59 241

Brion (1979) 125
CE Brion IE McCarthy IH Suzuki and E Weigold
Chem Phys Letters 67 115

Brion (1980) 125
CE Brion ST Hood IH Suzuki E Weigold and GRJ Williams
J El Spect 21 71

Brion (1981) 19,21
CE Brion and A Hamnett
Adv Chem Phys 45 2

Camilloni (1977) 18
R Camilloni A Giardini-Guidoni G Missoni G Stefani G Tiribelli and D Vinciguerra
AIP Conf Proc 36 205

Camilloni (1978) 18
R Camilloni A Giardini-Guidoni IE McCarthy and G Stefani
Phys Rev A 17 1634

Camilloni (1979) 278
R Camilloni G Stefani R Fantoni A Giardini-Guidoni
J El Spect 17 209

Cederbaum (1975a) 23
LS Cederbaum
J Chem Phys 62 2160

Cederbaum (1975b) 23
LS Cederbaum
J Phys B 8 290

Cederbaum (1977) 23,29,157
LS Cederbaum and W Domcke
Adv Chem Phys 36 205

Cederbaum (1978) 29,167
LS Cederbaum W Domcke J Schirmer W von Niessen GHF Diercksen and WP Kraemer
J Chem Phys 69 1591

Cederbaum (1980) 29,167,171
LS Cederbaum W Domcke J Schirmer and W von Niessen
Phys Scr 21 481

Chipman (1978) 140
DW Chipman
J El Spect 14 323

Chong 186
DP Chong
private communication

Chong (1974) 157
DP Chong FG Herring and D McWilliams
J Chem Phys 61 78

Clementi (1963) 134
E Clementi and DL Raimondi
J Chem Phys 38 2686

Clementi (1964) 134
E Clementi
J Chem Phys 40 1944

Clementi (1974) 38
E Clementi and C Roetti
At Data and Nucl Data Tables 14 177

Cook (1979) 125
JPD Cook CE Brion and A Hamnett
J El Spect 15 233

Cook (1980) 14,17,125
JPD Cook CE Brion and A Hamnett
Chem Phys 45 1

Cook (1981) 14,161
JPD Cook MG White CE Brion W Domcke J Schirmer LS Cederbaum and W von Niessen
J El Spect 22 261

Coulson (1944) 31,71
CA Coulson and WE Duncanson
Proc Camb Phil Soc 40 190
and references contained therein

Cruikshank (1968) 143
DWJ Cruikshank and BC Webster
Inorganic sulphur chemistry (ed G Nickless)
Elsevier Amsterdam

Dey (1977) 278
S Dey AJ Dixon KR Lassey IE McCarthy PJO Teubner E Weigold PS Bagus and EK Viinikka
Phys Rev A 15 102

Diercksen 163
GHF Diercksen and WP Kraemer
MUNICH Molecular Program System Reference Manual Special Technical Report
Max-Planck Institut fur Physik und Astrophysik

Diercksen (1974) 163
GHF Diercksen
Theor Chim Acta 33 1

Dirac (1958) 33
PAM Dirac
The Principles of Quantum Mechanics
Oxford University Press London

Dixon (1977) 125
AJ Dixon S Dey IE McCarthy E Weigold and GRJ Williams
Chem Phys 21 81

Domcke (1975) 192
W Domcke and LS Cederbaum
J Chem Phys 64 612

Domcke (1978) 126,139,141
W Domcke LS Cederbaum J Schirmer W von Niessen and JP Maier
J El Spect 14 59

Domcke (1979) 29,167,169,174,186,187,188
W Domcke LS Cederbaum J Schirmer W von Niessen CE Brion and KH Tan
Chem Phys 40 171

Epstein (1971) 280
IR Epstein
Chem Phys Letters 9 9

Epstein (1973) 31
IR Epstein
Acc Chem Res 6 145

Epstein (1977) 31
IR Epstein and AC Tanner
Compton Scattering (ed B Williams)
McGraw-Hill International

Giardini (1977) 170,174,187
A Giardini-Guidoni R Tiribelli D Vinciguerra R Camilloni and G Stefani
J El Spect 12 405

Goddard (1978) 30,141
J Goddard and IG Csizmadia
J Chem Phys 68 2172

Guest (1976) 134
MF Guest and WR Rodwell
Mol Phys 32 1075

Hamnett (1976) 21
A Hamnett W Stoll G Branton CE Brion and MJ van der Wiel
J Phys B 9 945

Hamnett (1977) 17,125
A Hamnett ST Hood and CE Brion
J El Spect 11 263

Hillier (1970) 134
LH Hillier and VR Saunders
Chem Phys Letters 5 384

Hillier (1971) 144
IH Hillier and VR Saunders
Mol Phys 22 193

Hood (1973) 4
ST Hood IE McCarthy PJO Teubner and E Weigold
Phys Rev A 8 2494

Hood (1976a) 30,125
ST Hood A Hamnett and CE Brion
Chem Phys Letters 39 252

Hood (1976b) 17
ST Hood A Hamnett and CE Brion
Chem Phys Letters 41 428

Hood (1977) 30,77,84,125,133,135,141,238
ST Hood A Hamnett and CE Brion
J El Spect 11 205

Huzinaga (1965) 162
S Huzinaga
J Chem Phys 42 1293

Inokuti (1971) 19,21,118
M Inokuti
Rev Mod Phys 43 297

Kaijser (1977) 280
P Kaijser and VH Smith Jr
Adv Quant Chem 10 37

Karlsson (1976) 127
L Karlsson L Mattsson R Jadrny T Bergmark and K Siegbahn
Phys Scripta 13 229

Komarov (1976) 280
FF Komarov and MM Temkin
J Phys B 9 L255

Koopmans (1933) 22
TA Koopmans
Physica 1 104

Kouba (1971) 203,212
JE Kouba and Y Ohrn
Int J Quant Chem 5 539

Kunz 58,72,203,213
AB Kunz and K Bedford
private communication

Kwart (1977) 145
H Kwart and KG King
'Reactivity and structure concepts in organic chemistry vol 1'
'd-orbitals in the chemistry of silicon phosphorous and sulphur'
Springer Berlin

Levin (1975) 71,278,280
VG Levin VG Neudatchin AV Pavlitchenkov and YuF Smirnov
J Chem Phys 63 1541

Lohmann 262
B Lohmann and E Weigold
private communication

Maier 139
JP Maier
private communication

Mattuck (1967) 24
RD Mattuck
A Guide to Feynman Diagrams in the Many-body Problem
McGraw-Hill London

McCarthy (1976a) 4,7,17,18,125
IE McCarthy and E Weigold
Phys Rep C 27 275

McCarthy (1976b) 4,18,125
IE McCarthy and E Weigold
Adv Phys 25 489

Messiah (1958) 276
A Messiah
Quantum Mechanics
North-Holland Amsterdam

Moore (1978) 223,242
JH Moore MA Coplan TL Skillman and ED Brooks
Rev Sci Instr 49 463

Neudachin (1969) 4
VG Neudachin GA Novoskol'tseva YuF Smirnov
Soviet Physics JETP 28 540

Rabalais (1977) 17,138
J Rabalais
Principle of ultraviolet photoelectron spectroscopy
Wiley New York

Ratner (1971) 144
MA Ratner and JR Sabin
J Am Chem Soc 93 3542

Risley (1972) 88,239
JS Risley
Rev Sci Instr 43 95

Rothenberg (1970) 143,144
S Rothenberg and HF Schaefer
J Chem Phys 53 3014

Schirmer (1977) 29,157,167
J Schirmer LS Cederbaum W Domcke and W von Niessen
Chem Phys 26 149

Schirmer (1978) 27
J Schirmer and LS Cederbaum
J Phys B 11 1889

Siegbahn (1969) 17
K Siegbahn C Nordling G Johansson J Hedman PF Heden K Harmin U Gelius T Bergmark L-O Werme R Manne and Y Baer
ESCA Applied to Free Molecules
North-Holland Amsterdam

Siegbahn (1972) 136,138
K Siegbahn C Nordling G Johansson J Hedman PF Heden K Harmin U Gelius T Bergmark L-O Werme R Manne and Y Baer
ESCA Applied to Free Molecules
North-Holland Amsterdam

Sinanoglu (1966) 203
O Sinanoglu and C Hollister
J Am Chem Soc 88 13

Suzuki (1980a) 125
IH Suzuki CE Brion E Weigold and GRJ Williams
Int J Quant Chem 18 275

Suzuki (1980b) 195,210,213
IH Suzuki E Weigold and CE Brion
J El Spect 20 289

Thouless (1961) 24
DJ Thouless
The Quantum Mechanics of Many-Body Systems
Academic Press New York

Tossell (1981) 198,261,263
JA Tossell JH Moore MA Coplan
J El Spect 22 61

Turner (1970) 127,136,141,173,175,195,196,197
DW Turner C Baker and CR Brundle
Molecular photoelectron spectroscopy
Wiley Interscience

Van Hoof (1980) 227
HA van Hoof and MJ van der Wiel
J Phys E 13 409

Veillard (1968) 163
A Veillard
Theor Chim Acta 12 405

Von Niessen (1977) 144
W von Niessen LS Cederbaum W Domcke and GHF Diercksen
J Chem Phys 66 4893

Weigold (1973) 125
E Weigold ST Hood and PJO Teubner
Phys Rev Letters 30 475

Weigold (1975) 125
E Weigold ST Hood and IE McCarthy
Phys Rev A 11 566

Weigold (1976) 125
E Weigold S Dey AJ Dixon IE McCarthy and PJO Teubner
Chem Phys Letters 41 21

Weigold (1978) 4
E Weigold and IE McCarthy
Adv At Mol Phys 14 127

White (1980) 161,168
MJ White T Leung and CE Brion
J El Spect 23 127

Williams (1978) 89
JF Williams
J Phys B 11 2015

Zeiss 135,136
GD Zeiss
private communication

Zeiss (1979) 30,146
GD Zeiss WR Scott N Suzuki and DP Chong
Mol Phys 37 1543

'Why, you have nearly finished it,
Mr. Frodo!' Sam exclaimed.
'Well, you have kept at it, I must say.'
'I have quite finished it, Sam,' said Frodo.